ICME2015

International Conference on Mechanical Engineering 2015
(ICME 2015) 18 – 20 December, 2015, Dhaka, Bangladesh

Paper ID : 037

Performance & Stability Analysis of a Three Lobe Journal Bearing With Varying Parameters: Experiments and Analysis

Nabarun Biswas[1, a], Dr. Prasun Chakraborti [2,b], Ankuran Saha[2, c], Srijit Biswas[1,d]

[1]*Department of Production Engineering, National Institute of Technology, Jirania, Barjala, Agartala, Tripura-799046, India.*
[2]*Department of Mechanical Engineering, National Institute of Technology, Jirania, Barjala, Agartala, Tripura-799046, India.*

[a)] Corresponding author: mechanical.biswas@gmail.com
[b)]pchakraborti@rediffmail.com
[c)]ankuran.saha@gmail.com
[d)]iamsrijit91@gmail.com

Abstract. 3-lobe Hydrodynamic oil journal bearings are widely used in heavy industries as a part of different rotating machinery due to their high level of performances. 3-lobe hydrodynamic oil journal bearing allows the transmission of large amounts of loads at a mean speed of rotation. In this present work, an attempt has been made to investigate the pressure domain and subsequent effects in a 3 lobe journal bearing under different static loads in a stable operating speed. Analytical calculations were carried out with codes generated using Matlab software. Experiments were performed in Journal Bearing test rig incorporating 3-lobe under different loads with stable operating speed of 1000 RPM. It has been observed that an increase in load resulted rise in pressure profile, maximum pressure angle and temperature. A further attempt has been made to see the effect of eccentricity ratio and dynamic viscosity considering no change in the RPM. It has also been observed that dynamic viscosity has a significant effect on the stable operating speed. With the reduction in static load, the stability of operating speed attained at higher values.

INTRODUCTION

To suppress instability under lightly loaded conditions multi-lobe journal bearings are preferable. To support the rotating machinery in bearings two lobes, three lobes and four lobes are vividly used. The recent demands for higher performance of automotive engines and turbo machinery require the crankshaft and connecting rod bearing to operate under more severe condition like higher speeds, higher loads and higher temperature. To meet these requirements plain bearing with symmetrical lobe has been developed. Various tests have been conducted to improve the performance of plain bearing under these conditions in both materials and design and possibility has been formed in modifying the geometry of the bearing. Although it is generally believed that surface unevenness impairs hydrodynamic performance. Memmott and Santiago [1] studied a classical sleeve bearing instability of an overhung compressor. The introduction of 2-lobe lemon bore bearing with suitable lubricating oil shown better performance compared to sleeve bearings as they are incompetent to under conditions of extensively increasing speed and vibration. The 2-lobe bearing actually worked as a seal which was fixed on the high-pressure side of the compressor. Better solution of the problem obtained by engaging a bearing seal arrangement with 4- lobe bearing with moderate preload. Martin and Ruddy [2] emphasized on effect of manufacturing tolerances on the stability of

profile bore bearings. Their key findings are: -The preface of new quantities of speed is independent of the clearance and the clearance is independent of speed. They provide a more specific study of a problem than quantities like M' and W' that occur due to many factors and are not independent of machining allowances. For 4-lobe bearing this method could be well executed. As there is no possibility of loss of thermal quantities over them, the tighter bearing tolerances results in higher instability at increased condition of speed and turbulence. The tolerances are classified in two different parts of them like the tolerances on the bearing itself and the tolerances on the shaft. Both of the clearances have an individual role in the instability in the bearings caused at very high speeds. The tolerances are based on the fact that tighter tolerances give the higher instability like vibrations, overheat and wear and tear. K. Raghunandana [3] investigated on "Inverse Design Methodology for the Stability Design of Elliptical Bearings Operating with Non-Newtonian Lubricants". Their key findings were: -The lubrication being measured Newtonian in nature incidentally allows in error in computation of many critical parameters. This study gives steady state results for different L/D and eccentricity ratios in the form of empirical equations. Therefore the simulation with the variety of data and with the aid of computational methods various factors like oil film density and oil film viscosity could be found out for various NON-NEWTONIAN fluids and for BINGHAM plastics too. Chris A. Papadopoulos et al. [4] worked on "Identification of clearances and stability analysis for a rotor journal bearing system."Their main findings are given below. Due to support rotating shafts for long periods of time, as a result, significant wear occurs on the surface of the bearings. Therefore, they require for a new clearance recognition method is required. Furthermore, having acknowledged these new clearances, the finding of gauging reliable future operation with regards to stability is also a significant task. Here, using the finite element method with 4DOF's per node the rotor is modelled, considering the effect of gyroscopic. The dynamic coefficients of the bearing are considered by solving the Reynolds equation, thus getting the pressure distribution of the oil film, and by finding the equilibrium zone. The 4×4 stiffness and damping matrices, counting the force-moment and displacement-rotation relations with all non-diagonal coupling terms, are taken into account for the research. Here, a recognized method for the bearing radial clearances is presented theoretically, using response measurements of the rotor at a particular point (usually the midpoint of the rotor). The different wear effect and two different speeds are considered for these measurements. The present theoretical work on this particular problem needs to be confirmed experimentally as well. The sum of the squares of the differences between the calculated and the computed responses at the aforesaid particular point and for two different speeds is used as an objective function to be minimized. The stability of the system as a function of the rotational speed and the wear is also examined. B. C.Majumder and M. C. Majumdar [5] worked on "theoretical investigation of stability using a non-linear transient method for an externally pressurized porous gas journal bearing". This work associated with the journal centre locus. As a result, the system stability can be achieved. B. C. Majumdar investigated the whirl instability of externally pressurized gas-lubricated journal bearings. The Quasi-static assumption is considered in this theoretical analysis. S.K.Kakoty and B.C Majumdar [6] experimented on "Effect of fluid inertia on the stability of oil journal bearings". To analyse the mass parameter (a measure of stability) also finding out the steady state individuality of finite journal bearings in mind the effect of fluid inertia an attempt was made. In this paper, analytical & experimental work has been revealed a multi-lobe bearing has found to be more stable under high load and a three lobe bearing possesses good stability characteristics as turbo machinery works on high speed and load hence would act has a better replacement for plain journal bearing. Previously very few authors have found those who investigated the stable domain under stable operating speed, dynamic viscosity, eccentricity and performance of 3-lobe bearing varying with speed, external loads, and lubrication oil. In this research paper first attempt (analytical part) has been done to see the effect of eccentricity ratio and dynamic viscosity on stable operating speed. It has been observed that dynamic viscosity has a significant effect on the stable operating speed. With the deduction in static load, the higher stable operating speed can be attained. And second attempt (experimental part) has been made to see that at a constant speed and with same lubrication oil, with the increase of load the pressure profile also increases for 3-lobe bearing. In the present work, it is also found that at a higher load the maximum pressure and maximum temperature gets generated along with the maximum pressure angle.

GEOMETRY OF 3-LOBE BEARING

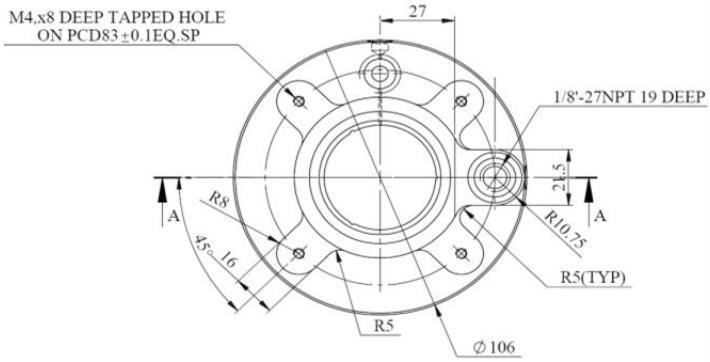

FIGURE 1. Experimental model of 3-lobe bearing

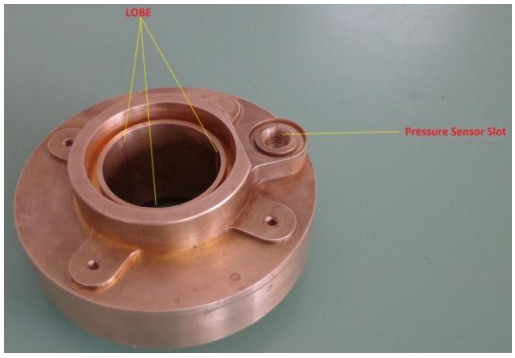

FIGURE 2. Three lobe bearing drawing

METHODOLOGY

Pressure distribution is attained by the relation,

$$P = 6\omega_j \mu \left(\frac{r_j}{c}\right)^2 \varepsilon \sin\theta\,(2+\varepsilon\sin\theta)/[(2+\varepsilon)^2(1+\varepsilon\cos\theta)^2] \quad \ldots.(1)$$

In order to find the generated load, the average pressure is determined from the equation (i), the generated load is calculated using the relation below.

$$W = P_{Avg} * L * D_j \quad \ldots. (2)$$

From the literature, the minimum film thickness can be derived from the relation

$$h_0 = mr_j(1-\varepsilon) \quad \ldots. (3)$$

The performance of the bearing is determined by varying the eccentricity ratio (ε) for a certain value of dynamic viscosity (μ) using Equation (ii).

The slope of the graph between Performance of the bearing and eccentricity ratio represents the stiffness of the lubricated film,

$$Stiffness\ (K) = {}^{\Delta W}/_{\Delta h_0} \quad \ldots. (4)$$

$$\text{Frequency (f)} = 1/2\pi\sqrt{Kg/w} \quad \ldots. (5)$$

The stable frequency of operation for a particular static load is determined using the relation (iv) and (v).

A Matlab program is generated to observe the effects of parameters like dynamic viscosity, eccentricity ratio on the stability of the 3-lobe bearing. 3D graphs are plotted to show the stable domain for different journal speed. Flow chart of the program is given in Fig. 4 and the setup of the bearing test rig is shown in Fig. 3

EXPERIMENTAL PROCEDURE

The journal is housed in spindle supported in the bearing. Spindle housing is fixed firmly to the base plate. The journal is rotated by an AC motor through pulley arrangements, on top of the spindle an RPM sensor disc is mounted to measure speed. Diameter and length of the brass bearing are made equal to get ratio l/d = 1. A narrow orifice inside bearing lets oil into the pressure sensor mounted area. The bearing is mounted on the bottom of a metallic bellow and on top of bellow a frictional torque load cell is mounted. Load cell unit is mounted onto indexing pulley. Indexing pulley is driven by the stepper motor. Angular range for the stepper motor is set up to 1800, in 90 steps. A lever arrangement is provided with a lever ratio of 1:5. To one end of the lever a loading pan is attached on which the weights can be placed in the range of 50N to 200N and speed 1000 RPM considered. In this experimental work SAE 20W-40 lubrication used. At the other end is mounted a ball bearing through which the load is applied to the brass bearing. The lever is pivoted to get 1:5 loading ratio. An oil filling arrangement is provided on

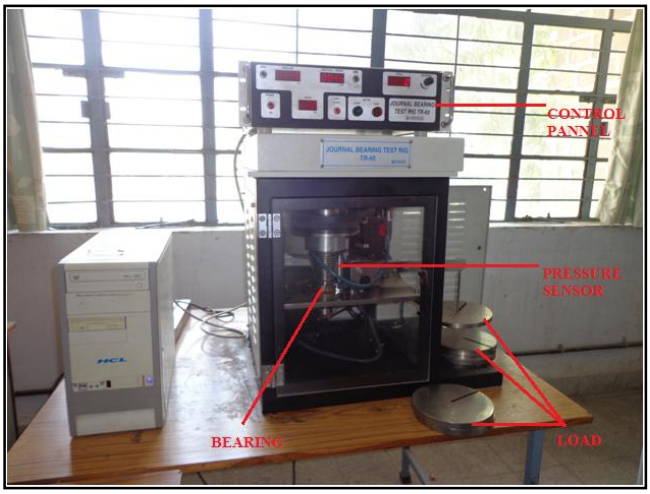

FIGURE 3. Journal Bearing Test Rig

the top of the base plate to gravity feed the brass bearing by means of a flexible tube before the start of the test to remove any trapped air. An oil sump is provided to ensure continuous lubrication of the journal bearing. The oil sump is placed on a bottom base plate, which is fixed on to the supporting structure. A calibrated pressure sensor to measure up to 1000psi is fixed to the bearing to measure pressure at various points around the journal (Fig no. 3). Output is 100mv for 1000 psi. Test parameter such as disc speed can be set with the front panel settings on the controller. The load is applied by dead weights through loading lever assembly. The pressure and Torque readings are displayed along with indexing angle during the test. Pressure and Angle readings are processed and serially transmitted through data acquisition cable.

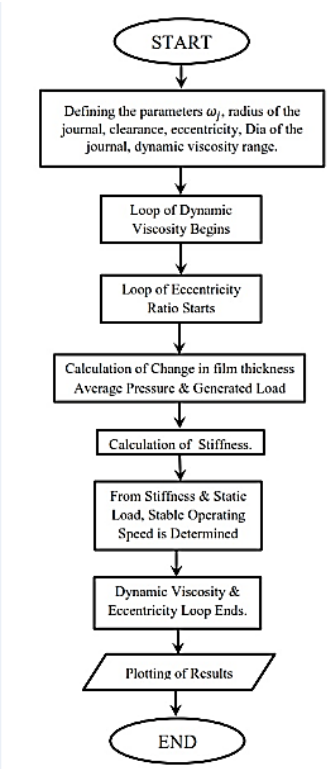

FIGURE 4. Flow chart of the Methodology

RESULTS AND DISCUSSIONS

Matlab Generated Results

In this present work, an attempt has been made to get a stable domain of operation of a bearing under varying eccentricity ration and dynamic viscosity. It has been observed that dynamic viscosity and eccentricity ratio has a significant effect on the stability of a bearing as the maximum stable operating speed gets affected due to the combined effect of these two. At the same time, the effect of static load on the journal is also investigated.

From figure 1 to 4 the stable domain of operation is generated using MATLAB Software. It has been observed that the stable domain speed of operation is very low compared to the operating speed for a larger domain under various static loads. For a higher dynamic viscosity, the maximum stable operating speeds get influenced significantly. It is seen that eccentricity ration has a very negligible effect on the stable operating speed at higher dynamic viscosity. However, with the increase of static load stable operating speed shows descending trend.

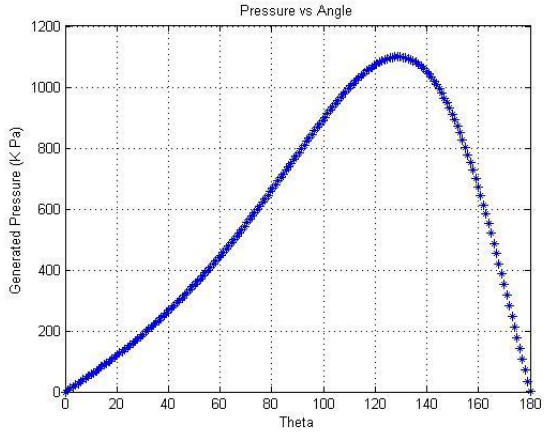

FIGURE 5. Generation of Pressure vs Angle (Has good resemblance with existing literature)

Generation of Pressure

The variation of generating pressure vs theta with the value of ω_j= 1000 rad/s and μ = Dynamic Viscosity, N-S/m^2. The generated pressure is considered for half cycle in order to calculate the average pressure. With the methodology used in "Stability Analysis of Hydrodynamic Journal Bearing using Stiffness Coefficients" we will formulate the stiffness and as well as stable frequency domain considering the effect of dynamic viscosity and eccentricity ration. The effect of Eccentricity ration and Dynamic Viscosity has been investigated. For different static load condition, it has been observed that stable frequency range gets significantly affected.

Journal speed of almost 9500 RPM

The maximum stable velocity 8810 RPM at $\mu = 0.08919$ N-s/$m^2$and eccentricity ratio 1. With journal speed 9500 RPM and 50 N load it has been observed that with variations of the eccentricity ratio from 0 to 1 a worth mentioning stable operating speed range from 4000 RPM to 8800 RPM is obtained.

With 100 N static load and with a dynamic viscosity value of 0.08919 the maximum stable operating speed is 6230 RPM. With the increase of static load stable operating frequency gets significantly decreased, but with higher values of 'mu' stable frequency increases.

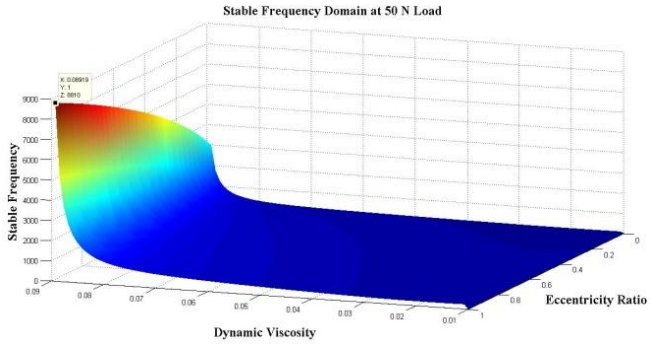

FIGURE 6. Stable domain of operation under 50 N static load on Journal in 9500 RPM journal speed.

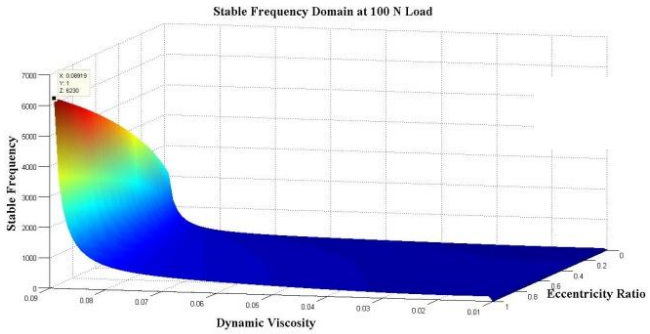

FIGURE 7. Stable domain of operation under 100 N static load on Journal in 9500 RPM journal speed.

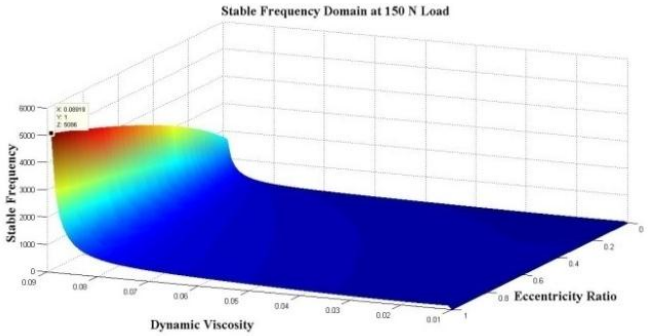

FIGURE 8**.** Stable domain of operation under 150 N static load on Journal in 9500 RPM journal speed.

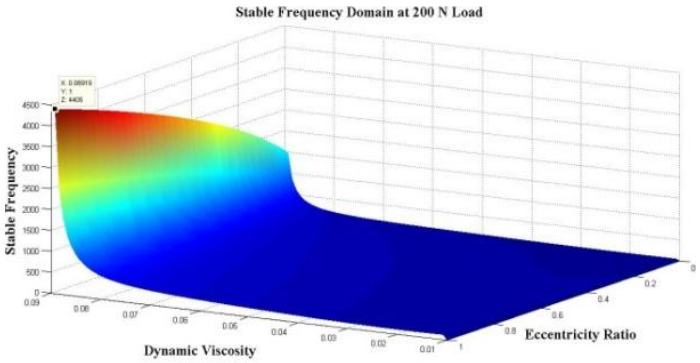

FIGURE 9. Stable domain of operation under 200 N static load on Journal in 9500 RPM journal speed.

Journal speed of almost 14500 RPM

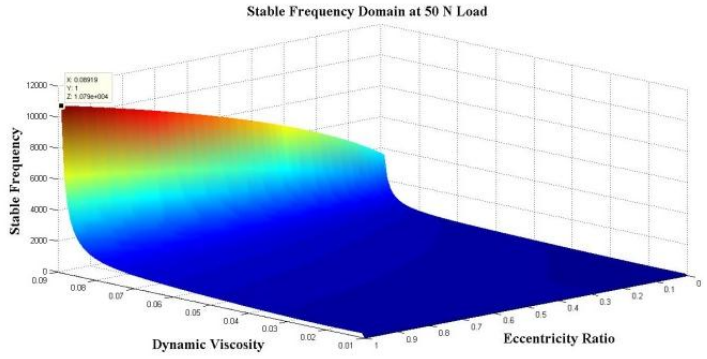

FIGURE 10. Stable domain of operation under 50 N static load on Journal in 14500 RPM journal speed.

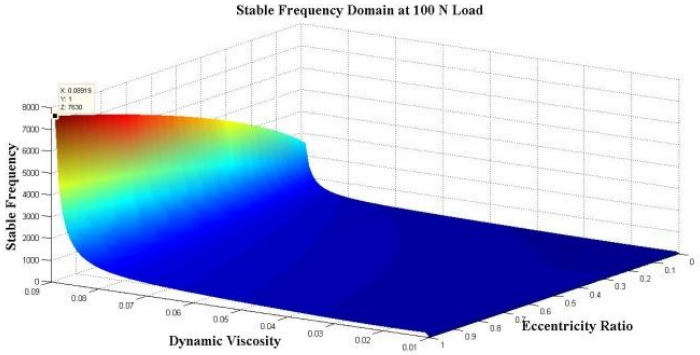

FIGURE 11. Stable domain of operation under 100 N static load on Journal in 14500 RPM journal speed.

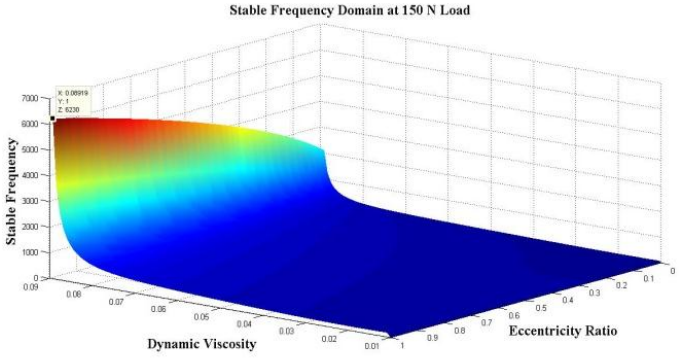

FIGURE 12. Stable domain of operation under 150 N static load on Journal in 14500 RPM journal speed.

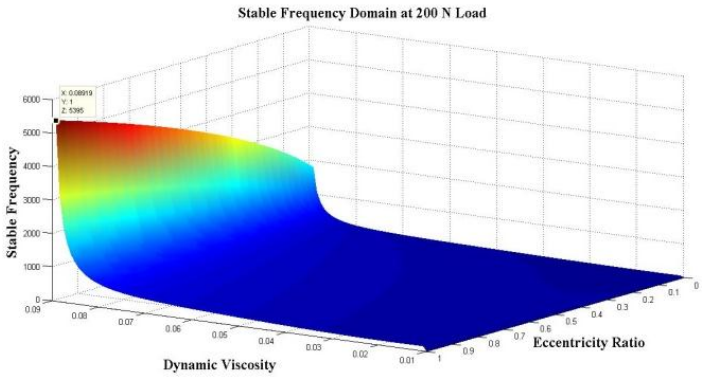

FIGURE 13. Stable domain of operation under 200 N static load on Journal in 14500 RPM journal speed.

Higher rotational speed gives an increase in stable operational speed in various static loads as shown in table 1.

Table 1. Variation of Stable operating speed with varying static load condition under different journal speed.

Static Load	**Maximum Stable Operating Speed**	
	At 9500 RPM Journal Speed	At 14500 RPM Journal Speed
At 50 N Static Load	8810 RPM	10790 RPM
At 100 N Static Load	6230 RPM	7630 RPM
At 150 N Static Load	5096 RPM	6230 RPM
At 200 N Static Load	4405 RPM	5395 RPM

Test Rig Generated Results

Pressure distribution and temperature of Lobe Journal Bearing

Lobe Bearing with Loads 50N and speed 1000 rpm
P_{max}- 833.17 kpa Initial temperature- 35° C
P_{max} angle- 96° Final temperature- 45° C

Lobe Bearing with Loads 100N and speed 1000 rpm
P_{max}- 984.84kpa Initial temperature- 40° C
P_{max} angle -97° Final temperature- 45° C

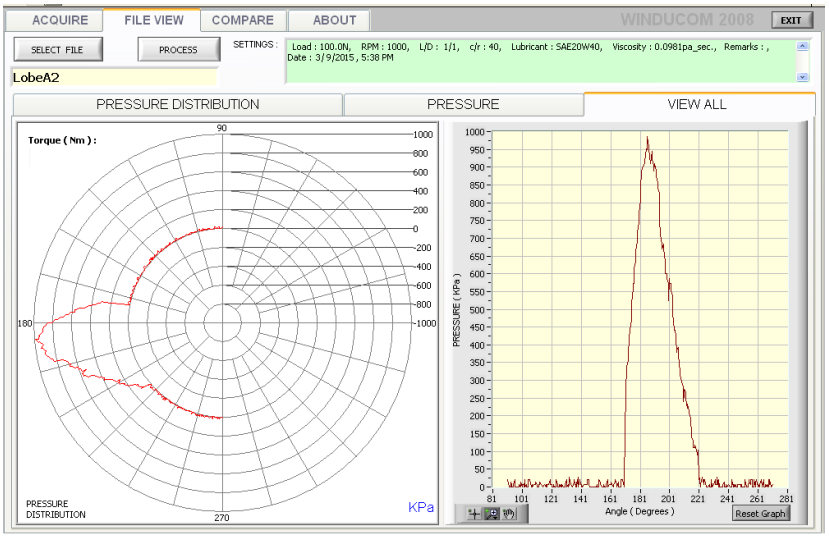

FIGURE 14. Pressure distribution of Lobe bearing at 50N load and 1000rpm

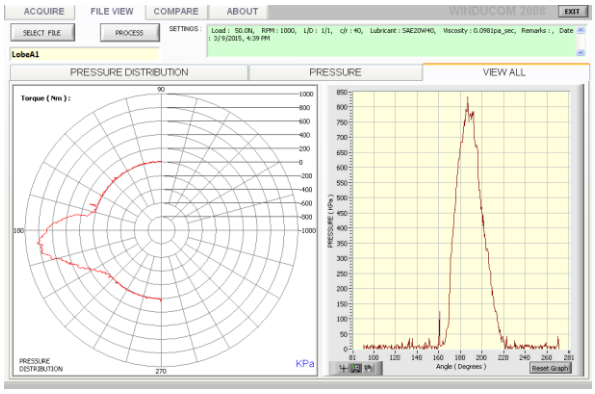

FIGURE 15. Pressure distribution of Lobe bearing at 100N load and 1000rpm

In the fig. 14, from the pressure profile of lobe bearing, it has been observed that the generated maximum pressure is 833.17 kpa at an angle of 96^0, in the condition of the load 50N and speed 1000 RPM while the temperature increased 35^0C from 45^0C.

In the fig. 15, from the pressure profile of lobe bearing, it has been observed that the generated maximum pressure is 984.84 kpa at an angle of 97^0, in the condition of load 100N and speed 1000 RPM while the temperature increased 40^0C from 45^0C.

Lobe Bearing with Loads 150N and speed 1000 rpm

P_{max}- 985.84 kpa Initial temperature- 35° C
P_{max} angle- 93 Final temperature- 47° C

Lobe Bearing with Loads 200 N and speed 1000 rpm

P_{max}- 1053.70 kpa Initial temperature- 35° C
P_{max}angle- 94° Final temperature- 49° C

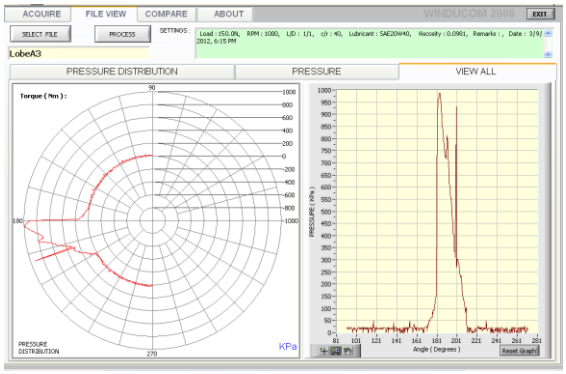

FIGURE 16. Pressure distribution of Lobe bearing at 150N load and 1000rpm

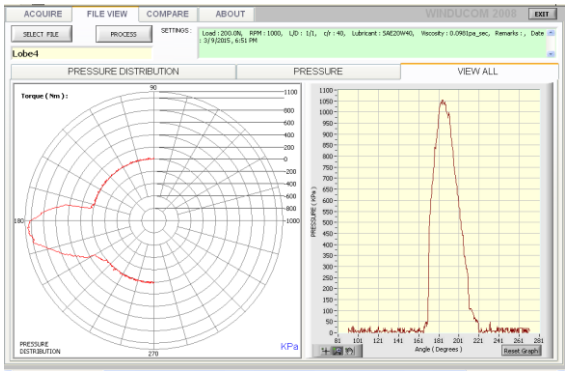

FIGURE 17. Pressure distribution of Lobe bearing at 250N load and 1000rpm

In the fig. 16, from the pressure profile of lobe bearing, it has been observed that the generated maximum pressure is 985.84 kpa at an angle of 93^0, in the condition of load 150N and speed 1000 RPM while the temperature increased 35^0C from 47^0C.

In the fig. 17, from the pressure profile of lobe bearing, it has been observed that the generated maximum pressure is 1053.70 kpa at an angle of 94^0, in the condition of the load 200N and speed 1000 RPM while the temperature increased 35^0C from 49^0C.

CONCLUSIONS

In this work, an attempt has been made to investigate the effects of parameters like dynamic viscosity & eccentricity ratio on the stable operating domain of a three lobe oil journal bearing. Journals are rotated under different static load and different RPM for observation. Matlab 3-D graphs have been plotted to represent the stability domain by showing the effect of dynamic viscosity & eccentricity ratio. In this experimental part, it has been observed that the nature of maximum pressure is steady in lobe hydrodynamic journal bearing at high load. The angle of maximum pressure gets shifted (reduces) as the load increases. It has been observed that with higher dynamic viscosity a significant increase of stable operating speed is attained. It is also observed that the increasing eccentricity ratio shows an increase in the maximum stable operating speed. With the increase of static load, declining trends of stable operating speed is observed. A higher journal speed a considerable increase of stable operating speed is observed. This analytical study may be helpful in the operation of a three lobe journal bearing in a preferred domain by controlling the parameters of operation. In the experimental part, it is found that at a constant speed and with same lubrication oil, with the increase of load the pressure profile also increases for 3-lobe bearing. In the present work it is also found that at higher loads (200N) maximum pressure and the maximum temperature gets generated along with the maximum pressure angle.

ACKNOWLEDGMENTS

Authors of the paper greatly acknowledge the support received from Department of Mechanical Engineering, and Production Engineering, National Institute of Technology, Agartala, Tripura, India.

REFERENCES

1. E.A. Memmott and O. De Santiago, “A classical sleeve bearing instability in an overhung compressor”, CMVA (2007).
2. F.A Martin and A.V. Ruddy, “The effect of manufacturing tolerances on the stability of profile bore bearings”, (1984)494-499 .
3. K. Raghunandana, “Inverse Design Methodology for the Stability Design of Elliptical Bearings Operating with Non-Newtonian Lubricants”, World Congress on Engineering and Computer Science, (2007)24-26.
4. C.A. Papadopoulos and P.G. Nikolakopoulos, G.D. Gounaris, “Identification of clearances and stability analysis for a rotor-journal bearing system”, Mechanism and Machine Theory ,**43 (4)** 411-426(2008).
5. M. C. Majumder and B. C. Majumdar, “Non-linear transient analysis for an externally pressurized porous gas journal bearing”, Wear, **132(1)**, 139-150, (1989).
6. S.K.Kakoty and B.C Majumdar, “Effect of fluid inertia on stability of journal bearings”, Journal of Trobology, **122,** 741-745, (2000).

ICME2015

International Conference on Mechanical Engineering 2015
(ICME 2015) 18 – 20 December, 2015, Dhaka, Bangladesh

Paper ID : 041

Mechanical Property Evaluation of PALF/Polyester Bio-Composite

Md. Milon Hossain[1a)], A.H.M Fazle Elahi[1b)], Shahida Afrin[2c)], Mubarak A. Khan[3d)], and M A Jalil[4e)]

[1]*Department of Textile Engineering, Khulna University of Engineering & Technology, Fulbari, Khulna-9203, Bangladesh*
[2]*Abdur Rab Serniabad Textile Engineering College, University of Dhaka, Dhaka-1000, Bangladesh*
[3]*Institute of Radiation and Polymer Technology, Bangladesh Atomic Energy Commission, Savar, Dhaka-1000, Bangladesh*
[4]*Department of Textile Engineering, Norhtern University Bangladesh, Banani, Dhaka-1213, Bangladesh.*

[a)]Corresponding author: milon_te@yahoo.com
[b)]fazle.elahi.ashek@gmail.com
[c)]safrin.te@gmail.com
[d)]makhan.inst@gmail.com
[e)]jalil.mbstu@gmail.com

Abstract. Searching for new type of materials from different renewable resources are increasing day by day. Pineapple leaf fiber (PALF) is relatively new member in this group and drawn the significant attention because of its low cost, light weight and non-toxicity. In this experiment, PALF/polyester composite was prepared by hand layup process. Chemical treatment was performed on the surface of PALF to enhance the quality of the composite. Different mechanical properties such as tensile strength, tensile modulus, and elongation at break percentage of the fabricated composite were evaluated as a function of PALF content. The results revealed that PALF content improves the composite performance significantly. Higher mechanical properties were reported for 30% PALF content. Tensile strength and tensile modulus increases about 131% and 172% respectively compared to neat polyester. Furthermore, chemical treatment proposed on fiber surface also increased the mechanical properties of the composite.

INTRODUCTION

With the increase of environmental awareness, bio fibers are being explored extensively by researchers in various applications. Natural fibers from vegetable origins come as a viable and ample substitute for the expensive synthetic fibers. These natural fibers have wonderful mechanical properties, lower cost, bio-degradability, and are abundantly available in nature [1]. In recent years, numerous studies were conducted on natural fibers to replace synthetic fibers as a reinforcement in composite [2-5]. Natural fiber composites are more economic compared to synthetic fiber based composites. This composites are suitable in different applications such as automobiles, building construction, furniture materials, packaging etc [6]. Among the different natural fibers, PALF contains

higher cellulose content which exhibits superior mechanical properties (70-82%) and comparatively low microfibrillar angle [7]. PALF are come from the leaves of the plant Ananas comosus (Bromeliaceae family) is one of the most essential tropical fruits in the world after banana and citrus [8]. Pineapple ranked 2nd among all the fruits produced in Bangladesh in terms of total cropping area (67842 acres). The total production of pineapple during 2010-2011 was 218.6 thousand metric tons [9]. Pineapple leaves are discarded as agricultural waste which can be obtained easily without additional cost input. The chemical composition of PALF constitute holocellulose (70–82%), lignin (5–12%), and ash (1.1%) [6]. Due to the presence of hydroxyl groups in the chemical structure of PALF it absorbs moisture from air thus make it hydrophilic in nature and moisture content varies between 3 to 13%. This hydrophilic nature of PALF fibers can be reduced by different chemical treatments which in turns increase the fiber/matrix adhesion of the composite materials resulting better composite quality and properties. Unsaturated polyester is found to be the potential matrix materials for PALF fibers [10]. An investigation was carried out by Uma Devi et. al [11] on the mechanical behavior of PALF/Polyester composite as a function of function of fiber loading, fiber length, and fiber surface modification. With the increase of fiber content composite mechanical properties improved significantly. In this work mechanical properties of PALF reinforced polyester composite were investigated as function of fiber content. To increase the fiber-matrix adhesion the composites sample were immersed in NaOH solution (5% w/v) for 12 hours and 24 hours.

EXPERIMENTAL

The experiment was carried out by hand layup process to fabricate the composite samples by varying the PALF content from zero to 35%. Different mechanical properties were evaluated and recorded.

Materials

Unsaturated polyester and methyl ethyl ketone peroxide (MEKP) were supplied by Polyolefin Company Limited; Singapore and PALF of GSM 200 was purchased from Bangladesh Jute Research Institute. The resin liquid solidify when hardener additives MEKP is added, which is transparent liquid. For the fabrication of PALF, 5% MEKP were added for each 100gm of polyester resin at room temperature. The polyester resin used in this experiment with density 1.35 g/cm3 and the composite were fabricated by using 60% polyester resin with 40% PALF fabric.

Methods

Methods of PALF Surface Modification

PALF fabric were immersed in caustic solution (5% w/v) for 12 hours and 24 hours at room temperature. To remove extra NaOH from the PALF surface, the PALF fabric were washed with distilled water along with a few drops of acetic acid. After rinsing the treated PALF fabric, it was air dried for 3 days.

Methods of Composite Fabrication

The composite specimens were prepared by manual lay-up process. Unsaturated polyester resin and MEKP hardener were taken in a beaker. They were then mixed well and made ready for laminating reinforced mats. At first, a melot paper was placed on dried bottom part. Then some of the prepared resin mixture was sprayed evenly on the paper. After that, a piece of PALF fabric was placed on the resin mixture and parts of resin mixture was sprayed

on the fabric. Another piece of PALF fabric was placed and similarly rest of the resin mixture spread on the mat and so on. Four layers of PALF fabric were sandwiched with polyester resin. A melot paper was placed on the mat following which top part of the open mold was kept on the paper. The prepared samples were allowed to cure under pressure at room temperature. The manufacturing process of PALF/Polyester by hand lay-up process is shown in the Fig. 1.

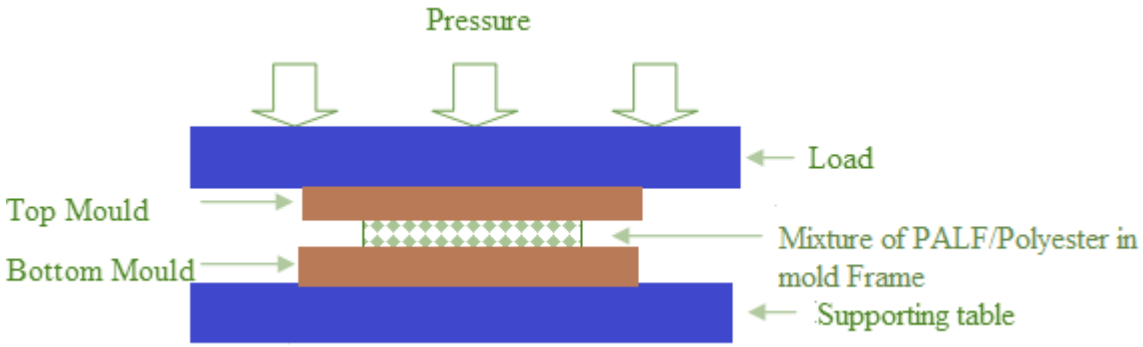

FIGURE1. Schematic diagram of PALF/Polyester manufacturing process.

Mechanical Testing of Composites

Tensile strength, tensile modulus and elongation at break% tests were conducted. For each test and type of composites, five specimens were tested and the average values were reported. Tensile tests were conducted according to ASTM D 638-01 using a Universal Testing Machine (Hounsfield series, model: INSTRON 1011, UK) with a cross-head speed of 10 mm/min as shown in the Fig.2 (a). The dimensions of the test specimen were (ISO 14125): 60 mm × 15 mm × 2 mm.Impact test for different fabricated composites were carried out according to ASTM D-256 as shown in the Fig. 2 (b). The length and width of the samples used in impact test were 61.5 mm and 12.7 mm respectively.

(a) (b)

FIGURE 2.a) Universal tensile testing machine b) Impact testing machine.

RESULTS AND DISCUSSION

Plain woven PALF reinforced polyester based composites were fabricated using open mould technique. The mechanical properties such as tensile strength, tensile modulus, elongation at break, were evaluated. The fabric weight fraction in the composites were varied from 0 to 35%. Tensile strength of the composites as a function of the fibre content is shown in Fig. 3. It is observed that tensile strength of the PALF/polyester composite increased significantly with the fibre content except for the higher fibre content percentage. Addition of 30% fibre content increase the tensile strength around 131%. Afterward further addition of 5% fibre decrease the tensile strength by almost 19%. This can be attributed to the high volume fraction fibres act as flaws and fibres are not properly aligned in the matrix. This may result in higher void content in the composite and shows lower tensile strength.

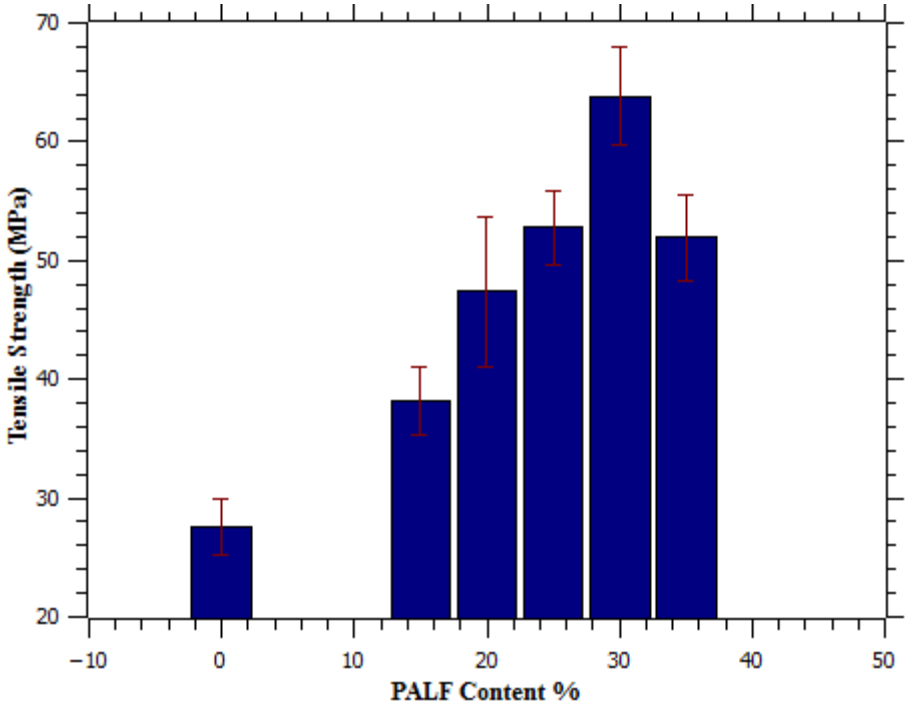

FIGURE 3. Tensile strength of PALF/composites.

Tensile modulus of PALF/Polyester composite is presented in the Fig. 4. An increasing trend in tensile modulus of the fabricated composite is evident except 35% fiber content. Highest tensile modulus of PALF/Polyester composite sample is observed 2.91 GPa (30% fiber content) whereas lowest tensile modulus is found by 1.88 GPa for the lowest addition of PALF content (15%) in composite compared to neat polyester. Composite sample containing 35% fiber content shows the deviation from the trend (regarding addition of PALF) and shows around 31% decrease in tensile modulus than the highest modulus.

Elongation of break in terms of different fiber content is illustrated in the Fig. 5. The elongation at break percentage is quite low in case of neat matrix. A gradual increasing trend is evident in elongation at break percentage for PALF/Polyester composite samples. Addition of PALF in pure polyester resin decreases the brittleness of polyester and, therefore, the elongation at break increases. It is note that failure elongation is almost 120% higher than the neat polyester observed for 35% PALF content.

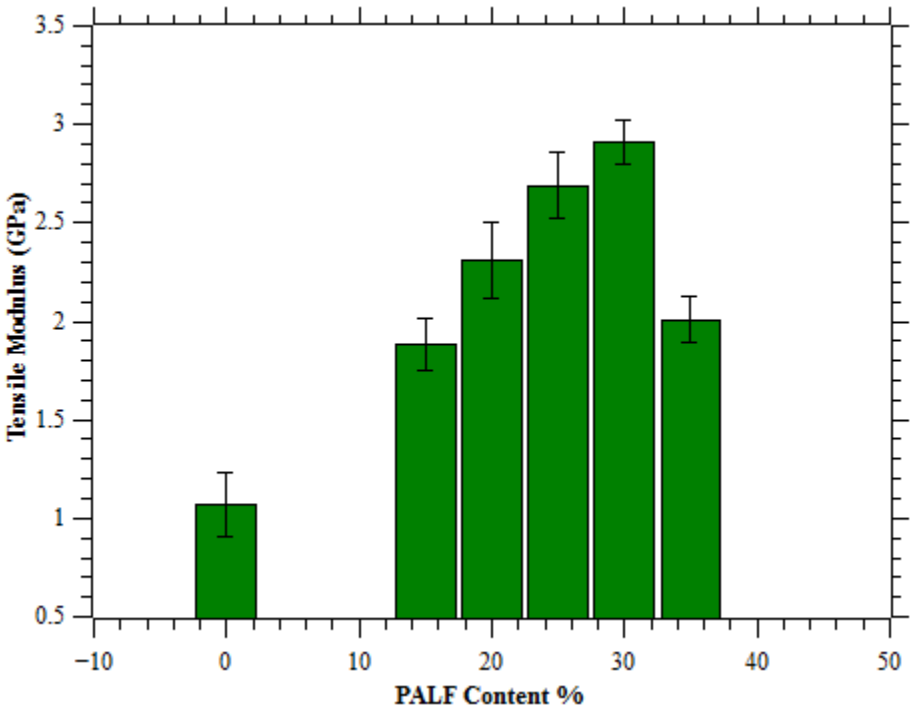

FIGURE 4.Tensile modulus of PALF/Polyester composite

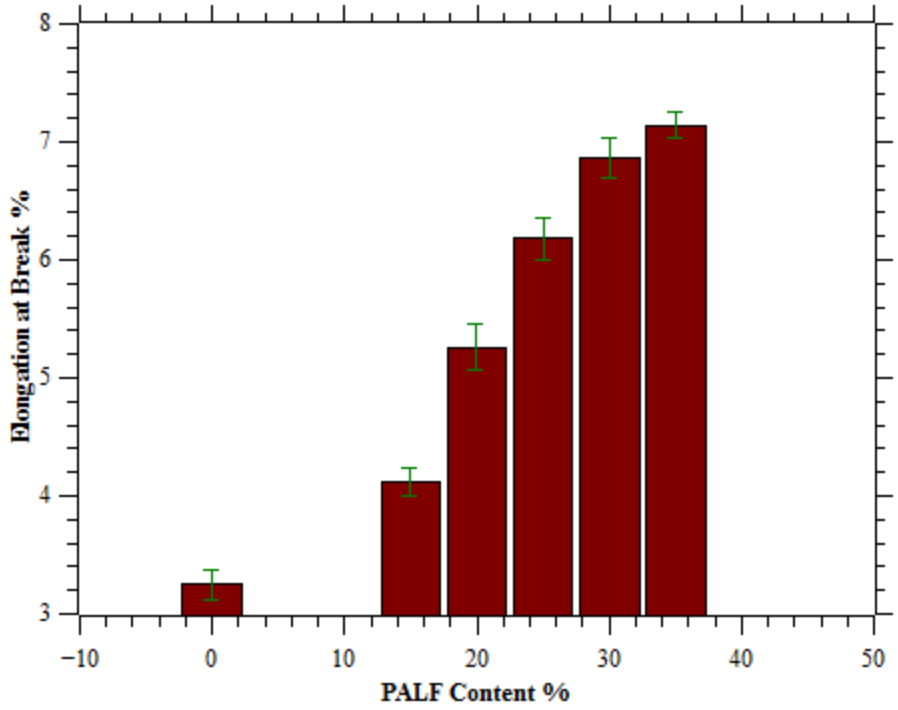

FIGURE 5. Elongation at break of PALF/Polyester composite

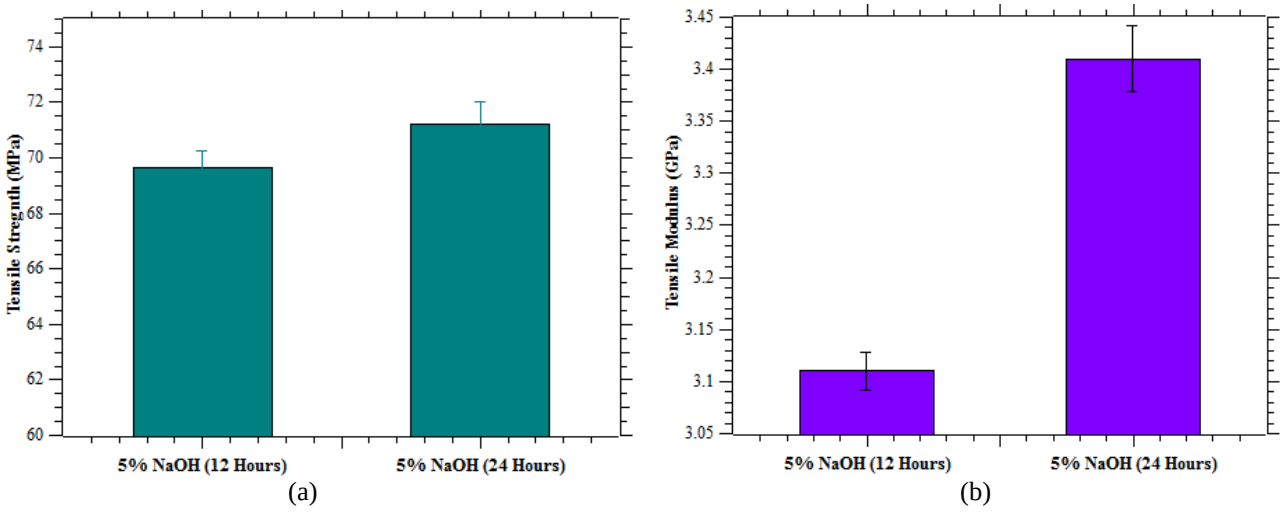

FIGURE 6. (a) Tensile strenght and (b) modulus of NaOH treated PALF/Polyester Composite

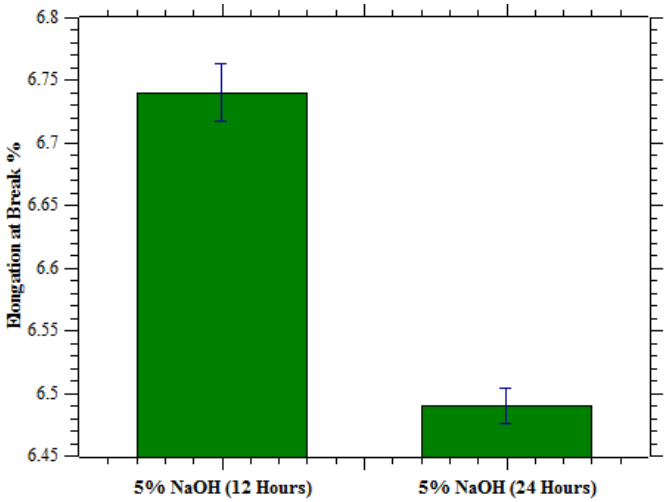

FIGURE 7. Elongation at break % of NaOH treated PALF/Polyester composites

The impact of chemical treatment on the PALF/Polyester composite is presented in the Fig. 6 and Fig. 7. The mechanical properties of the composite materials are greatly influenced by the interaction between fiber and matrix. The higher the interaction the higher the mechanical properties. The interfacial bond may be improved by the chemical treatment on the surface of the fiber. The result of 5% NaOH treatment for two different time period is found significant. It is observed that longer immersion times shows the best mechanical properties compared to shorter immersion times. Sample treated in NaOH for a day shows the highest tensile strength of 71.23 MPa than all other samples which is 11.55% higher than the maximum tensile strength of untreated sample. Tensile modulus of NaOH treated for 24 hours showed wonderful increase of 9.64% than sample treated for 12 hours. Alkaline immersion were more effective in removing different elements such as waxes, greases and impurities from the fiber surface. At longer alkaline immersion for coir fiber it was reported that the fibers were rendered more rugged and porous, without being significantly degraded, leading to better fiber wetting, to a stronger fiber/matrix interface and thus to better mechanical properties [12]. Though tensile strength and tensile modulus shows some improvement for longer immersion time; elongation at break decreases slightly below 4%.

CONCLUSIONS

It can be concluded from the above study that an effective bio-composite materials with sufficient mechanical properties can be fabricated by reinforcing PALF with polyester matrix. The mechanical properties of the PALF/Polyester composite increases with fiber content. The highest tensile strength and tensile modulus were recorded for 30% PALF content. Surface treatment of the composite by alkali promoted the fiber-matrix adhesion and thus yielded best mechanical properties. Higher immersion time shows the best mechanical properties. Finally, the investigated composite materials shows excellent mechanical properties and can be used in structural engineering applications..

ACKNOWLEDGMENTS

Authors are indebted to Institute of Radiation and Polymer Technology, Bangladesh Atomic Energy Commission for their laboratory facilities.

REFERENCES

1. M. S. Huda, L. T. Drzal, A. K. Mohanty and M. Misra, Compos. Interface **15,** 169– 191(2008).
2. A.K. Bledzki and J. Gassan, Prog. Polym. Sci **24,** 221-274 (1999).
3. S.K. Garkhail, R. W.H. Heijenrath and T. Peijs, Appl. Comp. Mater. **7,** 351-372 (2000).
4. F.G. Torres, O.H. Arroyo, and C. Gomez, J. Thermoplast. Comp. Mater. **20**, 207-223 (2007).
5. S. Mishra, A.K. Mohanty, L.T. Drzal, M. Misra, and G. Hinrichsen, Macromol. Mater. Eng. **289**, 955-974 (2004).
6. M. Asim, K. Abdan, M. Jawaid, M. Nasir, Z. Dashtizadeh, M. R. Ishakand M. E. Hoque, International Journal of Polymer Science, Article ID 950567 (2015).
7. L. U. Devi, S. S. Bhagawan and S. Thomas, Polym. Compos. **33,** 1064–1070(2012).
8. R. M. N. Arib, S. M. Sapuan, M. A. M. M. Hamdan, M. T. Paridah and H. M. D. K. Zaman, Polym. Polym. Compos. **12,** 341–348(2004).
9. Yearbook of Agricultural Statistics of Bangladesh, (Bangladesh Bureau of Statistics, 23rd Edition, Dhaka-2011), 124.
10. S. Mishra, M. Misra, S. S. Tripathy, S. K. Nayak and A. K. Mohanty, J. Reinf. Plast. Comp. **20,** 321-334(2001).
11. L. U. Devi, S. S. Bhagawan, and S. Thomas, J. Appl. Polym. Sci. **64,** 1739-1748(1997).
12. P. S. Mukherjee and K. G. Satyanarayana J. of Mat. Sci. **21,** 51-56(1986).

ICME2015

International Conference on Mechanical Engineering 2015
(ICME 2015) 18 – 20 December, 2015, Dhaka, Bangladesh

Paper ID : 046

Investigation of Displacement, Strain and Stress in Single Step Transversely Isotropic Elastic Bonded Joint

Md. Jakaria Apu[1, a)] and Md. Shahidul Islam [1, b)]

[1]*Dept. of Mechanical Engineering, Khulna University of Engineering & Technology, Khulna-9203, Bangladesh*

[a)]Corresponding author: apu.jakaria@gmail.com
[b)]shahidulbitk@gmail.com

Abstract. Bi-material joint is often used in many advanced materials and structures. Determination of the bonding strength at the interface is very difficult because of the presence of the stress singularity. In this paper, the displacement and stress fields of a transversely isotropic bi-material joint around an interface edge are determined. Autodesk Simulation Mechanical 2015 is used to carry out the numerical computations. Stress and displacement fields demonstrate that the values near the edge of joint where the stress singularity occurs are larger than that at the inner portion. From the numerical results, it is suggested that de-bonding of the interface may occur at the interface edge of the joint due to the higher stress concentration at the free edge.

Keywords: Transversely isotropic material, Finite element method, Bonded joint, Strength of bi-material joint, Single step joint.

INTRODUCTION

Bi-material joints can provide some advantages that cannot be provided by single material components. That's why adhesive bonding of dissimilar parts are widely used in the aerospace, automotive and electronic industries [1, 2]. Due to dissimilarity of material properties, de-bonding of bi-material joint initiates from the interface edge. A stress concentration occurs along the free edge of the interface, especially at the joint's vertex [3]. Besides, it is well known that there are discontinuities of material and geometry at the bonding edges in bonded joints. These discontinuities may cause singularities in the stress fields or very high stress concentration near the vertex of the bonding edges. This stress concentration/singularity may lead to the delamination initiation in the local area, and subsequently to the global failure of the joint structures [4, 5].

For the past three decades, researchers and engineers have been involved in the development of various techniques to analyze different kinds of bonded joints in composite structures. Efforts by the various groups have resulted in some useful computer programs [6]. One of the computer codes was written by Barthelemy, Kamat and Brinson [7]. They used eight-node elements for their analysis since the four-node element could not give good results. Harris and Adams [8] used a non-linear finite element method to predict strength of a bonded single-lap joint. The finite element program that they used was able to account for the large displacements and rotations that occur in a single lap joint, and allowed the effects of elasto-plasticity in both the adhesive and adherends to be modelled. Adams and Atkins [9] considered the strength of CFRP/steel lap joints loaded in tension and performed a detailed stress analysis of the shear and transverse stresses in the joint. Adams [10] used finite element methods for elastic and elasto-plastic case to predict strength of lap joints with composite adherends. Using the finite element approach, many researchers encountered problems trying to predict the strength of adhesively bonded joints because of stress singularities that exist if an interface results in a sharp corner. Therefore, several theoretical and experimental studies on the reduction of the stress singularity had been carried out [11-18].

In this paper the displacement, strain and stress of a transversely isotropic bi-material single step joint are determined by Finite Element Method. Titanium (Ti) and Zinc (Zn) are taken as the two dissimilar metal. Autodesk Simulation Mechanical 2015 is used to carry out the modelling and numerical computations. The characteristic of the joint under tensile load is investigated.

FORMULA OF ANALYSIS

In the absence of body forces, the equilibrium equations of elastic materials are expressed as follows [17]:

$$\sigma_{ij,j} = 0 \tag{1}$$

The constitutive relations are shown as follows:

$$\sigma_{ij} = C_{ijkl}\varepsilon_{kl} \tag{2}$$

The elastic strain-displacement relations are presented as follows:

$$\varepsilon_{ij} = \frac{1}{2}\left(u_{j,i} + u_{i,j}\right) \tag{3}$$

Where, $i, j, k, l = 1, 2, 3...$ and $\sigma_{ij}, \varepsilon_{ij}, u_i, C_{ijkl}$ are the component of stress, strain, elastic displacement, and elastic stiffness constant respectively.

For transversely isotropic material, taking *z*-axis parallel to the poling axis of the material, by convention, the constructive relation is expressed in the following form,

$$\{\sigma\} = [C]\{\varepsilon\} \tag{4}$$

Where, $\{\sigma\}$ and $\{\varepsilon\}$ are the stress and strain respectively, and $[C]$ is the elastic constant. The study which is concerned with a transversely isotropic (or unidirectional anisotropic) elastic material related to a material with the symmetry of a hexagonal crystal class 6 mm.

The following function maps a point in the local coordinate system to a point in global coordinate system for *N* nodes:

$$x = \sum_{i=1}^{N} N_i x_i, \quad y = \sum_{i=1}^{N} N_i y_i, \quad z = \sum_{i=1}^{N} N_i z_i \tag{5}$$

Where, (x, y, z) represent the Cartesian coordinate system and (x_i, y_i, z_i) represent the local coordinate system. The functions are linear combinations of the nodal coordinates. The coefficients N_1, N_2, N_3, N_4 are functions of ξ, η and ζ. They are the shape functions, so constructed that the eight corners of the hexahedron on the local coordinate system (ξ, η, ζ) are mapped to the eight nodes of the hexahedron on the global coordinate system $(\mathrm{x}, \mathrm{y}, \mathrm{z})$. The shape functions are given by

$$\begin{aligned}
N_1(\xi,\eta,\zeta) &= \frac{1}{8}(1-\xi)(1-\eta)(1-\zeta), \quad N_2(\xi,\eta,\zeta) = \frac{1}{8}(1+\xi)(1-\eta)(1-\zeta),\\
N_3(\xi,\eta,\zeta) &= \frac{1}{8}(1+\xi)(1+\eta)(1-\zeta), \quad N_4(\xi,\eta,\zeta) = \frac{1}{8}(1-\xi)(1+\eta)(1-\zeta),\\
N_5(\xi,\eta,\zeta) &= \frac{1}{8}(1-\xi)(1-\eta)(1+\zeta), \quad N_6(\xi,\eta,\zeta) = \frac{1}{8}(1+\xi)(1-\eta)(1+\zeta),\\
N_7(\xi,\eta,\zeta) &= \frac{1}{8}(1+\xi)(1+\eta)(1+\zeta), \quad N_8(\xi,\eta,\zeta) = \frac{1}{8}(1-\xi)(1+\eta)(1+\zeta)
\end{aligned} \tag{6}$$

Then the displacement field is obtained by

$$u = \sum_{i=1}^{N} N_i u_i, \quad v = \sum_{i=1}^{N} N_i v_i, \quad w = \sum_{i=1}^{N} N_i w_i \tag{7}$$

In matrix form Eq. (7) can be written as

$$u = Nq \tag{8}$$

Where, $u = \{u, v, w\}^{\mathrm{T}}$ and $q = \{u_1, v_1, w_1, u_2, v_2, w_2, ..., u_8, v_8, w_8\}^{\mathrm{T}}$.

Then the expression of strain becomes

$$\varepsilon = Du = DNq = Bq \tag{9}$$

And the expression of stress becomes

$$\sigma = C\varepsilon = CBq \tag{10}$$

The derivative of shape function, B is determined by computing the Jacobian matrix, J and J^{-1}. The notations are $J = \dfrac{\partial(x,y,z)}{\partial(\xi,\eta,\zeta)}$ and $J^{-1} = \dfrac{\partial(\xi,\eta,\zeta)}{\partial(x,y,z)}$.

Then,

$$\begin{bmatrix} \dfrac{\partial N_i}{\partial x} & \dfrac{\partial N_i}{\partial y} & \dfrac{\partial N_i}{\partial z} \end{bmatrix}^T = J^{-1} \begin{bmatrix} \dfrac{\partial N_i}{\partial \xi} & \dfrac{\partial N_i}{\partial \eta} & \dfrac{\partial N_i}{\partial \zeta} \end{bmatrix}^T \tag{11}$$

$$dV = dxdydz = |J| d\xi d\eta d\zeta \tag{12}$$

PROBLEM DESCRIPTION

Figure 1 represents the geometry of a typical case where a singular stress state occurs at the point O. The region surrounding the singular point is divided into a number of quadratic pyramidal elements with a summit O, with each element being located in spherical co-ordinate system *r, θ* and *φ* by its nodes 1 to 8.

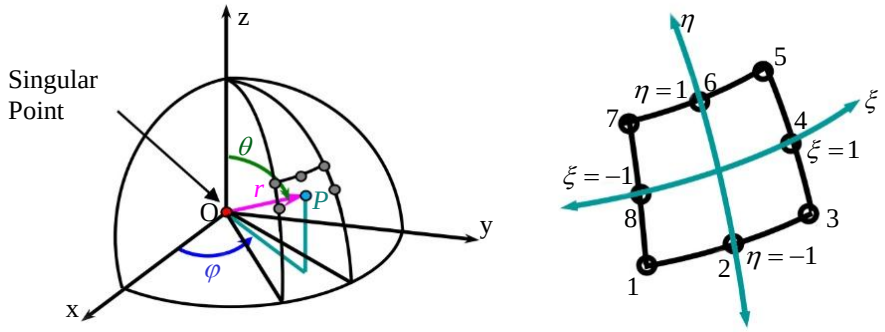

FIGURE 1. Element geometry and natural co-ordinates

The model considered for the analysis is shown in Figure 2. The dimensions are taken 40x20x20 mm in the *x*, *y* and *z* direction respectively. For the symmetric nature one fourth of the model is considered for analysis. The displacement in z-direction at the bottom of the model is fixed. The model is subjected to a uniform tension of 1 MPa. Zn and Ti are used as material 1 and material 2, respectively. The material constants are listed in Table 1.

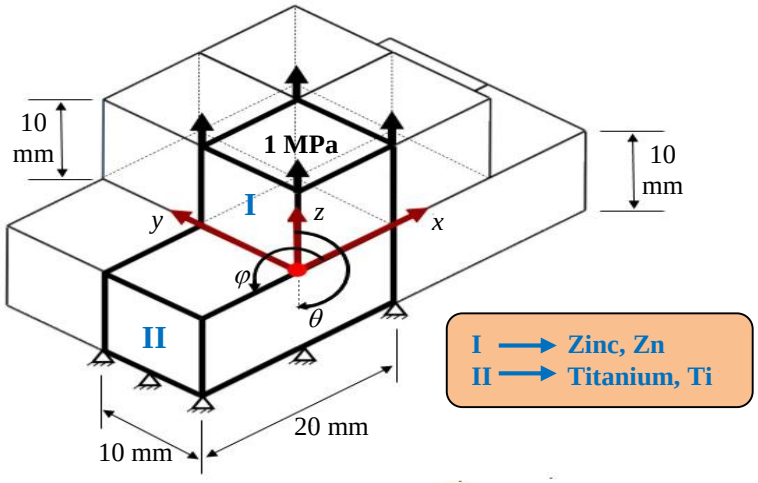

FIGURE 2. Model of analysis for elastic bonded joints.

TABLE 1. Material properties of transversely isotropic materials.

Material	$C_{11}(GPa)$	$C_{33}(GPa)$	$C_{44}(GPa)$	$C_{12}(GPa)$	$C_{13}(GPa)$
Zinc, Zn	161	61	38.3	34.2	50.1
Titanium, Ti	162.4	180.7	46.7	92	69

METHOD OF SOLUTION

Finite element method is used to carry out the numerical computation. The equations are solved by principle of virtual work method. The model of analysis shown in Figure 2 was created by the finite element code Autodesk Simulation Mechanical 2015. Fixed boundary condition is applied in the bottom surface. Symmetric boundary condition was applied in the two inner surface along *x* and *y* direction. A distributed load of 1 MPa was applied on the top surface along positive *z* direction. The mesh applied was a mixture of tetrahedron, pyramid, wedge and hexahedron. Overall mesh size was 0.5 mm whereas; at the vicinity of the vertex the mesh was refined to 0.0004035 mm. The total number of solid element was 520735.

ACCURACY VERIFICATION

In order to check the accuracy of finite element method the bi-material joint of Silicon and Resin having slanted side surface which was analyzed by Koguchi [18] in boundary element method, BEM has been analyzed again with the present method applying the same boundary condition. The obtained results have been compared with that obtained by Koguchi.

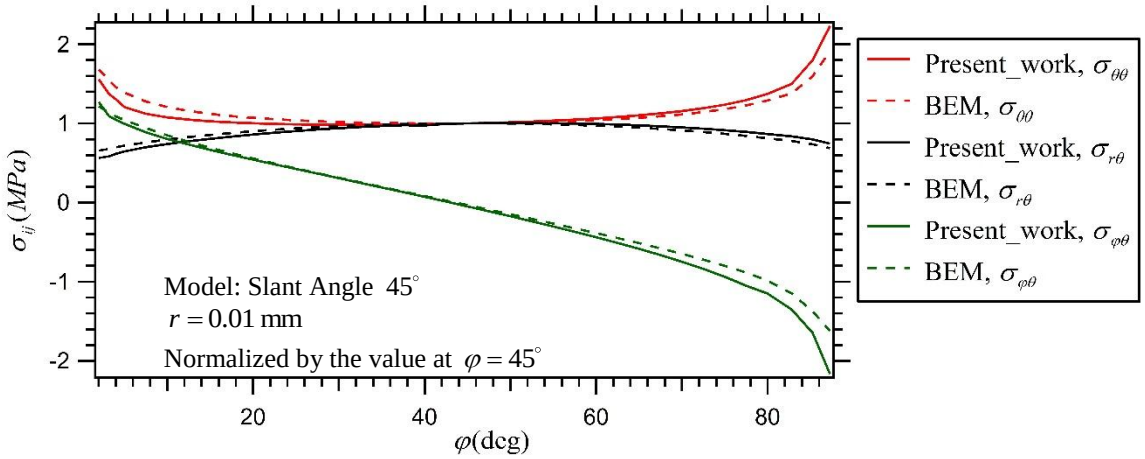

FIGURE 3. Comparison of normalized stress distribution obtained by FEM and BEM.

The graph is shown in Figure 3. Solid lines represent the results obtained by present work method and the dotted lines represent the results obtained by Koguchi. From the graph it has been seen that the results obtained by present method is very near the result obtained by BEM. Thus the accuracy of the finite element method is verified.

RESULTS AND DISCUSSIONS

The solution of the bi-material joint under tensile force as obtained by the present computational scheme is presented in this section. It is very difficult to represent the displacement, strain and stress near the edge and vertex of the interface of bonded joint in Cartesian coordinate system (*x, y, z*). Therefore in this analysis all the displacements, strains and stresses are converted from Cartesian coordinate system (*x, y, z*) to Spherical coordinate system (r, θ, φ). The components of displacement, strain and stress are plotted against various parameters.

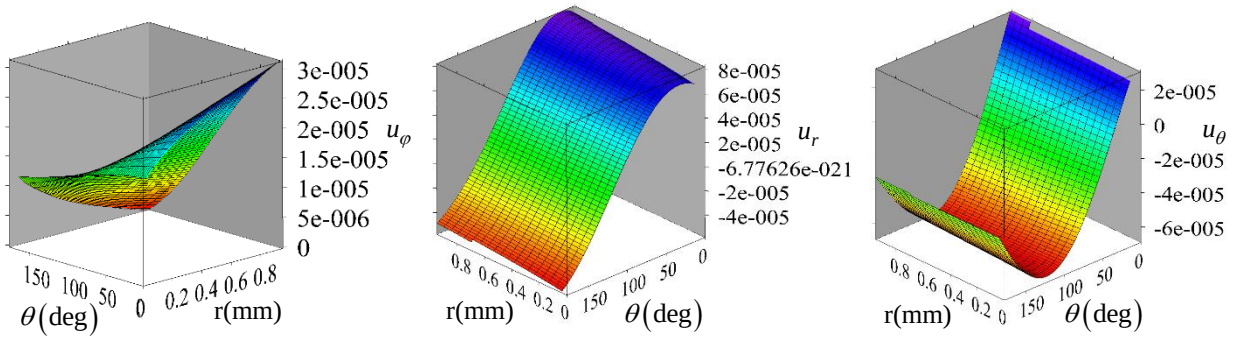

(a) (b) (c)

FIGURE 4. Change of displacement components (a) u_φ , (b) u_r and (c) u_θ .

In Figure 4 the distribution of displacement components with respect to radial distance r and angle θ are shown. It has been seen that the displacement components are continuous at the interface and have larger value toward the edges.

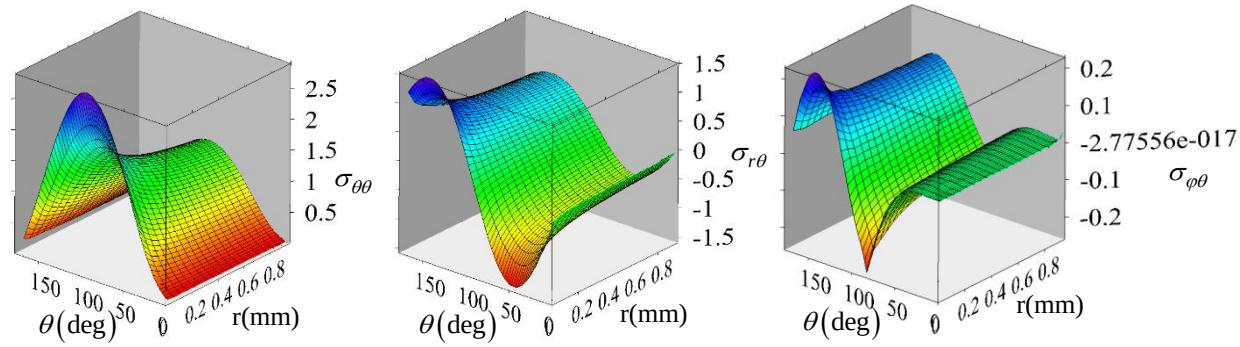

(a) (b) (c)

FIGURE 5. Change of stress components (a) $\sigma_{\theta\theta}$, (b) $\sigma_{r\theta}$ and (c) $\sigma_{\varphi\theta}$.

In Figure 5 the changes of stress components with respect to radial distance r and angle θ are shown. All stress components increase with the decrease of r. So the de-bonding will occur near the vertex. The maximum magnitude of stress occurs by $\sigma_{\theta\theta}$ at $\theta = 90^\circ$, which is the largest value among all the stress components. This results indicate that the de-bonding will initiate from the interface of the joint and $\sigma_{\theta\theta}$ will be responsible mostly for de-bonding.

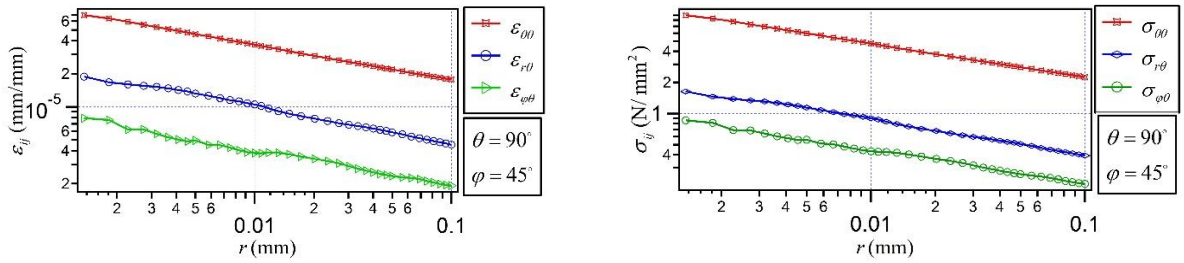

(a) (b)

FIGURE 6. (a) Changes of strain components with respect to *r*; (b) changes of stress components with respect to *r*.

In Figure 6 the changes of strain and stress components with the increase of radial distance are shown in the log-log chart. The curves are almost straight line in the log scale. It is seen that maximum strain and stress occur near the vertex. In Figure 7 The variation of stress components with respect to angle φ at a proximity of r = *0.*005mm from the vertex are shown. The values are normalized by the value at $\varphi = 45^\circ$. It has been seen that the larger stress occurs at the edge. The result obtained is convenient with the three dimensional plots.

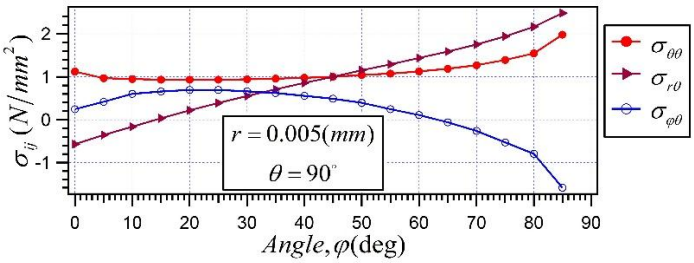

FIGURE 7. Changes of stress components with respect to angle φ

CONCLUSION

A numerical investigation of displacement, strain and stress is performed on transversely isotropic elastic dissimilar joint subjected to tensile load. From the numerical results, it has been seen for the elastic dissimilar joints that, (a) larger value of strain and stress occurs at the interfacial free edge of the elastic material joints and (b) It is suggested that de-bonding may initiate near the vertex of material joint.

REFERENCES

1. Wilmanski, K., *Fundamentals of Solid Mechanics*, first ed., (ROSE School, Pavia, Italy).
2. Lai, W. M., Rubin, D. and Krempl, E., *Introduction to Continuum Mechanics*, third ed., (Butterworth Heinemann, USA).
3. Dehkordi, A. R., "3D Finite Element Cosserat Continuum Simulation of Layered Geomaterials", M. Report, University of Toronto, Canada, 2008.
4. Goland, M. and Reissner, E., "The Stress in Cemented Joints", (Journal of Applied Mechanics, 1944), pp. A17-A26.
5. Pahoja, H. M., "Stress Analysis of an Adhesive Lap joint Subjected to Tension, Shear Force and Bending Moments", T. & A. M. Report 361, University of Illinois,(Urbana-Champaign, 1972).
6. Vinson, J. R., "Adhesive Bonding of Polymer Composites", in *Polymer Engineering Science*, Vol. 29, (1989), pp.1325-1331.
7. Adams, R. D., "The Mechanics of Bonded Joints", (IMechE, 1986), pp.17-24.
8. Adams, R. D., "Strength Predictions for Lap Joints Especially with Composite Adherents: A Review", in *J. Adhesion*, Vol. 30, (1989), pp.219-242.
9. Lessard, L., "Design of Joints in Composite Structures", in *Computer Aided Design for Composite Structures*, edited by S.V. Hoa, (Marcel Dekker Inc., NY, 1995), pp. 273-288.
10. Barthelemy, B. M., Kamat, M. P., and Brinson, H. F., "Finite Element Analysis of Bonded Joints", M. Thesis, Virginia Polytechnic Institute and State University, (Blacksburg, Virginia, 1984).
11. Harris, J. A., and Adams R. D., "Strength prediction for bonded single lap joints by non-linear finite element methods", *International Journal of Adhesion and Adhesives*, Vol. 4, No. 2, (1984), pp. 65-78.
12. Adams, R. D., Atkins, R. W., Harris, J. A., "Stress Analysis and Failure Properties of Carbon-Fibre-Reinforced-Plastic/Steel Double Lap Joints", *Journal of Adhesion*, Vol. 20, (1986), pp. 29-53.
13. HiIdebrand, M., "Non-linear Analysis and Optimization of Adhesively Bonded Single Lap Joints between Fibre-Reinforced Plastics and Metals", *Int. J. Adhesion and Adhesives*, Vol. 14, No. 4, (1994), pp.261-267.
14. Bogy, D. B., "Edge-Bonded Dissimilar Orthogonal Elastic Wedges Under Normal and Shear Loading", *Journal of Applied Mechanics*, Vol. 35, (1968), pp.460-466.
15. Dundurs, J., "Discussion of Edge-Bonded Dissimilar Orthogonal Elastic Wedges Under Normal and Shear Loading", *Journal of Applied Mechanics*, Vol. 36, (1969), pp.650-652.
16. Bogy, D. B., "Two Edge-Bonded Elastic Wedges of Different Materials and Wedge Angles under Surface Tractions", *Journal of Applied Mechanics*, Vol. 38, (1971), pp. 377-386.
17. Ding, H., Chen, W. and Zhang, L., "Elasticity of Transversely Isotropic Materials", in *Solid Mechanics and Its Applications*, Vol. 126, (2006), pp.4-24.
18. Koguchi, H., Antonio, J., "Analysis of the stress singularity field at a vertex in 3D-bonded structures having a slanted side surface", *International Journal of Solids and Structures*, Vol. 47, (2010), pp. 3131–3140.

ICME2015

International Conference on Mechanical Engineering 2015
(ICME 2015) 18 – 20 December, 2015, Dhaka, Bangladesh

Paper ID : 081

Temperature Rise and Wear of Sliding Contact of Alloy Steels

Arindam Roy Goswami[1, a)], Santanu Sardar[2, b)] and Santanu Kumar Karmakar [3, c)]

[1, 2, 3]*Deparment of Mechanical Engineering, Indian Institute of Engineering Science and Technology, Shibpur, Howrah-711103, West Bengal, India.*

[c)] Corresponding author: skk@mech.iiests.ac.in
[b)]san_becme@yahoo.co.in

Abstract. The tribo-failure of machine elements under relative sliding velocities is greatly affected by frictional heating and resultant contact temperature rise. Nevertheless, the tribo-failure of automotive components is a combined effect of mechanical, thermal and chemical phenomena. Over the decades, there have been developed a number of different mathematical models for predicting surface temperature rise at sliding contact under different geometries of asperity contacts and operating conditions. The experimental investigation is still relevant today to find out the surface temperature rise at sliding contact along with the outcomes of friction and wear under various operating conditions for real time applications. The present work aims at finding average surface temperature rise at different sliding velocities, normal loads with different surface roughness experimentally. It also involves to prepare two different rough surfaces of alloy steels and to study their influences in the process of generating contact temperature rise under a given operating conditions.

Keywords. Sliding velocity; average surface roughness; average surface temperature rise; coefficient of friction; specific wear rate.

INTRODUCTION

Temperature rise at asperity contacts of two machine elements in relative sliding motion is a challenging phenomena in respect of tribological characterization of automotive components. However, the temperature rise in the sliding micro-asperity contacts of two interacting surfaces can not be accessed accurately with any available tools like contact or non-contact typed temperature measuring instruments [1]. Researchers are still striving to develop new experimental methods coupled with numerical solutions for closer approximation of contact temperature rise. The temperature rise due to deformation along with frictional heat at asperity sliding contacts can be of a high order of magnitude with short duration. Kennedy revealed further that more than 95% of the energy dissipated occurs within the top 5 μm of the surface layer. Due to high temperature rise, oxidation may occur at asperity contacts. The effect of oxidation in sliding components and its consequent relation to contact temperature had been addressed by Quinn and Winer [2,3].

Moreover, any technique that tends to detect the maximum possible temperature at the contact zone, should have provision for accurate measurement of the temperatures at these micro asperity peaks. Blok first simplified the rubbing contact phenomenon by considering asperities as parallel perpendicular rods [4]. Archard presented a simpler formulation of the theory for both slow and rapid moving sliding contacts with the introduction of Peclet number (Pe) barring other surface parameters [5]. Previously, the researchers like Cook and Bhushan [6], Tian et al.[7] had worked on thermo-couple based technique to evaluate the contact temperature. Later on radiation based measurement method has been introduced and aided greatly to detect the temperature adjacent to the contact zone after dissipation of heat. Majcherczak et al. [8], Kyle et al. [9] and G. Sutter et al. [10] have carried out experiments with radiation based technique.

The present work primarily focuses to measure average surface temperature rise, co-efficient of friction (COF), specific wear rate at different sliding velocities, normal loads along with different surface roughness experimentally with long duration testing based on radiation technique.

EXPERIMENTAL SET-UPS

Tribo-testings have been carried out on a Pin-on-Disk Machine, shown in Fig.1(a), to measure average surface temperature rise, co-efficient of friction, wear rate with different materials and operating conditions as stated below. The alloy steels, SS304 and EN8 are selected as pin materials. Length and diameter of the test pins are taken as 40 mm and 6.3 mm respectively. The test pins are loaded against EN31 disk which is having 215 mm diameter, 8mm thickness, and an average hardness value of 681 BHN. The wear rate is calculated from the weight loss method. Composition and mechanical properties of these materials, tested in laboratory are given in Table 1 and Table 2.

(a) (b) (c)

FIGURE 1. *Experimental set-ups: (a) Pin-on-Disk Machine, (b) Optical Profiler and (c) Polishing Machine*

Average surface temperature rises are measured adjacent to the pin-on-disk contact by an infrared thermometer. The device can measure the temperature of a surface for a particular input value of emissivity of the same. Although emissivity is a surface property, some standard value of emissivity is taken with respect to material and its surface finish.

All experiments have been carried out in dry sliding condition at room temperature. The tests have been conducted at three different sliding velocities i.e. 1m/s, 2.5 m/s, 5 m/s, two normal loads of 20 N and 50 N, and two different ranges of centre line average surface roughness, R_a values of pin of 0.2-0.4 μm and 2-4 μm on a fixed track of the disk. As it is difficult to maintain a constant value of roughness for all test surfaces of pin and disk, an average roughness range has been considered. R_a value of the disk surface has been maintained in the range of 0.2-0.4 μm prior to all the tests. Duration of tests for the constant sliding distance of 3000m with sliding velocities of 1 m/s, 2.5 m/s and 5 m/s becomes 50 minutes, 20 minutes and 10 minutes with 133 rpm, 332 rpm and 664 rpm of disk respectively for selected radius of the fixed track of 72 mm for all the tests.

TABLE 1. *Compositions of selected pin and disk materials*

Percentage (%) Weight			
Element	**EN8**	**SS304**	**EN31**
C	0.39	0.08	1.5
Mn	0.8	2	0.52
Si	0.25	1	0.22
Cr	-	18	1.3
Ni	-	8.5	-
P	0.05	0.045	0.05
S	0.05	0.03	0.05

TABLE 2. *Mechanical properties of selected pin and disk materials*

Material	**Elastic modulus (GPa)**	**Hardness (BHN)**	**Thermal conductivity (W/mK)**	**Density (gm/cc)**
EN8	198	235	47	7.74
SS304	190	175	17	7.82
EN31	215	681	46.6	7.85

Surface roughness of both pin and disk have been set to the aforesaid range by polishing the surfaces in semi-automatic polishing machine, shown in Fig.1(c), prior to performing the wear tests. Cleaning of the pins has been

carried out in an ultrasonic vibro-cleaning bath before and after of each wear test. Weights of test pin are measured with an electronic weighing balance having sensitivity of 0.01 mg. Roughness measurements of unworn and worn surfaces for both pin and disk have been performed with optical profiler, shown in Fig.1(b). Co-efficient of friction (COF) is calculated from the frictional force displayed on the calibrated indicator of process controller of the Pin-on-Disk machine. The change of average surface temperature rises in °C with time adjacent to the junction of the Pin-on-Disk contact have been noted.

RESULTS AND DISCUSSIONS

Measured average surface temperature rises of EN8 and SS304 pins under 20 N and 50 N normal loads for a constant sliding distance of 3000m have been plotted in Fig. 2 for velocities of 1 m/s, 2.5 m/s, 5 m/s with R_a value in the range of 2-4 µm of pin surface. From the Figs.2a-2b, it has been observed that average surface temperature rise of SS304 is higher than that of EN8 under a fixed operating conditions. E. van der Heide et al. [11] have shown numerically that average surface temperature rise for a sliding contact pair is primarily influenced by thermal conductivity of the fixed body i.e. pin and it decreases with higher value of thermal conductivity. As SS304 has lower thermal conductivity than EN8, the higher temperature rise of SS 304 support the works of Heide et al.

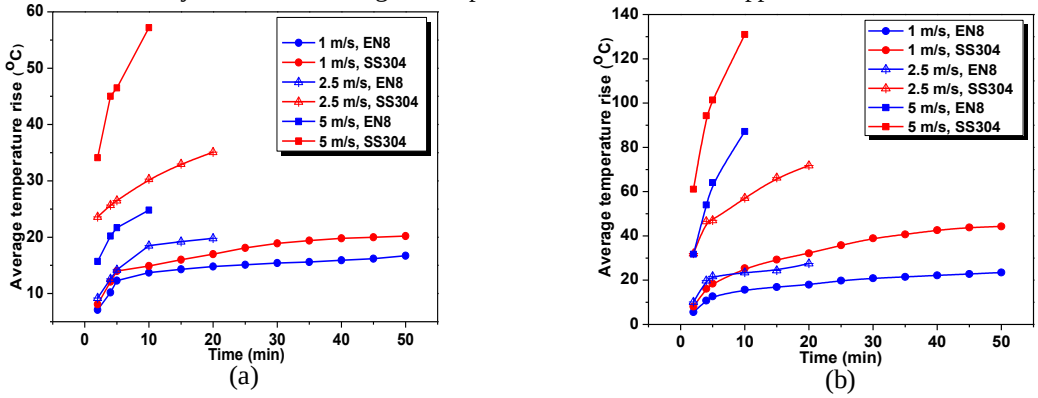

FIGURE 2. *Average surface temperature rise vs. time for EN8 and SS304 pins for a constant sliding distance of 3000m with a R_a value in the range of 2-4 µm of pin surface for sliding velocities of 1 m/s, 2.5 m/s, 5 m/s under normal load: (a) 20 N and (b) 50 N*

Average temperature rises with time have been plotted in Figs.3a-3c and Figs.4a-4c for EN8 pins and SS304 pins respectively for a constant sliding distance of 3000m for 1 m/s, 2.5 m/s, 5 m/s sliding velocity respectively, with two different normal loads and two different ranges of R_a. An increasing trend in average contact temperature rise with the increase in normal load and surface roughness has been observed in Figs.3a-3c. This result also finds support of the experimental work of Guha et al. [12]. A physical explanation of this observation is that for a rougher surface, the total frictional heat is distributed only over a small number of asperity contacts, causing an increase in individual maximum asperity contact temperature as well as average surface temperature rise.

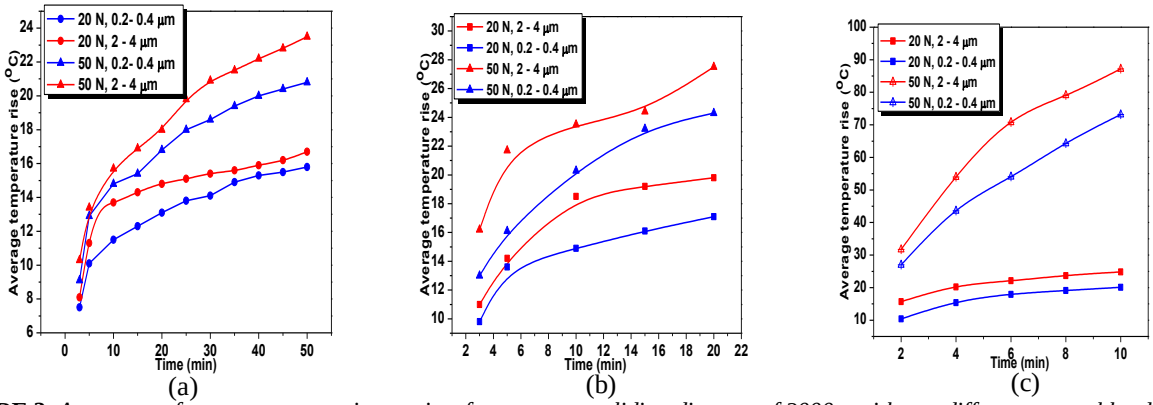

FIGURE 3. *Average surface temperature rise vs. time for a constant sliding distance of 3000m with two different normal loads and two different ranges of R_a for EN8 pins for sliding velocity of: (a) 1 m/s, (b) 2.5 m/s and (c) 5 m/s*

It can also be seen from Figs.4b-4c, that within the given range of normal loads of 20N & 50N for SS304 pins, the variation of average surface temperature rise with surface roughness values is negligible for sliding velocities of 2.5 m/s and 5m/s because of severe plastic deformation, whereas a considerable amount of variation is observed in Fig.4a for low sliding velocity of 1 m/s.

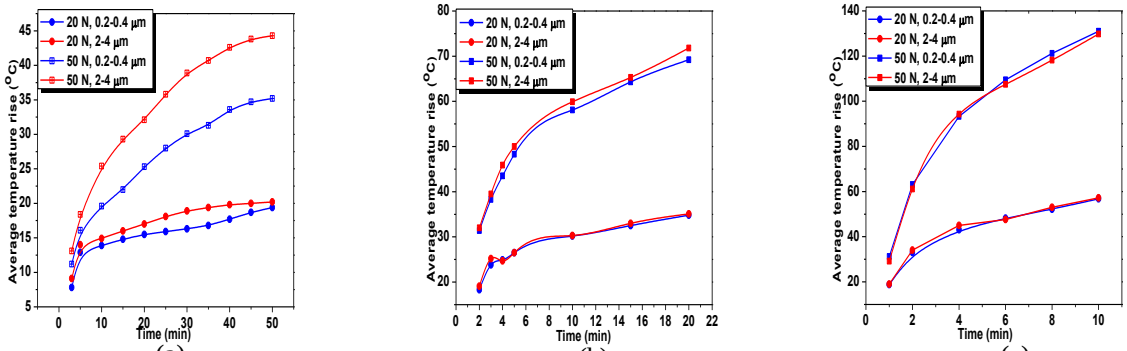

FIGURE 4. *Average surface temperature rise vs. time for a constant sliding distance of 3000m with two different normal loads and two different ranges of R_a for SS304 pins for sliding velocity of : (a) 1 m/s, (b) 2.5 m/s and (c) 5 m/s*

Comparisons of average surface temperature rises for a constant sliding distance of 3000m for different sliding velocities of 1 m/s, 2.5 m/s, 5 m/s under 20 N and 50 N normal loads with two different ranges of R_a of 0.2–0.4 µm and 2-4 µm for EN8 pins and SS304 pins are shown in Figs.5a -5b and Figs.5c-5d respectively.

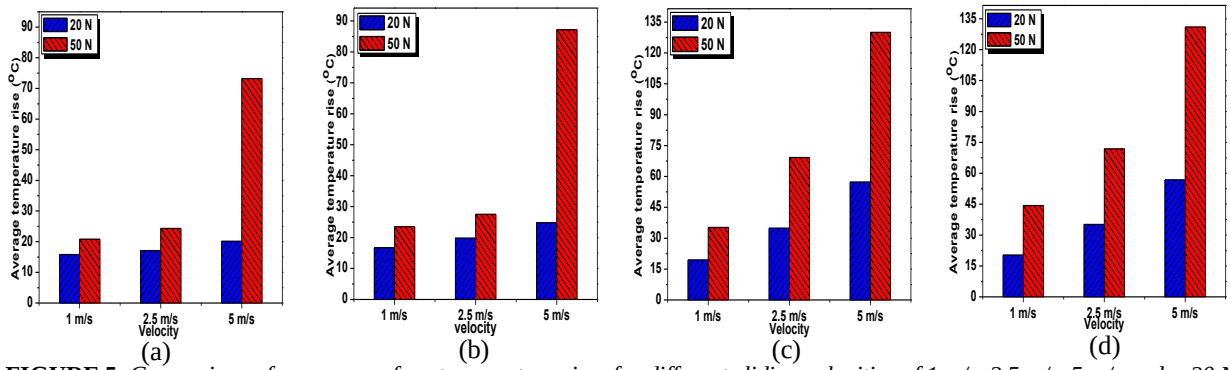

FIGURE 5. *Comparison of average surface temperature rises for different sliding velocities of 1 m/s, 2.5 m/s, 5 m/s under 20 N and 50 N normal loads with two different ranges of R_a of 0.2–0.4 µm and 2-4 µm: (a) & (b) for EN8 and (c) & (d) for SS304 pins*

It is clearly observed that average surface temperature rise for EN8 pin is gradually increasing with sliding velocities of 1 m/s and 2.5 m/s at 20N load and becomes sharply high at sliding velocity of 5m/s at 50N load for both ranges of R_a of 0.2–0.4 µm and 2-4 µm. However, average surface temperature rise for SS304 steel is gradually increasing with all sliding velocities under 20N and 50N normal load for both ranges of R_a of 2-4 µm and 0.2-0.4 µm.

Three dimensional surface images of unworn pin & disk are shown in Figs.6a & 6c and worn pin as well as disk under 50 N load and sliding velocity of 5 m/s are shown in Figs.6b & 6d. The typical sample 3D images, obtained from the optical profiler, represent the maximum value of peak heights under aforesaid condition. The images also depict a significant change of surface roughness for both pin and disk before and after test.

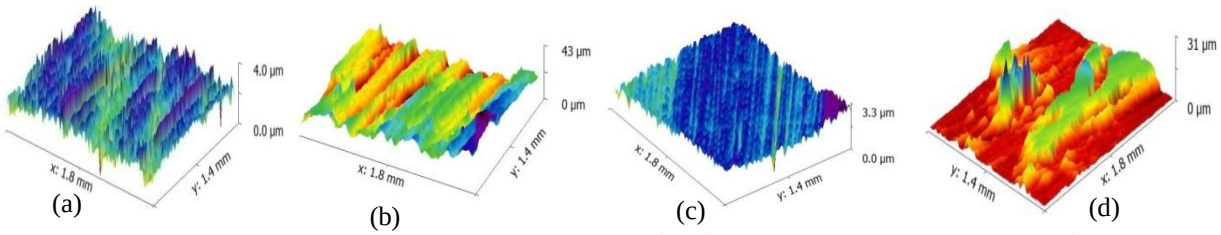

FIGURE 6. *Three dimensional sample images: (a) unworn & (b) worn for of EN8 pin and (c) unworn & (d) worn for EN31 disk*

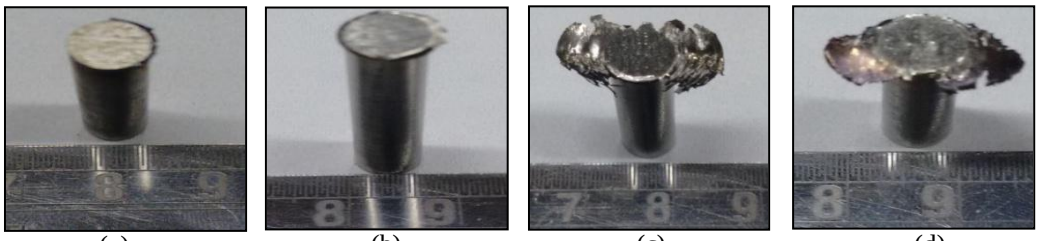

(a) (b) (c) (d)

FIGURE 7. *Worn-out test pins: (a) & (b) for EN8 and (c) & (d) for SS304*

The images of worn-out test pins of having two different ranges of R_a of 2-4 µm and 0.2-0.4 µm of under normal load of 50 N and sliding velocity of 5 m/s are shown in Figs.7a & 7b for EN8 and Figs.7c & 7d for SS304 respectively. It is observed that the temperature rise becomes highest for both EN8 and SS304 pin under the aforementioned operating condition. The images clearly indicate that SS304 pin undergoes severe adhesive wear due to high contact stress and temperature compared to EN8 pin.

It is observed that average COF decreases with the increase of sliding velocity and normal load for both EN8 and SS304 as shown in Fig.8. It may happen due to decreasing trend of shearing strength of junctions of asperity contacts with increasing temperature rise.

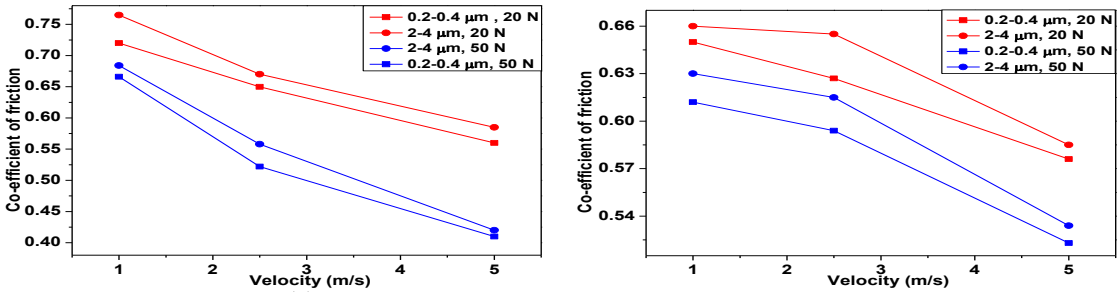

(a) (b)

FIGURE 8. *COF vs. sliding velocity: (a) EN8 and (b) SS304*

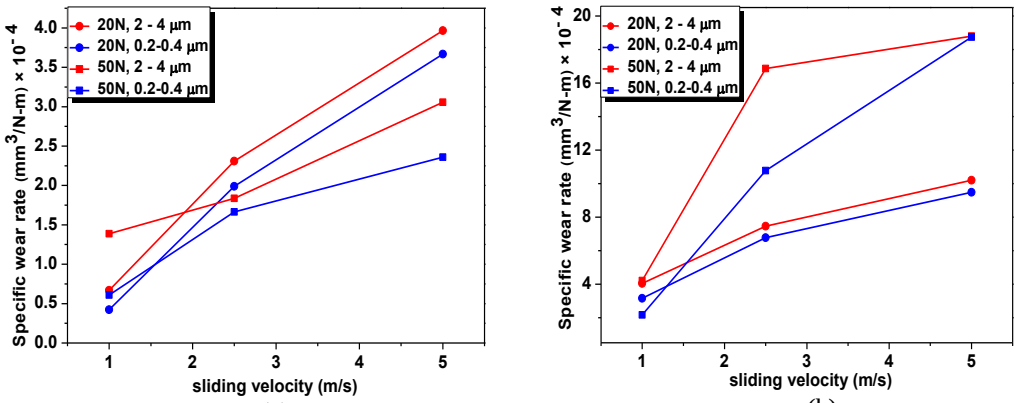

(a) (b)

FIGURE 9. *Specific wear rate of pin vs. sliding velocity: (a) EN8 and (b) SS304*

Figure 9 shows the variation of specific wear rate (i.e. volume loss per unit load per unit sliding distance) of pin against sliding velocity with two different ranges of R_a of 2-4 µm and 0.2-0.4 µm of pin for both EN8 and SS304 under normal loads of 20N and 50N under constant sliding distance of 3000m. The result clearly indicates an increasing trend of specific wear rate with increase of sliding velocity as well as R_a values for both EN8 and SS304 pins.

CONCLUSIONS

From the experimental results of tribo-testings of EN8 and SS304 pins, carried out under a specific range of operating conditions i.e. normal load, sliding velocity and R_a values, the following conclusions may be drawn.

- Average surface temperature rise increases always with increase of sliding velocity and normal load. An increasing trend of surface temperature rise is also found with higher R_a values upto sliding velocity of 2.5m/s.
- Average surface temperature rise for EN8 pin gradually increases with the increase of sliding velocity at 20N and 50 N load at sliding velocities of 1 m/s and 2.5 m/s. However, it becomes sharply high at sliding velocity of 5m/s under the normal load of 50 N compared to lower sliding velocities of 1 and 2.5 m/s.
- Wear of dry sliding contact is attributed due to adhesion in all carried out tests. Specific wear rate increases with the increase of sliding velocity and R_a values of pin surface for both EN8 and SS304.
- Average COF decreases with the increase of sliding velocity and normal load for both EN8 and SS304.

REFERENCES

1. F. E. Kennedy, "Frictional Heating and Contact Temperatures" in *Modern Tribology Handbook* edited by B. Bhushan (CRC Press, Boca Raton, FL, 2001), pp. 235-272.
2. T. F. J. Quinn, Tribology International **16**, 257-271 (1983).
3. T. F. J. Quinn and W. O. Winer, Wear **102**, 67-80 (1985).
4. H. A. Blok, "Theoretical study of temperature rise at surfaces of actual contact under oiliness lubricating conditions," Proceedings of the General Discussion on Lubrication and Lubricants, (I. Mech. E., London, 1937), pp. 222-235.
5. J. F. Archard, Wear **2**, 438-455 (1959).
6. N. H. Cook and B. Bhushan, ASME Journal of Lubrication Technology **96**, 59-64 (1973).
7. X. Tian, F. E. Kennedy, J. J. Deacutis and A.K. Henning, Tribology Transactions **35**, 491-499 (1992).
8. D. Majcherczak, P. Dufrenoy, Y. Berthier and M. Nait-Abdelaziz, Wear **261**, 467-476 (2006).
9. G. R. Kyle, I. B. Alexander, A. K. Brandon and W. G. Sawyer, Tribology International **62**, 208-214 (2013).
10. G. Sutter and N. Ranc, Wear **268**, 1237-1242 (2010).
11. E. Van der Heide and D. J. Schipper, Journal of Tribology **126**, 275-280 (2004).
12. D. Guha and S. K. Roy Chowdhuri, Wear **197**, 63-73 (1996).

International Conference on Mechanical Engineering 2015
(ICME 2015) 18 – 20 December, 2015, Dhaka, Bangladesh

Paper ID : 161

Development of Alloy Materials and Investigation of Tribological and Mechanical Properties

Md. Amanullah Kabir[1,a)], Pappa Kumar Paul[1], Sobahan Mia[2]

[1] *Department of Mechanical Engineering, Khulna University of Engineering & Technology*
[2] *Department of Mechanical Engineering, Khulna University of Engineering & Technology*
[a)]Corresponding author: akkuet2k10@gmail.com

Abstract. Aluminum and Aluminum based alloys are widely used in advanced Engineering applications now-a-days. For the vast applications and advantages of aluminum based alloys, authors decided to develop Aluminum based alloy by using local technology. In this project, by adding Cu and Zn independently in Aluminum hence mechanical and tribological properties had been examined. Alloys were developed by the process in which Cu and Zn (0-20 weight %) were independently mixed with pure Aluminum. After developing alloy materials ultimate tensile strength (UTS), hardness and wear had been measured. Addition of more than 15 % weight of Zn in aluminum was taken for raising its hardness. However, the hardness increases with percent addition of Cu. Above 4% of copper addition ultimate tensile strength goes downward and above 4% of zinc addition ultimate tensile strength goes upward linearly. Wear test experiment were carried out under normal load 5-12 N and sliding speed 300-700 rpm in both dry and wet condition. The weight of the test specimens were measured before and after test and for specified duration of time. The rate of wear of different compositions of aluminum alloy was observed by sliding it against stainless steel. Results show that the rate of wear by the addition of copper is much greater than the addition of zinc at constant normal load and sliding speed. After comparing all results hence future recommendation was given.

Keywords: Aluminum based alloy, Wear, Ultimate tensile strength.

INTRODUCTION

Alloys are made by mixing two or more elements, at least one of which being a metal. This is usually called the primary metal or the base metal, and the name of this metal may also be the name of the alloy. The other elements may or may not be metals but, when mixed with the molten base, they will be soluble, dissolving into the mixture. An alloy may be a solid solution of the elements (a single phase), a mixture of metallic phases (two or more solutions) or an intermetallic compound with no distinct boundary between the phases. Solid solution alloys give a single solid phase microstructure, while partial solutions exhibit two or more phases that may or may not be homogeneous in distribution, depending on the thermal (heat treatment) history of the material. An inter-metallic compound has one other alloy or pure metal embedded within another pure metal [1].

LITERATURE REVIEW

The story of aluminum's history of use in the U.S. now stretches over 100 years. The start was a modest one, however. Because of the complexities of refining aluminum from ore, aluminum was considered more rare and precious than gold or silver through most of the 19th century. A pure form of the metal was first successfully extracted from ore in 1825 by Danish chemist Hans-Christian. Techniques to produce aluminum in ways modestly cost-effective emerged in 1889. In 1865, Science fiction writer Jules Verne describes an aluminum space rocket in his novel, Journey to the Moon. In 1887, Austrian engineer Karl Josef Bayer developed a chemical process by which alumina can be extracted from bauxite, a widespread and naturally occurring aluminum ore. Both the Bayer and Hall-Her out processes are still used today to produce nearly all the world's aluminium [2]. In 2005, Adam L. Woodcraft, from Cardiff School of physics and Astronomy Cardiff University, 5, The Parade, Cardiff, CF24 3Yb, UK have used

Aluminium alloy for measuring Thermal conductivity in the cryogenic to room temperature range [3]. This paper describe a method of predicting the thermal conductivity of any aluminium alloy between the superconducting transition temperature and room temperature, based on a measurement of the thermal conductivity or electrical resistivity at a single temperature.

Experimental Methodology

Selection of Materials

Since in this project the alloy which is developed, is aluminum based alloy. So the majority percent of weight of this alloy is aluminum. Small amount of zinc, copper, nickel, tin, magnesium, silicon are used for developing alloy.

Preparing Specimen Using Sand Casting Method

In our project at first 114.3 millimeters (4.5 inch) diameter circular wood pattern was prepared for making circular disc. For preparing Sand mold at first sand was mixed with sodium silicate. Then by using wood pattern circular shape sand mold were prepared. Many small holes were made in the side of the mold which was acted as ventilator. Carbon-di-oxide gas was used for making hard that sand mold. Then those molds were coated with graphite layer and burned on fire. As a result those molds were very hard and less possibility to break down that mold.

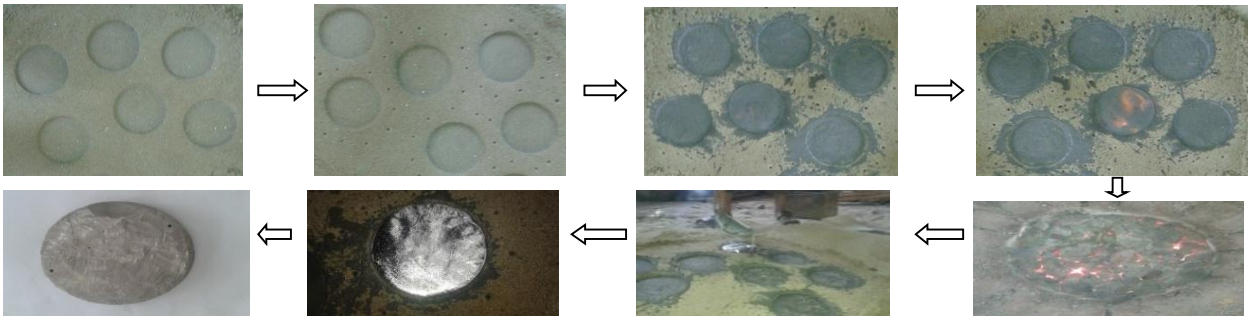

FIGURE1. Preparing alloy by using Sand casting method

Mechanical Properties Testing

Hardness testing

The Brinell scale characterizes the indentation hardness of materials through the scale of penetration of an indenter, loaded on a material test-piece. The typical test uses a 5 millimeters (0.195 in) diameter steel ball as an indenter with a 750 kgf (7.3 kN) force.

The indentation is measured and hardness calculated as:

$$\text{BHN} = \frac{2P}{\pi D(D-\sqrt{(D^2-d^2)})} \quad (1)$$

P=appied force,D=indenter diameter,d=diameter after indentation

Ultimate tensile strength testing

In our project the cast samples were machined to tensile configuration using BS 18 standard with the tensile bar gauge of length 76.2 millimeters (3 inch) and diameter of 12.7 millimeters (.5 inch). The testing was carried out by Universal testing machine.

Tribological Property Testing

In this project for testing wear pin on disc tribometer was used. The tests were carried out for different normal loads and at different sliding speeds of both dry and wet condition. And for this found the required wear rate by the influence of normal load and sliding speed.

FIGURE2. A Pin on Disc Tribometer

DATA ANALYSIS

TABLE 1. Chemical Composition of Aluminium Alloy (% weight)

No of Trial	Al	Zn	Si	Ni	Cu	Mg	Sn
01	100	0.0	0.0	0.0	0.0	0.0	0.0
02	70	20	1.0	1.0	6.0	0.5	1.5
03	75	16	0.5	2.5	4.5	1.0	1.5
04	79	12	0.5	3.0	3.0	1.0	1.5
05	84	8.0	0.5	3.0	2.0	1.0	1.5
06	88	4.0	0.5	3.5	1.5	1.0	1.5

TABLE 2. Data for Brinell Hardness in Chemical Composition of Aluminium Alloy

No of Observation	Types of Material	Load (Kg)	Indenter Diameter D (mm)	Measured Diameter d (mm)	BHN
01	Pure Al	750	5	3.80	55
02	4% Zn			3.73	57
03	8% Zn			3.61	62
04	12% Zn			3.39	72
05	16% Zn			2.90	103
06	20% Zn			2.50	143
07	4% Cu			3.68	59
08	8% Cu			3.35	74
09	12% Cu			2.83	108
10	16% Cu			2.60	131
11	20% Cu			2.36	162
12	8% Brass			3.20	83

TABLE 3. Data for Ultimate Tensile Stress in Chemical Composition of Aluminium Alloy

No of Observation	Types of Material	Ultimate Tensile Stress

		(MPa)
01	Pure Al	106
02	4% Zn	89
03	8% Zn	97
04	12% Zn	115
05	16% Zn	135
06	20% Zn	147
07	4% Cu	126
08	8% Cu	99
09	12% Cu	73
10	16% Cu	68
11	20% Cu	56

RESULT AND DISCUSSION

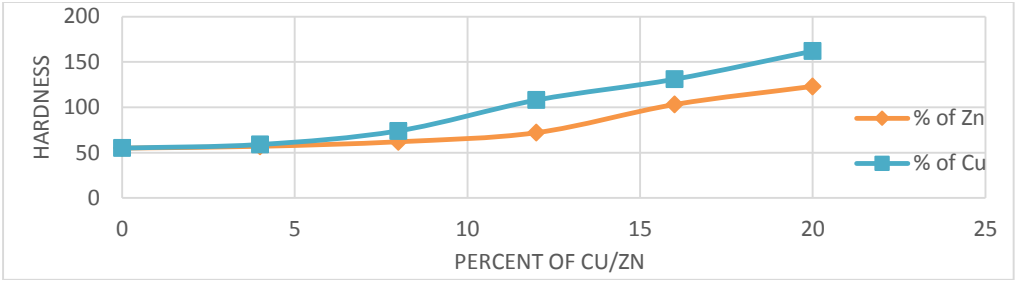

FIGURE 3. Hardness against Percent of Cu/Zn Addition in Aluminum

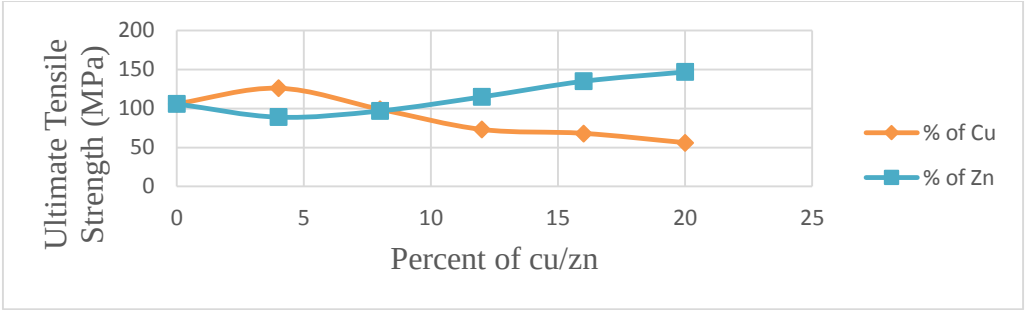

FIGURE 4. Ultimate Tensile Strength against Percent of Cu/Zn Addition in Aluminum

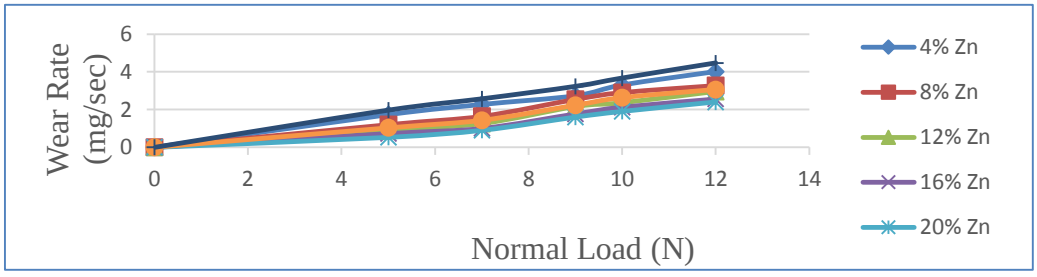

FIGURE 5. Influence of Normal Load on the Wear Rate by the variation of percentage of Zinc in Aluminum Alloy sliding against Stainless Steel Alloy sliding against Stainless Steel

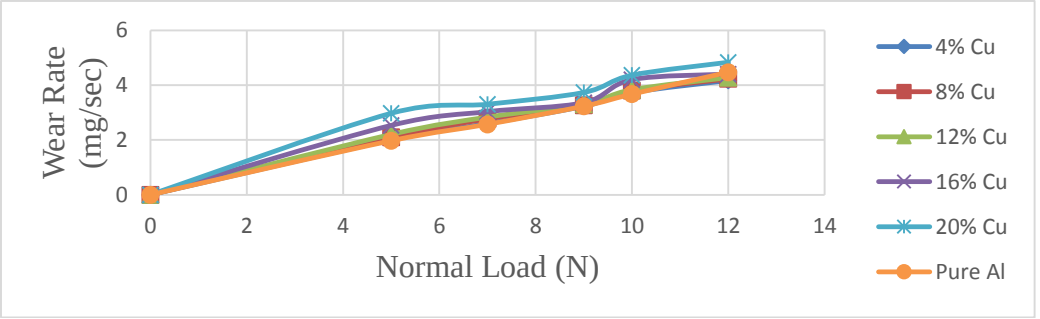

FIGURE 6. Influence of Normal Load on the Wear Rate by the variation of percentage of Copper in Aluminium Alloy sliding against Stainless Steel

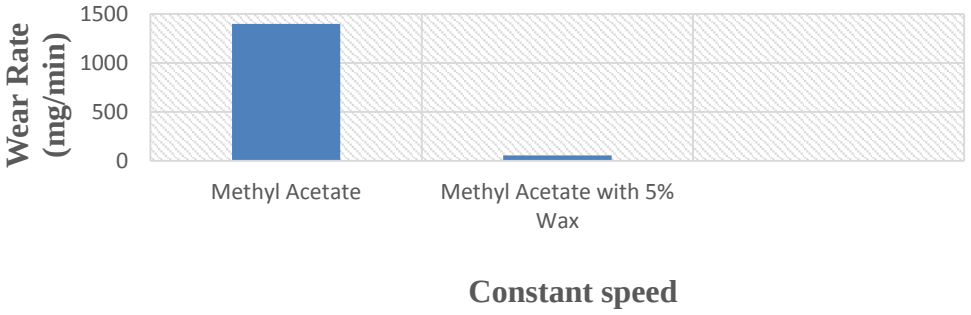

FIGURE 7. Rate of Wear by using different Additives in Aluminium Alloy sliding against Stainless Steel (wet condition)

In this research after developing alloy both mechanical and tribological properties were tested in cast samples.

In Figure 3, the hardness of both Cu and Zn addition on aluminum alloy were comparable and similar. However above 4% (weight) addition, the hardness of the resulting aluminum was higher with Cu addition than with Zn addition. It was noted that below 4% (weight) additions, the hardness of both alloys were same, where its influence on the precipitation of the intermetallics were negligible.

In Figure 4, the Ultimate Tensile Strength (UTS) of the aluminum alloy was increased from 106 MPa to a maximum of 127 MPa for Cu addition from 0-4%(weight), while the UTS correspondingly decreased from 106MPa to a minimum of 87MPa between 0-4%(weight) Zn additions. Beyond this range, the UTS decreased slowly as Cu addition were in excess of 4% (weight) the continuous addition of Cu decreased the precipitation of intermetallics which were noted that the strength decreased. Conversely the presence of Zn above 4 % (weight) did not depress the precipitation of intermetallics of the alloy. At Zn additions in excess of 4% (weight) the UTS increased steadily. Thus above 8 % (weight)Zn, the alloy showed the superior strength than that offered by Cu additions and specifically above 18 % (weight)the strength value of over 140 MPa was achieved. Above 8 % (weight).

In Figure 5, showed the variation of wear rate by the addition of zinc in aluminium alloy sliding over stainless steel with respect to various normal load. In this case sliding speed kept constant and it was 300 RPM. Here normal load were varied between range 5 Newton to 12 Newton. The curve should have uprising for decreasing percentage of zinc in aluminium alloy.

In Figure 6, showed the variation of wear rate by the addition of copper in aluminium alloy sliding over stainless steel with respect to various normal load. In this case sliding speed kept constant and it was 300 RPM. Here normal load were varied between range 5 Newton to 12 Newton. The curve should have uprising for increasing percentage of copper in aluminium alloy.

In Figure 7, showed that the rate of wear was very high when used Methyl Acetate as a lubricant. But by using 5% Wax in Methyl Acetate this rate was negligible.

CONCLUSION

- From this research, the following conclusions may be drawn:
- The hardness of the resulting aluminum was higher with Cu addition than with Zn addition.
- At the beginning of copper addition in aluminium the ultimate tensile strength is slightly increased but the further addition of copper in aluminium the ultimate tensile strength is gradually decreased.
- At the beginning of zinc addition in aluminium the ultimate tensile strength is slightly decreased but the further addition of zinc in aluminium the ultimate tensile strength is gradually increased.
- The rate of wear by the addition of copper is much greater than the addition of zinc at constant sliding speed.

FUTURE RECOMMENDATION

The following recommendation can be made for further study:

- It is recommended that since by adding 16-20% of Zinc the alloy shows better hardness and wear properties than pure aluminium, so it can be used in advanced applications in automotive parts.
- It is also recommended that by the replacement of copper and zinc in aluminium, Silicon and Manganese can be used for further investigation

REFERENCES

1. Bauccio, Michael (1003) ASM metals reference book. ASM International. ISBN 0871704781.
2. http://www.aluminum.org/aluminum-advantage/history-aluminum#sthash.
3. Adam L. Woodcraft, Cardiff School of Physics and Astronomy, Cardiff University,(March 2005). Predicting the thermal conductivity of aluminium alloys in the cryogenic to room temperature range, The Parade, Cardiff,CF243YB,UK.

ICME2015

International Conference on Mechanical Engineering 2015
(ICME 2015) 18 – 20 December, 2015, Dhaka, Bangladesh

Paper ID : 186

Properties of Micro-Nano Particle Size Admixtures of Alumina at Different Sintering Condition

Rahin Sifat[1,a)], Manira Akter[1,b)] and A.K.M. Bazlur Rashid[1,c)]

[1]*Department of Materials and Metallurgical Engineering, Bangladesh University of Engineering and Technology, Dhaka 1000, Bangladesh*

[a)]Corresponding author: rahinsifat@yahoo.com
[b)]manira.akter246@gmail.com
[c)]akmb.rashid@gmail.com

Abstract. Among various ceramic materials, alumina is mostly used material for its hardness and strength. There is a difference between the properties of alumina due to their different particle size. Also different holding time in the sintering temperature has effect on the sintering of alumina of different particle size. In this study, micro alumina and nano alumina were mixed in different ratios and sintered at different sintering condition to compare their mechanical properties that varied due to their different particle size distribution. In this work, conventional solid state sintering route was followed to prepare final samples. Six different particle size ratio of alumina (micro:nano= 100:0, 95:5, 90:10, 10:90, 5:95, 0:100) with a doping of 0.1% MgO were used. The sintering temperature was 1500^{o} C but sintering condition was different. After comparing the mechanical properties, it has been observed that relatively improved properties can be obtained by increasing nano particle percentages in the micro alumina than the reverse mixture.

INTRODUCTION

Alumina ceramics are highly used for structural purposes because of their high thermal resistance, good chemical stability, wear resistance and outstanding mechanical properties at high temperature [1,2,6]. Using solid state sintering process alumina can be shaped for mechanical uses but high porosity, low fracture toughness even after sintering has limited many of its uses [2].

The structural properties of ceramics are closely related to the particle size, size distribution, the microstructural characteristics (grain size, porosity and the presence of secondary phase) derived from their sintering process and so on [3]. To improve density and toughness of ceramic materials, many researches have been conducted recently and those employed the addition of second phase such as- fibers, whiskers or particles to the matrix [4,5]. Use of particles as second phase is more practicable than fibers or whiskers. The recent research showed that mechanical properties could be improved greatly by developing multiphase and multi scale nano composites [1]. More homogeneous structure can be obtained from an appropriate particle size distribution [6]. Also appropriate sintering condition is required to obtain high density, pore free microstructure and clean grain boundaries [3].

The application of ceramics where purity is required, admixture of multi scale particles of same material can be a good option. This study attempts to investigate the effect of particle size on the admixture of multi scale alumina particles. For this purpose nano and micro sized pure alpha alumina were mixed in 6 different ratios to study the possibility of improving mechanical properties.

EXPERIMENTAL PROCEDURES

Raw Materials

The raw material used in this work was alumina (Al_2O_3) of different particle sizes. Locally supplied micro-alumina with average particle size of 5-10 μm (using SEM) and alpha- Al_2O_3 nanopowder (containing 99.85% purity) with an average particle size of 150 nm (from BET SSA and SEM) produced by Inframat Advanced Materials were mixed in six different ratios to prepare the ceramics. MgO nanopowder (particle size ~30 nm) was added in each composition in 0.1 wt% to inhibit excessive grain growth. 6 different composition ratios of the admixtures are shown in Table 1.

TABLE 1. Experimental matrix (weight percentage)

Sample ID	Group 1			Group 2		
	S1	**S2**	**S3**	**S4**	**S5**	**S6**
Micro alumina	100	95	90	10	5	0
Nano alumina	0	5	10	90	95	100

Sample Preparation

The appropriate percentage of raw materials were weighed, dissolved in acetone and then, taken for milling for about 22 hours to obtain proper homogenization. The milling was carried out in a high density polyethylene (HDPE) pot containing zirconia balls. The slurry prepared from milling was extracted from the zirconia balls and was dried in a dryer for about 24 hours at 100^{o}C to evaporate moisture and acetone. The dried sample was crushed to the finest size possible. Liquid binder PVA (polyvinyl alcohol) was then added to the powder and compacted using a uniaxial pressing machine.

The green compacts were dried for 24 hours at about 100^{o}C. After drying the samples were sintered with proper sintering cycle. As the specific surface area is different for micro- and nano-sized alumina particles, sintering condition was different for group 1 and group 2 compositions.

Sintering Condition

Sintering temperature and time influence mechanical properties of alumina ceramics [2]. Due to the higher sintering stress, nanoparticles show higher densification rate than coarser particles. The densification of these powders is often accompanied by grain growth [9]. Rapid grain growth occurs at the final-stage of the sintering process [10]. In order to obtain full densification, proper sintering cycle is required.

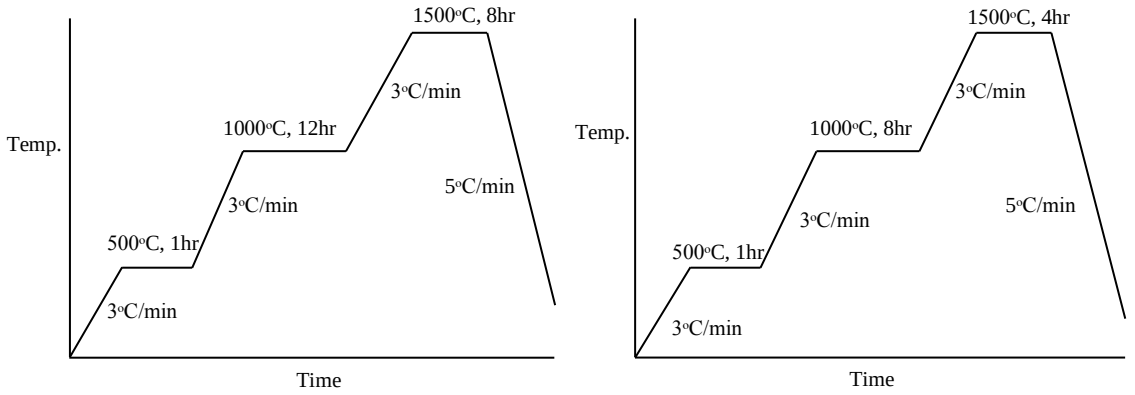

FIGURE 1. Sintering cycle for (a) Group 1 (b) Group 2

Figure 1 represents two different sintering cycles that were used for group 1 and group 2 compositions. As group 1 compositions contain micro alumina matrix, sintering cycle is longer than group 2 compositions.

Testing Method

Green densities of the compacted pellets were determined by measuring diameter and thickness of the pellet using slide callipers. After sintering, true density was measured using Archimedes' principle. Hardness was measured in VICKERS HARDNESS TESTER by applying 9.8N load for 10 seconds on group 1 samples and 19.6N load on group 2 samples. Microstructures were observed in Field Emission Scanning Electron Microscope (FESEM, Model: JEOL JSM-7600F).

RESULTS AND DISCUSSION

Density

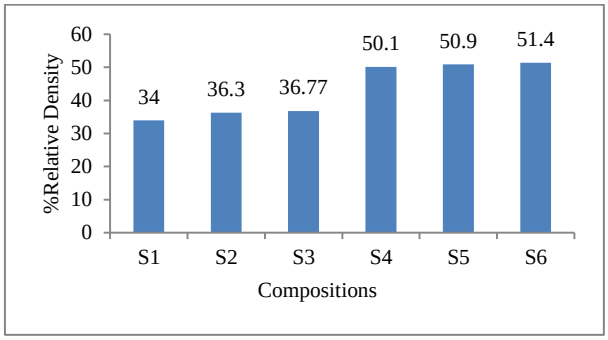

FIGURE 2. Variation of green density relative to the theoretical density obtained for different samples.

Green density is measured before sintering. Thus, it indicates the degree of compaction. Variation of green density with increasing nano alumina is plotted in Fig. 2. From the plot, with increasing 5% and 10% nano alumina, green density increases in a very small amount compared to 100% micro alumina (S1). Green density obtained for 100% nano alumina (S6) is relatively higher than S1 sample. Nanoparticles have higher surface area, which leads to better packing and higher density. By adding 5% and 10% micro alumina, green density slightly decreases from S6 towards S4 sample.

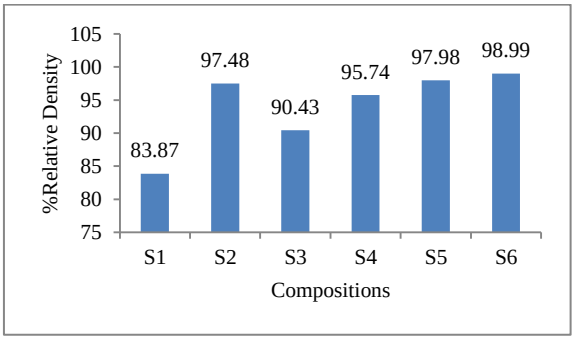

FIGURE 3. Variation of % relative density obtained for different samples after sintering

Variation of sintered density is presented in Fig. 3 as percentage relative density. It can be seen that minimum relative density was obtained for 100% micro-alumina because of its coarser particle sizes contributing to porous matrix. By mixing 5% nano alumina with 95% micro alumina, density increases tremendously because nanoparticles fill the pores of the micro alumina matrix [2]. By increasing nanoparticles to 10%, density of the matrix decreases.

This can be attributed to the agglomeration tendency of the nano-sized particles which causes to retain pores in the agglomerated zones. As a result density tends to decrease [7].

On the contrary, highest density was obtained for 100% nano alumina because of its smaller particle size and higher surface area providing higher driving force, which promoted densification [11]. Addition of micro particles to the nano alumina matrix tends to decrease density. From experimental studies, it has been observed that coarse particles can cause microstructural changes. Spatial heterogeneity and networks of coarse particles can be responsible for lowering the densification of nano alumina matrix [8].

Density of sample S2 and S5 (ratios of micro-nano particles of 95:5 and 5:95) can be compared from Fig. 3 and it can be observed that both the values are nearly equal and also very close to the density obtained by 100% nano alumina. So, it would be possible to obtain high density along with saving cost if alumina of 95:5 micro-nano particles ratio instead of 100% nano or 5:95 micro- nano particles ratio is used.

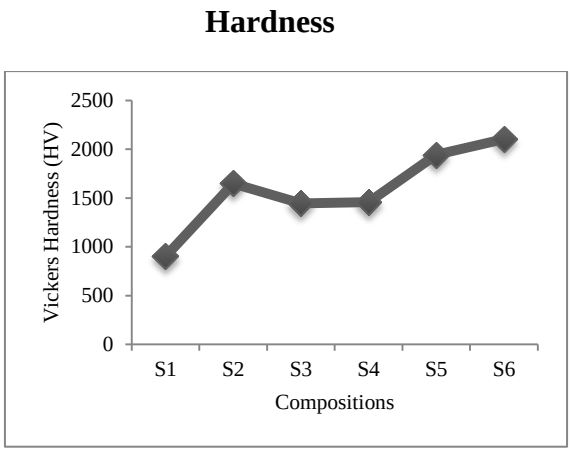

FIGURE 4. Variation of Vickers hardness (HV) obtained by different samples.

The effect of particle size distribution can have a great impact on hardness of alumina ceramics. Hardness values of different composition are presented in Fig. 4. A comparison has been represented in Fig. 5 between group 1 and group 2 compositions. It can be seen that the hardness of sample S6 is very high compared to sample S1. Nano particles contribute to better atomic packing which is homogenous, leading to this high hardness. Addition of 5% nano alumina in micro alumina matrix causes increase in hardness due to dispersion of nanoparticles. On the other hand, addition of 5% micro alumina in nano alumina matrix causes slight decrease in hardness due to coarse particles addition. Thus, difference between hardness value of sample S2 and S5 is much lower than that of sample S1 and S6. The difference between the hardness of sample S3 and S4 is nearly nil because in both cases hardness decreases. In sample S3 hardness decreases due to agglomeration of increased percentage of nanoparticles which inhibits proper dispersion [7]. In sample S4, hardness decreases because of increased percentage of large particles which impedes homogeneous distribution of nanoparticles.

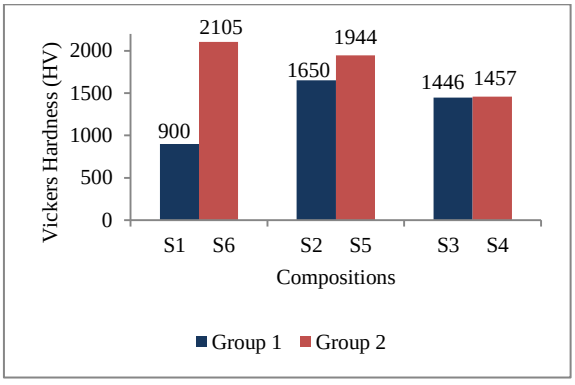

FIGURE 5. Comparison of Vickers hardness (HV) obtained by different samples.

Microstructural Observation

Group 1 and group 2 compositions were sintered at different sintering condition to obtain proper densification and proper grain growth according to their specific surface area. From Fig. 6(a), microstructure of 100% micro alumina exhibits excessive grain growth and high porosity. As in case of 100% micro alumina, coarse particles create large interspaces between them which cannot be consolidated even after sintering at 1500^{o}C for 8 hours. Figure 6(b) and 6(c) show that more densified microstructure was obtained in both cases, as added nanoparticles filled in the interspaces of large particles and excessive grain growth was inhibited.

Figure 6(d) shows dense microstructure as 100% nano alumina has high specific surface area, the agglomeration occurs easily and the agglomerate grows fast and develops into large grains at high sintering temperature. Figure 6(e) and 6(f) represent sample S5 and S4 which contain 5% and 10% micro alumina respectively. Micro particles have lower specific surface area and proper grain growth is inhibited by these large particles, which eventually produce relatively less dense microstructure than Fig. 6(d). As nanoparticles have tendency to form agglomerates, some agglomerates can be seen in Fig. 6(e) and 6(f).

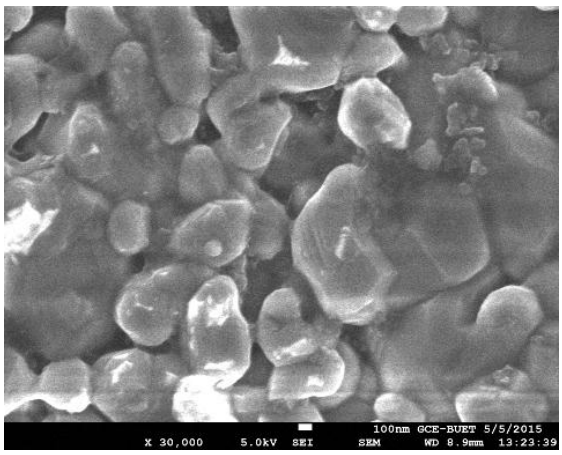

(a)

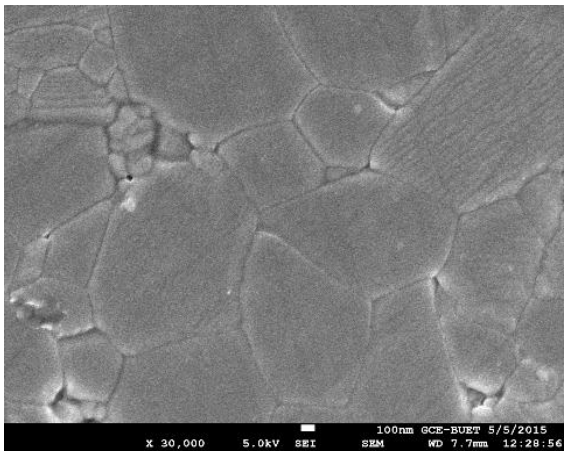

(b)

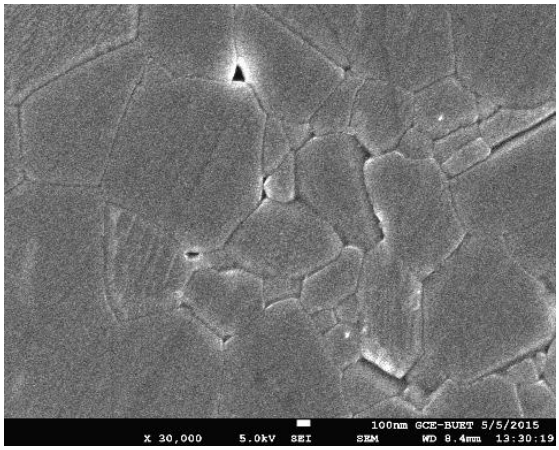

(c)

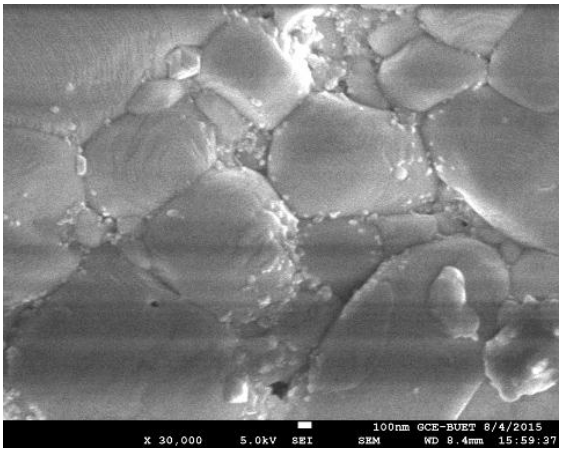

(d)

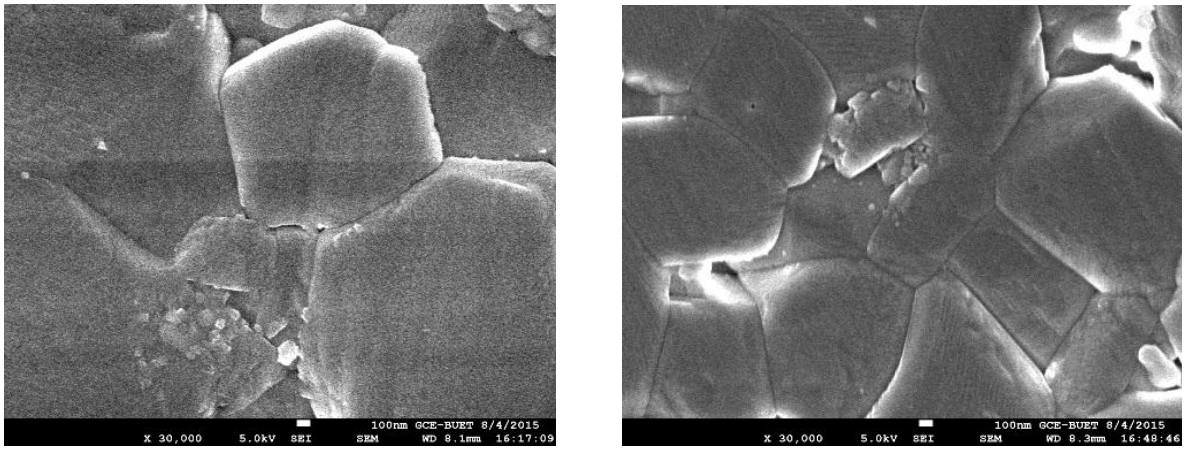

(e) (f)

FIGURE 6. SEM micrographs of six compositions (a)S1, (b)S2, (c)S3, (d)S6, (e)S5, (f)S4, x30,000

CONCLUSIONS

Micro alumina and nano alumina were mixed in six different ratios to find better particle size distribution, which leads to better mechanical properties. Two different sintering cycles were used to obtain proper densification. It has been observed that by adding 5% and 10% nano alumina to the micro alumina matrix improves microstructure and mechanical properties than purely micro alumina. Addition of 5% nanoparticles to the micro alumina increases density, hardness to such a high value that it can be compared with density and hardness of 100% nano alumina. On the contrary, by adding 5% and 10% micro alumina to the nano alumina matrix slightly deteriorate microstructure and mechanical properties than purely nano alumina.

ACKNOWLEDGEMENTS

We are very thankful to Prof. Dr. Md. Fakhrul Islam, Head, Dept of Glass & Ceramic Engineering, BUET for providing raw materials of Alumina and to let us perform our experiment under their lab facilities in Glass and Ceramic department. We are grateful to Rubayyat Mahbub Turjo (Asst. Professor of Glass and Ceramic Engineering Department, BUET) for his endless guidance throughout the work.

REFERENCES

1. X. Teng, H. Liu, and C. Huang, Mater. Sci. Eng. A **452-453**, 545-551 (2007).
2. Z. Yin, C. Huang, B. Zou, H. Liu, H. Zhu, and J. Wang, Ceram. Int. **39**, 4253-4262 (2013).
3. L. Moreira, L. Ponce, E. de Posada, T. Flores, Y. Peñaloza, O. Vázquez, and Y. Pérez, Ceram. Int. **41**, 11786-11792 (2015).
4. W. Acchar, Y.B.F. Silva, and C.A. Cairo, Mater. Sci. Eng. A **527**, 480-484 (2010).
5. B. Zou, C. Z. Huang, and H. L. Liu, Acta Mater. **55**, 4193-4202 (2007).
6. J. Li, Y. Pan, F. Qiu, L. Huang, and J. Guo, Mater. Sci. Eng. A **435–436**, 611–619 (2006).
7. M. T. Khorshid, S. A. J. Jahromi, and M.M. Moshksar, Mater. Design **31**, 3880-3884 (2010).
8. S. A. Schmidt and I. Nettleship, J. Euro. Ceram. Soc. **24**, 2741-2747 (2004).
9. A. S. A. Chinelatto, A. L. Chinelatto, C. L. Ojaimi, J. A. Ferreira, and E. M. J. A. Pallone, Ceram. Int. **40**, 14669-14676 (2014).
10. H. S. Kim, S. T. Oh, and Y. D. Kim, Ceram. Int. **40**, 14471-14475 (2014).
11. Z. R. Hesabi, M. Haghighatzadeh, M. Mazaheri, D. Galusek, and S. K. Sadrnezhaad, J. Euro. Ceram. Soc. **29**, 1371–1377 (2009).

ICME2015

International Conference on Mechanical Engineering 2015
(ICME 2015) 18 – 20 December, 2015, Dhaka, Bangladesh

Paper ID : 188

Microstructure Evolution and Electrical Characterization of Lanthanum Doped Barium Titanate ($BaTiO_3$) Ceramics

Masum Billah[1, a)], A. Ahmed[1, b)], Md. Miftaur Rahman[1, c)], Rubayyat Mahbub[2, d)], M. A. Gafur[3, e)],M. Shahriar Bashar[4, f)]

[1]*Department of Materials & Metallurgical Engineering, Bangladesh University of Engineering and Technology, Dhaka-1000, Bangladesh*
[2]*Department of Glass and Ceramic Engineering, Bangladesh University of Engineering and Technology, Dhaka-1000, Bangladesh*
[3]*Bangladesh Council of Scientific & Industrial Research (BCSIR), Dhaka-1205, Bangladesh*
[4]*Institute of Fuel Research & Development, Bangladesh Council of Scientific & Industrial Research (BCSIR), Dhaka-1205, Bangladesh*

[a)]Corresponding author: masum.buet09@gmail.com
[b)]jhinukbuetmme@gmail.com[c)]miftaurrahman@mme.buet.ac.bd
[d)]rubayyatm@gce.buet.ac.bd[e)]d_r_magafur@bcsir.gov.bd
[f)]bashar@agni.com

Abstract. In the current work, we investigated the structural and dielectric properties of Lanthanum oxide (La_2O_3) doped Barium Titanate ($BaTiO_3$) ceramics and established a correlation between them. Solid state sintering method was used to dope $BaTiO_3$ with 0.3, 0.5 and 0.7 mole% La_2O_3 under different sintering parameters. The raw materials used were La_2O_3 nano powder of ~80nm grain size and 99.995% purity and $BaTiO_3$ nano powder of 100nm grain size and 99.99% purity. Grain size distribution and morphology of fracture surface of sintered pellets were examined by Field Emission Scanning Electron Microscope and X-Ray Diffraction analysis was conducted to confirm the formation of desired crystal structure. The research result reveal that grain size and electrical properties of $BaTiO_3$ ceramic significantly enhanced for small amount of doping (up to 0.5 mole% La_2O_3) and then decreased with increasing doping concentration. Desired grain growth (0.80-1.3µm) and high densification (<90% theoretical density) were found by proper combination of temperature, sintering parameters and doping concentration. We found the resultant stable value of dielectric constant was 10000-12000 at 100-300 Hz in the temperature range of 30º-50º C for 0.5 mole% La_2O_3 with corresponding shift of curie temperature around 30º C. So overall this research showed that proper La^{3+} concentration can control the grain size, increase density, lower curie temperature and hence significantly improve the electrical properties of $BaTiO_3$ ceramics.

INTRODUCTION

Barium Titanate ($BaTiO_3$), a common versatile electro-ceramic, has a wide range of applications due to its excellent dielectric, ferroelectric and piezoelectric properties making it desirable for multilayered capacitors, positive temperature coefficient thermistors, ferroelectric thin film memories, piezoelectric transducers etc. [1,2,3]. It adopts perovskite type tetragonal lattice structure (ABO_3) with a high dielectric constant of 1500-2000 at room temperature but the dielectric constant would fluctuate [4] during operation under various conditions such as electrical field strength, operating temperature, humidity etc.

The various applications have resulted in many different studies aiming at preparation and characterization of $BaTiO_3$. Among them doping with donor or acceptor ions at small concentration in the A- or B- site is the most efficient and useful process to modify electrical properties. From different researches, it is found that semiconducting

$BaTiO_3$ can be produced by atmospheric reduction forming oxygen vacancy or by low concentration donor doping with trivalent ions (La^{3+}, Y^{3+}, Sb^{3+}) on Ba-site or pentavalent ions (Nb^{5+}, Ta^{5+}) on Ti-site [5,6,7,8].

Ionic radius is the main parameter determining the substitution site. In this case La^{3+} (1.15 Å) is exclusively incorporated at the Ba^{2+} (1.35 Å) site as its size is incompatible with that of Ti^{4+} (0.68 Å). Replacement of Ba^{2+} by La^{3+} ion produces an extra positive charge and due to electrical neutrality, an e^- is trapped by a Ti^{4+} ion followed by the equation (1) [9].

$$Ba^{2+}Ti^{4+}O_3^{2-} + x\ La = (Ba_{1-x}^{2+}\ La_x^{3+})\ Ti_{1-x}^{4+}\ (Ti^{4+}\ e^{1-})_x\ O_3^{2-} \quad (1)$$

Various research [9,10,11] showed that small concentration of La^{3+} in $BaTiO_3$ increase grain growth, decrease phase transition temperature hence enhancing dielectric properties. Adding a relatively low concentration leads to room temperature semiconducting ceramics with positive coefficient of resistivity (PTCR) effect whereas higher dopant concentration leads to insulating materials [9,10,11].

The main theme of this research was to fabricate undoped and La-doped $BaTiO_3$ ceramics with minimum porosity by solid state sintering, examine the influence of La doping on microstructure, crystalline structure & dielectric properties and determine the detail structure-property relationship.

EXPERIMENTAL PROCEDURE

Lanthanum doped Barium Titanate samples (BTL) were prepared from $BaTiO_3$ (size =100nm) and La_2O_3 (size =80nm) nano powders [Manufacturer: INFRAMAT (USA); Purity better than 99%]. Here La_2O_3 was used to dope for 0.3, 0.5, 0.7 mole% La (BTL3, BTL5 and BTL7). The powders were milled in the pot mill containing Yttria stabilized zirconia balls for 16-20 hours with a sufficient amount of acetone as the milling media. PVA (2% of sample wt.) was added as a binder after drying to remove milling media and then the mixture was stirred for 30-40 minute to ensure a homogenous binder distribution. The mixture was then dried and pressed into a disc shape (13mm diameter and 2.1mm average thickness) in a stainless steel die under the shape forming pressure of 1.5 tons. Next, the samples were placed for soaking in a box furnace (Model-NABERTHERM, HT 16/18, Germany) for binder removal at 500ºC for 1 hour (heating rate 2ºC/min). Sintering was performed at 1300º C for 2, 4, 8 hours (heating and cooling rate 3º C/min) in box furnace and cooled to room temperature in air atmosphere. Surface microstructure and grain size distribution of sintered pellets were examined by a Field Emission Scanning Electron Microscope, FE-SEM (Model-JEOL JSM-7600F, Japan) and crystal structure was detected using X-ray diffractometer, XRD (Model-BRUKER D8 ADVANCE, Germany). Temperature dependent dielectric constant was measured from 30º C to 145º C at various frequencies (100, 300, 500, 1k and 10 kHz) at a heating rate of 4º C/min using an Impedance Analyzer (WAYNE KERR 6500B series).

RESULTS AND DISCUSSION

The experimental results showed that better densification and moderate grain size were found when samples were sintered at a temperature of 1300ºC or more. The above finding conforms to previous results performed by some other research work [11,12]. Experimental results of percent theoretical density (%TD) and grain size of La_2O_3 doped $BaTiO_3$ sintered at 1300ºC are tabulated in Table 1. From these values, the sample sintered at 1300º C for 8 hours with a sintering rate of 3ºC/min was found to yield higher density and moderate grain size for all mole% of La_2O_3 doping.

Microstructure with lesser porosity and uniform density was found for all 0.3 mole% La_2O_3 doped samples. The average grain size of the samples sintered at 1300º C for 2 and 4 hours were in the range of 0.15-0.25 µm for both 0.5 and 0.7 mole% La_2O_3 doped samples.The effect showed an adverse effect on the electrical properties as a result of the too fine grain size. The holding time for sintering was insufficient in these cases although the slower sintering rate (3º C/min) provided longer sintering time. The micrographs of samples with different doping level of La_2O_3 mole fractions and sintered at 1300º C for 4 hours are showed in Fig.1 while Fig. 2 shows the microstructures of samples doped with different mole fractions of La_2O_3 and sintered at 1300º C for 8 hours.

TABLE 1. Percent theoretical density (%TD) and grain size of sintered La_2O_3 doped $BaTiO_3$ samples

Sample	Maximum Sintering Temp. (^{0}C)	Sintering Time (hour)	Doping mole%	% theoretical density	Average Grain Size (μm)
		2		95.57	0.51-0.68
BTL3	1300	4	0.3	95.11	0.67-1.07
		8		91.82	0.75-1.20
		2		72.77	0.21-0.41
BTL5	1300	4	0.5	88.61	0.25-0.43
		8		89.43	0.84-1.34
		2		69.26	0.16-0.29
BTL7	1300	4	0.7	73.40	0.19-0.28
		8		81.00	0.70-1.01

These results are correspond with the findings of different researchers [10,11,12] reporting the increase in boundary mobility with cation concentration for tri-valance donor cations, but it then decreases markedly above a doping threshold of 0.5 mole% which is controlled by the microstructure of doped samples. As La^{3+} ions have different valance state (+3) as compared to the Ba^{2+} or Ti^{4+} (+2 or +4 respectively), substitution of Ba^{2+} produce a charge imbalance which leads to charge compensation leading to excess or shortage of electrons or vacancies of cations or anions. According to the 'Doping anomaly' or 'Grain size anomaly' phenomenon [11,12] a drastic change of $BaTiO_3$ characteristics is found as a result of doping with higher valence donor cations compared to the host cations.

It is found that, for donor-doped $BaTiO_3$, a drop in resistivity is observed at first with the increase of donor concentration which is generally attributed to an electronic compensation mechanism that induces n-type semiconductor characteristics [10]. For La^{3+} ion which acts as a donor dopant, free electrons in the $BaTiO_3$ lattice can be generated in the grain according to equations (written in Kröger-Vink notation) bellow the doping threshold value [10,11]:

$$2La_2O_3 + 4TiO_2 = 4La_{Ba}^{\cdot} + 4Ti_{Ti} + 12O_0 + O_2 + 4e' \quad (2)$$

However, when dopant concentration is higher than the threshold, the dopant can be compensated by forming cation vacancies [10,11] at grain boundaries:

$$2La_2O_3 + 6TiO_2 = 4La_{Ba}^{\cdot} + 6Ti_{Ti} + 18O_0 + 2V_{Ba}'' \quad (3)$$

Or, act as acceptors to occupy the Ti-site:

$$La_2O_3 + 2e' = 2La_{Ti}'' + 3O_0 + V_0 \quad (4)$$

At the same time, the oxygen absorption at the grain boundaries act as an oxidation reaction which gradually propagates into the grains [10]:

$$2TiO_2 + O_2 = 2Ti_{Ti} + 6O_0 + 2V_{Ba}'' + 4h^{\cdot} \quad (5)$$

Above the threshold, the accumulation of Ba^{2+} vacancies in the space charge is associated with a depletion of oxygen vacancies. The diffusivity of oxygen ions across the grain boundary is expected to be slow due to their relatively large size which provides a possible mechanism for the significant reduction in grain boundary mobility yielding in finer grain. Such grain growth inhibiting mechanism has also been evident in the different research study of $BaTiO_3$ ceramic [10,11,12].

In our work, above the threshold value of 0.5 mole% doping, the grain size reduced prominently (<0.50 μm) which can be due to the pinning effect of excessive La_2O_3 [10,11,13]. A high concentration of La^{3+} ions at or near grain boundaries restricted grain growth during sintering and promoted fine grains which result in unfavorable dielectric properties. Although very insignificant energy is needed for the dopant to concentrate at the grain boundaries more energy is needed to incorporate a dopant ion into an individual lattice site in complex oxides which

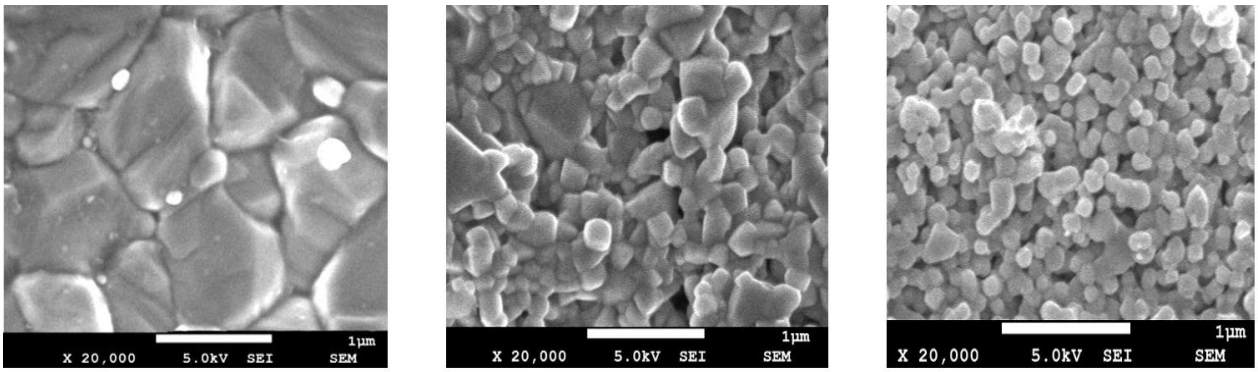

(a) (b) (c)

FIGURE 1. SEM micrograph of barium titanate samples sintered at 1300ºC for 4 hours holding (a) BTL3 (b) BTL5 (c) BTL7

is related to distortions, i.e. difference in ionic radii, and the formation of compensating defects during the incorporation of aliovalentions that have different valence states [11]. Thus, more energy was required in our research for the dopants to move inwards from the grain boundary by diffusion and thus reduce the pinning effect.

The required energy was provided by increasing the holding time to 8 hours at the maximum sintering temperature of 1300° C for all dopant concentration. So the average grain size of doped samples was about 1-1.2 µm, favorable for obtaining good electrical properties.

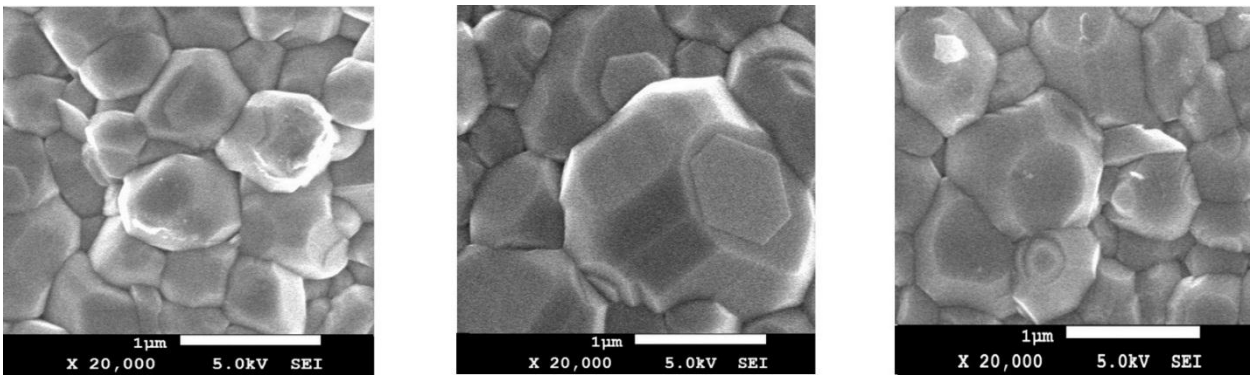

(a) (b) (c)

FIGURE 2.SEM micrograph of barium titanate samples sintered at 1300º C for 8 hours holding (a) BTL3 (b) BTL5 (c) BTL7.

The XRD results of lattice parameter in Table 2 showed that the tetragonality of $BaTiO_3$ crystal was reduced as the La_2O_3 doping level exceeds 0.5 mole% and at 0.7 mole % La_2O_3 doped Barium Titanate, the structure might retain the cubic phase to a greater degree. The corresponding changes in dielectric properties shown in Table 3 confirms the decrease of tetragonality as shifting the curie temperature from 100º C to 96º C when the La2O3 doping level increases from 0.5 mole% to 0.7 mole %. Moreover no trace of second phase appeared in the XRD analysis, which suggests that under the best sintering cycle (1300º C and 8 hours holding) almost all the La^{3+} ions were well diffused into the crystal structure of $BaTiO_3$ and reduced the pinning effect.

TABLE 2. Lattice parameters from XRD patterns of La_2O_3 doped $BaTiO_3$ samples

$Ba_{1-x}La_xTiO_3$	Sintering time (hr)	a (Å)	c (Å)	c/a	Cell Volume ($Å^3$)
$BaTiO_3$ (powder)	0	3.9993±0.002	4.0135±0.013	1.0035	64.20
$Ba_{0.997}La_{0.003}TiO_3$	8	4.0254±0.013	4.0032±0.004	1.0055	64.86
$Ba_{0.995}La_{0.005}TiO_3$	8	4.0061±0.003	4.0352±0.004	1.0073	64.76
$Ba_{0.993}La_{0.007}TiO_3$	8	4.0087±0.003	4.0038±0.002	1.0012	64.34

Dielectric Properties

The enhanced dielectric properties of BTL3, BTL5 and BTL7 ceramics obtained by solid state sintering for 8 hours at 1300º C have been studied. The temperature dependence of dielectric constant and dielectric loss as a function of donor concentration is presented in Fig 3**.** Dielectric dissimilarities were detected for the samples corresponding to tetragonal to cubic phase transition. The peak positions of all structural transitions were shifted to lower temperatures. The peaks became broadened and the peak position went higher (up to threshold doping %) as the lanthanum concentration increased. These plots also point out that up to 5 mole% addition of lanthanum leads to increase of dielectric constant. The observed peak temperatures corresponding to all structural transformation and dielectric constant values at 100 Hz for the samples are tabulated in Table 3.

TABLE 3. Theoretical density, grain size, curie temperature (T_C) and dielectric constant of best sintering cycles

$Ba_{1-x}La_xTiO_3$	Max. Sintering Temp. (ºC)	Sintering Time (hour)	Doping mole%	% theoretical density	Average Grain Size (µm)	T_C (ºC)	Dielectric Constant at room temp. and 100 Hz	Dielectric constant at T_C and 100 Hz
$Ba_{0.997}La_{0.003}TiO_3$	1300	8	0.3	91.82	0.75-1.20	110	6000	3200
$Ba_{0.995}La_{0.005}TiO_3$	1300	8	0.5	89.43	0.84-1.34	100	12700	8000
$Ba_{0.993}La_{0.007}TiO_3$	1300	8	0.7	81.00	0.70-1.01	96	1600	1200

According to the literature [15,16,17], for a particular temperature it is apparent that there is a decrease in dielectric constant with an increase of frequency and Fig. 4(a) conforms to this. It can be noted that dielectric constant for doped samples decreases rapidly with the increase of frequency and then stabilizes at a constant value. Therefore, addition of different concentration of lanthanum can be an effective way to control grain size and adjust the dielectric behavior.

Frequency dependent dielectric constant and dielectric loss of $BaTiO_3$ doped with different mole percentage of La_2O_3 and sintered at 1300ºC for 8 hours are shown in Fig. 4. Dielectric losses of all samples followed a similar pattern, they decreased with increase of temperature up to certain limit and increased as concentration of lanthanum became higher as shown in Fig. 3 and Fig. 4(b).

M.M. Vijatovic, B.D. Stojanovic [13] proposed two factors that can be responsible for this behavior. Lowering of Tc with lanthanum concentration may be due to size of La^{3+} (1.15 Å) which is smaller compared to Ba^{2+} (1.35 Å) and making the tetragonal phase unstable or due to creation of titanium vacancies destroying Ti–O–Ti linkages, responsible for ferroelectricity.

The pinning effect or influence of defect structure on doping level was found to affect grain size and grain size affects dielectric properties. Average grain size around 1 µm normally provides a good condition for dielectric properties of doped $BaTiO_3$. In this research, grain sizes in the range of 0.85-1.34 µm showed high dielectric constant, while increasing grain size deteriorated its property. The best stable value of dielectric constant as a function of temperature was obtained in the range 10000-12000 for 0.5 mole % La_2O_3 doped $BaTiO_3$ as shown in Fig. 3(b). It is evident from the figure that the curie point was shifted to about 100° C for BTL5 and to about 96° C for BTL7.

These results indicate at the influence of grain size on dielectric constant as well. As grain size of samples becomes smaller (~1/1.2 µm) by the influence of lanthanum concentration, dielectric constant becomes higher as noticed in the previous papers [12,13] as well.

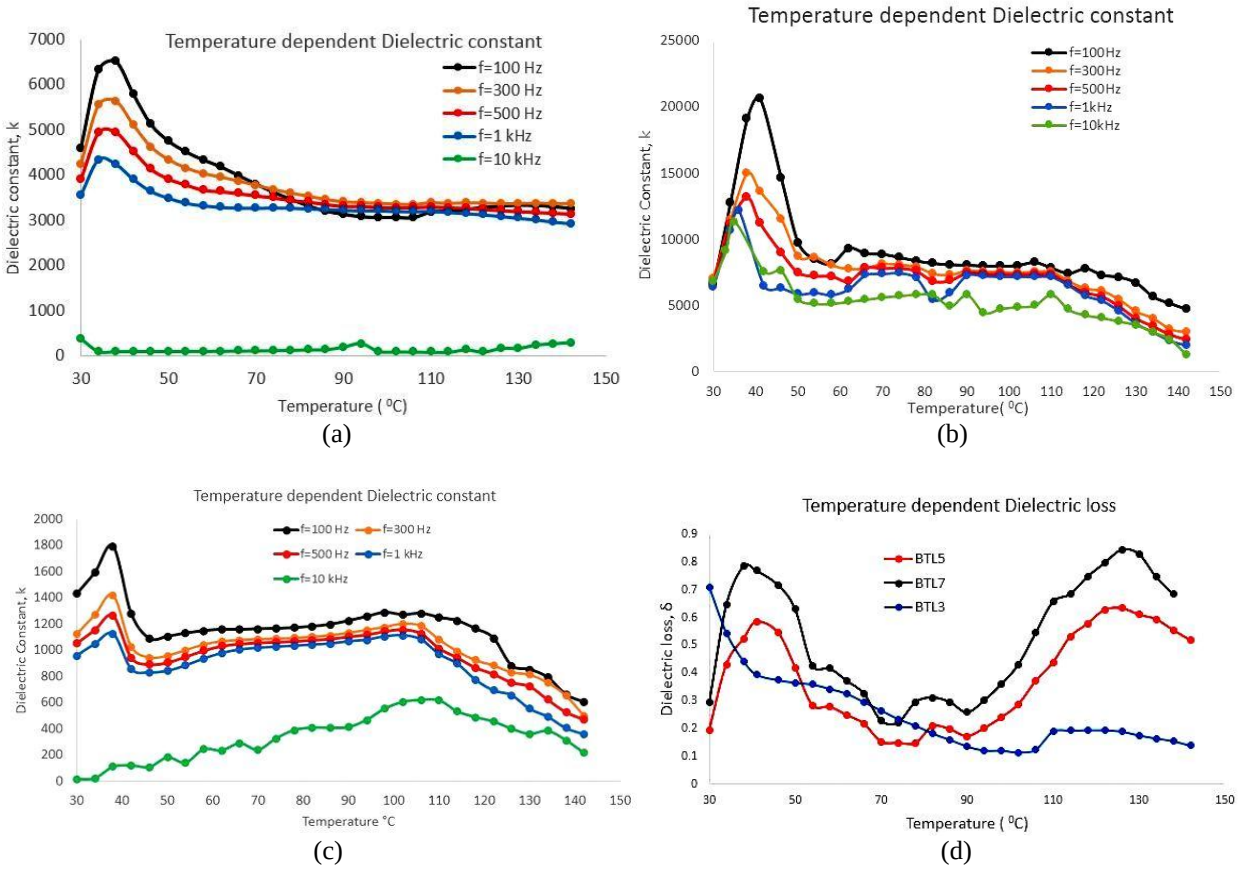

FIGURE 3. (a) Temperature dependent dielectric constant at different frequencies for 0.3 mole% La_2O_3 doped $BaTiO_3$ sintered at 1300º C for 8 hours, (b) temperature dependent dielectric constant at different frequencies for 0.5 mole% La_2O_3 doped $BaTiO_3$ sintered at 1300ºC for 8 hours, (c) temperature dependent dielectric constant at different frequencies for 0.7 mole% La_2O_3 doped $BaTiO_3$ sintered at 1300ºC for 8 hours, (d) temperature dependent dielectric loss at f=100 Hz for 0.3, 0.5 and 0.7 mole% La_2O_3 doped $BaTiO_3$ sintered at 1300º C for 8 hours.

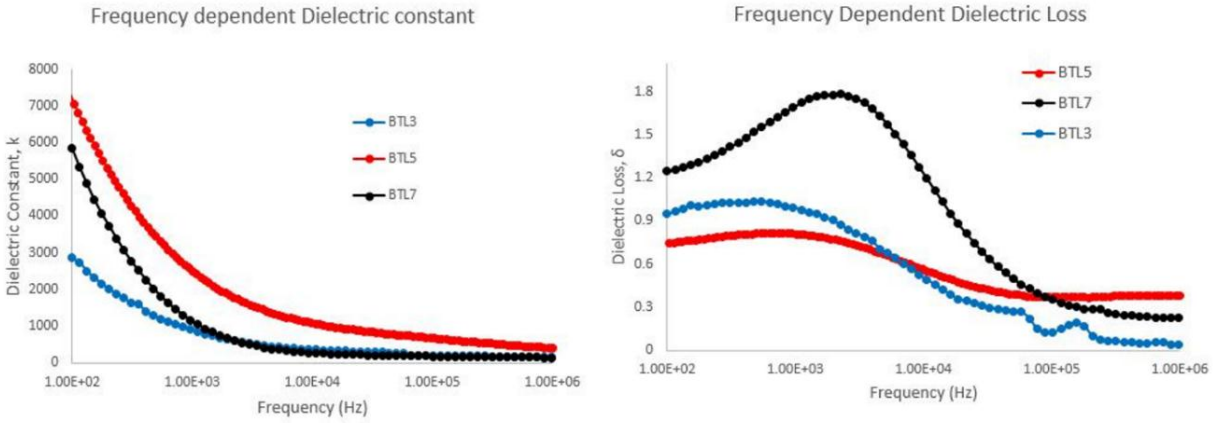

FIGURE 4. (a) Frequency dependent dielectric constant of 0.3, 0.5 and 0.7 mole% La_2O_3 doped $BaTiO_3$ sintered at 1300º C for 8 hours, (b) frequency dependent dielectric loss of 0.3,0.5 and 0.7 mole% La_2O_3 doped $BaTiO_3$ sintered at 1300ºC for 8 hours (determined at T=22º C)

Further research should be conducted of different ranges of intermediate mole percentage between 0.3, 0.5 and 0.7 mole% by polymeric precursor method for identifying detailed properties of lanthanum doped barium titanate.

CONCLUSIONS

In this work, moderate grain size of La doped $BaTiO_3$ was formed from sintering materials of 80-100nm size particles by conventional ball milling mixing process and solid state sintering method. The method appeared to be quite appropriate for the current work. By altering sintering temperature and holding time, grain size could be modified and hence the electrical properties were enhanced which also depended on dopant concentration.

Doping of La_2O_3 lowered the curie temperature by acting as a peak suppressor. Attractive dielectric constant was found with 1.0 - 1.2 µm grain size. The best stable of temperature dependent dielectric constant was found to be 13000 for 0.5 mole% doping of La_2O_3 with average 0.84-1.34 µm grain size. It was also found that, dielectric constant decreased with increasing applied frequency for a particular temperature.

ACKNOWLEDGMENTS

The author gratefully acknowledge the Glass and Ceramic Engineering Department, BUET and Bangladesh Council of Scientific and Industrial Research (BCSIR) for their consistent technical support.

REFERENCES

1. J.B. Xu, J.W. Zhai, X. Yao, Journal of Alloys and Compounds **467**, 567–571(2009).
2. H. Fan, L. Liu, , Journal of Electro-ceramic **22**, 291–296.(2009).
3. F. Wan, J.G. Han, Z.Y. Zhu, Phys. Lett. A, **372**, 2137–2140(2008).
4. Arlt G, Hennings D, De-With G, Journal of Applied Physics, **58**, 1619.(1985).
5. M.T. Biscaglia, V. Buscaglia, M. Viviani, P. Nanni, M. Hanuskova,, Journal of European Ceramic Society, **20**, , 1997–2007(2000).
6. F.D. Morrison, D.C. Sinclair, A.R. West, , Int. J .Inorg. Mater. 3, 1205–1210(2001).
7. Rubayyat Mahbub, Md. Sazzad Hossain, Md. Fakhrul Islam, Materiálové inžinierstvo (MEMI) Journal, 20, 45-53(2013).
8. Rajendra N. Basu, H. S. Maiti, Materials Research Bulletine **21(9),** 1107(1986).
9. B. Wodecka-Dus, D. Czekaj, Archives of Metallurgy and Materials, **54(4**), 923-933(2009).
10. Zhi Cheng Li, Bill Bergman, Journal of European Ceramic Society 25,441-445(2005).
11. Yoeng Jung Kim, June Won Hyun, Hee Soo Kim. Joo Ho Lee, Mi Young Yun. S.J. Noh and Yong Hyun Ahn, , Bulletin of Korean Chemical Society,**30(6),**1268-1273(2009).
12. Helen M.Chan, Martin P. Harmer and Donald M. Smyth, Journal of American Ceramic Society, 69[6],507-510(1986).
13. M.M. Vijatovic´, B.D. Stojanovic´, J.D. Bobic´, T. Ramoska, P. Bowen,, Ceramics International, **36**, 1817(2010).
14. Tadas Ramoška, J. Banys, R. Sobiestianskas, M. V. Petrovic, J. Bobic, B. Stojanovic, Processing and Application of Ceramics **4 (3),** 193–198(2010).
15. C. Barry Carter, M. Grant Norton, Ceramic Materials Science and Engineering (Springer, Third edition, 2007), pp.556-574.
16. Kingery, Bowen, Uhlman, Introduction to Ceramics (John Willey & Sons, Second edition, Singapore, 1976).
17. David W. Richerson, Modern Ceramic Engineering (Marcel Dekker, Second edition, 1992), pp.204-312.

ICME2015

International Conference on Mechanical Engineering 2015
(ICME 2015) 18 – 20 December, 2015, Dhaka, Bangladesh

Paper ID : 194

An Approximate Solution to the Stress and Deformation States of Functionally Graded Rotating Disks

Lakshman Sondhi[1, b)], Subhashis Sanyal[2, c)], Kashi Nath Saha[3, d)] and Shubhankar Bhowmick[2, a)]

[1]*Department of Mechanical Engineering, Shri Shankaracharya Group of Institutes, Bhilai, India*
[2]*Department of Mechanical Engineering, National Institute of Technology, Raipur 492010, India*
[3]*Department of Mechanical Engineering, Jadavpur University, Kolkata 700032, India*

[a)] Corresponding author: sbhowmick.mech@nitrr.ac.in
[b)]lsondhii@gmail.com
[c)]ssanyal.mech@nitrr.ac.in
[b)]kashinathsaha@gmail.com

Abstract. The present work employs variational principle to investigate the stress and deformation states and estimate the limit angular speed of functionally graded high-speed rotating annular disks of constant thickness. Assuming a series approximation following Galerkin's principle, the solution of the governing equation is obtained. In the present study, elasticity modulus and density of the disk material are taken as power function of radius with the gradient parameter ranging between 0.0 and 1.0. Results obtained from numerical solutions are validated with benchmark results and are found to be in good agreement. The results are reported in dimensional form and presented graphically. The results provide a substantial insight in understanding the behavior of FGM rotating disks with constant thickness and different gradient parameter. Furthermore, the stress and deformation state of the disk at constant angular speed and limit angular speed is investigated to explain the existence of optimum gradient parameters.

Keywords: Limit speed, rotating disk, functionally graded materials.

INTRODUCTION AND LITERATURE REVIEW

In functionally graded materials, the volume fraction of two materials, usually ceramic-metal mixture, is varied continuously as a function of position from one point to another along certain dimension(s). The composition change makes it possible to get the desired change in material properties with variation of the volume fraction. Rotating annular disks are widely used in mechanical engineering applications in form of rotors, impellers, cutters and storage devices, to name a few. Stress and deformation fields are induced and need to be determined for its mechanical design applications. In practical engineering applications, the load-carrying capacity of anisotropic or graded disks is much higher than that of the traditional isotropic disks of the same geometry. Moreover, the weight of the former is much lower than that of the latter as reported by some (Nemirovskii and Yankovskii, 2002). Tutuncu (2000) studied the instability problem of rotating polar-orthotropic disks and presented the stress redistribution solutions. Durodola and Attia (1997) investigated the displacement and stress components in FG orthotropic rotating disks by finite element method. A variational iteration based solution of elastic non-uniform thickness and density rotating disks has been reported by Hojjati and Jafari (2007). In a recent work, Callioglu et al. (2011) investigated the stress and deformation behaviour of annular rotating disks made of functionally graded materials by varying elasticity modulus and density according to a power law function with constant Poisson's ratio.

The present work reports the change in stresses and displacement states of rotating disks with functional variation in material properties. The problem is modeled by using variational principle, taking the radial displacement field as

the unknown dependent variable. Assuming, in such rotating disks, series approximation following Galerkin's principle, the solution of the governing equation is obtained. The application of variational principle yields advantage over classical approaches in terms of simplicity, being an integral formulation, and ease, due to the resulting algebraic solution. The validation of the present numerical scheme is carried out with existing literature. Corresponding to various rotational speeds, the stress and displacement field in the disk is estimated. The relevant results are reported in dimensionless form, and hence one can readily obtain the corresponding dimensional value for any geometry through appropriate normalizing parameters.

MATHEMATICAL FORMULATION

The mathematical formulation of a thin annular disk of inner radius a, outer radius b and having functionally graded material property is derived using Variational Principle. The geometry of disk is shown in Fig. 1. The disk rotates about its axis with an angular velocity of ω. The centrifugal load causes radial displacements in the disk depending upon the imposed boundary conditions. It is assumed that the disk is symmetric with respect to the mid plane, and being thin and carrying in-plane load, a state of plane stress (σz=0) persists in the disk. The present study is based on von-Mises' yield criteria, thus proposing that the distortional strain energy attributes to yielding. Denoting U as the strain energy stored in the disk and V being the work potential, the solution for the displacement field is obtained from the minimum potential energy principle:

$$\delta(U+V)=0 \tag{1}$$

$$U=\frac{1}{2}\int(\sigma\varepsilon)dv=\frac{1}{2}\int(\sigma_\theta\varepsilon_\theta+\sigma_r\varepsilon_r)dv \tag{2}$$

$$V=-\int u(\omega^2 r)dm \tag{3}$$

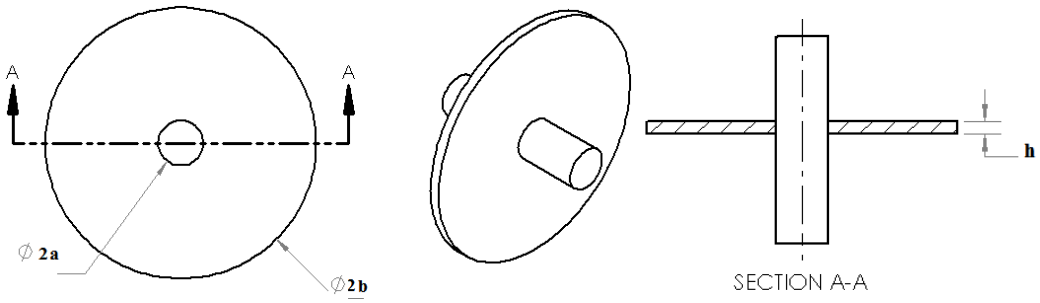

FIGURE 1. Rotating disk mounted on a shaft.

The material property follows the power law grading along the radial direction (Eq. 4). In the present work, the variation is considered for Young's modulus and density of the disk (Callioglu et al.). The Poisson's ratio is assumed to be constant.

$$E(r)=E\left(\frac{r}{b}\right)^n \tag{4}$$

$$\rho(r)=\rho\left(\frac{r}{b}\right)^n \tag{5}$$

The distribution of Young's modulus and density along the disk radius following the property distribution given in Eqs. (4-5) is shown in Fig. 2(a-b). Under plane stress conditions, the constitutive relations are as follows:

$$\varepsilon_r=\frac{(\sigma_r-\mu\sigma_\theta)}{E(r)},\quad \varepsilon_\theta=\frac{(\sigma_\theta-\mu\sigma_r)}{E(r)} \tag{6}$$

Due to the rotational symmetry, the strain-displacement relations are given by

$$\varepsilon_r = \frac{du}{dr} \quad , \quad \varepsilon_\theta = \frac{u}{r} \tag{7}$$

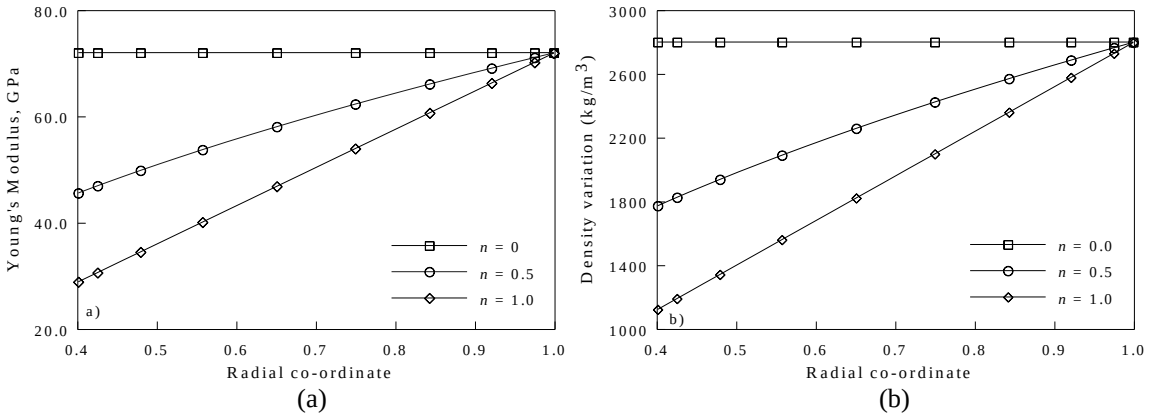

(a) (b)

FIGURE 2. (a) Young's modulus and (b) density variation according to power law material grading

Here ***u*** is the displacement component in the radial direction. On substituting Eqs. 6-7 in Eq. (2), the expression for strain energy becomes

$$U = \frac{\pi}{1-\mu^2}\int_a^b \left\{ E(r)\frac{u^2}{r} + E(r)2\mu u\frac{du}{dr} + E(r)r\left(\frac{du}{dr}\right)^2 \right\} h dr \tag{8}$$

Substituting Eqs. (3 and 8) in Eq. (1), the governing equation takes the following form,

$$\delta\left[\frac{\pi}{1-\mu^2}\int_a^b \left\{ E(r)\frac{u^2}{r} + E(r)2\mu u\frac{du}{dr} + E(r)r\left(\frac{du}{dr}\right)^2 \right\} h dr - 2\pi\omega^2 \int_a^b \rho(r) r^2 u h dr \right] = 0 \tag{9}$$

Eq. (9) is expressed in normalized co-ordinate (ξ) to facilitate the numerical computation and subsequently, the governing equation is expressed as:

$$\delta\left[\frac{\pi}{1-\mu^2}\int_0^1 \left\{ E(r)\frac{(u)^2}{\xi} + E(r)2\mu u\frac{du}{d\xi} + E(r)\xi\left(\frac{du}{d\xi}\right)^2 \right\} h d\xi - 2\pi\omega^2 b^3 \int_0^1 \rho(r)\xi^2 u h d\xi \right] = 0 \tag{10}$$

The displacement functions $u(\xi)$ in Eq. (10), can be approximated by a linear combination of sets of orthogonal coordinate functions as

$$u(\xi) \cong \sum c_i \phi_i, \qquad i = 1, 2, \ldots\ldots\ldots, nf. \tag{11}$$

The set of orthogonal functions ϕ_i are developed through Gram–Schmidt scheme, in which a starting function is used to generate the higher order orthogonal functions. The starting function ϕ_0, necessary in the first hand, is so selected as to satisfy the boundary conditions $\boldsymbol{u}_{(0)} = 0$ and the radial stresses at the inner and the outer of the disc are equal to zero, i.e. $\boldsymbol{\sigma_r} = 0$ at $\boldsymbol{r} = \boldsymbol{a}$ and $\boldsymbol{r} = \boldsymbol{b}$. The displacement function that satisfies above-boundary conditions is given below:

$$\phi_0(r)=\frac{\omega^2 r\ (3+\mu)}{8}\left[\frac{\rho(r)b^2(1-\mu)}{E(r)}-\left\{\frac{\rho(r)\left(1-\mu^2\right)r^2}{E(r)(3+\mu)}\right\}\right] \tag{12}$$

The function $\phi_0(r)$ is the start-function and using Gram–Schmidt orthogonalization scheme, an orthogonal set of polynomial functions, $\phi_i(r)$ are generated. The governing functional is obtained in matrix form by substituting Eq. (10) in Eq. (9):

$$\delta\left[\begin{array}{l}\dfrac{\pi}{1-\mu^2}\displaystyle\int_0^1\left\{E(r)\left(\frac{\left(\sum c_i\phi_i\right)^2}{\xi}+2\mu\left[\left(\sum c_i\phi_i\right)\frac{d}{d\xi}\left(\sum c_i\phi_i\right)\right]+\xi\ \left[\frac{d}{d\xi}\left(\sum c_i\phi_i\right)\right]^2\right)\right\}hd\xi- \\ 2\omega^2b^3\displaystyle\int_0^1\rho(r)\left\{\xi^2\sum c_i\phi_i\right\}hd\xi\end{array}\right]=0 \tag{13}$$

The operator 'δ', when replaced by $\frac{\delta}{\delta c_j}$, $j=1,2,\ldots n$, according to Galerkin's error minimization principle, the following equation is obtained.

$$\frac{1}{1-\mu^2}\sum_{i=1}^{n}c_i\int_0^1E(r)\left\{\frac{\phi_i\phi_j}{\xi}+\left(\mu\left(\phi_i'\phi_j+\phi_i\phi_j'\right)+\left(\xi\phi_i'\phi_j'\right)\right)\right\}hd\xi=\omega^2b^3\sum_0^1\int_0^1\rho(r)\left\{\xi^2\phi_i\right\}hd\xi \tag{14}$$

In Eq. 14, $(\,)'$ indicates differentiation with respect to normalized coordinate ξ.

RESULTS AND DISCUSSIONS

The numerical values of the different system parameters, considered in the present work are as follows. The inner and outer radii of the disc are ***a*** = 40 mm and ***b*** = 100 mm. Since it is considered that elasticity modulus and density vary in the radial direction in accordance with Eq. (4), thus, in accordance, an aluminum alloy (7075-T6) is selected as a disc material and its elasticity modulus is ***E*** = 72 000 MPa, mass density is $\boldsymbol{\rho}$ = 2800 kg /m3, $\boldsymbol{\mu}$= 0.3 and yield stress, $\sigma_0 = 503$ MPa. The grading parameter ***n*** is chosen as 0, 0.5 and 1.0. For ***n*** = 0, the disc assumes a homogeneous and isotropic state.

The validation of the present numerical scheme is made with the Callioglu [5] and are presented in Fig. 3 (a-c). In accordance with the cited reference, stress and displacement state of the disk is reported at an angular velocity, $\boldsymbol{\omega}$ = 15 000 min−1. As for boundary conditions of the annular disc, they are assumed to be free at the inner and outer radii. The results obtained are found to be in good agreement with the benchmarks reported in [5]. This establishes the foundation for carrying out further investigations of functionally graded rotating disks having different non-linear material behavior using the relatively simple and faster numerical model reported in the present study.

Further the radial and tangential strains are plotted in Fig. 4 (a-b) for different grading parameter, ***n***. The plots provide an insight into the variations in strain field for increasing grading parameter value. It is observed that with increase in ***n***, the radial and tangential strain induced in the disk reduces thus giving way to fall in stress values as corroborated in Fig. 3 (a-b). An interesting insight into the disk behavior, as depicted from the stress and strain fields plotted in Fig. 3-4 is that increasing the grading parameter increases the rotational capacity if the disk as lower stress values are obtained at same rotational speed for larger values of ***n***. Further it is interesting to note from Fig 3(b) that with increase of ***n***, the range of stresses reduces with in the disk geometry. The difference of maximum and minimum stresses defines the range and it is observed that increasing ***n***, at a given angular speed, reduces the range in a graded disk compared to an isotropic disk. This is significant as lower range of stresses inside the disk indicates more uniform stress distribution. This, otherwise, could be obtained by altering the geometry which may not always be a ready solution to achieve disks of uniform strength.

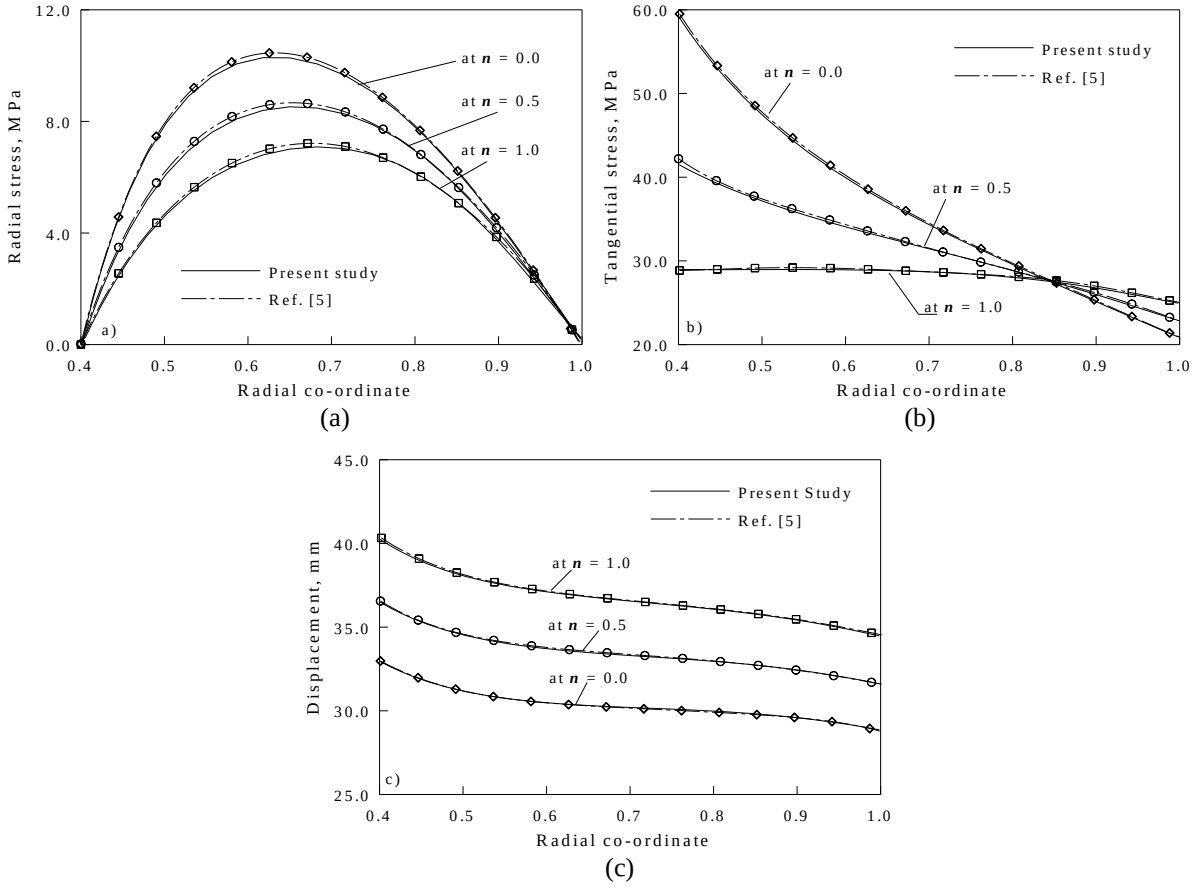

FIGURE 3. Effect of grading parameter on (a) radial stress, (b) tangential stress and (c) displacement of rotating disk.

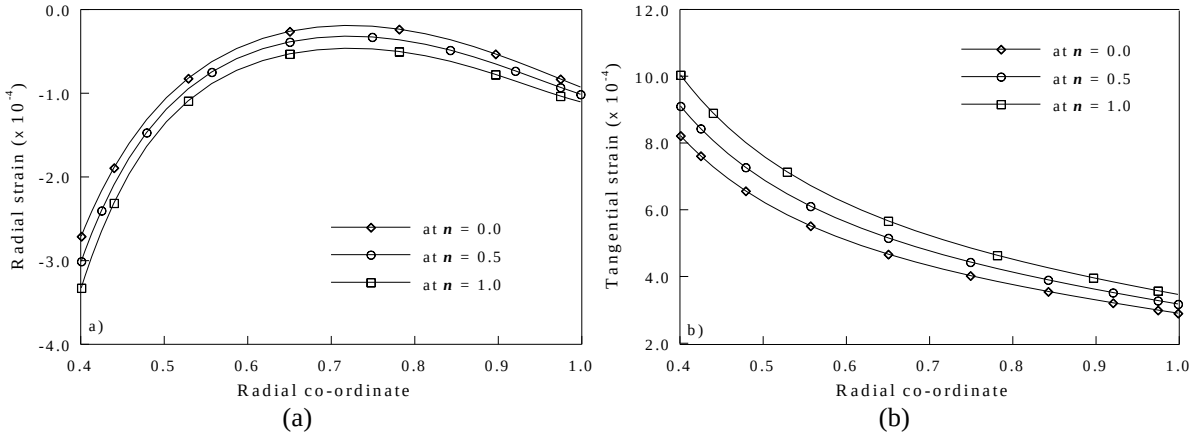

FIGURE 4. Effect of grading parameter on (a) radial and (b) tangential strain of rotating disk.

CONCLUSION

The present work employs a numerical scheme to obtain an approximate solution to stress and deformation states of rotating disk made of functionally graded material. The validation of the present numerical scheme is carried out substantially with existing literatures and good agreement is reported. The effect of the gradient parameter ***n*** is studied

on the stress, strain and displacement field of the disk. It is observed that with an increase in grading parameter ***n***, the disk strength improves and approaches that of a disk having uniform strength.

NOMENCLATURE

a	Internal radius of the disk
b	Outer radius of the dish
c_i	The vector of unknown coefficients
h	Thickness of the disk
n	Gradient parameter
r, θ, z	Radial, tangential and axial directions respectively
u	Displacement field of the disk
E	Elasticity modulus
ρ	Mass density
E_r	Elasticity modulus of the disk material in the radial direction
ρ_r	Mass density of the disk in the radial direction
U	Strain energy of the disk
V	Potential energies of the disk due to rotation
δ	The variational operator
μ	Poisson's ratio
$\varepsilon_r, \varepsilon_\theta$	Strains in radial and tangential direction respectively
σ_r, σ_θ	Stresses in radial and tangential direction respectively
σ_0	Yield stress of the disc material
σ_{vm}	von Mises stress
φ_i	The set of orthogonal polynomials used as coordinate functions.
ξ	Normalized radial co-ordinate ((r-a)/(b-a))
ω	Dimensional angular speed of the disk
Ω	Dimensionless angular speed of the disk
ω_1	Dimensionless limit elastic speed of the disk
Ω_1	Limit elastic speed, ($\omega_1 b \Big/ \sqrt{\rho / \sigma_0}$)

REFERENCES

1. Y. V. Nemirovskii, A. P. Yankovskii, Mech. Compos. Mater. **38**, 1–15 (2002).
2. N. Tununcu, Int. J. Mech. Sci. **37**, 873–881 (2000).
3. J. F. Durodola, J. E. Adlington, Key. Eng. Mater. **31**, 1199–1206 (1997).
4. M. H. Hojjati, S. Jafari, Far East. J. Appl. Math. **29**,185–200 (2007).
5. H. Callioglu, N. B. Bektas, M. Sayer. The Chinese Soc. Theor. and App. Mech. **27**, 950–955 (2011).

International Conference on Mechanical Engineering 2015
(ICME 2015) 18 – 20 December, 2015, Dhaka, Bangladesh

Paper ID : 201

Characterization of Tensile Fracture in Heat Treated Al-6Si-0.5Mg (-0.5Cu) Automobile Engine Block Alloy under Different Strain Rates

A. Hossain[1, a)] F. Gulshan[2] and ASW. Kurny[2, b)]

[1]*MSTE Plant (KTL), Sylhet Gas Fields Ltd., Golapgonj, Sylhet-3160*
[2]*Department of Materials and Metallurgical Engineering, Bangladesh University of Engineering and Technology, Dhaka-1000, Bangladesh*

[b)]Corresponding author: aswkurny@mme.buet.ac.bd
[a)]ah_buetmmesgfl@live.com

Abstract. This paper focuses on a typical automotive engine block Al-6Si-0.5Mg (-0.5Cu) alloys to characterize its fractographic appearance at various strain rates after tensile rupture. 0.5wt% Cu addition to Al-6Si-0.5Mg alloy increases the fracture strength and ductility all over the strain rates. Evaluation of fracture strength and ductility at the three strain rates (10^{-4}, 10^{-3} and $10^{-2}s^{-1}$) showed that strain rates affect the above properties and fracture behavior significantly. The material strength obviously increases with the increase of the strain amplitude where ductility reduces. The tensile fracture surfaces mainly exhibit the dimples and shear type dimples pattern under the low strain rates. Ordinary transcrystalline cleavage (facets, quasi-cleavage) and brittle fracture is observed under high strain rates.

INTRODUCTION

The aging-hardenable cast aluminum alloys, such as A356, are being increasingly used in the automotive industry due to their relatively high specific strength and low cost, providing affordable improvements in fuel efficiency. Eutectic structure of A390 can be refined and its properties can be improved by optimized heat treatment [1]. T6 heat treatment is usually used to improve fracture toughness and yield strength. It is reported that those factors influencing the efficiency of heat treatment of Al-Si hypoeutectic alloys include not only the temperature and holding time [2], but also the as-cast microstructure [3-5] and alloying addition [6-8].

The T6 heat treatment of Al-7Si-0.3 Mg alloy includes two steps: solution and artificial aging; the solution step is to achieve α (Al) saturated with Si and Mg and spheroidized Si in eutectic zone, while the artificial aging is to achieve strengthening phase (Mg_2Si). Recently, it is shown that the spheroidization time of Si is dependent on solution temperature and the original Si particle size [9-11]. A short solution treatment of 30 min at 540 or 550°C is sufficient to achieve almost the same mechanical property level as that with a solution treatment time of 6h [12]. From thermal diffusion calculation and test, it is suggested that the optimum solution soaking time at 540 °C is 2h [13]. The maximum peak strength of various Cu content Al-6Si-0.5Mg alloys could be reached within 1hr when ageing at 225ºC [14]. However, few studies are on the effect of combined treatment with short solution and short aging.

Addition of Cu to Al-Si alloys leads to the formation ofAl_2Cu phases and other intermetallic compounds, which influences the strength and ductility [15-17]. In high copper content alloys, complete dissolution of the Al_2Cu phase is sluggish and a longer time must be chosen to allow maximum dissolution of this intermetallic phase. However, solution treating the alloy for a long time is expensive and may not be necessary to achieve the optimum strength. Moreover, the coarsening of the microstructural constituents and the possible formation of secondary porosity that forms after prolonged annealing at those temperatures can deleteriously affect the mechanical properties [18]. For Al-Si-Mg alloys, the age hardening is caused by the precipitation of β" and/or β' phases (precursor of Mg_2Si phases) [19-20]. For Al-Si-Mg-Cu alloys, the precipitation behaviors are rather complicated and several phases such as β (Mg_2Si), θ ($CuAl_2$), S ($CuMgAl_2$) or Q ($Cu_2Mg_8Si_6Al_5$) in metastable situations may exist [21-23].

Therefore, it is the purpose of this work to study the tensile response of various Cu content commercial Al-6Si-0.5Mg alloys deformed in the stain rate range of 10^{-4} to $10^{-2}s^{-1}$ and, further, to investigate the microstructural changes.

MATERIALS AND EXPERIMENT PROCEDURE

The alloys were prepared by melting Al-7Si-0.3Mg (A356) alloys and adding Al & Cu into the melt. The chemical compositions of the alloys were presented in Table 1. The cast samples were ground to remove the oxide layer from the surface and were homogenised for 24 hours 500ºC. Samples for tension tests were prepared from the homogenised plates according to ASTM B-557M-06 standard (subsize, E8 M–04). The tension test samples were solution treated at 540ºC for 120minutes and quenched in ice-salt-water solution. The samples were subjected for ageing at 225 ºC for 1hr. Tensile testing was carried out in an Instron testing machine at three different cross-head speeds: 0.15, 1.5 and 15mm/minute which are equal to the nominal strain rates of 10^{-4}, 10^{-3} and 10^{-2} s^{-1} respectively for each alloys. The averages of three consistent test results were accepted as the tensile value for the corresponding sample. Fractographic observations of the fractured surfaces of selected samples were carried out in a Scanning Electron Microscope.

TABLE 1. Chemical compositions (wt %) of the alloys

Alloy	Si	Mg	Cu	Ni	Ti	Al
Al-6Si-0.5Mg	5.902	0.461	0.007	0.005	0.099	Bal.
Al-6Si-0.5Mg-0.5Cu	6.033	0.517	0.558	0.006	0.094	Bal.

RESULTS AND DISCUSSION

Fracture Stress-Strain Curves over a Wide Range of Strain Rates

Enhancing strain rates results in an obvious increase in fracture strength (Fig. 1). When the strain rates are below $10\text{-}^{3}s^{-1}$, work hardening decreases strongly. Work hardening decreases strongly during the plastic deformation of samples at $10^{-4}s^{-1}$, and sometimes necking phenomenon is observed in this strain rate before fracture. Al-6Si-0.5Mg-0.5Cu alloy shows the highest fracture strength while reference Al-6Si-0.5Mg alloy shows the lowest fracture strength at all strain rates.

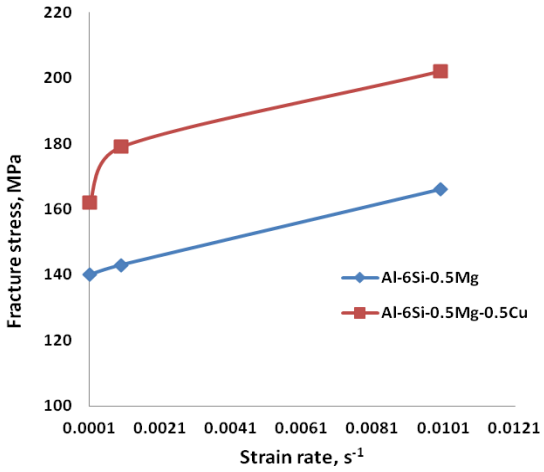

FIGURE 1. Typical fracture stress-strain curves of Al-6Si-0.5Mg (-0.5Cu) alloys.

Strain Rate Dependency of Ductility (%Elongation)

Figure 2 shows the variation of ductility (% elongation) of the alloys with strain rates. It is observed that at the strain rate for which strength is maximum ($10^{-2}s^{-1}$), the ductility values of the alloys pass through minima. The ductility value of the peak aged Al-6Si-0.5Mg-0.5Cu is found to be higher than the reference alloy in the examined strain rates. The ductility increased markedly with the addition of 0.5wt% Cu in all strain rates.

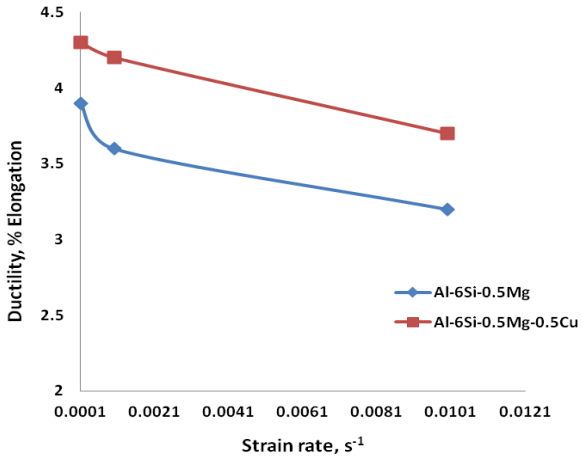

FIGURE 2. Typical ductility (%Elongation)-strain curves of Al-6Si-0.5Mg (-0.5Cu) alloys.

Effect of the Strain Rate on Fracture Surface and Structure

Figure 3 and Fig. 4 show the SEM micrographs of the fracture surfaces of the Al-6Si-0.5Mg and Al-6Si-0.5Mg-0.5Cu alloy at various strain rates. 0.5wt% Cu addition to Al-6Si-0.5Mg alloy increases the number of dimples and their sizes. Cu free Al-6Si-0.5Mg alloy shows the more shallow dimples and many transcrystalline facet planes (Fig. 3.a) but the 0.5wt% Cu content alloy (Fig. 4.a) increases the dimples depth and number. The deeper dimples at lower strain rate indicate the ductile tearing.

Figure 4.a and Fig. 4.b represent the classical ductile profile with existence of dimples with different sizes. At lower strain rate ($10^{-4}s^{-1}$) the dimples are larger and deeper than the higher strain rates ($10^{-3}s^{-1}$, $10^{-2}s^{-1}$) tensile testing samples. The cleavage facets (Fig.4.c) are mainly created at high strain hardening tensile testing.

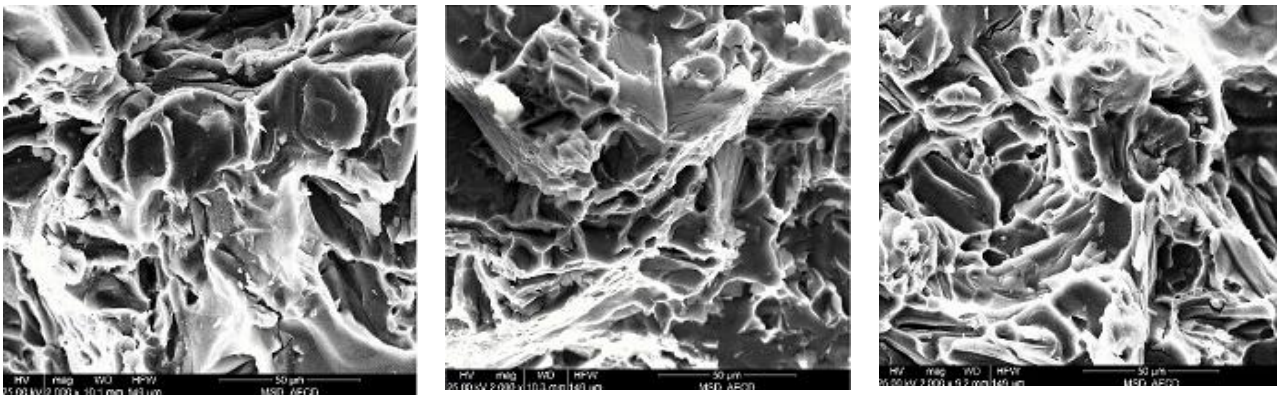

(a) (b) (c)

FIGURE 3. Al-6Si-0.5Mg alloy SEM micrographs of fracture surfaces at the strain rates (a) $10^{-4}s^{-1}$; (b) $10^{-3}s^{-1}$; (c) $10^{-2}s^{-1}$.

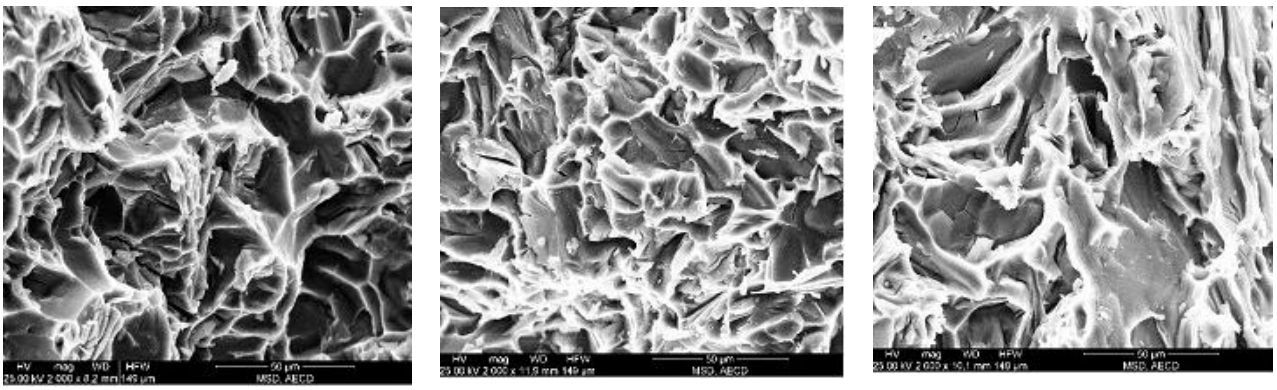

(a) (b) (c)

FIGURE 4. Al-6Si-0.5Mg-0.5Cu alloy SEM micrographs of fracture surfaces at the strain rates (a) $10^{-4}s^{-1}$; (b) $10^{-3}s^{-1}$; (c) $10^{-2}s^{-1}$.

CONCLUSIONS

The following conclusions could be drawn.

- Strain rate was found to affect the fracture strength, ductility and fracture behavior of the Al-6Si-0.5Mg (-0.5Cu) alloys. As the strain rate increased, fracture strength increased but ductility decreased. Under the same strain rate conditions, the Al-6Si-0.5Mg-0.5Cu alloy showed more clear increase in strength and ductility than the reference alloy.
- The fracture surfaces mainly exhibited the deeper and higher number dimples pattern under the low strain rates, ordinary dimple fracture surfaces were observed. In the alloys, the dimple size and depth increased as the strain rate decreased. The fracture surface has some transcrystalline cleavage planes and river patterns, there were also a few tearing ridges and dimples exist at the higher strain rate.

REFERENCES

1. L. Wan, J. Luo, G. Lan and Q. Liang, Journal of Huazhong University of Science and Technology: Natural Science Edition **36(8)**, 92−95 (2008).
2. E. Raincon, H. F. Lopez and H. Cineros, J. Mater Sci Eng A **519(1−2),** 128−140 (2009).
3. A. Mandal, M. Chakraborty and B. S. Murty, J. Mater Sci Eng A **489(1−2),** 220−226 (2008).
4. K. Lee, Y.N. Kwon, and S. Lee, J. Alloys Compounds **461(1−2)**, 532−541 (2008).
5. A. Vencl, I. Bobic, and Z. Miskovic, J. Wear **264 (7−8),** 616−623 (2008).
6. Y. Birol, J. Alloys Compounds **484(1)**, 164−167 (2009).
7. K. Tokaji, J. Mater Sci Eng A **396(1−2),** 333−340 (2005).
8. A M. Kliauga, E. A. Vieira and M. Ferrante, J. Mater Sci Eng A **480(1−2),** 5−16 (2008).
9. E. OgrisG, A. Wahlen, H. Luchinger and P. J. Uggowitzer, J. Light Metals **2(4),** 263−269 (2002).
10. E. Sjolander and S. Seifeddine, J. Mater Design **31**, 44−49 (2010).
11. B. Liu and Y. Xue, J. Special Casting & Nonferrous Alloys **26 (12)**, 802−805 (2006).
12. D.L. Zhang, L.H. Zheng and D.H. Stohn, J. Light Metals **2(1),** 27−36 (2002).
13. Z. Yu, H. Zhang, B. Sun and G. Shao, J. Heat Treatment **24(5)**, 17−20 (2009).
14. A. Hossain and A.S.W. Kurny, Universal Journal of Materials Science **1(1)**, 1-5 (2013).
15. S. G. Shabestari and H. Moemeni, J. materials Processing Technology **153-154,** 193-198 (2004).
16. M. Jin, Li. Jing, and J. G. Shao, Journal of alloys and Compounds **437**, 146-152 (2007).
17. Y.J. Li, S. Brusethaug and A. Olsen, Scripta materilia **54**, 99-103 (2006).
18. R. Smerd, S. Winkler, C. Salisbury, M. Worswick, D. Lloyd and M. Finn, International Journal of Impact Engineering **32**, 541–560 (2005).
19. S. Shivkumar, C. Keller and D. Apelian, AFS Trans **98**, 905-911(1990).
20. K.T. Kashyap, S. Murali, K. S. Raman and K. S. Smurthy, Mater Sci. **9,** 189–203 (1993).

21. I. C. Barlow, W. M. Rainforth, and H. Jones, J. Mater Sci., **35,** 1413–1418 (2000).
22. W. Reif, J. Dutkiewicz, R. Ciach, S. Yu and J. Krol, J. Materials Science and Engineering A**, 234-236 (30)** 165-168 (1997).
23. R. K. Mishra, G. W. Smith, W. J, Baxter, A. K. Sachdev and V. Franetovic, J. Mater Sci., **36,** 461–468 (2001).

ICME2015

International Conference on Mechanical Engineering 2015
(ICME 2015) 18 – 20 December, 2015, Dhaka, Bangladesh

Paper ID : 206

Fabrication and Comparison of Properties of As Cast and Hot Forged Aluminium Alloy-Alumina Composites

Farzana Ferdous [a],Sheikh Jaber Nurani[b], Chandan Kumar Saha [c], and M. N. Haque [d]

Department of Materials and Metallurgical Engineering, Bangladesh University of Engineering and Technology, Dhaka 1000, Bangladesh

[b]Corresponding author: sheikh.jaber.nurani@gmail.com
[a]ffj025@gmail.com
[c]chandan.buet08@gmail.com
[d]nhaque@mme.buet.ac.bd

Abstract. Metal matrix composites with unique properties are growing every day and widely used in different industries because of their high mechanical properties. Present work is focused on the study of behaviour of Al_2O_3 reinforced Aluminium Alloy composites produced by the stir casting technique and the effect of hot forging on it. Among the ceramic particles Al_2O_3 is favorable since it does not react with the matrix at high temperature and does not create undesired phases. The fabrication of Aluminium Alloy composites with different weight percentage of Al_2O_3 particles up to 0-15% in step of five were processed by stir casting method as it gives better matrix particle bonding. It was found that an increase in the Al_2O_3 content in scrap piston alloy contributed in enhancing the hardness of the composites. The developed composites were subjected to hot compaction at a temperature of 300ºC for half an hour using a hammer. Hardness, density and optical microstructure analysis of both as cast and forged aluminium alumina composites were examined. Hot forged composites exhibit higher hardness than as cast composites as forging reduces the porosity of the composites. Density and microstructural analysis supports that increase in hardness. Optical micrograph indicates uniform distribution of particles and refined grain structure of hammered samples. When compared with as cast matrix alloy and composite, hot hammered alloys and its composites exhibits higher extent of grain refinement. Porosity decreased in the hammered samples compared to as cast samples due to hammering.

INTRODUCTION

Metal Matrix Composites (MMCs) are an interested group of advanced materials which are under serious consideration to replace conventional materials as they have opened up unlimited possibilities for modern material science & development. Aluminium-Matrix Composites (AMCs) reinforced with particles and whiskers are widely used for a large number of structural applications such as those in the aerospace, automotive, defense and electricity industries because of their superior properties [1]. Metal matrix composite materials are the most promising because of their superior strength to weight ratio, good ductility, high strength and modulus, low thermal expansion coefficient, excellent wear resistance, corrosion resistance, high temperature creep resistance and better fatigue strength are worth mentioning [2, 3].

Fabrication of the particulate reinforced composite materials can be performed by adding the reinforcing particles into liquid matrix through liquid metallurgy route by casting [4-7]. Stir casting is highly preferred among the entire liquid state production routes as it's less expensive and more amenable to mass production. Size, shape and volume fraction of the reinforcement, matrix material and reaction at the interface have immense effect on the mechanical properties of MMC materials [8]. The interface between the matrix and reinforcement is very important factor in determining the properties of MMCs. The crack deflection at the interface have influence on toughness and so have the relaxation of peak stress near the interface on ductility [9-10]. Nurani studied the properties of Al alloy

based Al_2O_3 particle reinforced composite materials and concluded that mechanical properties like hardness, tensile strength of the composite materials significantly improved by the use of reinforcements [11]. In the present study, Al_2O_3 particle with three different weight fraction (5, 10 and 15) were used in the production of the samples.

It is reported that secondary processing of AMMC's by processes like extrusion, rolling, forging can lead to improved bond between matrix and reinforcement, reduction or elimination of porosity, break up of particle agglomerates, homogeneous distribution of reinforcements all of which contributes to quality products [12-13]. Amongst the various metal forming procedures, forging has emerged as an important secondary processing operation due to its ability to produce high strength products within short duration [14]. EZATPUR et al. investigated secondary process hot extrusion of Al/Al_2O_3 and found porosity decreased in the extruded ones by approximately 50% [13]. Raja et al. have carried out research on cast and forged Al6082/SiCp composites and found that, tensile strength of forged composites is higher in comparison with the cast ones [15].

In this project, microstructure and mechanical properties of a stir-cast and hot forged aluminium matrix composite reinforced with alumina particles were examined. In the light of the above, the present investigation deals with fabrication and comparative study of as cast and hot forged aluminium alloy alumina composites.

EXPERIMENTAL

In current work, Al piston alloy was used as matrix material. 5 kg of scrap Al piston alloy was melted in pit furnace above its melting temperature at 800C. The molten metal was poured in a sand mould at 750ºC. The molten metal when solidified yielded rectangular shaped bar which was used as matrix alloy. The composition of the matrix alloy is determined by OES analysis which is shown in table 1.

TABLE 1. Composition of matrix alloy

Si	Cu	Mg	Mn	Fe	Ni	Zn	Cr	Al
9.78	3.20	0.58	0.56	0.36	0.21	0.12	0.02	Bal

Alumina particle of mesh size +200 to -140 (74-105 µm) was used as reinforcement material. The particles were preheated at 800ºC for 1.5 hours to improve wettability. Desired composite samples were fabricated by stir casting technique utilizing mechanical mixing of molten alloy. At first, 1 kg of matrix alloy was placed in pit furnace with graphite crucible. Temperature was raised to 800ºC to melt the master alloy. Then degasser was used to remove dissolved gases. Master alloy melt was transferred to holding furnace of the stir casting machine. Preheated alumina particles were gradually added into the molten metal. The mixed molten metal was stirred for duration of 5 minitues using a mechanical stirrer and speed of the stirrer was maintained at 500 rpm.

FIGURE 1. Preparation of composites by stir casting method

The content of alumina particle injected into the molten alloy was chosen as wt. percentage of 5%, 10%, 15%. Finally the mixed molten metal was poured into permanent cast iron mould at a pouring temperature of 650ºC. After cooling to room temperature the composites were removed from the metal mould. Three different composite material was prepared.

As cast matrix alloy and alumina reinforced composites were subjected to metallographic, hardness and density tests. Hardness tests were carried out in a Rockwell hardness testing machine using F scale. The experimental density of the composites was obtained by the Archimedean method through weighing small pieces cut from the composite cylinder first in air and then in water. In addition, the theoretical densities were calculated using the mixture rule. Then all the cast samples were hammered over recrystallization temperature. Each of the samples was heated in muffle furnace at 300ºC for 0.5 hour and hammered. After hot forging, the samples were again subjected to metallographic, hardness and density tests. And we get the opportunity to compare the mechanical properties of as cast and forged matrix alloy and composites.

RESULT AND DISCUSSION

Effect of Hot Forging on Hardness

From fig. 2 it is seen that hardness increases with the addition of alumina particles. Alumina particulates are ceramic materials that are hard which influence the hardness of soft matrix positively. Hard ceramic particulates also inhibit the motion of dislocation and increase the hardness [16].

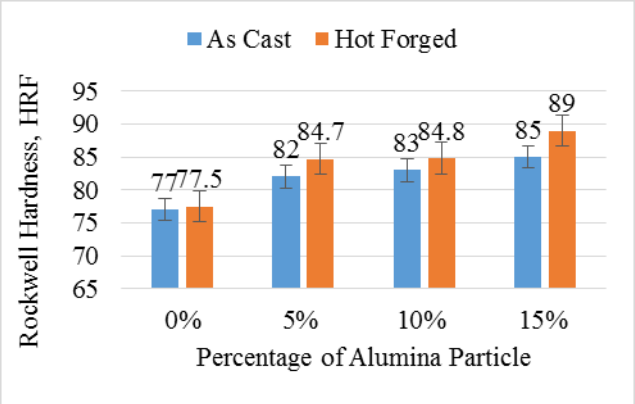

FIGURE 2. Comparison of hardness of as cast and hot forged composites

Hardness comparison of as cast and hot forged composites shown in fig. 2. From that figure it is shown that all the hot forged composite has higher hardness than as cast composite. This happen due to work hardening and decrease in porosity after hot forging [17]. The decreased porosity of composite is due to applied compressive force during hot forging which will fill the voids and other discontinuities present in the as-cast composites. Forging in hot condition gives better densification. The porosity increases with increasing the alumina mass fraction.

This is due to the effect of low wettability and agglomeration at high content of reinforcement and pore nucleation at the matrix/Al_2O_3 interfaces. So that composite containing 15% alumina particle has maximum porosities. After hot forging this porosities are removed significantly and maximum increase in hardness is observed than the other composite containing lesser amount of alumina particle.

Effect of Hot Forging on Density and Porosity

Relation of density and porosity with percentage of reinforcement is shown in fig. 3. Higher porosity and lower density leads to poor mechanical properties. Therefore, it is necessary to obtain good density composites by adopting secondary processing technique like hot forging. The effect of hot forging process on the density and percent porosity of the composites is illustrated in fig. 3 as a function of reinforcement content.It is observed from the given figure that there's existence of porosities in the produced composites. It is however a positive sign that the percent porosities are between 0.89 – 3.49% which is within the acceptable range of 4% porosity reported in literature as the maximum permissible in cast metal matrix composites [3].

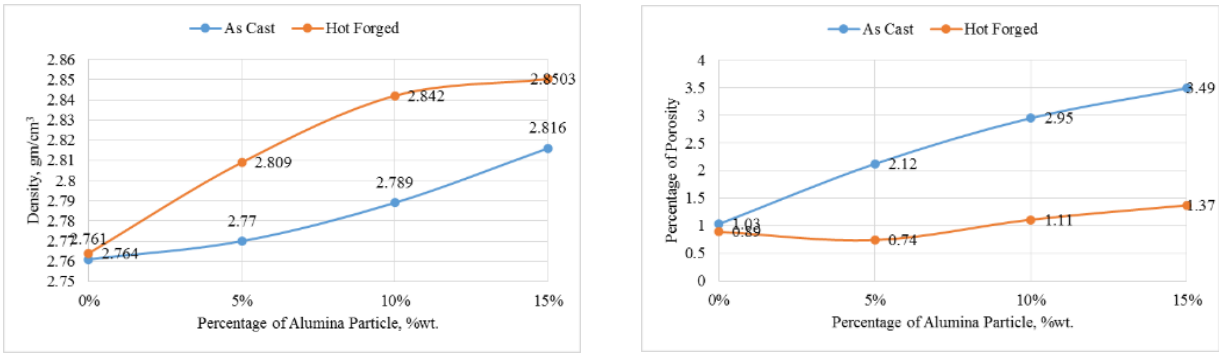

(a) (b)

FIGURE 3. Comparison of (a) Density and (b) Porosity of as cast and hot forged composite

As seen in the fig. 3, due to hot forging process porosity level becomes lower in hot forged composites than that of as cast composites. It is revealed that the amount of porosity in the composite samples increases with increasing weight percentage of Al_2O_3 particles. Further from figure above, hot forged composites reinforced with 10% and 15% alumina shows abrupt substantial increase in density than hot forged matrix alloy and 5% alumina reinforced composite. The reason behind this substantial increasing trend in density of 10% and 15% alumina reinforced composites is the presence of much more porosity in them than matrix alloy and 5% alumina composite. There is a possibility of happening more densification under compressive load during hot forging when the porosity level is high.

Effect of Hot Forging on Microstructure

Typical optical micrographs of the matrix alloy and alumina reinforced composite materials before and after the hot forging process are shown in Fig. 4. The prepared composites microstructure contains primary α-Al dendrites and eutectic silicon, primary silicon, intermetallic and Al_2O_3 particles [11].

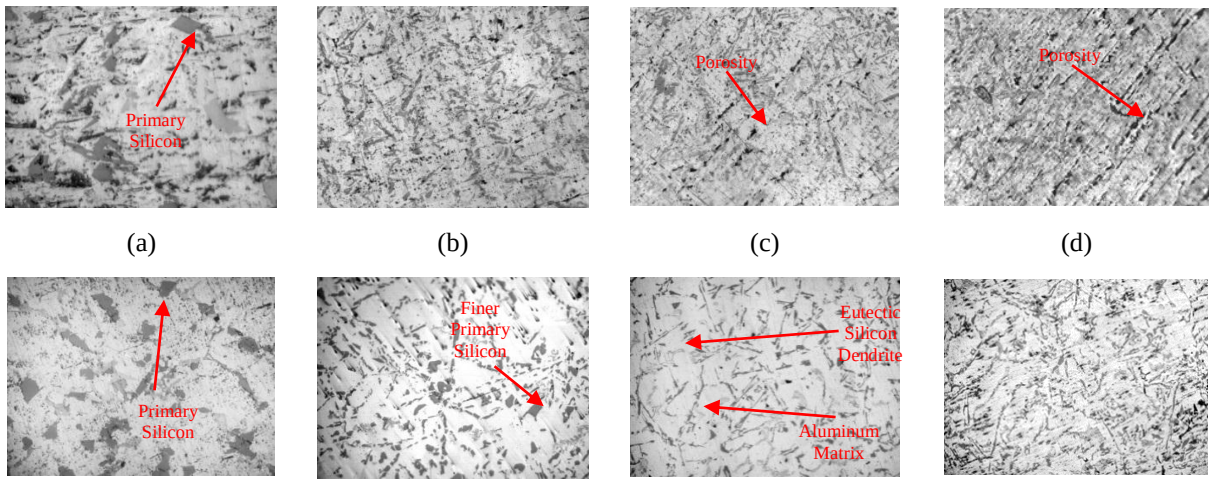

(a) (b) (c) (d)

(e) (f) (g) (h)

FIGURE 4. Comparison of micrographs of as cast and hot forged composites; (a) as cast matrix alloy, (b) as cast composite containing 5% alumina particle, (c) as cast composite containing 10% alumina particle, (d) as cast composite containing 15% alumina particle, (e) hot forged matrix alloy (f) hot forged composite containing 5% alumina particle, (g) hot forged composite containing 10% alumina particle, (h) hot forged composite containing 15% alumina particle

From fig. 4 it is seen that, with increase in addition of particle, grain size of both as cast and forged sample decreases. The most significant difference between the as-cast and the hot forged composite microstructures is that the large silicon becomes much smaller after hot forging as the grain size of Si becomes smaller [18].Mechanical properties improves due to that reduction of grain size by hot forging. Substantial reduction in porosity has been achieved after hot forging which resulted in improved properties. From the microphotographs in fig. 4 it is observed that the Al_2O_3 particle clusters which were initially present at few places in the as-cast composites after forging agglomerations/clusters have become sufficiently less [19].

Further studies of the microstructures of hot forged samples in fig 3 shows that the particles are distributed in a fairly uniform manner within the matrix alloy. Some particle orientation have also been occurred as a result of forging. Generally, inclusions cause weakness in the surrounding material. Hot forging causes these inclusions to break up and distributes them throughout the mass of metal. Hot forging causes break up of irregular structures of materials and recrystallize the mass of material into a finer grain structure.

CONCLUSION

Doing the elaborate research work on the effect of hot forging on scrap aluminium alloy alumina composite we reached to the following conclusion-

1. Composites are fabricated by stir casting method.
2. Hardness increased with increase in alumina content due to presence of hard ceramic particles and there is prominent increase in hardness in forged composites due to work hardening and decrease in porosity after hot forging.
3. Porosity was comparatively decreased in forged matrix alloy and composites than as cast matrix alloy and composites. The porosity level is higher in 10% and 15% alumina composites than matrix alloy and 5% alumina composite. That's why hot forged 10% and 15% alumina composites showed abrupt substantial increase in density than hot forged matrix alloy and 5% alumina reinforced composite
4. Due to hot forging microstructure became finer and uniformly distributed than as cast composites and properties improved significantly.

ACKNOWLEDGMENTS

The authors gratefully acknowledge Bangladesh University of Engineering and Technology for lab facilities and financial support of this work. We express our sincere gratitude to Professor Dr. M.N Haque and A.K.M.B Rashid for their kind assistance, thoughtful suggestion, constant guidance, supervision and intense co-ordination towards the successful completion of this work. We are also thankful to other lab coordinators.

REFERENCES

1. S. A. Sajjadi, H. R. Ezatpour, and H. Beygi, Mat SciEng A **528**, 8765-8771 (2011).
2. S. A. Sajjadi, H. R. Ezatpour, and M. T. Parizi, Mater Design **34**, 106-111 (2012).
3. M. kok, Journal of Materials Processing Technology **161**, 381-387, (2005).
4. N. Natarajan, S. Vijayarangan, and I. Rajendran, International journal of Vehicle Design **44**, 339-359(2007).
5. S. V. Prasad, and R. Asthana, Tribology Letters **17**, 445-453 (2004).
6. S. Amirkhanlou, and B. Niroumand, Transactions of Nonferrous Metals Society of China **20**, 788−793 (2010).
7. S. A. Sajjadi, M. T. Parizi, H. R. Ezatpour, and A. Sedghi, Journal of Alloys and Compounds **511**, 226−231 (2012).
8. K. U. Kainer, Basic of metal matrix composites, (Wiley-VCH, Germany, Weinheim, 2006).
9. S. Kumar, J. A. Theerthan, National Institute of Technology Rourkela, India, 1−57 (2008).
10. N. Parvin and M. Rahimian, ActaPhysicaPolonica Series A **121**, 108-110 (2012).
11. S.J. Nurnai, C.K. Saha, and M.N. Haque, International Journal of Innovative Science and Modern Engineering (IJISME) **3**, 75-79 (2015).
12. I. Ozdemir, U. Cocen, and K. Onel, Composite Science and Technology **60**, 411–419 (2000).
13. S.A. Sajjadi, H. R. Ezatpour, M.T. Parizi, Transactions of Nonferrous Metals Society of China **23**, 1262-1268 (2013).

14. R. Keshavamurthy, S. S. Ahmed, A. M. Laxman, N.H. A. Kumar, M. N. Shashidhara, and Y. V. Reddy, Advanced Materials Manufacturing & Characterization **4**, 87-92 (2014).
15. I. Dutt, S.M. Allan, and J.L. Hafley, Journal of Metallurgical and Material Transections **22**, 2553 (1991).
16. R. Thimmarayan, and G.Thanigayarasu, The International Journal of Advanced Manufacturing Technology, 48, 625-632 (2010).
17. M. A. Herbert, R. Maiti, R. Mitra, and M. Chakraborty, Trans. Indian Inst. Met., 60, 235-240 (2007).
18. H. S. Lee, J. S. Yeo, S. H. Hong, D. J. Yoon, and K. H. Na, Journal of Materials Processing Technology **113**, 202-208 (2001).
19. K.K. Deng, X. J. Wang, W.M. Gan, Y.W. Wu, K.B. Nie, K. Wu, M.Y. Zheng, and H. G. Brokmeier, Materials Science and Engineering A **528**, 1707–1712 (2011).

International Conference on Mechanical Engineering 2015
(ICME 2015) 18 – 20 December, 2015, Dhaka, Bangladesh

Paper ID : 210

Studies on Tensile Properties and Fracture Behavior of Al-6Si-0.5Mg (-Cu or/and Ni) Alloys at Various Strain Rates

A. Hossain[1, a)] F. Gulshan[2] and ASW. Kurny[2, b)]

[1]*MSTE Plant (KTL), Sylhet Gas Fields Ltd., Golapgonj, Sylhet-3160*
[2]*Department of Materials and Metallurgical Engineering, Bangladesh University of Engineering and Technology, Dhaka-1000, Bangladesh*

[b)]Corresponding author: aswkurny@mme.buet.ac.bd
[a)]ah_buetmmesgfl@live.com

Abstract. The aim of this paper is to evaluate the effects of various strain rates on the tensile properties of Al-6Si-0.5Mg cast alloys with Cu or/and Ni additions and to establish data on the stress–strain behavior of the alloys with applications in automotive engineering. Experimental alloys of the following composition were prepared by melt processing technique. Both microstructure and the mechanical properties were investigated. The uniaxial tension test was carried out at strain rates ranging from $10^{-4}s^{-1}$ to $10^{-2}s^{-1}$. Tensile strengths were found to increase with ageing temperature and the maximum being attained at peak age condition (1hr at 225ºC). The additions of Cu or/and Ni resulted in an increase in tensile strength and 2wt% Cu content alloy (Al-6Si-0.5Mg-2Cu) showed maximum strength. Evaluation of tensile properties at three strain rates (10^{-4}, 10^{-3} and $10^{-2}s^{-1}$) showed that strain rates affected the tensile properties significantly. At higher strain rates the strength was better but ductility was poor.

INTRODUCTION

Good forge and machinability, corrosion resistance and high strength-to-weight ratio make heat treatable aluminium alloys suitable for various crucial applications in the automotive industry, such as engine blocks, pistons and cylinder heads. The mechanical properties of Al alloys containing Si, Cu, Mg has been found to depend on distribution and shape of the silicon particles. The strengthening of these alloys during age-hardening has been attributed to the precipitation of Mg and Cu-rich phases [1-3].

Addition of Cu to Al-Si alloys leads to the formation of Al_2Cu phases and other intermetallic compounds, which influences the strength and ductility [4]. In high copper content alloys, complete dissolution of the Al_2Cu phase is sluggish and a longer time must be chosen to allow maximum dissolution of this intermetallic phase. However, solution treating the alloy for a long time is expensive and may not be necessary to achieve the optimum strength. Moreover, prolonged annealing can lead to the formation of porosity and it has been shown that porosity deleteriously affect the mechanical properties [5]. For Al–Si–Mg alloys, the age hardening is caused by the precipitation of β" and/or β' phases (precursor of Mg_2Si phases) [6-7]. For Al–Si– Mg–Cu alloys, the precipitation behaviors are rather complicated and several phases such as β (Mg_2Si), θ ($CuAl_2$), S ($CuMgAl_2$) or Q ($Cu_2Mg_8Si_6Al_5$) in metastable situations may exist [8-9].

A lot of works on the microstructure, heat treatment and mechanical behavior of Al-Si-Mg-Cu alloys have been done. The major advantages of Cu addition are increase in strength and hardness, both in the as-cast and in the heat-treated condition. Addition of Cu also affects corrosion resistance and ductility. Nickel is almost insoluble in aluminium (nickel solubility is about 0.05 weight % at 640 ºC, and less than 0.005 weight % at 450ºC). The adding of nickel up to 2 weight % increases the strength of aluminium, but reduces its ductility [10]. Addition of Ni leads to the formation of Al_3Ni in the aluminum matrix through eutectic reaction during solidification. In previous works Ni was identified to significantly enhance the high-temperature performance of Al-Si foundry alloys, though just to a certain level, depending on the fraction of eutectic phase in the alloy. Ni stabilizes the continuity of the eutectic network by increasing the volume fraction of rigid phases (Si + Al_3Ni) in the eutectic [11-13].

Results of tests on aluminium alloys at different strain-rate levels have been reported by a number of investigators. At room temperature, a very low, yet slightly positive, increase in flow stress with strain rate [14]. Similar observations regarding rate sensitivity of AA7003-T79 and AA7108-T6 alloys in tension have been reported

[15]. Flow stress and fracture strain of AA6005-T6 alloys were shown to have rather strong positive strain-rate sensitivity [16].

The aim of this paper is to evaluate the effects of various strain rates on the tensile properties of Al-6Si-0.5Mg cast alloys with Cu or/and Ni Additions and to establish data on the stress–strain behaviour of the alloys with applications in automotive engineering.

EXPERIMENTAL

Al and Al-Si master alloy, contained in a clay-graphite crucible, was melted in a gas-fired pot furnace. Copper, in the form of sheet (99.98% purity), was then added by plunging. Magnesium (99.7% purity) in the form of ribbon and packed in an Al-foil was added to the melt. The final temperature of the melt was maintained at 900±15°C. Before casting, the melt was degassed with solid hexachloroethane (C_2H_6) and homogenized by stirring at 700°C. Casting was done in a metal mould measuring 15mm x 150mm x 300mm and preheated to 200°C. All the alloys were analysed by wet chemical and spectrochemical methods simultaneously. The chemical compositions of the alloys are presented in Table 1.

The cast samples were ground to remove the oxide layer from the surface and were homogenised for 24 hours 500°C. Samples for tension tests were prepared from the homogenised plates according to ASTM B-557M-06 standard (Sub-size standard ASTM E8 M-04). The tension test samples were solution treated at 540°C for 120 minutes and quenched in ice-salt-water solution. The quenched tensile specimens were ageing up to 300°C for 1hr to optimize tensile strength. Tensile testing was carried out in an Instron testing machine at three different cross-head speeds: 0.15, 1.5 and 15mm/minute which are equal to the nominal strain rates of 10^{-4}, 10^{-3} and 10^{-2} s^{-1} respectively for each alloy. The averages of three consistent test results were accepted as the tensile value for the corresponding sample. Fractographic observations of the fractured surfaces of selected samples were carried out in a Scanning Electron Microscope.

TABLE 1. Chemical compositions (wt %) of the alloys

Alloy	Si	Mg	Cu	Ni	Fe	Sn	Ti	Al
Al-6Si-0.5Mg	5.902	0.461	0.007	0.005	0.146	0.004	0.099	Bal
Al-6Si-0.5Mg-2Cu	5.801	0.497	1.980	0.003	0.300	0.001	0.094	Bal
Al-6Si-0.5Mg-2Ni	5.965	0.454	0.007	2.202	0.141	0.001	0.088	Bal
Al-6Si-0.5Mg-2Cu-2Ni	5.760	0.501	1.968	2.001	0.265	0.001	0.081	Bal

RESULTS AND DISCUSSION

Effect of Ageing Temperatures on Tensile Strength

The results of the variation of ultimate tensile strength (fracture strength) under various aging conditions of the alloys are shown in Fig. 1. The test values obtained at a strain rate of testing $10^{-3}s^{-1}$ are used to plot the graph. From the nature of variation in tensile strength with aging temperature of the alloys, the tensile strength is an average of three tensile specimens. It can be seen that a maximum ultimate tensile strength is 249 MPa for Al-6Si-0.5Mg-2Cu alloy, which was obtained at 225°C and Al-6Si-0.5Mg-2Cu-2Ni alloy shows very close to the Al-6Si-0.5Mg-2Cu alloy. Al-6Si-0.5Mg-2Ni alloy shows higher strength than the Cu and Ni free Al-6Si-0.5Mg alloy [17-18].The UTS of the alloys decreases gradually when the test temperature is beyond 225°C. The Cu and Ni free alloy (Al-6Si-0.5Mg) shows the lower variation in tensile strength all over the aging temperatures.

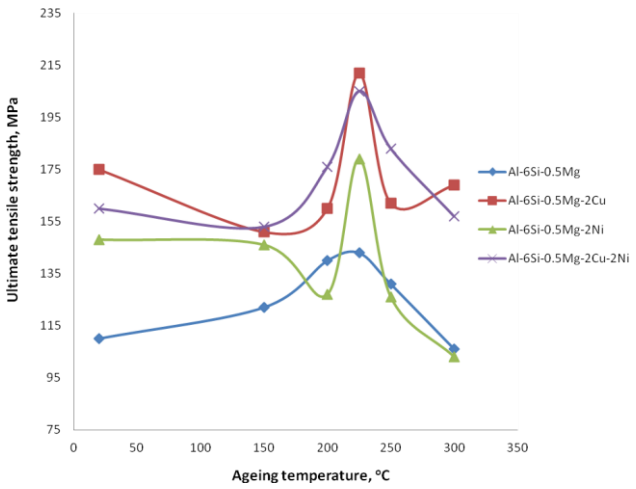

FIGURE 1. Ultimate tensile strength of the investigated alloys at different ageing temperatures.

Effect of Strain Rate on Ultimate Tensile Strength

The ultimate tensile stress - strain rates curves of the alloys (aged at 225°C for 1hr) are plotted in Fig. 2. The tensile test experiments are conducted at three different strain rates (10^{-4}, 10^{-3} & $10^{-2}s^{-1}$) for evaluation their effects on tensile properties. Enhancing strain rates results in an obvious increase in fracture strength. When the strain rates are below $10^{-3}s^{-1}$, work hardening decreases strongly for the alloys. In the case of Al-6Si-0.5Mg-2Ni and Al-6Si-0.5Mg-2Cu-2Ni alloys work hardening decrease strongly during the plastic deformation of sample at $10^{-4}s^{-1}$, and sometimes necking phenomenon is observed in this strain rate before fracture. The tensile strength increases more pronounced with the increase of strain rates and 2wt% Cu content Al-6Si-0.5Mg alloy. Al-6Si-0.5Mg-2Cu alloy shows the highest ultimate tensile strength all over the strain rates. But Al-6Si-0.5Mg-2Cu-2Ni alloy shows lower than Al-6Si-0.5Mg-2Cu alloy. The ultimate tensile strength of reference alloy (Al-6Si-0.5Mg) and 2wt% Ni containing alloy (Al-6Si-0.5Mg-2Ni) do not show significant change with the increase of strain rates.

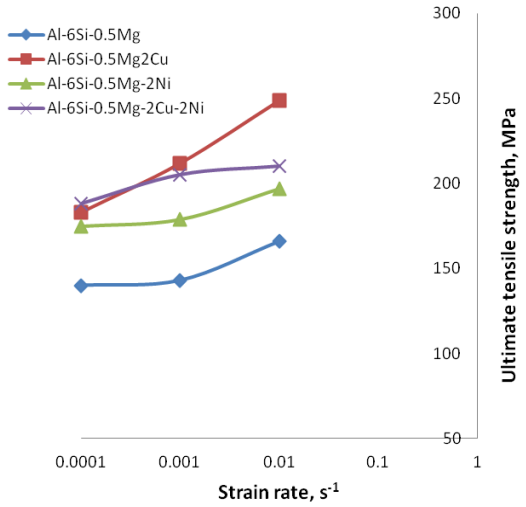

FIGURE 2. Ultimate tensile strength- strain rate curves of the peakaged alloys.

Effect of Strain Rate on Yield Strength

Figure 3 indicates that the yield strength (0.2% proof strength) vs. strain rates of the alloys. The increasing in proof strengths with strain rates of the alloys is very similar to the ultimate tensile strengths. With increase of strain rate and the maximum yield strength is being attained at $10^{-2}s^{-1}$. 2wt%Cu content Al-6Si-0.5Mg alloy (Al-6Si-0.5Mg-2Cu), was found to be highest yield strength among the investigated alloys all over the strain rates. The higher yield strength is due to the effect of precipitation hardening and higher strain hardening.

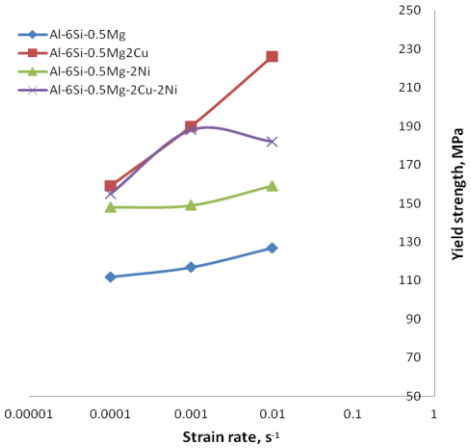

FIGURE 3. Yield strength- strain rate curves of the peakaged alloys.

Effect of Strain Rate on Ductility

Figure 4 demonstrates the variation of ductility (% elongation) with strain rates of the alloys. It is observed that at the strain rate for which strength is maximum ($10^{-2}s^{-1}$), the ductility values of the alloys pass through minima. The ductility value of the aged Al-6Si-0.5Mg-2Ni alloy is found to be less than all other alloys all over the strain rates. It was recorded maximum ductility at the strain rate of $10^{-4}s^{-1}$. Al-6Si-0.5Mg-2Cu alloy shows the maximum ductility all over the strain rates, so Cu has a significant effect on ductility than individual Ni or combined Cu-Ni additions to Al-6Si-0.5Mg alloy.

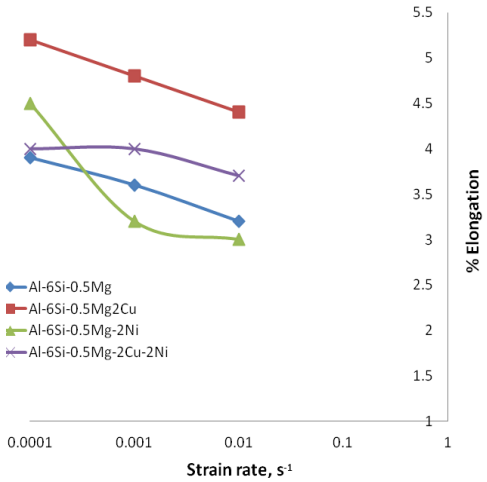

FIGURE 4. Ductility (%elongation) - strain rates curves of the peakaged alloys.

Microstructural Observation

The Figure 5 illustrates the scanning electron image with EDX spot analysis of the peakaged Al-6Si-0.5Mg-2Ni alloy. Al is present both in solid solution with the matrix and precipitates. Mg and Si combine to form a compound of Mg_2Si, which in turn forms a simple eutectic system. The spot1 EDS result indicates the Al-Si eutectic as fibrous like modified structure. The spot2 is mainly 1.10 wt% Mg containing aluminum solid solution. The EDS analysis of spot3 shows the rounded like eutectic Si phase and spot4 indicates the presence of Ni containing compound Al_3Ni.

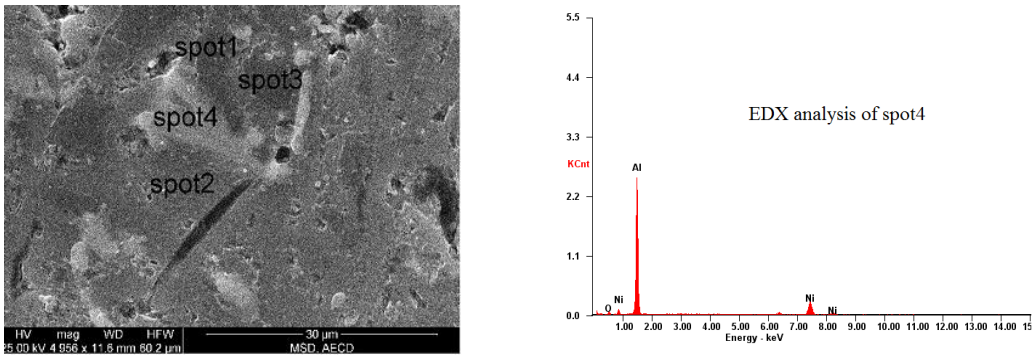

(a) (b)

FIGURE 5.(a)SEM micrograph of Al-6Si-0.5Mg-2Ni alloy after at 225°C for 1 hour; (b)the corresponding EDS spectra of spot4.

To study the complex eutectic mixture, EDX analysis using the scanning electron microscope (SEM) was carried out to identify the finer intermetallic compounds. As shown in Fig. 6, four spots were quantified and the EDS analysis reveals its chemical composition. The EDS analysis of spot1 represents the eutectic Al-Si phase which is more modified than the as cast structure. The chemical composition of the eutectic is 46.55wt% Al and 53.45wt% Si. Spot2 is the mainly aluminum matrix with 1.01wt% Mg. And spot3 is mainly the aluminium matrix with 1.01wt% Mg and spot4 is mainly the Al-Ni content (Al_3Ni) intermetallic compound.

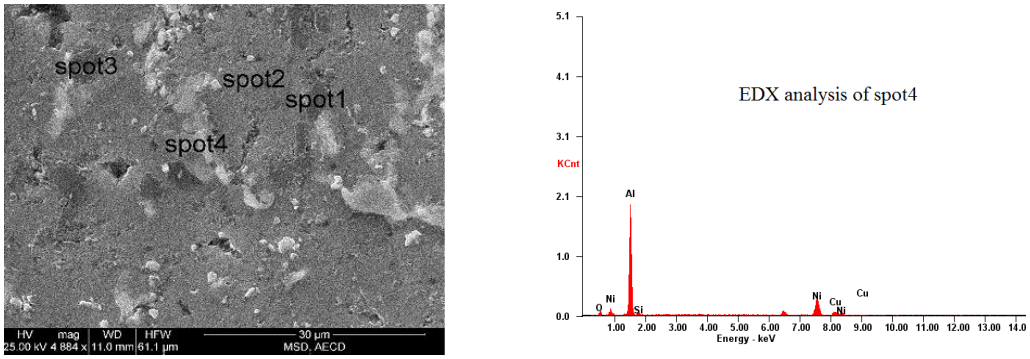

(a) (b)

FIGURE 6. (a)SEM micrograph of Al-6Si-0.5Mg-2Cu-2Ni alloy after aged at 225°C for 1 hour; (b) the corresponding EDS spectra of spot4

Effect of Strain Rate on Fracture Behavior

Figure 7 shows typical fracture morphologies of the alloys tested at a strain rate of $10^{-4}s^{-1}$. The precipitate particle fracture, interface debonding and matrix crack are main failure modes of aluminum based alloys. The tensile behaviors of the alloys are controlled by particle strength, particle matrix interface strength, and matrix strength and also affected by the strain rates. On a microscopic scale, the fracture surfaces appear to contain many microvoids in the matrix. The matrix–particles decohesion is also observed for these alloys. The void coalescence occurs when the void elongates to the initial intervoid spacing. This leads to the dimpled appearance of the fractured surfaces. Al-

6Si-0.5Mg, Al-6Si-0.5Mg-2Ni and Al-6Si-0.5Mg-2Cu-2Ni alloy show some brittle fracture surfaces but Al-6Si-0.5Mg-2Ni alloy shows the maximum brittle fracture surfaces among the alloys. 2wt% Cu containing alloy (Al-6Si-0.5Mg-2Cu) shows the maximum ductile fracture surface with higher and depth dimples. Then Al-6Si-0.5Mg-2Cu-2Ni alloy (2 wt% Cu+ 2wt% Ni) shows some ductile fracture surface area due to Cu content. So 2wt% Cu content alloy shows the maximum and 2wt% Ni content alloy shows the minimum ductility among the alloys.

Figure 8 shows the fracture surfaces of Cu and Ni containing Al-6S-0.5Mg-2Cu-2Ni alloy at the strain rates of $10^{-3}s^{-1}$ & $10^{-2}s^{-1}$.With the increase of strain rates the void coalescence occurs more rapidly and the load cannot be transferred from the matrix to the particles & precipitates, as a result the ductility of the materials decrease at higher strain rate.

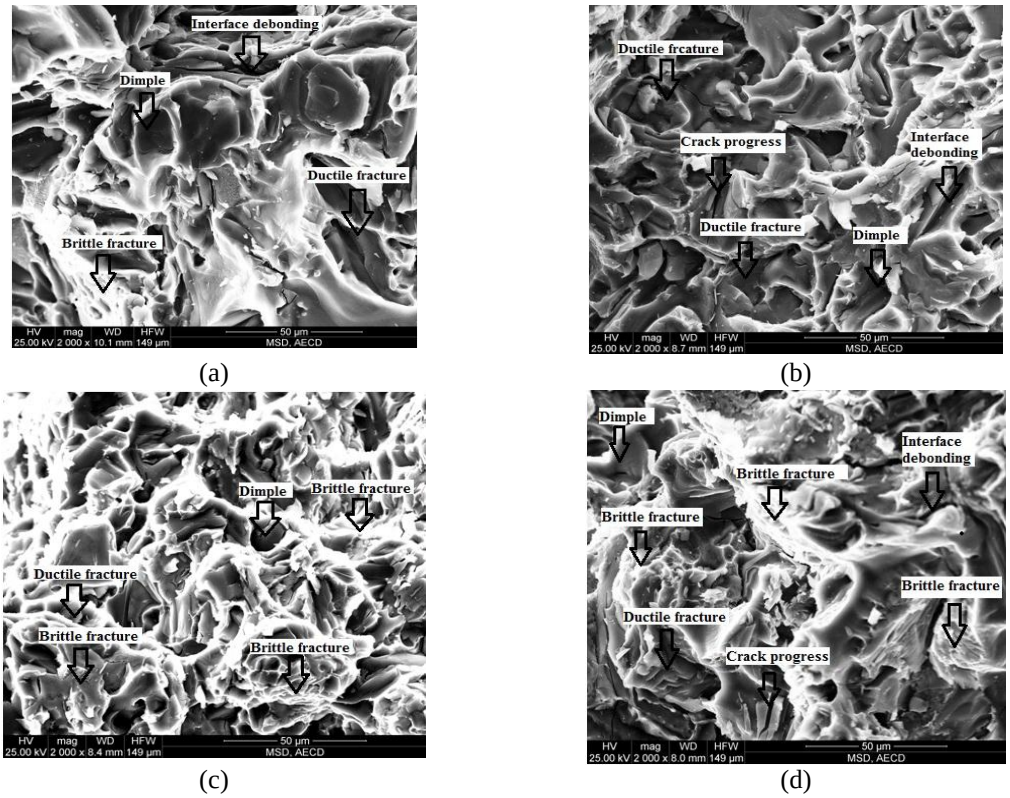

FIGURE 7. Tensile fracture SEM micrographs of (a)Al-6Si-0.5Mg; (b)Al-6Si-0.5Mg-2Cu; (c)Al-6Si-0.5Mg-2Ni; (d)Al-6Si-0.5Mg-2Cu-2Ni alloys (strain rate 10^{-4} s^{-1})

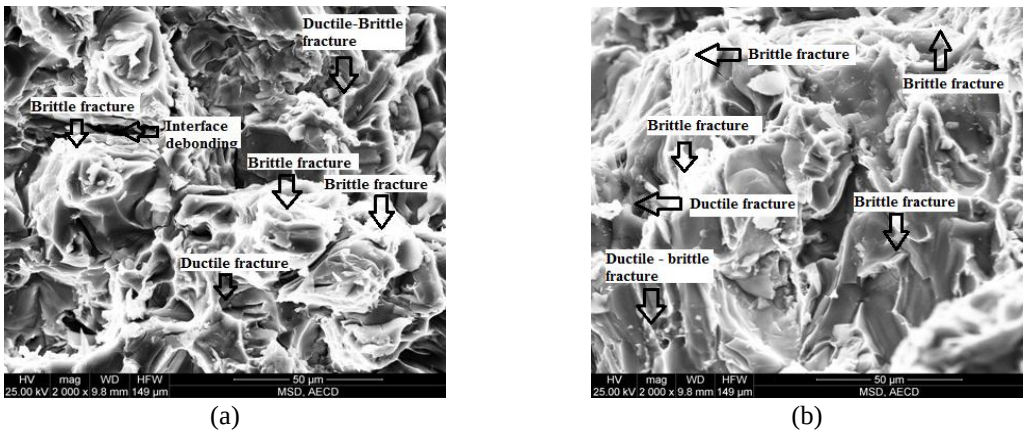

FIGURE 8. Tensile fracture SEM micrographs of Al-6Si-0.5Mg-2Cu-2Ni alloy at (a) $10^{-3}s^{-1}$; (b) $10^{-2}s^{-1}$ strain rate.

CONCLUSIONS

The effect of 2wt% Cu on tensile properties were more pronounced than 2wt% Ni or 2wt% Cu & Ni addition to Al-6Si-0.5Mg in the peak-aged condition. Ultimate tensile strength and yield strength increased with increasing strain rate but ductility reduced. 2wt% Cu content alloy (Al-6Si-0.5Mg-2Cu) shows the maximum strength and improved ductility all over the strain rates among the investigated alloys. 2wt% Ni content alloy (Al-6Si-0.5Mg-2Ni) shows the lowest ductility all over the experimental conditions.

REFERENCES

1 Y. Haizhi, J. of Mat. Engineering and Performance **12 (3)**, 288-297 (2003).
2 S. Seifeddine, Literature review - Vilmer project 2007; Jönköping University, Sweden.
3 F. Grosselle, G. Timelli and F. D. Bonollo, J. Materials Science and Engineering A **527,** 3536-3545 (2010).
4 Y.J. Li, S. Brusethaug and A. Olsen, Scripta materilia **54**, 99-103 (2006).
5 C.H. Ca´ceresa, M.B. Djurdjevicb, T.J. Stockwellb and J.H. Sokolowskib, Scripta Materialia **40(5),** 631-637 (1999).
6 S. Shivkumar, C. Keller and D. Apelian, AFS Trans **98,** 905-911(1990).
7 K.T. Kashyap, S. Murali, K.S. Raman and K.S. Smurthy, Mater Sci **9,** 189-203 (1993).
8 L. Hurtalova, J. Belan, E. Tillova and M. Chalupova, Mater. Sci. (Medziagotyra) **18(3),** 228-233 (2012).
9 E. Tillová, M. Chalupová, L. Hurtalová, M. Bonek and L.A. Dobrzański, Journal of Achievements in Materials and Manufacturing Engineering **47(1),** 19-25 (2011).
10 D. Batalu, G. Coşmeleaţă and A. Aloman, , Metalurgia International **11(8)**, 36–45, (2006).
11 W. Guiqing, S. Qingzhou, F. Liming, H. Luo and J. Cainian, Materials and Design **28,** 1001-1005 (2007).
12 F. Stadlerl, H. Antrekowitsch1, W. Fragner, H. Kaufmann and P. J. Uggowitzer, Mater. Sci. Forum **690**, 274-277 (2011).
13 F. Stadlerl, H. Antrekowitsch1, W. Fragner, H. Kaufmann and P. J. Uggowitzer, International Journal of Cast Metals Research **25(4),** 215-224, (2012).
14 L.D. Oosterkamp, A. Ivankovic, G. Venizelos, Mechanical Science and Engineering A **278,** 225-235 (1999).
15 A. Reyes, O.S. Hopperstad, O.G. Lademo and M. Langseth, Computational Materials Science **37,** 246-268 (2006).
16 T. Børvik, A.H. Clausen, M. Eriksson, T. Berstad, O.S. Hopperstad and M. Langseth, International Journal of Impact Engineering **32,** 35-64 (2005).
17 A. Hossain and A.S.W. Kurny, Universal Journal of Materials Science **1(1),** 1-5 (2013).
18 A. Hossain, A.S.W. Kurny, Chemical and Materials Engineering **2(1),** 9-13 (2014).

ICME2015

International Conference on Mechanical Engineering 2015
(ICME 2015) 18 – 20 December, 2015, Dhaka, Bangladesh

Paper ID : 222

Fabrication and Mechanical Properties of A319 and Fly Ash, Metal Matrix Composites

Md. Rubaiet Shattique[1, a)], Md. Golam Kibria[1, b)], Md. Abdul Halim[1, 2, c)], Sheikh Jaber Nurani[1, d)], Md. Adnan Karim[1, e)], and Dr. A S W Kurny[1, f)]

[1]*Department of Materials and Metallurgical Engineering, Bangladesh University of Engineering and Technology, Dhaka 1000, Bangladesh*
[2]*Department of Materials Science and Engineering, King Abdullah University of Science & Technology, Thuwal, Saudi Arabia*

[a)] Corresponding author: shattique.buet@gmail.com
[b)] kibria.buet004@gmail.com
[c)] halim.mrnd@waltonbd.com
[d)] sheikh.jaber.nurani@gmail.com
[e)] babonbuet@gmail.com
[f)] aswkurny@mme.buet.ac.bd

Abstract. To obtain enhanced properties than single alloy, metal matrix composites are formed, which is an engineered material of two dissimilar materials. An A319 aluminum alloy containing 3.5%Cu and 6% Si was used as the matrix and fly ash as the filler material in this study. Conventional foundry techniques was used to produce the composites. The fly ash was added in 5%, 7%, 10%, 12% and 15 wt. % to the molten metal. Fluidity, hardness, density, mechanical properties, impact strength, dry sliding wear, slurry erosive wear, and corrosion tests were carried out for the composites. At least five samples were prepared for each test. Microstructure examination was done using a scanning electron microscope to obtain the distribution of fly ash in the aluminum matrix.

INTRODUCTION

Metal matrix composites (MMCs) are new branch of advanced materials tailored from a combination of two or more materials (one of which is a metal and the other a non-metal) in which properties can be tailored or advanced then the parent materials. It has been reported that particle size and wear parameters (sliding speed, material property, normal load) influence the wear of the material [1–3]. In metal matrix composites fly ash particles can be potential discontinuous dispersoids. These particles are low-cost and low-density reinforcements, which are available in large quantities as a waste by-product in thermal power plants.fly ash, namely, precipitator (solid particle) and cenosphere (hollow particle). The major chemical constituents of fly ash are SiO_2, Al_2O_3, Fe_2O_3 and CaO. Mineralogically, the fly ash constitutes the aluminosilicate glasses containing quartz, mullite, hematite, magnetite, ferrite, spinel, anhydride and alumina [4]. When fly-ash particles are introduced, it reduces the density of Al alloys, improves damping properties, hardness, wear resistance and stiffness and [14–710]. Aluminum–fly ash composites have potential applications as covers, pans, shrouds, casings, pulleys, manifolds, valve covers, brake rotors, and engine blocks in automotive, small engine and the electromechanical industry sectors. The fly ash reinforced aluminum matrix composites are also termed as ‘Ash alloys’ [4]. Two common techniques of producing fly-ash reinforced aluminum MMC are Liquid metal stir casting [5, 9, and 11] and Infiltration techniques [9–11].

Sannino et al [12] had an extensive review dry sliding wear characteristics of composites based on aluminium and Deuis [13] on their abrasive wear behavior. In these studies fly ash was separated into cenosphere and precipitator fly ash. The use of precipitator

Fly ash in aluminum decreases the density of composites and increases their wear resistance [14]. Bienias et al. [15] reported the pitting corrosion behaviour and corrosion kinetics of Al alloy with precipitator fly ash (9 vol. %, 75–100 μm) composites. It was found that fly ash particles lead to an enhanced pitting corrosion of the composite in comparison to unreinforced matrix.

In this paper, Al–3.5% Cu alloy with fly ash (as received from Barapukuria coal fired power plant) as reinforcing particulates were introduced and successfully fabricated using the stir casting method. Fly-ash was added in 5%, 7%, 9%, 11% and 15% weight percentage. Fluidity, mechanical properties, dry sliding wear, slurry erosive wear, and the corrosion behaviour of the MMCs were thoroughly investigated.

METHODOLOGY

Fly ash, rice husk, hydrated lime mixtures and gypsum as a binder were used for the construction of bricks. Optimizing the process variables like composition of the mixture, pressure and curing conditions, the finalized properties of the produced bricks were established.

Hydrated lime, rice husk and gypsum were gathered from the local market. Besides, the main component fly ash was collected from Barapukuria Thermal Power Plant. XRF spectrometry was used to examine the composition of the fly ash.

TABLE 2. Chemical composition of Barapukuria Power plant fly-ash

Compound	SiO_2	Al_2O_3	Fe_2O_3	CaO	MgO
Mass Fraction,%	48.20	42.24	3.37	3.31	0.20

Dehydrating the raw materials in a muffle furnace at 110°C, required amount of ingredient was weighed using a delicate electronic balance. To ensure constant size of the bricks a common weight of mixture was used every single time to satiate the mold cavity. 6 X 3.5 cm was the measurement of the mold cavity opening. A hydraulic press was used to apply pressure. As a minimum of five bricks were prepared for each specimen type.

The bricks were then removed and finally cured. Curing was done using water spray in air, by keeping the bricks immersed in water under wet cloth. Bricks formed under various pressures were also cured for different periods in optimum curing condition.

RESULTS AND DISCUSSIONS

Effect of Fly-ash Content on Hardness

The results (Fig. 1) show, with increasing fly ash content hardness, tensile strength, compression strength, and impact strength of the composites increases. Clearly hardness is increasing with the addition of fly ash. This may occur due to the dispersion of hard fly ash particulates within comparatively softer A319-Cu- Si alloy [7].

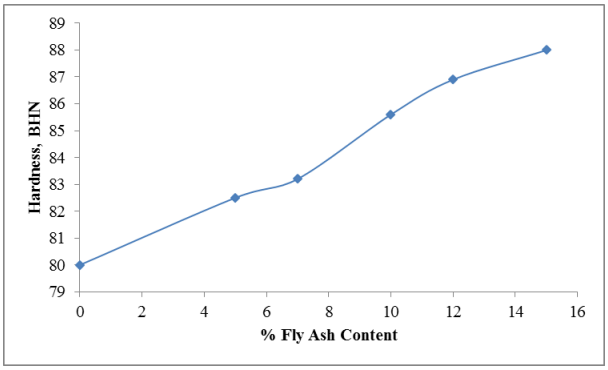

FIGURE 1. Hardness change at different Fly Ash content

Effect of Fly-ash Content on Density

Density decreases with the increase of fly ash content in the composite which is shown in fig. 2. As density of matrix alloy is 2.745 g/cm^3 and the density of fly ash is 2.09 g/cm^3, it decreases the total density of the composite.

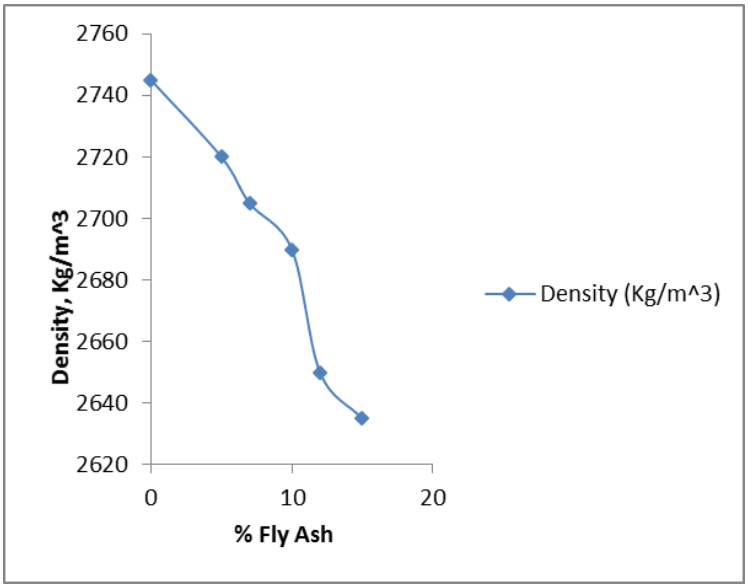

FIGURE 2. Density change at different Fly Ash content

Effect of Fly-ash Content on Tensile Strength

Not only tensile strength is increasing with the addition of fly ash but also it is greater for smaller cross-section. However, fly ash, revealing hard and lighter microsphere, hinders the movement of dislocation motion as well as refines the matrix. This refinement results in improved tensile strength. Heat transfers faster from the mold in the case of smaller cross section, results in a finer structure which consequently gives better tensile strength.

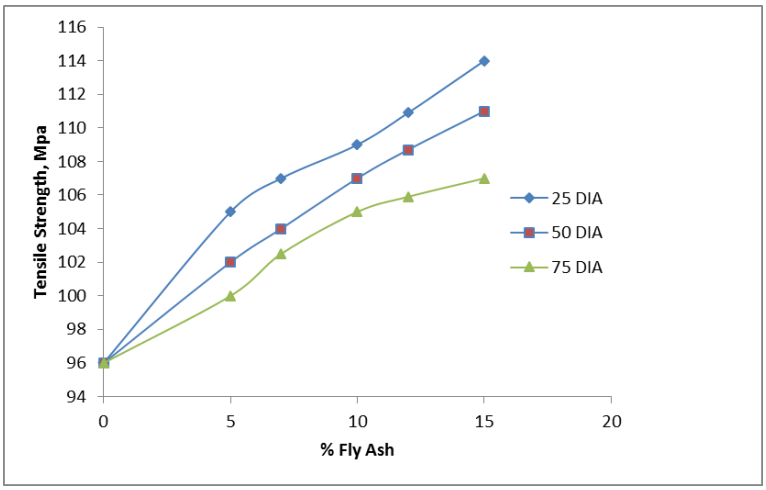

FIGURE 3. Tensile strength change at different Fly Ash content

Effect of Fly-ash Content on Compressive Strength

Similar with tensile strength, addition of fly ash particles also increases compressive strength by hardening the base alloy. Besides, fly ash reinforcement possessing higher weight percentage, may improve the material density which results in greater compressive strength.

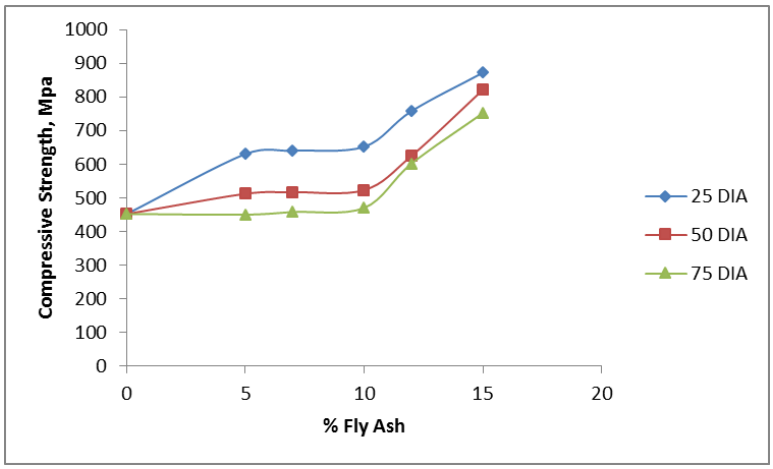

FIGURE 4. Compressive strength change at different Fly Ash content

Effect of Fly-ash Content on Impact Strength

The impact strength (Fig. 5) also increases with increasing fly ash content. This may be due to the presence of hard fly ash particulates.

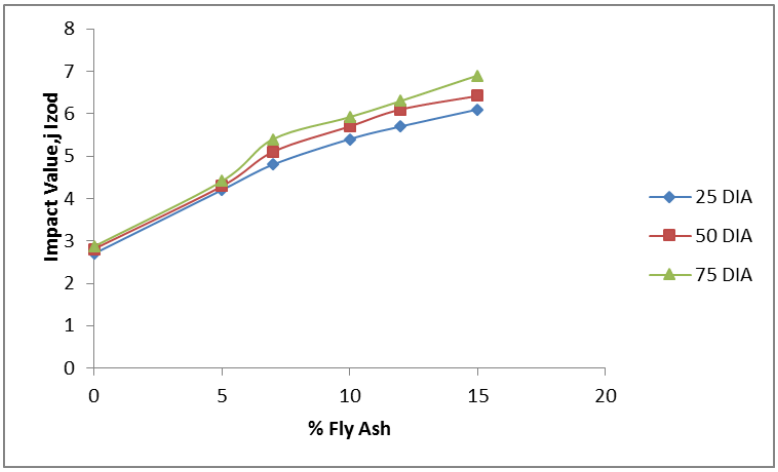

FIGURE 5. Impact value (Izod) change at different Fly Ash content

Effect of Fly-ash Content on Waer Properties

Figure 6 reveals the dry sliding wear stuffs. There is strong evidence of wear reduction with fly ash particle addition. In reality, fly ash is abrasive in nature and average particle size taken for this experiment is in the range of 1µm to 10µm which is greater in size than the particles singled out during the course of wear. So, the more is the fly ash, the more is the particle present to strengthen the matrix and less is the ploughing action. Thus we get improved wear resistance with increasing fly ash content.

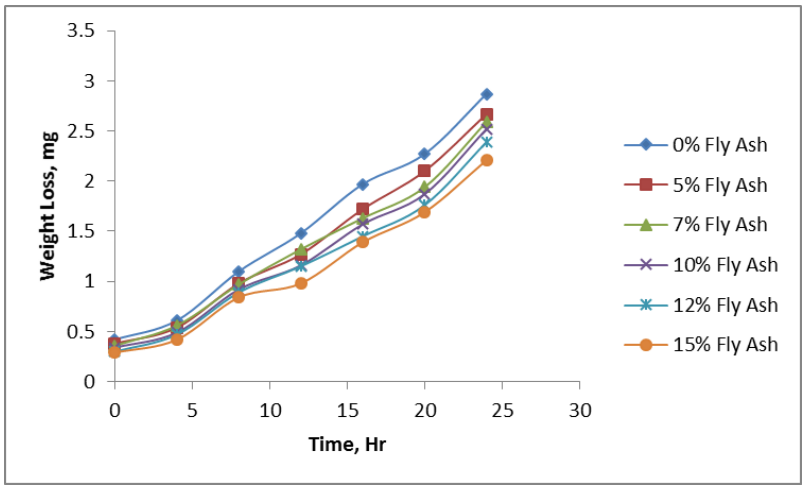

FIGURE 6. Variation of wear properties with time

CONCLUSION

Although casting endeavor for all the fly-ash percentages were carried out in this study, MMCs containing up to 15% fly ash particles were easier to fabricate. Uniform distribution of fly ash in the matrix was observed. The hardness increases with an increasing percentage of the fly ash particulates whereas, the fluidity and density decreases. The tensile strength, compression strength, and impact strength increase with an increasing percentage of fly ash particulates. The dry sliding wear resistance increases with an increasing percentage of fly ash. Corrosion increases with an increasing percentage of fly ash content. Further research can be carried out for the MMC's properties prepared by compocasting and squeeze casting method.

REFERENCES

1. T. S., Eyre Tribol. Int., (1976) 203
2. K.J. Bhansali, and R. Mehrabian, J. Metals, **34**, 30(1982).
3. F.M. Hosking, F.F. Portillo, R. Wunderlin, and R. Mehrabian, J. Mater. Sci., (1982), 477.
4. P. K. Rohatgi, JOM, **46**, 55-59 (1994).
5. R. Q. Guo, and P. K. Rohatgi, Metall Mater Trans B, **29**, 519–25 (1998).
6. P. K. Rohatgi, R.Q. Guo, P. Huang, S. Ray, Metall Mater Trans, **28**, 245–250 (1997).
7. P. K. Rohatgi, Z. Grony, J. Sobczak, N. Sobczak, Trans Foundry Res Int., 143–160 (1993).
8. P. K. Rohatgi, R. Q. Guo, B. N. Keshavaram, G. Golden, AFS Trans, **103**, 575 (1995).
9. G. Golden, EPRI J, **19**, 46 (1994)
10. B. N. Keshavaram, K.G. Satyanarayana, B. Majumdar, P.K. Rohatgi and B. Duttagur, Proc of the 6th Int Conf on Fracture ICF, 6 New Delhi; 1984. pp. 2979.
11. J. Sobczak, N. Sobczak, P.k. Rohatgi, In: Ciach R, editor. NATO ASI Ser – 3, High Technol. Kluwer Academic Publishers; 1998. p. 109.
12. A. P. Sannino, and H.J. Rack, Wear, **216**, 1 (1995).
13. R. L. DEUIS, C. SUBRAMANIAN, J. M. YELLUP., Wear, **201**, 132 (1996).
14. Q. Guo, P.K. Rohatgi, Metal. Mater. Trans. B, **29B**, 519 (1998).
15. J. Bienias, M. Walczak, B. Surowska, J. Sobczak, J. Optoelectronics Adv. Mater., **5**, 55 (2003).

International Conference on Mechanical Engineering 2015
(ICME 2015) 18 – 20 December, 2015, Dhaka, Bangladesh

Paper ID : 253

A Vibration Control System Using Negative Stiffness Mechanism.

Md. Emdadul Hoque [a)], Fazlur Rashid [b)], Ashfaq Mohammad Saad[c)] and Mominul Islam[d)]

[1] *Department of Mechanical Engineering, Rajshahi University of Engineering & Technology, Bangladesh*

[a)]Corresponding author: emdadulhoque@gmail.com ,
[b)]frrashed10@gmail.com ,
[c)]ashfaqmohammadsaad10@gmail.com
[d)]islam.mominul72@gmail.com

Abstract. Along with the increasing degree of industrialization vibration is also increasing and vibration has its bad impact which creates damage, disturbances etc. Due to this bad impact of vibration various industry of large to small are spending a large amount of dollar. Therefore, we have to reduce vibration in lower level. For reducing vibration, this paper represents an active (zero power magnetic suspension) vibration control system and a passive high negative stiffness system. In active vibration (zero power magnetic suspension system) control system an electromagnet and a permanent magnet uses in the magnetic suspension system and flux to circulate in the magnetic circuit. Magnetic fields generate by moving charges or current. Depending upon the gap between electromagnet and the suspended object vibration is isolated by the attractive force of the electromagnet. In passive high negative stiffness system an added system combined with main isolation system. The combination of main isolation system and an added negative stiffness system has an advantage to attain its natural frequency zero without change its static displacement. But, when the main isolation system's has high negative stiffness, the stiffness of the added negative stiffness system is correctively high. This problem only suffers by passive vibration control system than active one. For this reason this paper represents both active and passive vibration control system. In such cases where the main isolation system's has high negative stiffness than the stiffness of the added negative stiffness system then use active vibration control system by using zero power magnetic suspension system. First of all, we present analytical model of active vibration control system and passive high negative stiffness system and then present the experimental model with experimental result. Active vibration control system consists of two parts: original system (mass, main spring) and electromagnet and permanent magnet but passive high negative stiffness system consists of two parts: original system (mass, main spring) and negative stiffness system .At first study analytically non- linear system and finally set up experimental model with linear system due to its attainability of very low natural frequency than non-linear one that can be used in high stiffness system. From this two vibration control system result comparable.

INTRDOUCTION

Any motion that repeats itself after an interval of time is called vibration or oscillation. A vibratory system in general includes a means for storing potential energy (spring or elasticity), a means for storing kinetic energy (mass or inertia), and a means which energy is gradually lost (damper). A vibration of a system involves the transfer of its potential energy to kinetic energy and kinetic energy to potential energy alternately. If the system is damped some energy is dissipated in its cycle of vibration and must be replaced by external source if a state of steady vibration is to be maintained [1]

In the spring kinetic energy is converted to potential energy when the spring is moving upward, and potential energy is converted to kinetic energy when the spring is moving downward. Plucking the spring supplies the energy to the system and the air damps the vibration and slows it. There are different classes of vibration: free (undisturbed) and forced (disturbed), damped and undammed (has negligible or no damping), nonlinear and linear, and random deterministic.[2]

A body or structure is deformed when an external load or force is applied. This is a common problem in engineering fields. This external disturbance may be static or dynamic. So to decrease the deformation under load magnetic suspension system can be applied. Magnetic suspension can be achieved by using electromagnet and permanent magnet. Electromagnet or permanent magnet in the magnetic suspension system causes flux to circulate in a magnetic circuit and magnetic fields can be generated by moving charges or current. Depending upon the gap

between electromagnet and the suspended object the deformation under load can be decreased by the attractive force of the electromagnet. Stiffness is defined as the force per unit deflection. In negative stiffness system, the vibrating object moves to an equilibrium position located in the direction opposite to the applied force. An isolated object with negative stiffness is unstable. So to make the system stable, combine the system with a positive stiffness is the ratio of applied force to deflection. This force and deflection is in generalized co-ordinate .Positive stiffness occur when the deformation is in same direction as the external force, corresponding to a restoring force that the deform body back to its equilibrium Position.

Theoretical Approach

For Negative Stiffness System

When load is applied to the mass (m) then in the main spring (k_o) displacement occurred. To reduce the displacement and vibration, negative stiffness mechanism apply by using normal spring($k_{1)}$ and negative stiffness spring(k).The mathematical proof of this mechanism is shown below:

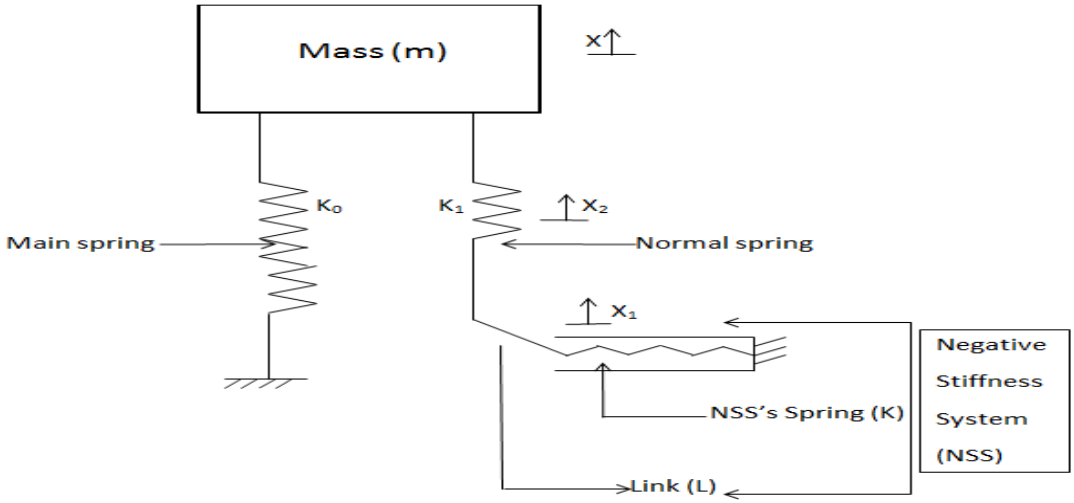

FIGURE 1. System with Negative Stiffness

Potential energy of the Negative stiffness system is given by , [3,4]

$$U=\frac{1}{2}kx_3^2+\frac{1}{2}k_1x_2^2 \quad (1)$$

Here, $X_3=(\partial-l)+\sqrt{(l^2-x_1^2)}$

Put the value of x_3 in equation (1) and differentiating we get

$$\partial k/\partial x=\partial^3U/\partial x^3=-(3kl^2(\partial-l)x)/(l^2-x^2)^{5/2} \quad (2)$$

Where, ∂ is spring initial deflection and l is bar length.

If ∂=l then from equation (2) the first derivative of NSS's stiffness will be zero [5]. That's why we are interested to use this system in Negative stiffness system because for maximum or minimum value first derivative will be zero.

$$\partial^2k/\partial x^2=\partial^4U/\partial x^4=-(3kl^2(\partial-l)((l^2-x^2)^{5/2}-5x^2(l^2-x^2)^{3/2}))/(l^2-x^2)^5 \quad (3)$$

Since the value of second derivative is negative so the maximum value of stiffness is zero at ∂=l. using this concept vibration is controlled by passive negative stiffness mechanism system [6].

For Zero Power Magnetic Suspension System

Magnetic suspension system can be achieved by using electromagnet and permanent magnet. Electromagnet and permanent magnet in the magnetic suspension system causes flux to circulate in a magnetic circuit, and

magnetic fields can be generated by moving charges or current. Depending upon the gap between electromagnet and the suspended object vibration is isolated by the attractive force of the electromagnet.

Attractive force of an electromagnet, $F = K\frac{I^2}{\partial^2}$ [7] (4)

In the above equation (4), K is attractive force co-efficient for electromagnet, I is coil current and ∂ is the gap between electromagnet & suspension system.

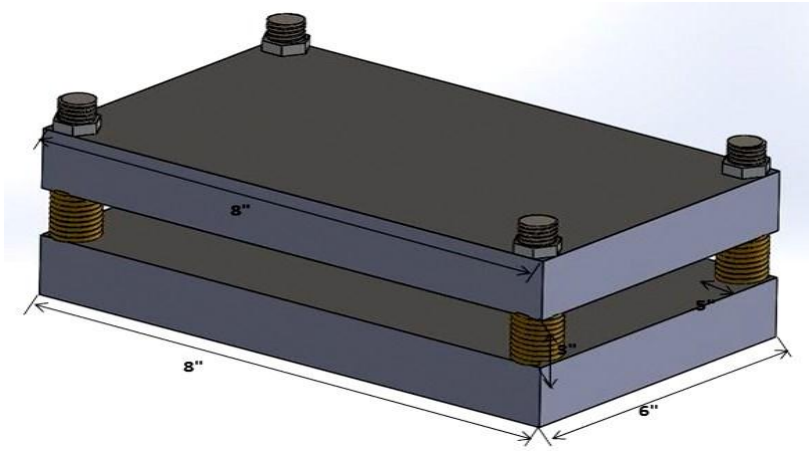

FIGURE 2. Zero Power Magnetic Suspension System

In the design shown above of zero power magnetic suspension system, at the center of the upper plate an electromagnet is set up which creates electromotive force in the opposite direction of applied load by using a permanent magnet in the lower plate so that the displacement of the spring is reduced and so stiffness become zero.

Existing Model for Negative Stiffness System

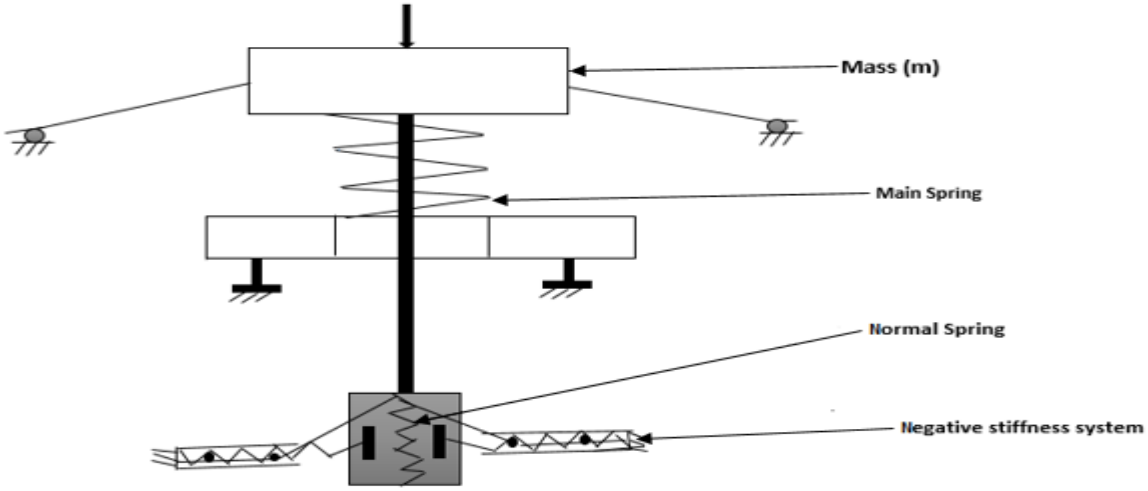

FIGURE 3. Experimental Model for Negative Stiffness System [6]

The Figure 3 shows the experiment model and this model consists of two parts one is Negative Stiffness System (NSS) and main system with mass and main spring. The mass (m) is supported the rod 4. Basically this main system is supported by base 3 [7]. Again two bars 2 hinged at the center supported at their outer ends on pivots which are free to move horizontally with mass (m). The Negative Stiffness System consists of negative stiffness spring 6 in

both side and knuckle to control the spring length and normal spring. The supported bar 7 is finally connected with rectangular box 5 with whole parts.

Real Model of Vibration Control System

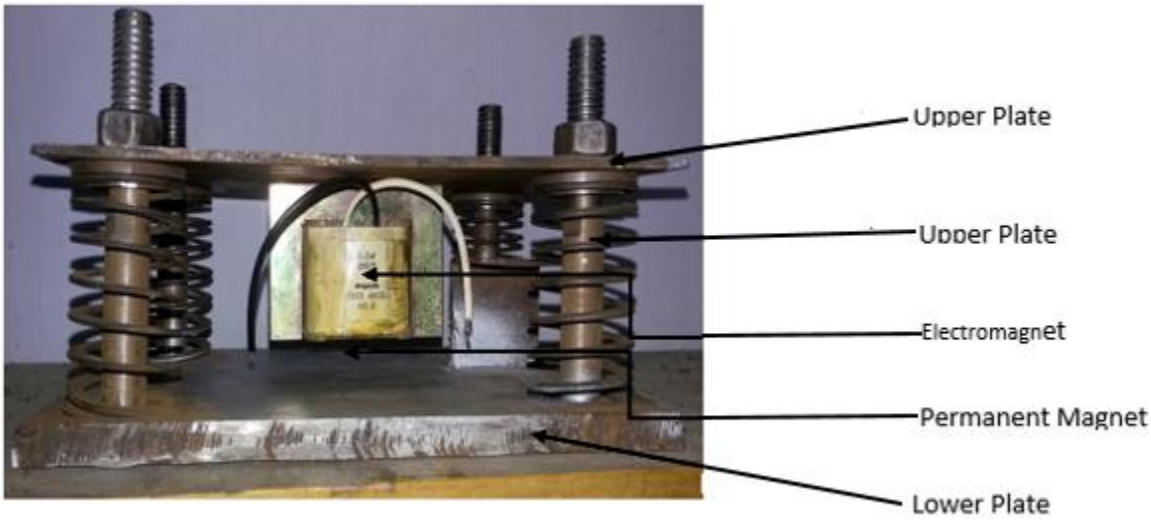

FIGURE 4. Arrangement for active Vibration Control System

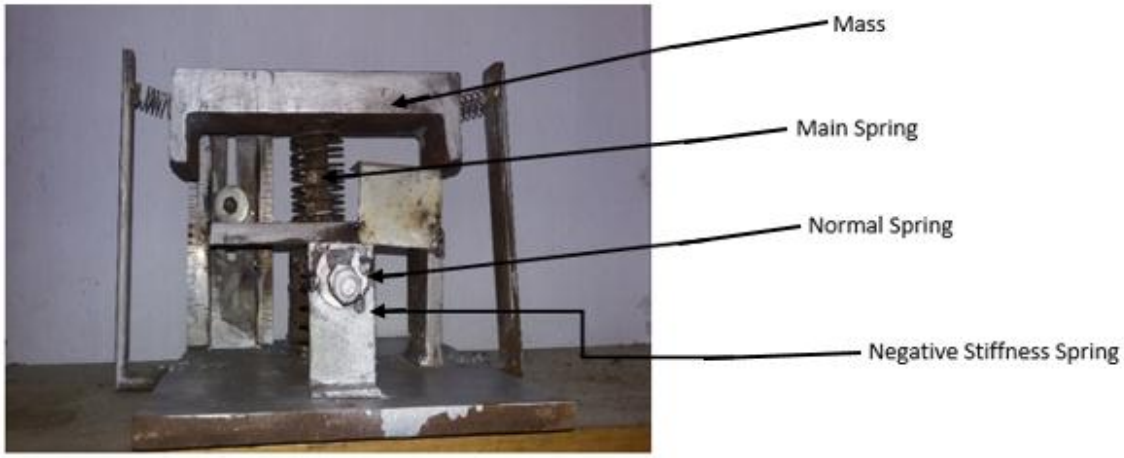

FIGURE 5. Real Model of Negative Stiffness System

Table & Stiffness Measurement Curve for Negative Stiffness System

TABLE 1. Table & curve for Main spring

Load (N)	Deflection (mm)
13	7.1
15	8.18
17	9.18
19	10.07
24	12.85

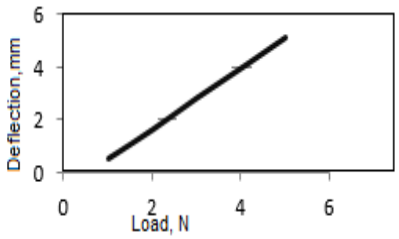

TABLE 2. Table & curve for Normal Spring

Load (N)	Deflection (mm)
2	.88
3	2.01
4	3.33
5	4.47
6	5.73

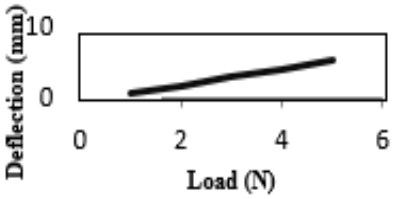

TABLE 3. Table & curve for Negative Stiffness Spring

Load (N)	Deflection(mm)
1	.56
2	1.66
3	2.86
4	3.99
5	5.15

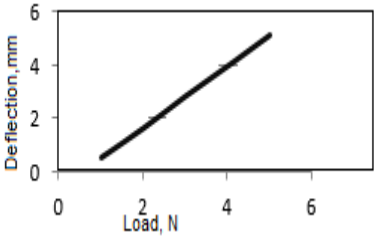

RESULTS

In the experimental setup of active vibration control system, maximum 3 A current can apply to the electromagnet and the maximum obtained electromotive force is 15 N. So in this way completely reduce the applied load of the same amount of electromotive force that is 15 N. The current and force calculation table is shown below:

TABLE 4. Table for Active vibration Control System

No of observation	Current (A)	Force (N)
1	1	5
2	2	10
3	3	15

In the experimental setup, eddy current displacement sensor was used to measure the displacement of the mass when the load was applied in the negative stiffness mechanism structure. Before using the eddy current displacement

sensor, calibration of the sensor was performed which shown that maximum 5 mm displacement can be measured appropriately by this sensor. This output was obtained by using digital oscilloscope. The calibration of the sensor of displacement and corresponding voltage is shown below.

TABLE 5. Table for Calibration of Eddy Current Displacement Sensor (Negative Stiffness System)

No of Observation	Displacement (mm)	Input Voltage (V)	Output Voltage (V)
1	1	25	7.0
2	2	25	7.8
3	3	25	8.6
4	4	25	9.5
5	5	25	10.0
6	6	25	10.0

After performing the passive vibration control system using negative stiffness mechanism, the displacement was reduced. The data of the reduced displacement with NSS and without NSS is shown below:

TABLE 6. Table for Passive Vibration Control System

No of Observation	Load (N)	Without NSS (mm)	With NSS (mm)
1	17	9.18	4.0
2	19	10.07	5.6
3	24	12.85	7.1

DISCUSSION

Vibration has an adverse effect. So the effect of vibration must be reduced. For this reason active and passive vibration control system is shown in our experimental design. When the initial length of spring and the length of bar is equal then the maximum stiffness is zero for Negative stiffness system otherwise maximum stiffness is not zero. The experimental model for Negative Stiffness System was applied external load and the displacement was measured by eddy current displacement sensor [8]. Electromagnet [3] and a permanent magnet were used for active vibration control. Depending upon the gap between electromagnet and the suspended object vibration is isolated by the attractive force of the electromagnet since when the main isolation system's has negative stiffness, the stiffness of the added negative stiffness system is correctively high. This problem only suffers by passive vibration control system than active one. But effective passive vibration control is important one due to its low cost and simplicity. In our active vibration control system maximum amount of attractive force of electromagnet is 15 N and in passive Negative Stiffness System maximum applied load 24 N and displacement reduces from 12.85 mm to 7.1 mm.

CONCLUSION

To reduce vibration active and passive vibration isolation is important due to its low cost and simplicity. In there a new model of active and passive vibration isolation system was proposed and its control performances were

investigated. In passive vibration the approach was based on stiffness minimization by adding a mechanism containing the spring with adjustable 'Negative stiffness' & in case of active vibration stiffness minimization by adding a mechanism containing electromagnet, permanent magnet & spring. Both the linear and non-linear system has analyzed and concluded that its work in real system. Due to this simple construction element, enhance, its price will be very low and has increased its workability in working area.

REFERENCES

1. Singiresu S. Rao, Mechanical Vibration 5th edition
2. Kanak Kalita and Abir Dutt, Free vibration analysis of isotropic and composite rectangular plate International Journal of Mechanical Engineering and Research. ISSN No. 2249-0019, Volume 3, 12~100.
3. Joseph Edward & Charles R. Mischke , Machine Design , McGraw-Hill International 5th Edition,Newyork 1989.
4. Thompson, J. M. T. and Hunt, G. W., 1980, A General Theory of Elastic Stability, A Wiley Interscience Publication, pp. 5~125.
5. Chapra, S. C. and Canale, R. P., 1985, Numerical Method for Engineers, McGraw Hill, pp. 250~310. Mizuno, T., Takasaki M., Suzuki, H. and Ishino, Y., 2003, Development of a
6. Three-axis Active vibration isolation system using zero-power magnetic suspension, Proceedings of the 42nd IEEE, Conference on decision and control, Maui, Hawaii, USA, pp. 4493~4498.
7. A.Frank D'Souza and Vijay K.Garg, 1984, Advanced Dynamics, Prentice-Hall, New Jersey, chapter-6&9.
8. Md. Emdadul Hoque and Takeshi Mizuno, Magnetic levitation technique for active vibration control Park, S. T. and Luu, T. T., 2005, a new method for reducing natural frequency of single Degree of freedom system, Journal of Sound and vibration. Vol-300 pp 422-428, 2007.

ICME2015

International Conference on Mechanical Engineering 2015
(ICME 2015) 18 – 20 December, 2015, Dhaka, Bangladesh

Paper ID : 367

Effect of Temperature and Geometric Parameters on Elastic Properties of Tungsten nanowire: A Molecular Dynamics Study

Sourav Saha[1,a)] SatyajitMojumder[1], Monon Mahboob[1] and M Zahabul Islam[2]

[1]*Department of Mechanical Engineering, Bangladesh University of Engineering and Technology, Dhaka-1000, Bangladesh.*
[2]*Department of Mechanical and Nuclear Engineering, The Pennsylvania State University, University Park, Pennsylvania 16802, USA*

[a)]Corresponding author: souravsahame17@gmail.com

Abstract. Tungsten is a promising material and has potential use as battery anode. Tungsten nanowires are gaining attention from researchers all over the world for this wide field of application. In this paper, we investigated effect of temperature and geometric parameters (diameter and aspect ratio) on elastic properties of Tungsten nanowire. Aspect ratios (length to diameter ratio) considered are 8:1, 10:1, and 12:1 while diameter of the nanowire is varied from 1-4 nm. For 2 nm diameter sample (aspect ratio 10:1), temperature is varied (10K ~ 1500K) to observe elastic behavior of Tungsten nanowire under uniaxial tensile loading. EAM potential is used for molecular dynamic simulation. We applied constant strain rate of 10^9 s^{-1} to deform the nanowire. Elastic behavior is expressed through stress vs. strain plot. We also investigated the fracture mechanism of tungsten nanowire and radial distribution function. Investigation suggests peculiar behavior of Tungsten nanowire in nano-scale with double peaks in stress vs. strain diagram. Necking before final fracture suggests that actual elastic behavior of the material is successfully captured through atomistic modeling.

INTRODUCTION

Mechanical properties of metallic nanowires are of immense importance from both academic and practical point of views. For developing MEMS and NEMS systems these properties can be utilized to produce effective devices. However, experimental investigations for every possible type of metallic nanowires are impractical from economic point of view. Molecular dynamics has been serving this purpose for many years [1 – 4]. Chen et al. studied deformation behavior of Au nanowires under uniaxial tension at high strain rates at different temperatures along [001], [011] and [111] directions [5]. It was found that structural behavior at nanoscale was significantly different from bulk Au. Ductility of nanowires seemed to increase at high strain rate while strength of nanowires reduced with higher temperature. Branicio and Jose-Pedro [6] studied deformations on nickel nanowires subjected to uniaxial strain at 300 K using EAM method. Applying strain rates, from 0.05 to 15% ps^{-1}, they found elastic behavior up to 11.5% strain with corresponding stress of 9.4 GPa. Koh and Lee [7] investigated Pt and Au nanowires in conjunction to one another. Higher strain rate caused crystalline to amorphous transition in those nanowires. Setoodeh et al. made a molecular dynamics study on Ni nanowires under uniaxial loads at different temperatures. From their investigation it was revealed that yield stress during compression is much lower than yield stress during tension. Moreover, strength decreased linearly with temperature [8]. Debnath et al. studied elastic-plastic properties of Au nanowire in the dimeter range of 1-200 nm [9]. They found Au nanowires in the range of diameters 1–6 nm

showed higher sensitivities for their modulus and strength. Sainath et al. [10] recently investigated size dependent tensile deformation and fracture behavior of bcc iron nanowires. The investigation showed Young's modulus, yield and flow stresses decreased rapidly with increase in nanowire size up to 11.42 nm followed by gradual decrease approaching towards saturation at larger size.

Single-crystal tungsten nanowire possesses outstanding field-emission, optical, electrical, and mechanical properties and wide application prospect as toughening-filling, photoelectric, and structural materials. It can be prepared by methods of high-temperature gas-phase deposition [11], electrochemical etching [12], and RF sputtering [13], where the growth process of tungsten nanowire cannot be controlled properly. A relatively new method of metal-catalyzed vapor-phase reaction has been firstly used to prepare the single-crystal tungsten nanowire [14] of high purity and complete body-centered cubic structure (BCC) [15]. Mechanical properties of tungsten nanowire were analyzed recently by Bin et al [16]. They found four different stages of failure of Tungsten nanowires. They also mentioned the crystal orientation had little effect on the elastic modulus but great effect on the tensile strength, which is mainly affected by surface energy. The 〈111〉 crystal orientation has the smallest surface energy and thus the largest tensile strength. However, current investigation differs from this one in its purpose. In this investigation we do not seek to find failure mechanism since it is already apparent. Rather we focus on fracture behavior at nanoscale at different temperatures and aspect ratios.

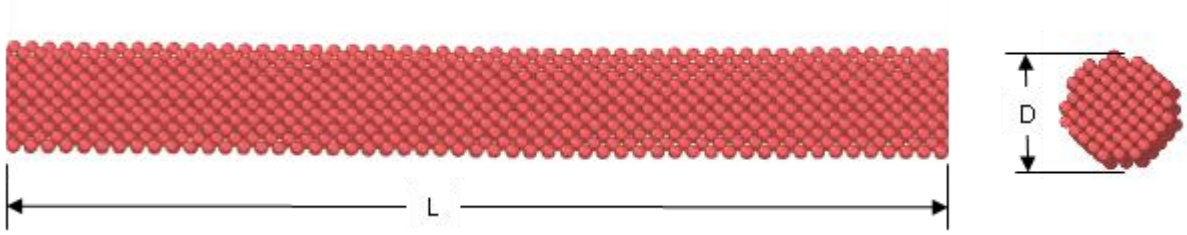

FIGURE 1. Schematic diagram of Tungsten nanowire. The cross section of the nanowire is in the right.

METHODOLOGY

We applied EAM (Embedded atomic method) potential for performing molecular dynamics simulation. EAM potential [17] describes the interatomic interaction between the tungsten atoms properly. Previously, different metallic nanowires were investigated using EAM potential and it predicted quite accurate results compared to first principle calculations and experiments. For our verification we calculated the Young's modulus (YM) of Tungsten using EAM potential and found the value of YM is 417 GPa. Our result holds good agreement with the experimental result of 411 GPa.

All the simulations are carried out using LAMMPS [18] software package. Tungsten has a body centered cubic (BCC) lattice structure having lattice constant of 3.17 A^o. Cylinder shape of the nanowire is considered and the crystal orientations are <1 0 0> for x direction, <0 1 0> for y direction and <0 0 1> for z direction. Tensile loads is applied along x direction in crystal plane of <1 0 0>. Time step considered for present simulation is 1 fs which is quite good for nanowire simulation. Initially energy minimization is carried out to optimize the geometry. Later equilibration is carried out in constant energy for 10 ps. Pressure equilibration is carried out under desired temperature for 50 ps at an damping factor of 0.3. This releases the residual stresses of the nanowire and relaxes it. Later, tensile load is applied at a constant strain rate of 10^9 (s^{-1}). Atomic stress were calculated based on the definition of virial stress, which is expressed as,

$$\sigma_{ij}^{\alpha} = \frac{1}{\Omega^{\alpha}}\left(\frac{1}{2}m^{\alpha}v_i^{\alpha}v_j^{\alpha} + \sum_{\beta=1,n} r_{\alpha\beta}^{j} f_{\alpha\beta}^{i}\right) \quad (1)$$

whereα,β are the atomic indices and i, j denote indices for the Cartesian co-ordinate system.r and f are the atomic distances between the atoms of different indices and interatomic force. $m$and v is the mass and velocity of the atom and Ω is the atomic volume. Simulations are carried out until the fracture of the nanowire. Different diameters (1-4 nm) of the nanowire are investigated using the above mentioned procedure. Also, the temperature is varied within a wide range (10-1500 K). YM is calculated using the elastic region of the stress strain curve.

RESULTS AND DISCUSSION

Effect of Varying Temperature

Tensile stress vs strain curves for <1 0 0> oriented 2 nm diameter tungsten nanowires at different temperatures are shown in Fig. 2(a). Computed stress shows a characteristics linear elastic region with strain upto a certain portion. Later an abrupt fall in stress value occurs. Further tensile load causes oscillation of stress values with strain. This region is plastic deformation region for the nanowire. Finally, a secondary peak in stress value occurs and the nanowire fails. This kind of phenomenon in nanowire is quite obvious and previously reported for BCC Fe nanowire. The effect of temperature is very much prominent. At higher temperature the yield strength for the nanowire decreases. At 10 K the yield strength is about 24 GPa which reduces to 10 GPa at 1500 K. Also at higher temperature both the first and second peaks occur at relatively lower strain. For 10 K the first peak occurs at 7% strain value which reduces to 5% at 1500 K. Also the second peak for 10 K occurs at 58% strain which reduces to 45% at 1500 K. This occurs because at lower temperature there is higher initial residual stress inside the nanowire but at higher temperature due to thermal fluctuation the nanowire is more thermally relaxed. The yield strength for the nanowire shows an inverse relationship with temperature. From Fig. 2(b), the variation of Young's modulus with temperature can be found. Young's modulus value reduces with the temperature. A general trend of the young modulus value shows a sharp change in Young's modulus upto 1000 K. After 1000 K the Young's modulus value reduces in a slower rate. This phenomenon is quite obvious because of perfect crystal structure at low temperature. Young's modulus values reduce from 470 GPa to 280 GPa as temperature increases from 10K to 1500K.

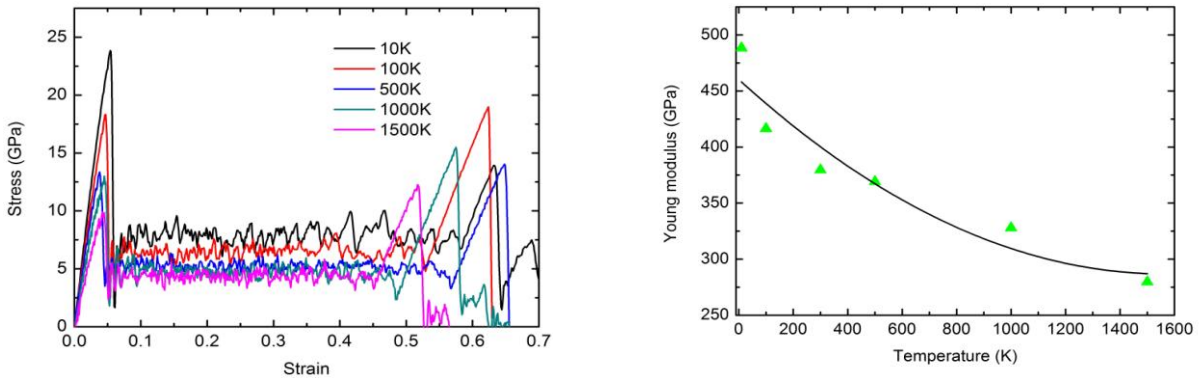

(a) (b)

FIGURE 2. Effect of temperature on (a) stress strain plot (b) Young's modulus for tungsten nanowire of 2nm diameter at strain rate 10^9 (s^{-1}).

Effect of Varying Diameter

Figure 3(a) shows stress strain plot for different diameters of the nanowire at 300 K at a strain rate of $10^9(s^{-1})$. As mentioned earlier for varying temperature there is double-peak in stress strain curve for different diameters of the nanowire. However, when the diameter is very low (1nm) it fails at a lower strain value of 27.5% and there are several peaks observable. However, with the increment of diameter it shows two peaks in stress strain plot. But when the diameter is increased further (to 4nm) there is no sign of second peak. This result is consistent with previously published literature. After a certain diameter metallic nanowire do not show a second peak. The yield strength of the nanowire reduces from 27 GPa (for nanowire diameter 1nm) to 12 GPa with the increment of nanowire diameter (4nm). Yielding occurs at lower strain value for higher diameter nanowire. Yield strength shows an inverse relationship with diameter of the nanowire which can be expressed as

$$\sigma_y = \sigma_{\infty+} \frac{K}{D}, \tag{2}$$

where $\sigma_{y,}$ is the yield strength, σ_∞ is the initial stress value, K is any constant and D is the diameter of the nanowire. At lower diameter the nanowire holds perfect crystallographic structure which enhances its elastic property but at higher diameter the shape effect is more prominent and reduces the strength of the nanowire due to crystal dislocations and slip. Young's modulus value also decreases with the increment of diameter (see Fig. 3(b)). At higher diameter of the nanowire the change in Young's modulus is less steep. Young's modulus decreases as the nanowire shows plastic deformation at lower strength at strain at higher diameter.

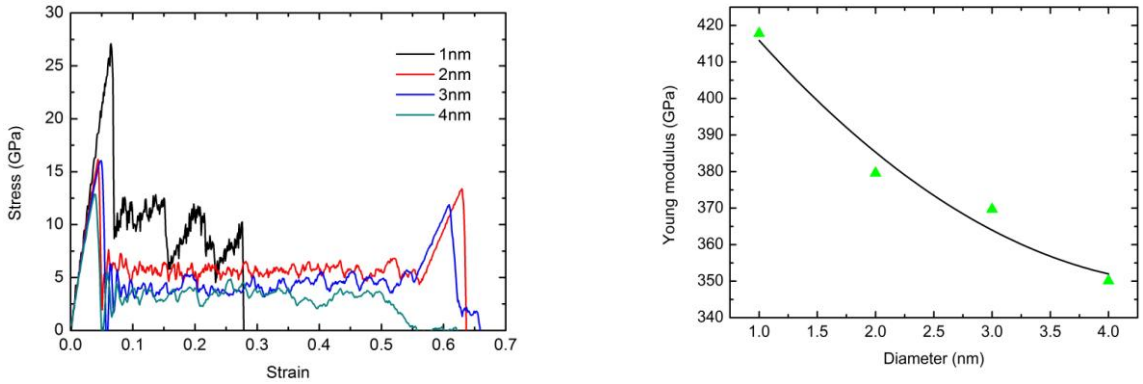

(a) (b)

FIGURE 3. Effect of diameter on (a) stress strain plot (b) Young's modulus of Tungsten nanowire at 300 K at strain rate of 10^9 (s^{-1}). The length to diameter ratio (l/d) is chosen as 10. Tensile load is applied in <1 0 0> direction of the nanowire.

Effect of Length to Diameter Ratio

Effect of length to diameter ratio on stress strain plot is shown in Fig 4. For the present calculation the diameter of the nanowire is kept fixed at 2 nm. Only the length is varied to obtain different *L/D* ratio. As the nanowire length increased it shows higher yield strength. And the yield strength value decreases as the nanowire length is shortened. Also the longer nanowires show higher elastic region in stress-strain plot. For all the cases double peak in stress strain diagram is visible. Another interesting observation is shorter nanowire fails at higher strain of 65% whereas longer nanowire (*L/D*= 12) fails at a strain of 58% only. Therefore increment of length can enhance elastic property but causes an earlier fail in the material.

Fracture Mechanism and Behaviour

Fracture mechanism in Tungsten nanowire is shown in Fig 5. As one can see after the linear elastic zone a slip in the nanowire is visible. Later this slip propagates along opposite of the loading direction which collapse the BCC structure of the tungsten nanowire. Through the whole stress oscillation regime this slip propagates and amorphisation of the nanowire occurs. This can be visible from strain rate 6.4% to 56.2%. After this region second peak region is found where the amorphous nanowire failed like a brittle material. At strain rate of 63.7% the material fails completely. These results are interpreted using the radial distribution function plot in Fig. 6. At oscillating regime the crystal structure collapses and it helps the nanowire to become more brittle.

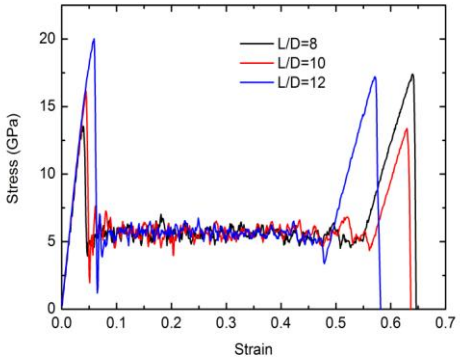

FIGURE 4. Effect of *L/D* ratio on stress vs strain plot for 2nm diameter tungsten nanowire at temperature 300 K and strain rate 10^9 (s^{-1}).

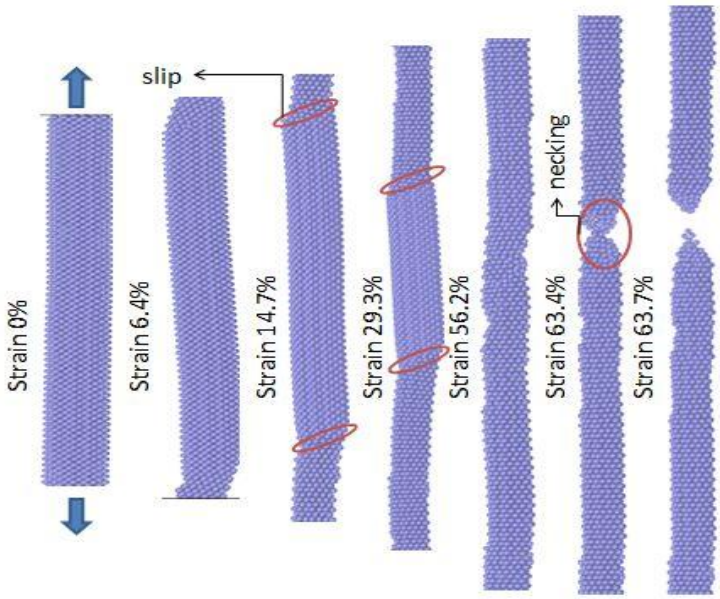

FIGURE5. Fracture mechanism in Tungsten nanowire for a diameter of 2nm at temperature of 300 K and strain rate 10^9 (s^{-1}).

CONCLUSIONS

Tungsten is a promising material as a nanowire. On the basis of results following conclusions can be made

- Yield strength and Young's modulus decrease with the temperature for Tungsten nanowire. Young's modulus values decreases slowly after 100 K.
- At larger diameter the nanowire shows a lower yield strength and Young's modulus. At higher diameter the nanowire stress strain plot shows only a single peak.
- Increment of *L/D* contributes to higher elastic property however causes an earlier failure in a lower strain value.
- At the oscillation regime of stress, the plastic deformation in nanowire occurs which is initiated by a slip and then it propagates in opposite direction of applied load.
- Elastic region of the nanowire reduces for increment of both diameter and temperature.

REFERENCES

1. B. Wu, A. Heidelberg, and J. J. Boland, Nat. Mat. **4**, 525-529(2005).
2. Z.L. Wang, Z.R. Dai, R.P. Gao, Z.G. Bai, J.L. Gole, Appl. Phys. Letters. **77**, 3349-3351(2000).
3. D.L. Chen, T.C. Chen, Nanotech. **16**,2972 (2005).
4. P.H. Sung, C.D. Wu, T.H. Fang, J. Phys D: App. Phy. **45**, 215303 (2012).
5. D.L. Cheng, T.C. Chen, Nanotech. **16**,2972 (2005).
6. P.S. Branicio, J. Rino, Phys. Rev. **62**, 16950 (2000).
7. S.J.A. Koh, H.P. Lee, Nanotechnology **17**, 3451-3467 (2006).
8. A.R. Setoodeh, H. Attariani, M. Khosrownejad, Comp. Mat. Sci**44**, 378-384 (2008).
9. S.K.D. Nath, S.G. Kim, J. App. Phys. **112**, 123522 (2012).
10. G. Sainath, B.K. Choudhary, T. Jayakumar, Comp. Mat. Sci., **104**, 76-83 (2015).
11. V. Sreeram, C. Hari, K.S. Mahendra, J. Amchem. Soc. **125**, 10792−10793 (2003).
12. L.G. Olivier, W.A. Joachim, C.J. Moon, C.G. Peter, T.Y. John, Nano Lett. **2**, 191-193 (2002).
13. K. Tansel, P.I. Wang, G.C. Wang, T.M. Lu, Thin Solid Films **493**, 293-296 (2005).
14. S.L. Wang, Y.H. He, J. Zou, Y. Jiang, J. Xu, B.Y. Huang, C.T. Liu,, P.K. Liaw, J. Cryst. Grow. **306**, 433-436 (2007).
15. S.L. Wang, Y.H. He, X.S. Fang, J. Zou, Y. Wang,, H. Huang, P.M.F.J. Costa, M. Song, B.Y. Huang, C.T. Liu, P.K. Liaw, Y. Bando, G. Golber, Adv. Mat.**21**, 2387-2392 (2009).
16. M.A. Bin, Q. Rao, Y. He, Nonferr. Met. Soc. China **24**, 2904-2910 (2014).
17. M.S. Daw, M.I. Baskes, Phys. Rev. B **29,** 6443 (1984).
18. S. Plimpton, J. Comp. Phys. **117**, 1-19 (1995).

ICME2015

International Conference on Mechanical Engineering 2015
(ICME 2015) 18 – 20 December, 2015, Dhaka, Bangladesh

Paper ID : 373

Effect of Processing Parameters on Fly-ash Brick Properties

Md. Rubaiet Shattique, Md. Golam Kibria, Md. Tamim Zaki, Sheikh Jaber Nurani[a)], Md. Abdul Halim, and Dr. A S W Kurny

Department of Materials and Metallurgical Engineering, Bangladesh University of Engineering and Technology, Dhaka 1000, Bangladesh

[a)] Corresponding author: sheikh.jaber.nurani@gmail.com

Abstract. Fly-ash bricks give a comprehensive solution towards recycling of fly-ash and since there is no requirement of firing to produce them, they are also eco-friendly bricks; little or no carbon-dioxide is emitted during their entire production cycle. As bricks are the most essential and widely utilized building materials in the construction industry, the significance of developing an alternative eco-friendly brick is substantial in modern times. In this paper we investigated the effect of different processing parameters on the properties of fly-ash bricks. Later the results were calculated and analyzed. At least five samples were prepared to study each result.

INTRODUCTION

Bangladesh is the 8th largest populous country with 160 million people. Each year 3, 00,000 to 4, 00,000 rural people migrate to Dhaka. The existing people as well as new migrants need housing facility. At present in Bangladesh the annually required shelter varies from 3 lakh to 5.5 lakh units. Bangladesh will need to construct approximately four million new houses annually to accommodate the growing population [2]. Rapid urbanization in the country has created a booming construction industry and spurred the production of 8.6 billion bricks each year, with demand for the bricks rising at an annual rate of about 5.28 percent [1].

Though not formally recognized as an industry, brick-making is a significant economic activity in Bangladesh (Ministry of Industries 2010).The country's overwhelming dependence on bricks is due to its lack of stones in any sizable quantity or other alternative building materials at comparable cost. Table 1 summarizes the main characteristics of the brick sector in Bangladesh [3]. From the above table it can be evidently stated that manufacturing of conventional bricks consumes massive amounts of clay, coal and firewood which has a tremendous negative effect on the environment. Again substantial amount of CO_2 emission contributes greatly in air pollution. In such times where we need to save the environment from imminent catastrophe there is a greater need for brick manufacturing processes which does not harm our environment.

The aim of this work is to evaluate the technical quality of fly ash based bricks as prospective construction material. The sample bricks were made using the two types of raw materials; sand and ceramic dust and were cured at different parameters. The physical and mechanical properties and the durability of the bricks were then compared to each other and to conventional bricks, so as to assess whether the quality of the bricks had been enhanced or at least maintained. The use of such technology could produce cost savings in raw materials for brick manufacturers and serve as an efficient means of recycling a waste product. This new technology has important economic and social impacts on the use of industrial waste residue and environmental protection.

METHODOLOGY

Fly ash, rice-husk ash, sand/ceramic dust and hydrated lime mixtures with gypsum as a binder were used to make bricks. Process variables like the composition of the mix, pressure, curing conditions, etc. were optimized. Finally the

properties of the bricks produced under the optimum conditions were determined. Snapshot of Bangladesh's Brick Sector is given in table 1.

TABLE 1. Snapshot of Bangladesh's Brick Sector [4-7]

Parameter	Value
Estimated total number of coal-fired kilns	5,000
Number of natural gas fired kilns	20
Annual brick production	17.2 billion
Value of output	TK83 billion (~US$1.2 billion)*
Coal consumption	3.5 million tons
Value of imported coal	TK22.6 billion (~US$322 million)
Firewood consumption	1.9 million tons
Clay consumption	45 million tons
Total employment (incl. supply of clay and coal, transport of bricks)	~1 million people
Growth rate of the construction industry (1995-2005)	5.6%

Fly ash used in this study was collected from Barapukuria Thermal Power Plant. Rice-husk ash was collected from local brick fields. The other ingredients hydrated lime; sand and gypsum were collected from the local market; ceramic dusts produced as by product of ceramic industries were collected as well. The major ingredients in fly-ash are presented in Table 2.

TABLE 2. Chemical composition of Barapukuria Power plant fly-ash

Compound	SiO_2	Al_2O_3	Fe_2O_3	CaO	MgO
Mass Fraction,%	48.20	42.24	3.37	3.31	0.20

Brick specimens were produced under the conditions given in Table 3 for ceramic dust. At least five bricks were made for each specimen type. Before making a brick, each ingredient of the raw materials was dried in a muffle furnace at 110℃ for 24 hours.

(a) (b)

FIGURE 1. (a) Hydraulic press, (b) Fly ash-sand-lime-gypsum bricks

Required amount of each ingredient was weighed, 9%, 12%, 14% and 18% moisture was added and the components were mixed thoroughly. To ensure uniform size of the bricks a known weight of mixture was used each time to fill the mold cavity. Dimension of the mold cavity opening was 6 X 3.5 cm. A hydraulic press was used to apply pressure for a period of 15 Sec [Fig. 1(a)].

The bricks [Fig. 1(b)] were then ejected and finally cured. Curing was done in air, using water spray, by putting the bricks under wet cloth and by keeping the bricks immersed in water. Bricks formed under various pressures were also cured for different periods in optimum curing condition.

TABLE 3. Test parameters of fly ash-ceramic dust brick

Brick Code	Ceramic Dust Weight, %	Fly-Ash Weight, %	Lime Weight, %	Gypsum Weight, %	Forming Pressure (psi)	Curing Process	Compression Time (sec)	Water Content, %	Mesh Size
C1	10	80	10	2	1000	In air	15	14	60
C2	20	70	10	2	1000	In air	15	14	60
C3	30	60	10	2	1000	In air	15	14	60
C4	40	50	10	4	1000	In air	15	14	60
C5	40	52	8	4	1000	In air	15	14	60
C6	40	54	6	4	1000	In air	15	14	60
C7	40	56	4	4	1000	In air	15	14	60
C8	40	58	2	4	1000	In air	15	14	60
C9	40	50	10	6	1000	In air	15	14	60
C10	40	50	10	8	1000	In air	15	14	60
B1	40	50	10	10	2000	In air	15	14	60
B2	40	50	10	10	2000	In air	15	14	60
B3	40	50	10	10	2000	In air	15	14	60
B4	40	50	10	10	2000	In air	30	14	60
B5	40	50	10	10	2000	In air	60	14	60
M6	40	50	10	10	2000	In air	60	14	60
M7	40	50	10	10	2000	In air	60	14	60
M8	40	50	10	10	3000	In air	15	14	140
M9	40	50	10	10	3000	In air	15	14	140
M10	40	50	10	10	3000	In air	15	14	270
M11	40	50	10	10	3000	In air	15	14	270
M12	40	50	10	10	3000	In air	15	9	60
M13	40	50	10	10	3000	In air	15	9	60
F14	40	50	10	10	3000	In air	15	12	60
F15	40	50	10	10	3000	In air	15	18	60
F16	40	50	10	10	3000	Steam	15	14	60
F17	40	50	10	10	3000	Steam	15	14	60
F18	40	50	10	10	3000	Water	15	14	60
F19	40	50	10	10	3000	water	15	14	60
F20	40	50	10	10	1000	In air	15	14	60
F21	40	50	10	10	3000	In air	15	14	60

The Compressive strength was determined by applying load on the specimen using a Universal Testing Machine. Load was applied on an area measuring 6 mm X 3.5 mm [The size of one face of the entire brick].
ASTM Designation C 67 – 00 was followed to measure the absorption capacity, A as follows.

$$\mathrm{A}, \% = \frac{(\mathrm{W}-\mathrm{D})}{\mathrm{D}} \quad (1)$$

In equation (1) W is the saturated weight in grams and D is the dry weight of the brick.

After measuring dry weight D (gm) as mentioned earlier, the bed surface of the brick (the face measuring 6mm × 3.5mm) was caused to absorb water for 1 min. Water was wiped out completely from the surface of the brick within 10 s of removal from contact with the water and weight D' (gm) was determined within 2 minutes. Initial rate of absorption IRA, %= D'-D was then calculated [ASTM Designation C 67-00].

ASTM Designation C 67 – 00 was followed to determine apparent porosity P, % = [(W - D)/ V], Open pore volume, cm^3 = W – D and impervious pore volume, cm^3 = D – S.

This test was carried out according to ASTM C67-08. For this test, one brick was vertically placed in water with one end immersed and another brick stored in ambient condition. After 7 days both bricks were dried in oven at 110℃ for 24 hours. Then both bricks were observed from 10 ft. distance under not less than 50 fc with normal vision. If any difference is observed because of presence of any salt deposit then the rating is reported as ‘effloresced’. If no difference is noted, the rating is reported as ‘not effloresced’.

Radio activity of the mixture of optimum composition was examined from Health Physics Division of Bangladesh Atomic Energy Commission.

Effects of four different curing processes i.e. in still air, with water spray twice a day, keeping the specimen under wet cloth and keeping the specimen immersed under water for seven days were examined. Finally the effect of long duration curing was studied. For optimum composition and different compaction pressure one set of bricks were cured in air for five weeks. Another set was cured in air for one week and then for four weeks under water.

After 7 days of curing period bricks were dried at 110°C for 24 hours and then allowed to cool to room temperature. Dry weight D (grams) was then measured. Following that the bricks were immersed for 24 hours in water at room temperature and suspended weight S (grams) was measured. The bricks were then removed, the surface water was wiped off with a damp cloth and the saturated weight W (grams) was measured within 5 min after removing the bricks from the water bath. Unit volume weight B, grams/cm^3 = D/ V,

$$\text{Unit volume weight, B } \left(\frac{g}{cm^3}\right) = \frac{D}{V} \quad (2)$$

In equation (2) volume V, cm^3 = (W - S) was calculated.

RESULTS AND DISCUSSIONS

Effect of Particle Size on Unit Volume Weight & Compressive Strength

Particle size was varied from Mesh No. 60 to Mesh No. 270. Unit volume weight increased with the finer particle sizes i.e. highest unit volume weight at mesh No. 270 particles. Other properties remained uninfluenced by the particle size of brick constituents. Fig. 2(a).

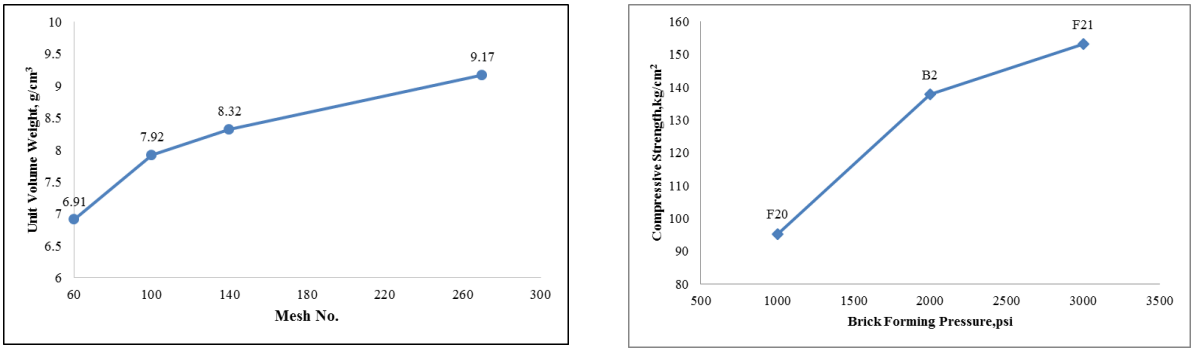

(a) (b)

FIGURE 2. (a) Effect of particle size on unit volume weight, (b) Effect of brick forming pressure on compressive strength

Compressive strength increases with the brick forming pressure. At 7 days curing in air, the highest compressive strength was found that was 147 kg/cm^2. High pressure results to higher compaction of the constituents and less pore inside the bricks. This results is shown in Fig 2(b).

Unit Volume Weight & Initial Rate of Absorption

Unit volume weight increases with increased brick forming pressure. Higher pressure results to more compaction and higher density. A maximum unit volume weight of 7.21 g/cm3 was at 3000 psi and a minimum of 2.21 g/cm^3 at 1000 psi fig. 3(a). Initial rate of absorption is primarily affected by the open pore of bricks. Initial Rate of Absorption (IRA) decreases with increasing brick forming pressure. Initial rate of absorption of bricks made under 1000 psi pressure exceeded 30 gm and so according to ASTM C 67 – 00 these bricks should be wetted before laying. From fig. 3(b) we see that, with increasing brick forming pressure IRA decreased below 30 gm. Lowest IRA of 14.84 g was found for a pressure of 3000 psi. So these bricks are not needed to be wetted before laying.

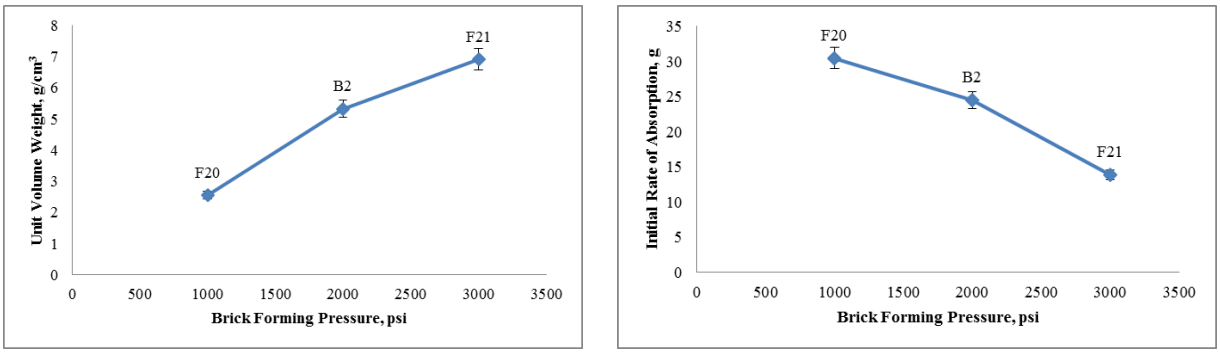

(a) (b)

FIGURE 3. (a) Effect of brick forming pressure on unit volume weight, (b) Effect of brick forming pressure on initial rate of absorption

Effect of Water Content on Unit Volume Weight & Absorption Capacity

Water absorption capacity of the bricks is insensitive to the water added during brick forming. For all 9%, 12% and 18% added water during brick forming the absorption capacity remained unaffected. Unit Volume weight increases with increasing water content during brick formation which is shown in fig. 4(a). At 9% water content the unit volume weight was found 6.6 g/cm^3 which increased to 8.9 g/cm^3. From fig. 4(b), it is observed that water content does not affect the absorption capacity much.

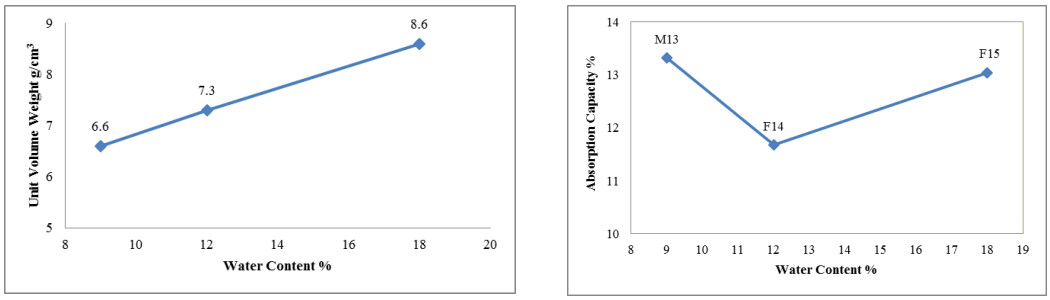

(a) (b)

FIGURE 4. (a) Effect of water content on unit volume weight, (b) Effect of water content on absorption capacity

Effect of Water Content on Compressive Strength

Compressive strength initially increased with increasing added water initially, but then decreased after a specific percentage of water. Highest value was found for 14.5% initial water content.

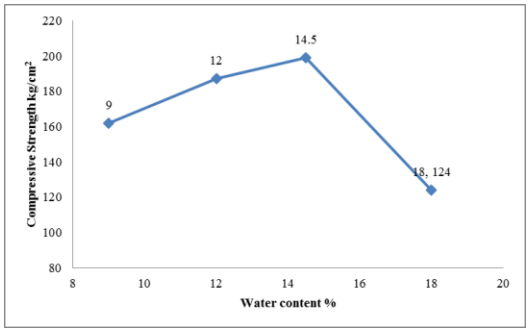

FIGURE 5. Effect of water content on compressive strength

This can be attributed to the required amount of optimum water content for the optimum pozzalonic reaction to occur. Anything more than the required amount does not affect the reaction behind the strength building of the bricks. Fig. 5.

Effect of Compression Time on Apparent Porosity & Open Pore Volume

Apparent porosity increases with the time of compression at constant pressure. Apparent porosity was found to be 19.75%, 23.8% and 26% respectively for 15s, 30s and 60s compression time. Fig. 6(a).

Open pore volume of the bricks decreases with the compression time. For 15s of compression the open pore volume was 4.4 cm^3. This volume decreased to 2.8 cm^3 at 60s compression time. However the change was not so drastic when the bricks were compressed for 30s (3 cm^3) and 60s (2.8 cm^3) Fig. 6(b).

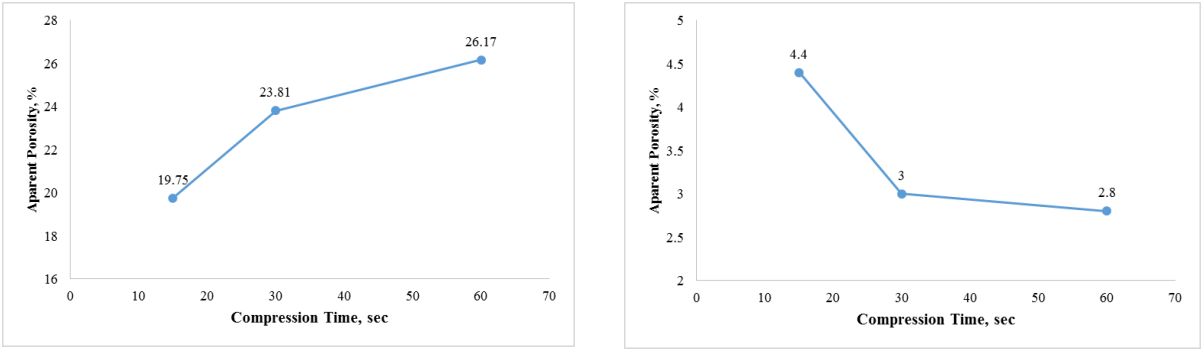

(a) (b)

FIGURE 6. (a) Effect of compression time on apparent porosity, (b) Effect of compression time on open pore volume

CONCLUSION

In this paper the effect of particle size, compression time, initial water content and brick forming pressure on different properties of bricks were thoroughly investigated. From this investigation we can conclude that fly-ash bricks with added water content of 14.5%, compressed at 3000 psi for 30 seconds will bear the optimum brick properties. These results are crucial for making superior quality bricks with very high productivity rate. Further investigation can be carried out to study the effect of different kind of curing techniques on brick properties.

REFERENCES

1. R. Arifur, Energy Sector Management Assistance Program (ESMAP) of the World Bank, 6, 14-29 (2006).
2. M. A. Rahim, Golden Research Thoughts, 1, 1-4 (2011).
3. Environment, Climate Change, and Water Resources Unit, Introducing Energy-efficient Clean Technologies in the Brick Sector of Bangladesh (Energy Sector Management Assistance Program (ESMAP), The World Bank, Washington, 2011), Report No. 60155-BD, pp. 1-81.
4. M. A. Imran, M. A. Baten, B. S. Nahar and N. Morshed, Int. J. Agril. Res. Innov. & Tech. **4**, 70-75 (2014).
5. W. Kahn, IEEE Transactions on Antennas and Propagation **5**, 1952-1955 (2003).
6. E. Gomes and I. Hossain, Energy for Sustainable Development **7**, 66-76 (2003).
7. L. Croitoru and M. Sarraf, Journal of Environmental Protection **3**, 476-484 (2012).

ICME2015

International Conference on Mechanical Engineering 2015
(ICME 2015) 18 – 20 December, 2015, Dhaka, Bangladesh

Paper ID : 401

In Vivo Measurement of Mechanical Properties of Human Long Bone by Using Sonic Sound

M. Jayed Hossain[1,a)], M. Moshiur Rahman[1,b)] and Morshed Alam[1]

[1]*Department of Mechanical Engineering, Bangladesh University of Enigneering and Technology, Dhaka 1000, Bangladesh*

[a)]Corresponding author: zed.hossain06@gmail.com
[b)]mailofmodhiur@gmail.com

Abstract. Vibration analysis has evaluated as non-invasive techniques for the in vivo assessment of bone mechanical properties. The relation between the resonant frequencies, long bone geometry and mechanical properties can be obtained by vibration analysis. In vivo measurements were performed on human ulna as a simple beam model with an experimental technique and associated apparatus. The resonant frequency of the ulna was obtained by Fast Fourier Transformation (FFT) analysis of the vibration response of piezoelectric accelerometer. Both elastic modulus and speed of the sound were inferred from the resonant frequency. Measurement error in the improved experimental setup was comparable with the previous work. The in vivo determination of bone elastic response has potential value in screening programs for metabolic bone disease, early detection of osteoporosis and evaluation of skeletal effects of various therapeutic modalities.

INTRODUCTION

Progress in clinical characterization of bone relies on developing a means to clinically assess all of the important determinants of bone quality, specifically, the intrinsic material properties of a bone (stiffness and brittleness) versus the macroscopic structural properties [apparent mass density (g/cc), structural shape and distribution of cortical mass, trabecular architecture, extent of unrepaired micro damage, and defects associated with the accelerated remodeling in early menopause]. The macroscopic properties measured with bone mineral method may give an inadequate indication of skeletal status in osteoporosis. There may be existence of regions of dead, week bone, which are normally or even excessively mineralized. Thus bones which appear normal with respect to mineral mass may still be usually susceptible to fracture. The breaking strength of bone is correlated with its geometry and Youngs modulus which can be clinically to evaluate bone quality. Because the speed of sound in a material is a function of its density and elastic properties and measurement of the speed of sound propagation in bone offers one approach to estimation of the approximate Youngs modulus of this material [1, 2, 3].

Either a wave transmission test or the measurement of the steady-state vibration characteristics can be the approach for estimating the Youngs modulus. ANAST el al. (1958) studied the transmission time of ultrasonic wave in the tibia and found reduction in speed in patients with fractures and osteoporosis subjects compared to normal adult [4]. Thompson et al. (1976) studied the mechanical properties of the human ulna by means of mechanical impedance tests and proposed the impedance testing for evaluation of bone-fracture healing rate and degree of healing [5]. Tower et al (1993) showed that the resonant frequency of the human tibia is proportional to its stiffness and it increases as fractured tibia heals [6]. In vivo measurement of steady-state vibration analysis of the human ulna was performed by Jurist (1970) and resonant frequency was showed as a direct index of the integrity of ulna. Jurist preformed the examination with motor driven audio oscillator for excitation and oscilloscope for recording the frequency response [1, 7].

The purpose of this paper is to device an improved experimental setup for analyzing in vivo the vibration characteristics of the ulna for approximating the resonance frequency to determine the Youngs modulus. Youngs modulus along with sound speed in the human ulna can be used for evaluating bone characteristics.

THEORETICAL BACKGROUND FOR RESONANT FREQUENCY

The vibratory properties of long bone, such as the ulna, may be modeled on the fundamental equation describing a vibrating bar using resonance frequency (F_o), length of the bone (L), velocity of wave propagation (C) as

$$F_oL = KC$$

K is a proportionality constant dependent on the mode of vibration and boundary. This relationship may be exploded to study the elastic properties (average value of Youngs modulus of over the cross section of the bone, Y and average density of bone, ρ) of long bones, because $C = \sqrt{Y/\rho}$. This formula for C describes longitudinal, low frequency sound propagation in bars which are long in comparison with their width. The usual equation for the velocity of longitudinal elastic wave propagation in extended solids using bulk modulus, B and shear modulus, G

$$C = \sqrt{\left(B + \frac{4G}{3}\right)/\rho}$$

.

This equation is inapplicable for bars with dimensions comparable to the wave length of the sound being propagated. The average density is affected by any muscle or other tissues which may be couple to the bone. However the acoustical impedance of bone is so much larger than that of soft tissue at low frequency that any coupling effects are small.

If transverse modes of vibration in a bar are considered, it can be shown that at resonance, $F_oL = kv$ where v is the phase velocity and k is a proportionality constant dependent on the mode of vibration and boundary. The $v = \sqrt{2\pi FCR}$ at a frequency F and R, the radius of gyration of the cross section of the bar about the neutral axis. And when the expression for v is substituted into the transverse resonance equation, one obtains, $F_oL = \left(2\pi k^2 R/L\right)C$.

If the bone of interest is assumed to be congruent in all people, the ratio R/L is fixed, and for a given mode of vibration, a new constant of proportionality can be defined: $K^* = \frac{2\pi k^2 R}{L}$. Thus for a transverse resonance: $F_oL = K^*C$. Since K and K^* are both arbitrary constants, the general equation $F_oL = KC$ may be used to describe the resonating long bone if it is understood that K is a function of the mode of vibration, boundary condition, and the shape of the bone [1].

The ratio Y/ρ is identical with the ratio of Youngs modulus, integrated over the cross section of the bone [8]. The linear density may be estimated by mono-energetic photon absoptiometric measurement of bone mineral. If the shape and boundary conditions of the bone under consideration are assumed to be constant, then the vibration mode is fixed, and F_oL is thus proportional to $\sqrt{Y/\rho}$. Therefore, one could in principle obtain the relative value of Youngs modulus integrated over the cross section of the bone by calculating the product of $(F_oL)^2$ and the mineral mass per unit length of bone obtained by photon absorptiometry. For the purposes of this study, the F_oL values of different subjects will be directly compared.

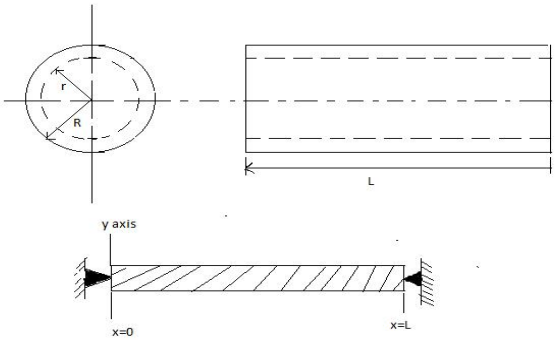

FIGURE 1. Model proposed by Jurist and Kianian, 1973 [7]

As a simple conceptual model Figure 1 proposed by Jurist and Kianian in 1973 in which the ulna may be considered to be cylindrical tubes of length L with an outside diameter of $0.05L$ inside diameter of $0.033L$ [7]. This

tube is attached to rigid supports at each end by hinges which simulate the joints. The values of K are then 0.5000 and 0.0235 for the fundamental longitudinal and transverse modes of vibration, respectively. It is recognized that ulna is not a uniform cylinder, and that the joints do not act as true hinges. Thus, the actual K values for the ulna may vary considerably from these estimates. In addition since the ulna is not symmetrical about the long axis,K values for transverse resonances may vary with the plane of vibration. These considerations are major factories in determining the reproducibility and clinical applicability of the technique. If C is assumed to be about 2900 ms^{-1} and the ulnar$L$ is assumed to be 30cm, the model predicts a fundamental transverse resonant frequency of about 230Hz. Considering the limitations of the model, the predicted transverse resonant frequency is in reasonable agreement with experimental values, typically150-300Hz, for healthy subjects. If the ulna is excited by a constant acceleration sinusoidal driving source of variable frequency, it will exhibit a maximum acceleration response or resonance at a frequency, F_a which is approximately equal to the resonant frequency F_o.

INSTRUMENTATION

The apparatus used to measure ulna resonant frequency is showing Figure 2. Figure 2 also illustrates the standard arm position used in the study in an attempt to hold boundary condition constant. At the Jurist model used oscillator amplifier combination energize the loud speaker driver where variable frequency had been controlled from oscilloscope. But in this model a frequency generator was used to produce variable frequency instead of oscillator. The frequency generator has been made through simple circuit diagram using IC 8038 to produce variable frequency. Then this frequency sent to loud speaker through power amplifier. Then signal was passed to Ulnar one end to the other end where piezoelectric material was used as a accelerometer to receive this vibration and send it to the computer for FFT analysis.

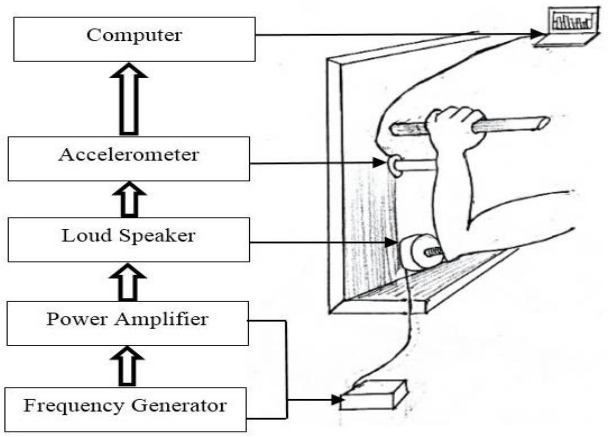

FIGURE 2. Apparatus used for bone resonance measurement

EXPERIMENTAL DATA

The length L of Ulna was measured with a metric rule. F_aL was determined by tuning the oscillator to obtain maximum response on the FFT analyzer. Since the frequency of maximum acceleration response is approximately equal to the resonant frequency $F_a \approx F_o$, the product F_aL was calculated in order to obtain a quantity proportional to $\sqrt{Y/L}$. F_a was determined repeatedly by tuning the variable frequency generator to maximum response. During the test, the forearms were carefully repositioned to hold the mode of vibration constant.

Bone is elastically anisotropic. Considering the differences associated with the histology of the bone tissue and from which it is taken, the compact bone density (approximate value) was used for calculation [9].

DISCUSSION

The experimental data in Table 1 showed the standard deviation of average frequency of ulna was 3.5%. Since error in measurement of F_a and L was independent and the length measurement precision of the Ulna was approximately 2%, the product F_aL has a precision of 5.5% or less for a F_a precision of 3-4%. As biological variations are so large, a precision of 5.5% is acceptable for comparison ofF_a values of different subjects. For the same subject, the length of the Ulna may be assumed to be constant and Fa measurements may be directly compared.

TABLE 1. Mechanical properties of Ulna under examination

Ulna Length **L**(cm)	**Avr Frequency** $F_z(Hz)$	**Std Deviation of** $F_a, \sigma\,(\%)$	**Average Density** $\rho\left(Kg/m^3\right)$	**Youngs Modulusl** $Y\,(GPa)$	**Speed of Sound** $C, \left(ms^{-1}\right)$
25	265.8	3.5	1700	13.60	2827.70
27	265.9	3.3	1700	15.90	3058.26

Youngs modulus measured ultrasonically by Rho et. al. was 14.8 $GPa(S.D.1.4)$ [3]. The Youngs modulus calculated from the experimental data was 13.6GPa with a variation of approximately 8% in same subject which was comparable with previous work of Rho et al.

A triangular wave signal of 25Hz was modulated when the frequency generator was tuned to maximum response. If the wave signal was of 50Hz, different sets of Fa were found. As the frequency modulation range changed, approximate frequency measured by FFT also shifted toward higher values.

The frequency of maximum acceleration response is only approximately equal to the resonant frequency. A simple spring mass dashpot model might be used in correction of F_a measurement as a function of resonance peak width. The typical width of resonance peak of 2.5-3.5 provides 2-4% precision of F_a measurement which is comparable with standard deviation of repeated determination in Table 1. Hence, the simple damped oscillator model can give approximate value for completely simulating the vibrating Ulna.

The repositioning and muscle tension has an effect on measurement F_a which was minimized by determining Fa 6-10 times while the orientation of forearm and gripping was maintained similar.

In the in vivo tests on human bones, the intervening soft tissue between the transducers and the bone also attuned the signal to a great extent. Therefore, the stress wave propagation velocity which is passing through soft tissue, cortical and cancellous bone is expected to be significantly lower.

CONCLUSION

Detecting osteoporosis disease or assessing fracture healing of human bone, Radiographic imaging, Computed Tomography (CT scan) and Magnetic Resonance Imaging (MRI) have being commonly used techniques. Though radiographic imaging is a cost effective and low radiating technique, studies have concluded that radiography has lower accuracy in separating dead and weak bone regions which appear normal with respect to mineral mass but still susceptible to fracture [10]. CT scan and MRI could provide more effective results than radiographic imaging but limited in uses due to higher cost along with other limitation such as CT scan needs more radiation dose, MRI scanner has detrimental effects on the metallic artificial organs of human body [11].

Relationship of breaking strength of long bone with age of the subject, bone geometry and elasticity is used in the predicting the breaking loads of bones with absorptiometry or vibratory measurement in living subjects [12]. In vivo vibration analysis of long bone, lower resonant frequency has observed in bone affected with osteoporosis disease than normal bone [13]. Basis on the above information, a compact and digital instrumentation has proposed in this paper. Vibration analysis has been performed to determine the in vivo mechanical properties of Ulna with the proposed instrumentation with sonic sounds which provides comparable results with previous studies.

The computerized system, flexible operation, low cost and no known detrimental effects on the subjects comparing other available techniques promise a great potential to this instrumentation in screening programs for metabolic bone disease, early detection of osteoporosis, fracture healing assessing and evaluation of skeletal effects of various therapeutic modalities.

The instrumentation shall be verified for the reproducibility in large number of human subject (affected and non-affected) with varying arm position, muscle tension and other variables.

ACKNOWLEDGMENTS

The authors would like to thank Professor Dr. Md. Maksud Helali and Department of Mechanical Engineering, Bangladesh University of Enigneering Technology, Dhaka as most of the research work was done under his supervission during undergraduate thesis in Mechanical Engineering Department.

REFERENCES

[1] John M. Jurist, In vivo determination of the elastic response of bone - 1. Method of ulnar resonant frequency, Physics in Medicine and Biology, Volume 15, Page 417, 1970.

[2] Timothy K. Hight, Robert L. Piziali and Donald A. Nagel Natural Frequency Analysis of Human Tibia, Journal of Biomechanics, Volume 13, Pages 139-147, 1980.

[3] J. Y. Rho, R. B. Ashman and C. H. Turner, Young's modulus of trabecular and cortical bone material: ultrasonic and micro tensile measurements, Journal of Biomechanics, Volume 26, Pages 111-119, 1993.

[4] I. M. Siegel, G. T. Anast and T. Fields, The determination of fracture healing by measurement of sound velocity across the fracture site, Surg Gynecol Obstet, Volume 107, pages 327-332, 1958.

[5] G. A. Thompson, D. R. Young and D. Orne, In vivo determination of mechanical properties of the human ulna by means of mechanical impedance tests: experimental results and improved mathematical model, Medic and Biological Engineering, Volume 14, Pages 253-262, 1976.

[6] S. Tower Stephen, K. Beals Rodney and J. Duwelius Paul, Resonant Frequency Analysis of the Tibia as a Measure of Fracture Healing, ournal of Orthopaedic Trauma, Volume 7, Pages 552-557, 1993.

[7] John M. Jourist and Kianpour Kianiani, Three Models of Vibrating Ulna, Journal of Biomechanics, Volume 6, Pages 331-342, 1973.

[8] Cameron J.R, Mazess R.B. and Sorenson J.A., Precision and accuracy of bone mineral determination by direct photon absorptiometry, Invest Radiol, Volume 3, Pages 141-150, 1968.

[9] Elastic anisotropy of bone, http://silver.neep.wisc.edu/ lakes/BoneAniso.html.

[10] Saam Morshed, Current Option for Determining Fracture Union, Advances in Medicine, Volume 2014, Pages 12 2014.

[11] Bone Infection Diagnosis, http://www.pdrhealth.com/diseases/bone-infection/diagnosis

[12] B. Sherwood Mather, Variation with age and sex in strength of the femur, Medical and biological engineering, Volume 6, Pages 129-132, 1968.

[13] G. van der Perre and G. Lowet, In vivo assessment of bone mechanical properties by vibration and ultrasonic wave propagation analysis, The Bone Journal, Volume 18, Pages S29-S35, 1996.

[14] Paul V. Spiegl and John M. Jurist, Prediction of Ulnar Resonant Frequency, Journal of Biomechanics, Volume 8, Pages 213-217, 1975.

[15] Subrata Saha and Roderic S. Lakes, Effect of Soft Tissue on Wave Propagation and Vibration Test for Determining the In Vivo Properties of Bone, Journal of Biomechanics, Volume 10, Pages 393-401 1977.

[16] R. J. Collier, O. Nadav and T. G. Thomas, The Mechanical Resonance of a Human Tibia: Part I-In Vitro, Journal of Biomechanics, Volume 15, Pages 545-553 1982.

ICME2015

International Conference on Mechanical Engineering 2015
(ICME 2015) 18 – 20 December, 2015, Dhaka, Bangladesh

Paper ID : 426

Optimization of Truss Structure Using Finite Element Analysis

Md. Emdadul Hoque[a)], Samarjith Biswas[b)], Mohammad Imran Khan[c)]

Department of Mechanical Engineering,
Rajshahi University of Engineering & Technology, Rajshahi-6204, Bangladesh.
a)emdadulhoque@gmail.com
b)samar.jith.biswas@gmail.com
c)imran.khan.ruet@gmail.com

Abstract: This paper presents a technique for selecting the most effective truss design from the available truss structures for a specific purpose and further optimization for a set of constraints. In this study the action of applied force on each beam of truss structure has been analyzed to have an optimum design using finite element analysis, which is based FEM. The basic concepts of FEM is to replace any complex shape with some very simple shapes (like triangles) which represents the exact model of the combined part. With the dint of optimization technique integrated with finite element analysis packages, the design cost and time has been reduced to a great extent. Truss optimization process consists of three types of optimization- topology optimization, size optimization and geometry optimization. This study concerns about minimization of stress, displacement and cost of the truss element, where cost minimization is based on minimization of the weight of the structure.

INTRDOUCTION

For many years Engineers have been interested in developing truss structure while tremendous pressure is placed on material that is unable to bear significant weight. Used in modern construction such as towers, buildings and bridges of all size, trusses allow builders to extend the dimensions of the structures and create interesting shape. So it is very important to find out an optimum truss structure of specific purpose. A truss is an assemblage of long sender members which are connected at their ends. In engineering a truss is a structure that consists of two –force members only, where the members are organized so that, the assemblage as a whole behaves like a single object [1].As stability is achieved by cross braces to from triangle, truss design mainly contains triangles. Bars are connected by joints which are called nodes. For analysis joints are assumed to act like hinges, which permits free rotation of the bars around the joints and concentrated forces are acts at the joints .That means the bar support a force which is aligned along the direction of the bar .The principle force in each element in a truss is axial tension or compression .The force in the bar of a truss structure is assumed as positive when corresponding to tension and they are considered as negative when representing to compression. [2]. Optimization is the process of selecting the values of some dependent variables such as cost,

weight, stress based on some independent variable like loads restraints deflection etc. Normally it is related to the maximization or minimization of a function depending on the allowed set of input values .Computer Aided Engineering (CAE) is used as finite element analysis (FEA) and motion simulation have been used by the design engineers for producing better design in the recent years as the most powerful numerical analysis tool. FEA is capable of analyzing any kind of arbitrary shape of structure of homogeneous, non-homogeneous or anisotropic material [3].

APPROACH TO ANALYSIS

In a general sense optimization means minimization or maximization. In mathematics optimization is the process of selecting the best element from some set of available alternatives [4]. Modern optimization method perform shape optimization on components generated within a choice of CAD packages. There need no file translation because they are capable of exchanging data via direct memory transfer between the CAD and FEA software [5]. In case of mechanical design optimization, the resolution of the method is determined by how accurately the FEA analysis can copy the actual physical behavior [6].In this study as linier static FEA has been performed, there are some inherent assumptions and approximations. As for example here displacement is considered to be infinitesimal, thus there is no chance of occurring motion or material nonlinearities.

Truss optimization normally concern about three types of optimization -size, shape and topology optimization. Size optimization is the process of selecting the optimum value of member's cross sectional area. The optimization is carried out by mathematical optimization algorithms with different objective function e.g. maximum stiffness or minimum weight [7]. This size optimization problem is further extended by restricting the member cross section area to take only certain pre –species discrete. Shape or geometry optimization is a complex phenomenon compared with the size optimization. In shape optimization the coordinates of the structural are considered as design variable which is modified during the optimization. The main complexity lying behind shape optimization is in the difficulty of transforming the change of structure to the finite element mesh. In topology optimization the nodal coordinates are taken as design variable while size and geometry of the structure are kept fixed. A web based interface for topology optimization presented by Tcherniak D & Sigmund O [8] and [9] Papadrakankis & Tsompanikis presented an advance solution method in topology optimization and shape sensitivity analysis.

STEPS OF ANALYSIS

The first stage of FEA is to build a model of the structure in a solid modeler (FIGURE-1). In this study solid model of five common type of truss has been build up in SolidWorks. In commercially available FEA, solvers have no capability to understand geometry as it is thought of in CAD. An FEA solver only understand nodes, and the connectivity of the nodes, which are elements [10]. As every truss is made of multiple individual part, meshing is an essential step this case. A better mesh represents the geometry of the template more accurately. It is assumed that the CAD geometry adequately represent the case for the study purpose

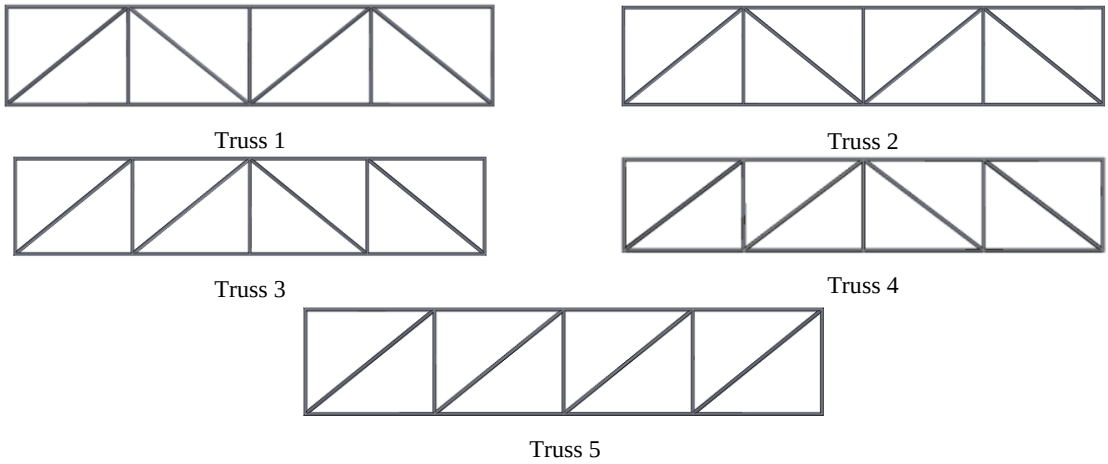

FIGURE 1. FEA model of trusses

The second step is to assign material for the part. For FEA analysis it is assumed that the material properties are same for all parts in the structure. But this assumption has a limitation that most of the manufacturing process require different kind of materials for its different portion. So in the time of selecting the properties of the material the limitation is kept in mind. Normally modern FEA system have a material library with a lot of standardized material with their important properties. The material properties found in the material library may be more accurate than they are actually. There is also a field for user defined material with custom properties. The bending behavior of a beam is linearly proportional to Yong's modulus .If the material stiffness very plus minus 10%, the bending behavior will vary plus or minus 10%.In this case it is important to take a combination of properties for consideration. In this study the most common material Alloy steel is used as the truss material, the properties are as follows. (TABLE 1)

TABLE 1. Properties of Alloy steel

Property	Value	Unit
Elastic Modulus	125735.6976	N/m^2
Poisson Ration	0.28	N/A
Shear Modulus	473005.7196	N/m^2
Density	7700	Kg/m^3
Tensile Strength	723825600	N/m^2
Yield Strength	62042200	N/m^2

The third step of FEA is meshing, where the unnecessary parts such as logo, extension of sharp corners are omitted. As the truss structure is formed by combining many bars so there are many sharp corners, which yield a false infinite stress. The correctness of a study is a function of quality of meshing. Good quality of meshing is the indication of more accurate result of study. Meshing is very important in this case for avoiding such kind of unexpected stress rises. After meshing the solid body may look like a part but it is not enough for a correct study. Automatic meshing is usually very simple but most of the time the designer don't have the access to the source code in this case. In fact FEA is the way of introducing the geometry of the model to FEA solver. As every truss element is build up with multiple beam, meshing is very important step in this case. While using shell and beams it is assumed that these element can adequately represent the geometry and can capture the structural response of the system.

The fourth and most important step the selection of the region where the load will be applied and types of load and their magnitude. All types of load notation is available in the FEA packages. For simplicity point load has been applied in this study. Assigned boundary condition are normally termed as restraint in FEA. The choice of restraints for a model is difficult which is normally taken by the design engineers. The magnitude of stress may vary depending on the decision of the restraints. Factor of safety is an important issue in this case, for avoiding the uncertainty that may occur for the variation of decision for fixture and supports

After assigning the load and the fixture, the model is ready for run. The build in code in FEA package solve the liner system of equation depending on the input variables. Then the time for checking the results. The stress and displacement is compared with the assumed one. If the result is not satisfactory the above steps are reviewed once again for better result. SW automatically generate a document for better viewing the result. Normally for structural studies the deflection, reaction and stress are important for checking. There is also a graphical display, where the number of contours and their maximum and minimum ranges can be controlled. It may happen that the color contour plots often do not produce good imitation. In this case graphs may play an important role. There are so many theories which helps for finding out the results of falling of structural materials. In this case it should be considered that the loading and support uncertainties may cause the variation in material properties that may affect the strength and unexpected failures. Accuracy in FEA depends on properly defining the problems, gaining an understanding of the type of analysis to be run and maintaining the integrity of the mathematical model.

PROBLEM FORMATION

In this study SolidWorks has been used to create the models of the truss structures. Material properties, constraints and applied load has been kept constant for a meaningful comparison among the structures. For constructing the truss

structure 33.7×4.0 mm, is pipe is used. At first a 2-D, sketch of each truss has been drawn. Then the structure member has been added using the "Weldments" toolbar. After that material has been assigned. The span of each truss was kept 5 meter and height is 2 meter. The mathematical model of those trusses are consists of set joints which are connected by straight members with all the joints and all the member are assumed to be located in a common plane. All members are connected to their end joints and that is why no moment is transmitted between the joints and their members. The connection between the member and joint at each end considered to be equivalent to a frictionless pin thus it can permit unrestricted rotation of the end of the member about the axis perpendicular to the plane of the structure. The comparisons are based on the restriction by the architectural design and that is why the span and depth of the trusses are fixed. A 22 kN static Load has been applied on each node have a minimum factor of safety around 3.5.

RESULTS

The result shows that the tuuss1, has minimum amount of bending stress in both direction 1 and direction 2. It has the higher value of "minimum factor of safety" next to truss 5 and lower value of Maximum displacement next to truss 4. It has the minimum weight after truss 2 and truss 5, as shown in FIGURE 2, 3 and Table 2.

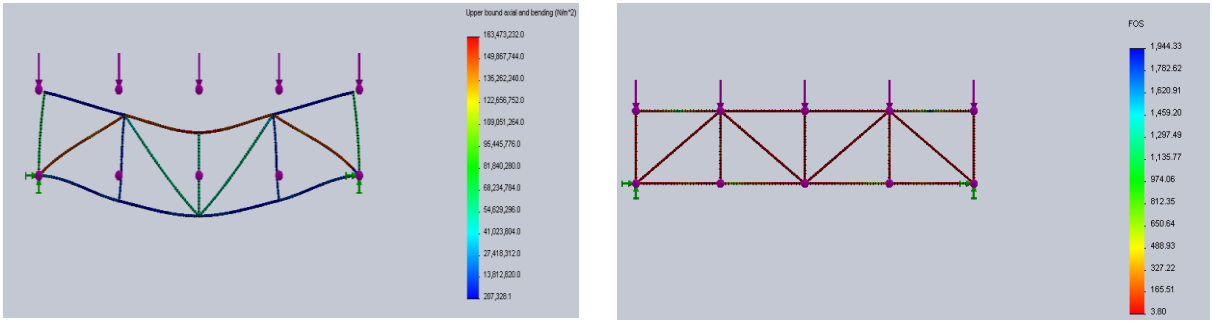

(a) (b)

FIGURE 2. (a) Upper bound Bending and Axial stress; (b) Factor of safety.

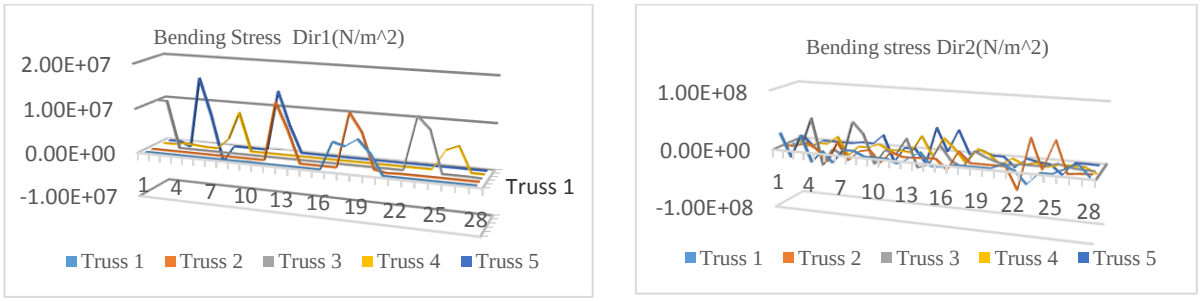

(a) (b)

FIGURE 3. (a) Bending stress in direction 1; (b) Bending stress in direction 2.

TABLE 2. The resultant data of the five truss

Truss structure	Weight(Kg)	Max. Axial(N/m^2)	Max. Bending Dir1(N/m^2)	Max. Bending Dir2(N/m^2)	Upper bound Bending and Axial stress	Max. Displacement (mm)	Minimum FOS
Truss 1	60.68	46812000	7287540	27511200	163473232	4.669	3.80
Truss 2	60.66	140518000	13046000	49401200	159945856	5.594	3.88
Truss 3	60.64	140621000	11857200	47915100	161966048	6.989	3.83
Truss 4	60.71	29195800	8718050	28045900	158000960	3.29	3.83
Truss 5	60.67	140506000	15273400	39501000	166590240	5.424	3.72

Optimum Truss

From the above discussions it is clear that the truss-1 is the best truss among the five trusses for this specific condition. So truss-1, if taken for the optimization process. Form the stress plot of truss-1, it is found that stress is maximum at the upper horizontal member (top chord) and minimum at the lower horizontal member. There is also a stress variation among the diagonal and vertical member. So the inside and outside diameter of the three types of members are taken as the design variable in this optimization process. After 723 times run the software picks up the most optimum truss structure. The weight of the optimum truss is 47.23 kg , while the weight of the initial truss is 60.68 kg , that is about 22 percent reduction of mass , maintaining the other things almost same as shown in FIGUE 5&6.

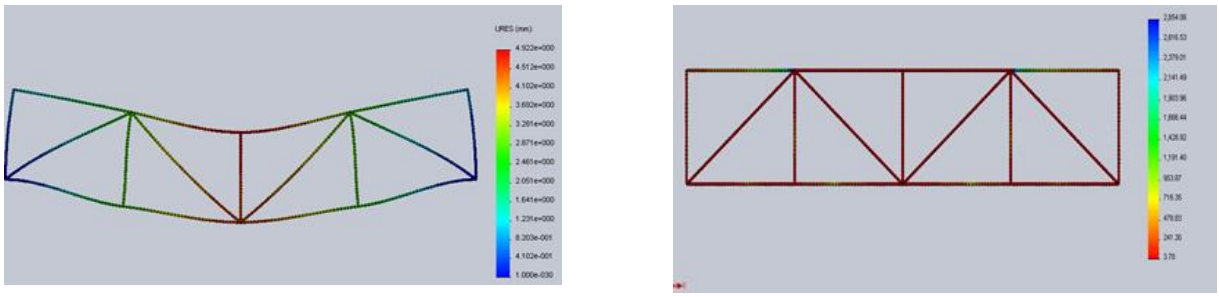

(a) (b)

FIGURE. 5. (a) Displacement of optimum truss; (b) Factor of safety of optimum truss

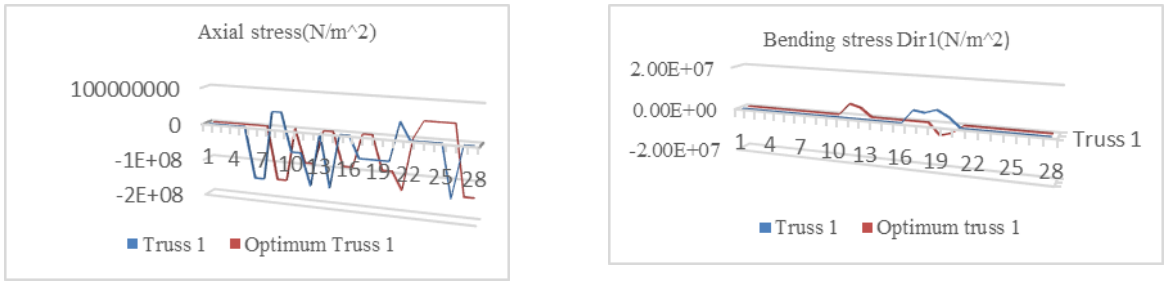

(a) (b)

FIGURE.6. (a) Axial stress; (b) Bending stress.

CONCLUSIONS

This study can be used to determine the most efficient truss shapes in term of weight among the various available truss structure for a definite set of design constraints. In this study circular pipe is used for comparing the result of five common type of truss which will later help to save time of design by avoiding the efforts of trial and error. This study showed the weight of the different truss structures and their resultant output, thus helps to compare the cost of materials among the various type of truss structure. This study is a simple method that helps to choose the optimal truss shapes and is suitable to be applied to other similar studies. More complex truss structure can easily be analyzed in this method and instead of using static load dynamic load can also be used.

REFERENCES

1. J. Ed Akin, Finite Element Analysis Concepts vid SolidWorks , Rice University, Houston ,Texas ,2009.
2. Plesha, Michael E.; Gray, Gary L, Engineering Mechanics: Statics (2nd ed.), New York, 2013, pp. 364-407...
3. Ching, Frank, A visual Dictionary of Architecture (2ndEd.) Hoboken, N.J, Wiley, 2012 277.
4. The Nature of Mathematical Programming, *Mathematical Programming Glossary*, INFORMS Computing Society.
5. Ulises F. Gonzaez, A Discussion on Modern Design Optimization Tools: Full Associativity of CAD, FEA and Event Simulators .AGOR. Inc.
6. Kowik, J and Osborne, MR –Methods for Unconstrained Optimization Problems, American Elsevier Publishing Co. Inc. New York 1968.
7. Marjanocvic , Isaiovic, Blagojevic , Structural optimization in CAD Software, *49 th anniversary of the Faulty of Technical sciences ,novi SAD Machine Design*, ISSN 1821-1259
8. Tcherniak D., Sigmund O, A web-based topology optimization program, Sturctural Multidis Optima, 22,2001, pp179.187
9. Papadrakankis M., Tsompanikis Y., Advanced solution methods in topology optimization and shape sensitivity analysis, Engineering Computations, Vo. 13, No. 5, 1996. pp 57-90
10. Vince Adams, Abraham Askenaxi, Building Better Products with Finite Element Analysis, Onward Press.

ICME2015

International Conference on Mechanical Engineering 2015
(ICME 2015) 18 – 20 December, 2015, Dhaka, Bangladesh

Paper ID : 507

Micromechanics Model for Predicting Anisotropic Electrical Conductivity of Carbon Fiber Composite Materials

Mohammad Faisal Haider[1, a)], Md. Mushfique Haider[2], Farzana Yasmeen[1]

[1]*Department of Mechanical Engineering, University of South Carolina, SC 29208, USA*
[2]*Department of Mechanical Engineering, Bangladesh University of Engineering and Technology, Bangladesh*

[a)]Corresponding author: haiderm@email.sc.edu

Abstract. Heterogeneous materials, such as composites consist of clearly distinguishable constituents (or phases) that show different electrical properties. Multifunctional composites have anisotropic electrical properties that can be tailored for a particular application. The effective anisotropic electrical conductivity of composites is strongly affected by many parameters including volume fractions, distributions, and orientations of constituents. Given the electrical properties of the constituents, one important goal of micromechanics of materials consists of predicting electrical response of the heterogeneous material on the basis of the geometries and properties of the individual phases, a task known as homogenization. The benefit of homogenization is that the behavior of a heterogeneous material can be determined without resorting or testing it. Furthermore, continuum micromechanics can predict the full multi-axial properties and responses of inhomogeneous materials, which are anisotropic in nature. An effective electrical conductivity estimation is performed by using classical micromechanics techniques (composite cylinder assemblage method) that investigates the effect of the fiber/matrix electrical properties and their volume fractions on the micro scale composite response. The composite cylinder assemblage method (CCM) is an analytical theory that is based on the assumption that composites are in a state of periodic structure. The CCM was developed to extend capabilities variable fiber shape/array availability with same volume fraction, interphase analysis, etc. The CCM is a continuum-based micromechanics model that provides closed form expressions for upper level length scales such as macro-scale composite responses in terms of the properties, shapes, orientations and constituent distributions at lower length levels such as the micro-scale.

INTRODUCTION

Multifunctional composites materials are currently being used not only in aircraft but also in a wide variety of structural applications in which they are subjected to a wide spectrum of electrical loading. In such kind of application electrical properties need to be studied for fail-safe operation. Electrical behavior of composites has attracted increased interest to understand reliability under electrical effects and also to provide multi-functional performance (coupled structural-thermal-electrical) in different applications [1-5]. This inherently multi-physical behavior needs to be understood and analyzed to facilitate new multi-functional material design. An essential first step towards that goal is to understand how electrical properties depend on local details (e.g. micro-structure). Composite materials have heterogeneous electrical properties (carbon/epoxy) at the local level but can be different at the global level. As a result electrically conductive of polymer composites have been attracting interest from academic and industrial communities.

The electrical conductivity of two phase composite media has been studied by various researchers [6-8]. Electrical resistivity prediction of dry carbon fiber media as a function of thickness and fiber volume fraction combining empirical and analytical formulas has been done [7]. An experimental investigation of through-thickness electrical resistivity of CFRP laminates has been done by M Louis et al. [9]. T.A Ezquerra et al. has measured alternating-current electrical properties of carbon-fiber polymeric composites [10]. Y lin et al. has improved through thickness electrical conductivity by adding carbon nanotube addition on the through-thickness of CFRP laminates for aircraft applications [11]. But it is very important to understand how electrical conductivity of composites is affected by volume fractions, distributions, and orientations of constituents. Given the electrical properties of the constituents, one important goal of micromechanics of materials consists of predicting electrical response of the heterogeneous material on the basis

of the geometries and properties of the individual phases. There are only few reports available on the micromechanics model for predicting electrical properties of composite materials.

In this study an effective electrical conductivity estimation is performed by using classical micromechanics techniques (composite cylinder assemblage method) that investigates the effect of the fiber/matrix electrical properties and their volume fractions on the micro scale composite response. Micromechanics schemes such as the Mori-Tanaka method, the Self-Consistent Method are good approximation methods for composites with a low volume fraction of reinforcements in a resin. Fiber reinforcements can be considered inclusions in the resin matrix. These treatments assume that one single inclusion is embedded into infinite domain and that each inclusion is far enough apart to neglect their interactions [12]. The advantage of composite cylinder assemblage method (CCM) is that it is an analytical theory that is based on the assumption that composites are in a state of periodic structure. The CCM was developed to extend capabilities variable fiber shape/array availability with same volume fraction, interphase analysis, etc.

MICROMECHANICS MODELING

In cylindrical coordinates the following electrical equilibrium equation can be written for orthotropic materials

$$\sigma_r \frac{\partial^2 \phi}{\partial r^2} + \sigma_\theta \left(\frac{1}{r^2} \frac{\partial^2 \phi}{\partial \theta^2} + \frac{1}{r} \frac{\partial \phi}{\partial r} \right) + \sigma_z \left(\frac{\partial^2 \phi}{\partial z^2} \right) = 0 \tag{1}$$

Here, σ = electrical conductivity and ϕ = electric potential.

Further assume that the material is transversely isotropic so, $\sigma_r = \sigma_\theta = \sigma_2$ and $\sigma_z = \sigma_1$. Now to evaluate conductivity in axial and transverse direction consider the cases in axial $(\phi = \phi(z))$ and transverse direction $\phi = \phi(x) = \phi(r, \theta)$. Axis *x* is an arbitrary radial direction along which the electrical conductivity is the same. Now assuming that potential is variable separable. So $\phi(z, r, \theta) = Z(z) R(r) \Theta(\theta)$

Now equation (1) can be written as

$$\sigma_z \left(\frac{\partial^2 Z}{\partial z^2} \right) = 0 \tag{2}$$

$$\frac{\partial^2 R}{\partial r^2} \Theta + \left(\frac{1}{r^2} \frac{\partial^2 \Theta}{\partial \theta^2} R + \frac{1}{r} \frac{\partial R}{\partial r} \Theta \right) = 0 \tag{3}$$

Solution of equation (2) and (3) are respectively

$$\phi = Az + B \tag{4}$$

$$\phi = \left(Cr + \frac{1}{r} D \right) cos\theta \tag{5}$$

Where *A, B, C, D* are constants to be determined from boundary and/or interface conditions.

Here the entire composite cylinder assemblage in Fig. 1 is embedded in a two layer whose material properties are the same as the material properties of the effective solid homogeneous material of Fig. 1. Constant A, B, C, D from equation (4) and (5) can be found from two phase Composite Cylinders model.

Axial Conductivity

The two phase composite cylinder assemblage is used to determine the effective axial conductivity consists of two concentric cylinders or phases (Fig. 1), each of which is assumed to have isotropic material symmetry and has a potential of the form

$$\phi^f = A^f z + B^f \quad for\, 0 \le r \le r_f \tag{6}$$

$$\phi^m = A^m z + B^m \ \ for\, r_f \le r \le r_m \tag{7}$$

Where, superscript *f*= fiber and superscript *m*= epoxy matrix

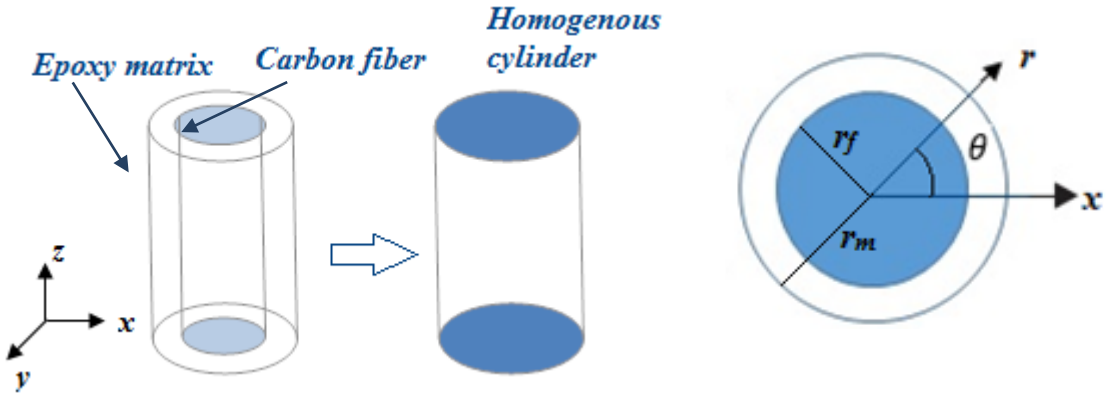

FIGURE 1. Two phase Concentric Composite Cylinders Model

Boundary Condition: the following boundary condition is imposed in order to determine the axial conductivity

$$\phi^{f,m}\left(z = -\frac{L}{2}\right) = \phi_0 \tag{8}$$

$$\phi^{f,m}\left(z = \frac{L}{2}\right) = \phi_0 + \Delta\phi \tag{9}$$

By using boundary condition equation (8) and(9), equation (6) and (7) give the following values

$$A^f = A^m = \frac{\Delta\phi}{L} \tag{10}$$

$$B^f = B^m = \phi_0 + \frac{\Delta\phi}{2} \tag{11}$$

Thus the nonzero electric field component in each phase is determined to be

$$E_z{}^{f,m} = -\frac{\partial\phi^{f,m}}{\partial z} = -A^{f,m} \tag{12}$$

So the nonzero current flux in axial direction is

$$J_z{}^{f,m} = \sigma^{f,m} E_z{}^{f,m} = -\sigma^{f,m} A^{f,m} \tag{13}$$

So the axial conductivity can be expressed as following equation

$$\sigma_1 = \frac{J_z}{E_z} \tag{14}$$

The current flux J_z is are the spatial averages of the electric current density along the *z* axis

$$J_z = \frac{1}{V}\iiint J_z{}^{f,m} dV \tag{15}$$

And electric field can be written as follow

$$E_z = E_z{}^f = E_m{}^m = -\frac{\Delta\phi}{L} \tag{16}$$

Using equation (15) and (16) into equation (14) the following expression can be written

$$\sigma_1 = \frac{\frac{1}{V}\iiint J_z{}^{f,m} dV}{E_z} \tag{17}$$

$$\frac{1}{V}\iiint J_z{}^{f,i,m}dV = \frac{1}{V}[\iiint J_z{}^{f}dV + \iiint J_z{}^{i}dV + \iiint J_z{}^{m}dV] \tag{18}$$

Here, $V = \pi r_m{}^2 z$ and $dV = r\,dr d\theta dz$. After solving equation(17), axial conductivity σ_1 .can be found as follows

$$\sigma_1 = \left[\sigma^f V_f + \sigma^m (1 - V_f)\right] \tag{19}$$

Here, V_f = fiber volume fraction. This is rule of mixture of axial conductivity.

Transverse Conductivity

Due to the variation of the cylindrical surface area in the transverse direction, the law-of mixture rule is not applicable for calculating the electrical conductivity in this direction. In order to determine the transverse electrical conductivity σ_2, the system is subjected to uniform electric field E_0 along x at a large distance sufficiently far away (Fig. 2) . The two phase composite cylinder assemblage is used to determine the effective transverse conductivity consists of two concentric cylinders or phases (Fig. 1), each of which is assumed to have isotropic material symmetry and has a potential of the form

$$\phi^f = \left(C^f r + \frac{1}{r} D^f\right)\cos\theta \quad for\, 0 \le r \le r_f \tag{20}$$

$$\phi^m = \left(C^m r + \frac{1}{r} D^m\right)\cos\theta \quad for\, r_f \le r \le r_m \tag{21}$$

Where, superscript *f*= fiber and superscript *m*= epoxy matrix

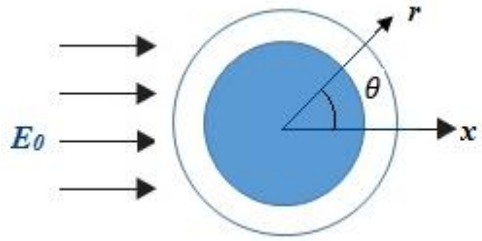

FIGURE 2. Two phase composite cylinder system is subjected to uniform electric field

Boundary Condition: the following boundary condition is imposed in order to determine the axial conductivity
At $r = 0$ potential should have finite value so, $D^f = 0$
From continuity equation,

$$\phi^f\,|_{r=r_f} = \phi^m\,|_{r=r_f} \tag{22}$$

$$J^f\,|_{r=r_f} = J^m\,|_{r=r_f} \tag{23}$$

Equation (23) can also be written as follows

$$\sigma_f \frac{\partial \phi^f}{\partial r}|_{r=r_f} = \sigma_m \frac{\partial \phi^m}{\partial r}|_{r=r_f} \tag{24}$$

From boundary,

$$-\frac{\partial \phi^m}{\partial r}|_{r=r_m} = E_0 \cos\theta \tag{25}$$

or,

$$\phi^m\,|_{r=r_m} = -E_0 r_m \cos\theta \tag{26}$$

From equation(22), (24) and (26) the constant C^f , C^m , D^m can be found from following equation

$$\begin{bmatrix} 1 & -1 & -\frac{1}{r_f^{\,2}} \\ 1 & -\frac{\sigma_m}{\sigma_f} & \frac{1}{r_f^{\,2}}\frac{\sigma_m}{\sigma_f} \\ 0 & 1 & \frac{1}{r_m^{\,2}} \end{bmatrix} \begin{bmatrix} C^f \\ C^m \\ D^m \end{bmatrix} = \begin{bmatrix} 0 \\ 0 \\ -E_0 \end{bmatrix} \tag{27}$$

After solving the above equation for coefficients, the electric potential can be found from equation (20) and (21)

$$\phi^f = -\frac{2\sigma_m E_0 r\cos\theta}{\sigma_m\left(1+v_f\right)+\left(1-v_f\right)\sigma_f} \tag{28}$$

$$\phi^m = -\left[\frac{\sigma_m+\sigma_f}{\sigma_m\left(1+v_f\right)+\left(1-v_f\right)\sigma_f}+\frac{1}{r^2}\frac{\left(\sigma_m-\sigma_f\right)r_f^{\,2}}{\sigma_m\left(1+v_f\right)+\left(1-v_f\right)\sigma_f}\right]E_0 r\cos\theta \tag{29}$$

Electric field and current flux can be found from the following expression

$$E_r^{\,f,m} = -\frac{\partial\phi^{f,m}}{\partial r} \tag{30}$$

$$J_r^{\,f,m} = \sigma E_r^{\,f,m} \tag{31}$$

$$E_\theta^{\,f,m} = -\frac{\partial\phi^{f,m}}{\partial\theta} \tag{32}$$

$$J_\theta^{\,f,m} = \sigma E_\theta^{\,f,m} \tag{33}$$

Now, transverse conductivity can be express as

$$\sigma_2 = \frac{J_x}{E_0} = \frac{\frac{1}{V}\iiint J_x^{\,f,m}dV}{E_0} \tag{34}$$

Where,

$$\frac{1}{V}\iiint J_x^{\,f,m}dV = \frac{1}{V}\left[\iiint\left(J_r^{\,f}\cos\theta - J_\theta^{\,f}\sin\theta\right)dV + \iiint\left(J_r^{\,m}\cos\theta - J_\theta^{\,m}\sin\theta\right)dV\right] \tag{35}$$

Now from equation (34) and (35)

$$\sigma_2 = \sigma^m\frac{\left[\sigma^f\left(1+V_f\right)+\sigma^m\left(1-V_f\right)\right]}{\left[\sigma^f\left(1-V_f\right)+\sigma^m\left(1+V_f\right)\right]} \tag{36}$$

This is the equation for transverse conductivity.

RESULTS AND DISCUSSION

It should be mentioned that the CCM micromechanics model in the current work was developed based on the assumption of uniformly distribution of straight carbon fibers in polymers. And the interaction between one fiber to another fiber is neglected. Micromechanics modeling results for the effective axial electrical conductivity and transverse conductivity are presented in Fig. 3 and Fig. 4. Figure 3 shows the variation of axial electrical conductivity with fiber volume fraction. Equation (19) represents the equation for the axial electrical conductivity. Which is linear in nature that means the axial conductivity directly depends on the amount of carbon fiber and the conductivity of carbon fiber. As the volume fraction of carbon fiber increases the conductivity increases. Matrix is less conductive than carbon fiber so the values of effective axial conductivity of composite is between the value of matrix conductivity and carbon fiber conductivity.

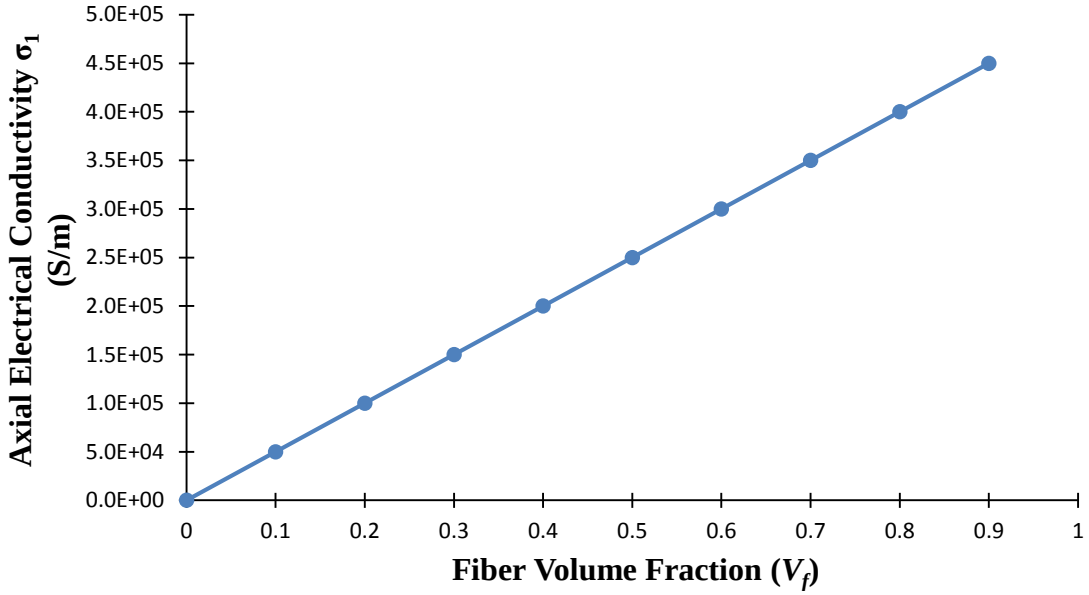

FIGURE 3. Variation of axial electrical conductivity with fiber volume fraction (σ_f / σ_m = 5e5)

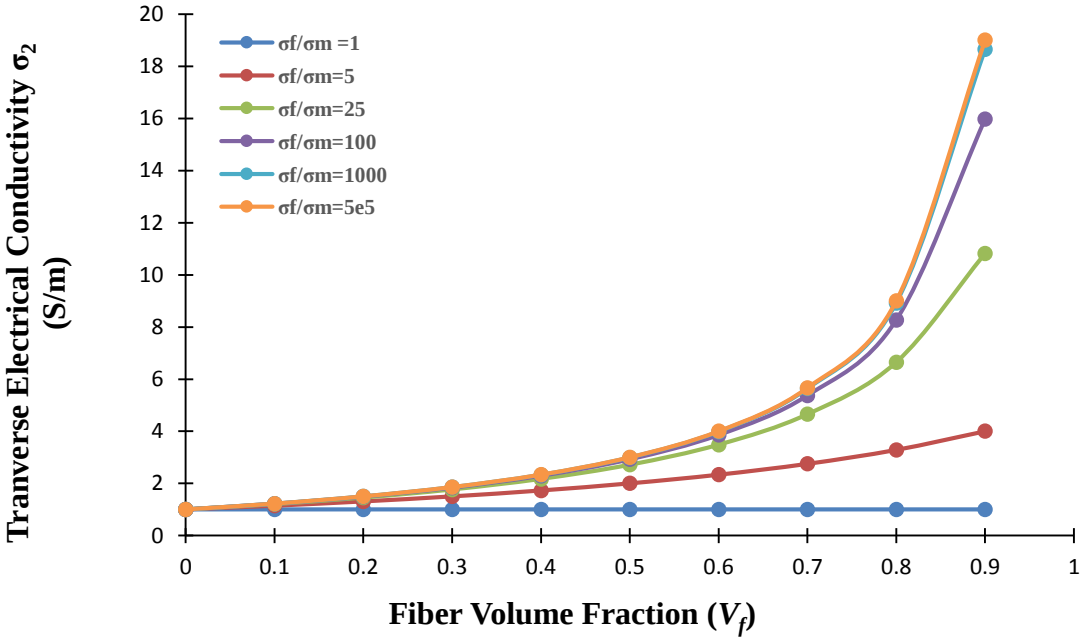

FIGURE 4. Variation of transverse electrical conductivity with fiber volume fraction

Figure 4 shows the variation of transverse conductivity of composite materials with fiber volume fraction. In the transverse direction as there are no direct conduction path so conductivity is much lower than the axial direction. There is no significant change in conductivity in transverse direction even up to certain fiber volume fraction. As the fiber volume fraction increases the conductivity increases. Figure 4 shows different conductivity data for different carbon fiber conductivity to matrix conductivity ratio. At low carbon fiber to matrix conductivity ratio there is no significant change in effective transverse conductivity of composite with fiber volume fraction but as the conductivity ratio increases the transverse conductivity also increases. It should also be noted that though the transverse conductivity

increases with the ratio of fiber conductivity to matrix conductivity but that is not significant compared to axial conductivity.

Another fact is that the transverse conductivity increases with the ratio of fiber conductivity to matrix conductivity up to a certain limit. Beyond that limit there is no significant change in transverse conductivity with carbon fiber to matrix conductivity ratio. It should me mentioned that for polymeric composites, the fiber-to-matrix conductivity ratio is very high. (For example, for a carbon fiber/epoxy polymer matrix composite, σ_f/σ_m = 1e5). The transverse electrical conductivity of the composite in such cases changes appreciably only for large fiber volume fractions. Figure 4 shows that, for high σ_f/σ_m ratios, the contribution of the fiber conductivity only increases substantially for a fiber volume fraction greater than 80%. These fiber volume fractions are not practical and in many cases are physically impossible due to the geometry of fiber packing.

CONCLUSION

A micromechanics model has been developed to assess the impact of the fiber volume fraction and the electrical conductivity of fiber and matrix on the electrical conductivity of polymer composites. Modeling of the micromechanics model developed has been used to qualitatively identify the potential causes for changing in conductivity both axial direction and transverse direction with fiber volume fraction. From the micromechanics model, it is observed that the axial conductivity directly depend on fiber volume fraction and electrical conductivity of carbon fiber composite and the transverse conductivity significantly change for a fiber volume fraction greater than 80%. Due to high fiber-to-matrix conductivity ratio there is no significant improvement of conductivity compared to axial conductivity.

REFERENCES

1. M. F. Haider, P.K. Majumdar, K. L. Reifsnider, Study of damage in Carbon fiber reinforced Composites Due to Electric Current, American Society for Composites 28th Technical Conference September 9-11, 2013 State College, Pennsylvania, USA.
2. P.K. Majumdar, M. F. Haider, K. L. Reifsnider, AC Conductivity and Microstructural Changes of Composite Materials, International Conference on Lightning and Static Electricity (ICOLSE) 2013 , Seattle , Washington, USA. (Hosted by Boeing).
3. P.K. Majumdar, M. F. Haider, K. L. Reifsnider, Effect of Fiber Orientation on AC Conductivity of Composite Materials, SAMPE 2013 conference, 6-9May , 2013, California, USA.
4. P.K. Majumdar, K.L. Reifsnider, Md., R. Raihan, M. F. Haider, Study of Damage Evolution in Composite Materials Using 3D X-ray Microscope, SAMPE 2013 conference, 6-9May , 2013, California, USA.
5. P.K. Majumdar, M. F. Haider, K. L. Reifsnider.,Multi-Physics Response of Structural Composites and Framework for Modeling using Material Geometry, 54th AIAA/ASME/ASCE/ASC structures, structural Dynamics, and Materials conference, 8-11 Aprl 2013, Boston, Massachusetts, USA.
6. S. Torquato, "Effective electrical conductivity of two-phase disordered composite media". J Appl Phys, 58 (10) (1985), pp. 3790–3797
7. J.H. Greenwood, S. Lebedat, J. Bernasconi , "The anisotropic electrical resistivity of a carbon fibre reinforced plastic disc and its use as a transducer" J Phys E Sci Instrum, 8 (1975), pp. 369–370
8. J. Kovacik, "Electrical conductivity of two-phase composite material" Scri Mater, 39 (2) (1998), pp. 153–157
9. M Louis, S.P Joshi, W Brockmann, An experimental investigation of through-thickness electrical resistivity of CFRP laminates, Composites Science and Technology, Volume 61, Issue 6, May 2001, Pages 911-919, ISSN 0266-3538
10. T.A Ezquerra, M.T Connor, S Roy, M Kulescza, J Fernandes-Nascimento, F.J Baltá-Calleja, Alternating-current electrical properties of graphite, carbon-black and carbon-fiber polymeric composites, Composites Science and Technology, Volume 61, Issue 6, May 2001, Pages 903-909.
11. Yueguo Lin, Marco Gigliotti, Marie Christine Lafarie-Frenot, Jinbo Bai, Damien Marchand, David Mellier, Experimental study to assess the effect of carbon nanotube addition on the through-thickness electrical conductivity of CFRP laminates for aircraft applications, Composites Part B: Engineering, Volume 76, July 2015, Pages 31-37
12. Makvandi, Resam, and Andreas Öchsner. "On a Finite Element Approach to Predict the Thermal Conductivity of Carbon Fiber Reinforced Composite Materials." Defect and Diffusion Forum. Vol. 354. 2014

ICME2015

International Conference on Mechanical Engineering 2015
(ICME 2015) 18 – 20 December, 2015, Dhaka, Bangladesh

Paper ID : 522

Analysis of a Hybrid Balanced Laminate as a Structural Material for Thick Composite Beams with Axial Stiffeners

Partha Modak[1], M. Jamil Hossain[1,a)] and S. Reaz Ahmed[1]

[1]*Department of Mechanical Engineering, Bangladesh University of Engineering and Technology, Dhaka 1000, Bangladesh*

[a)]Corresponding author: jamil917@gmail.com

Abstract. An accurate stress analysis has been carried out to investigate the suitability of a hybrid balanced laminate as a structural material for thick composite beams with axial stiffeners. Three different balanced laminates composed of dissimilar ply material as well as fiber orientations are considered for a thick beam on simple supports with stiffened lateral ends. A displacement potential based elasticity approach is used to obtain the numerical solution of the corresponding elastic fields. The overall laminate stresses as well as individual ply stresses are analysed mainly in the perspective of laminate hybridization. Both the fiber material and ply angle of individual laminas are found to play dominant roles in defining the design stresses of the present composite beam.

INTRODUCTION

Hybrid composites contain more than one type of fiber in a single matrix material. In principle, several different fiber types may be incorporated into a hybrid, but it is more likely that a combination of only two types of fibers would be most beneficial Chamis and Lark [1]. Hybrid composites have unique features that can be used to meet various design requirements in a more economical way than conventional composites. This is because expensive fibers like graphite can be partially replaced by less expensive fibers such as glass Chou and Kelly [2]. Some of the specific advantages of hybrid composites over conventional composites include balanced strength and stiffness, balanced bending and membrane mechanical properties, balanced thermal distortion stability, reduced weight and/or cost, improved fatigue resistance, reduced notch sensitivity, improved fracture toughness, and improved impact resistance Chamis and Lark [1].

Elasticity problems are usually formulated either in terms of stress function or displacement parameters Timoshenko and Goodier [3]. The stress function approach accepts boundary conditions only in terms of loadings, boundary restraints cannot be imposed on the function appropriately. Axial stiffeners at the lateral ends of a simply supported beam are usually modeled in terms of a mixed mode of boundary conditions. The conventional mathematical models of elasticity are not adequate to handle the problems of mixed boundary-value problems of laminated composites, and thus a displacement potential based elasticity approach is used to formulate and analyze the elastic field of the present beam problem.

The analysis as well as design of structural components of laminated composites has now been entirely dependent on FEM software, and the corresponding applications in the literature are quite extensive Chou [4], Koli and Chandrashekhara [5], Mallela and Upadhyay [6], Zhang and Yang [7], Masud and Panchandeh [8], Biswal and Gosh [9]. Recently, a displacement-potential based elasticity approach has been developed for the boundary value problems of laminated composites Ahmed and Modak [10], which has eventually opened up an effective alternative avenue to obtain analytical as well as numerical solutions of practical stress problems of laminated composites.

A careful and accurate analysis of stresses in individual plies of various fiber stiffness as well as orientation is of utmost importance to determine the corresponding failure condition of the laminated beam. The present research addresses a new stress analysis of a hybrid balanced laminate to investigate its suitability as a structural material of a thick simply-supported composite beam with axial stiffeners at its lateral ends. For three different balanced laminates composed of dissimilar ply material as well as fiber orientations, the overall laminate as well as individual ply stresses

are analyzed for the beam mainly in the perspective of laminate hybridization. Some of the results are also compared with those of conventional approach to verify the conformity of the present results with traditional ones.

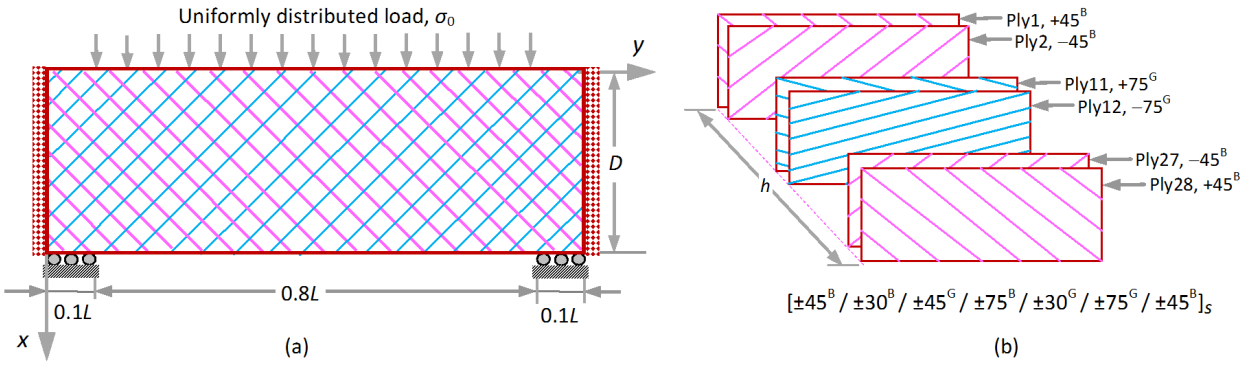

FIGURE 1. Loading and geometry of the laminated composite beam: (a) geometrical modeling, (b) material modeling.

MATHEMATICAL FORMULATION AND NUMERICAL SOLUTION

The two differential equations of equilibrium for the problems of symmetric laminated composites in terms of displacement components of plane elasticity, in absence of body forces, are as follows Modak and Ahmed [11]:

$$A_{11}\frac{\partial^2 u_x}{\partial x^2} + 2A_{16}\frac{\partial^2 u_x}{\partial x \partial y} + A_{66}\frac{\partial^2 u_x}{\partial y^2} + A_{16}\frac{\partial^2 u_y}{\partial x^2} + (A_{12} + A_{66})\frac{\partial^2 u_y}{\partial x \partial y} + A_{26}\frac{\partial^2 u_y}{\partial y^2} = 0 \tag{1}$$

$$A_{16}\frac{\partial^2 u_x}{\partial x^2} + (A_{12} + A_{66})\frac{\partial^2 u_x}{\partial x \partial y} + A_{26}\frac{\partial^2 u_x}{\partial y^2} + A_{66}\frac{\partial^2 u_y}{\partial x^2} + 2A_{26}\frac{\partial^2 u_y}{\partial x \partial y} + A_{22}\frac{\partial^2 u_y}{\partial y^2} = 0 \tag{2}$$

The coefficients, A_{ij} are the elements of extensional stiffness matrix $[A]$, which are various functions of elastic properties (E_1, E_2, G_{12}, ν_{12}) Jones [12]. For a symmetric laminated composite, the mid-plane strains are assumed to be the global strains, as the curvature effect under in-plane loading can be neglected Jones [12]. Moreover, for a symmetric laminate with even number of plies, A_{16} and A_{26} are zero. In the present lamination theory, a scalar function $\psi(x, y)$ is defined in terms of the displacement components of plane elasticity as follows Ahmed and Modak [10]:

$$\begin{bmatrix} u_x \\ u_y \end{bmatrix} = \begin{bmatrix} \alpha_1 & \alpha_2 & \alpha_3 \\ \alpha_4 & \alpha_5 & \alpha_6 \end{bmatrix} \begin{bmatrix} \frac{\partial^2\psi}{\partial x^2} & \frac{\partial^2\psi}{\partial x \partial y} & \frac{\partial^2\psi}{\partial y^2} \end{bmatrix}^T \tag{3}$$

where, α_i are various material constants. For a symmetric laminated composite, the values of the coefficients are obtained as $\alpha_1 = \alpha_3 = \alpha_5 = 0, \alpha_2 = 1$, $\alpha_4 = -A_{11}/(A_{11} + A_{66})$ and $\alpha_6 = -A_{66}/(A_{11} + A_{66})$ Ahmed and Modak [10]. The values of the coefficients are determined in such way that α has to satisfy the second equilibrium Eq. 2 only. Expressing Eq. 2 in terms of the scalar function, the single differential equation of equilibrium for the symmetric laminated composites is obtained as follows:

$$\frac{\partial^4\psi}{\partial x^4} + \left(\frac{A_{22}}{A_{66}} - \frac{A_{12}^2}{A_{11}A_{66}} - \frac{2A_{12}}{A_{11}}\right)\frac{\partial^4\psi}{\partial x^2 \partial y^2} + \frac{A_{22}}{A_{11}}\frac{\partial^4\psi}{\partial y^4} = 0 \tag{4}$$

From the standard stress-strain relations of laminated composites, the corresponding expressions of stress components in terms of the function, $\psi(x, y)$, are,

$$\begin{bmatrix} \sigma_{xx} \\ \sigma_{yy} \\ \sigma_{xy} \end{bmatrix} = \frac{1}{h(A_{12} + A_{66})} \begin{bmatrix} 0 & A_{11}A_{66} & 0 & -A_{12}A_{66} \\ 0 & A_{12}^2 + A_{11}A_{66} - A_{11}A_{22} & 0 & -A_{22}A_{66} \\ -A_{11}A_{66} & 0 & A_{12}A_{66} & 0 \end{bmatrix} \begin{bmatrix} \frac{\partial^3\psi}{\partial x^3} & \frac{\partial^3\psi}{\partial x^2 \partial y} & \frac{\partial^3\psi}{\partial x \partial y^2} & \frac{\partial^3\psi}{\partial y^3} \end{bmatrix}^T \tag{5}$$

Stresses at individual plies of the laminate are calculated from the global mid-plane strain (ε_{ij}) and the respective transformed reduced stiffness matrix, $[Q]$ of the ply Ahmed and Modak [10].

A uniform rectangular 53×53 finite-difference mesh-network is used to discretize the beam, which includes an imaginary boundary immediate exterior neighbor to the physical boundary. The differential equations associated with the equilibrium and boundary conditions are replaced by their corresponding difference equations. The order of local truncation error has been kept ($O(h^2)$) for all the expressions developed. Multiple differencing schemes are adopted to manage the asymmetric boundary conditions for different segments of the boundary. Finally, the nodal solutions of the primary variable (ψ) are used to calculate the elastic field of the beam through the respective difference equations of body parameters.

GEOMETRY, LOADING AND MATERIAL OF THE COMPOSITE BEAM

The geometry and loading of a simply-supported laminated beam under a uniform loading is illustrated in Fig. 1. The opposing lateral ends of the beam are assumed to be stiffened by axial stiffeners S. R. Ahmed and Modak [13]. The aspect ratio (L/D) of the beam is kept 4 for the present analysis. Two different FRC laminas, boron/epoxy and glass/epoxy, with various fiber orientations are considered to form the symmetric hybrid balanced laminate for the beam. Along with the hybrid laminate, two additional identical laminates of boron/epoxy and glass/epoxy are considered for the comparative analysis. The effective mechanical properties of the composite lamina are listed in Table 1. The laminates are assumed to be composed of twenty eight plies having an overall thickness, $h = 14$ mm. The material modelling of the hybrid laminated beam together with its stacking sequence is shown in Fig. 1, while the laminates of boron/epoxy and glass/epoxy follow the identical sequence of fiber orientations.

RESULTS OF THE ANALYSIS

The results of the present investigation are presented mainly for the critical sections of the laminated beam, particularly in the form of tables and graphs. In all cases, stresses are normalized with respect to the maximum intensity of applied loading, σ_0. The stress fields of a boron/epoxy and glass/epoxy ply with identical fiber orientation ($\theta = 75^o$) and location in the hybrid laminate are presented in the form of maximum principal stresses in Fig. 2. The boron/epoxy ply is found to be much critically stressed than the glass/epoxy ply of the same laminate, even though the shapes of the distributions are quite similar. The fiber material (i.e., stiffness) does not affect the distribution pattern of stress field, rather affects the intensity. It can be revealed from the present analysis that the terminal points of the local supports at the bottom surface ($x/D = 0, y/L \approx 0.1/0.9$) are the most critical sections of the beam in terms of stresses.

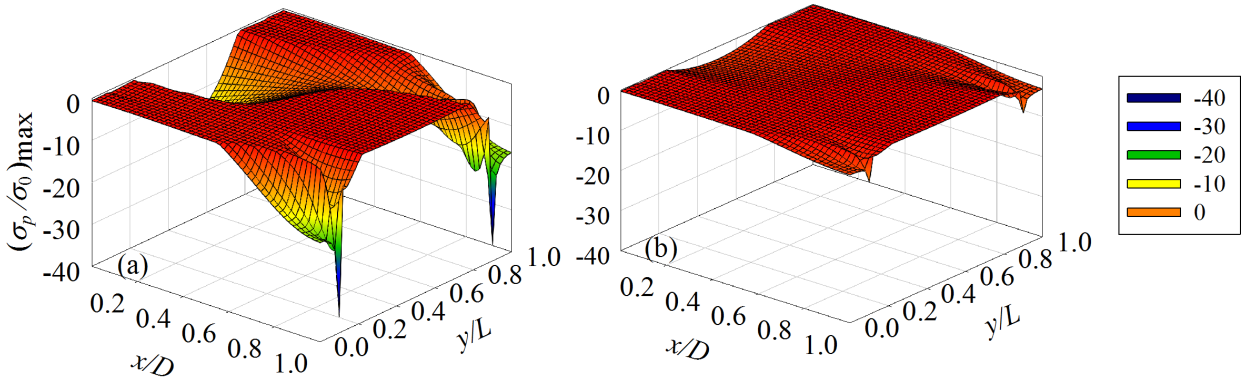

FIGURE 2. Principal stress (maximum) fields of individual plies of the hybrid laminated beam: (a) boron/epoxy (75^o); (b) glass/epoxy (75^o).

Table 2 lists the overall laminate stresses at the critical section of the beam for the case of boron/epoxy, glass/epoxy as well as the hybrid laminates considered. Among the stress components, the flexural stress component is found to play the most dominant role in defining the state of stresses. It would be worth mentioning that the critical values of all the components of stress for the hybrid laminate are almost identical with those of boron/epoxy and glass/epoxy laminates. In other words, the effect of hybridizing boron/epoxy and glass/epoxy laminas for a beam on simple supports is almost negligible when analyzed in the perspective of overall laminate stresses.

TABLE 1. Properties of unidirectional fiber-reinforced composite lamina used to obtain the numerical results.

Property	Symbol	Glass/epoxy	Boron/epoxy
Elastic modulus along the fiber direction	E_1 (GPa)	38.6	204.00
Elastic modulus perpendicular to the fiber direction	E_2 (GPa)	8.27	18.50
Shear modulus	G_{12} (GPa)	4.14	5.59
Major Poisson's ratio	ν_{12}	0.26	0.23

TABLE 2. Overall laminate stresses at the critical sections of the local supports, $y/L \approx 0.1$ or 0.9.

Laminate	σ_{xx}/σ_0	σ_{yy}/σ_0	σ_{xy}/σ_0
Hybrid laminate	-8.84	-12.69	2.41
Boron/epoxy laminate	-8.79	-12.81	2.40
Glass/epoxy laminate	-9.07	-12.88	2.30

Fig. 3 shows the distribution of normalized bending stress along the stiffened end of the beam for individual plies of different laminates as a function of fiber orientation of the plies. The distributions of bending stresses are found to be affected by both the fiber orientation and hybridization of ply materials in terms of magnitude as well as nature of variation. The stress developed in the boron/epoxy ply is much higher when it is in the hybrid laminate, than that in the pure boron/epoxy laminate (see Fig. 3(a), (c)). However, an opposite phenomenon is observed when we consider the case of glass/epoxy ply. The maximum value of bending stress developed in the boron/epoxy ply, $\theta = 30^o$, increases by 48% when hybridized with glass/epoxy plies to form the laminate (Fig. 3(a)). On the other hand, the bending stresses at the critical region in an identical glass/epoxy ply are found to decrease 65% when hybridized with boron/epoxy plies (Fig. 3(b)), which, in turn, reveals that the glass/epoxy plies are more severely affected by hybridization than the boron/epoxy plies. This effect of hybridization is further found to become more prominent for both the boron/epoxy and glass/epoxy plies, when the ply angle increases from 30^o to 75^o (Fig. 3(c) and (d)).

TABLE 3. Comparison of critical ply stresses of the three different laminates as a function of ply angle

Laminate	$\theta = 30^o$			$\theta = 45^o$			$\theta = 75^o$		
	σ_{xx}/σ_0	σ_{yy}/σ_0	σ_{xy}/σ_0	σ_{xx}/σ_0	σ_{yy}/σ_0	σ_{xy}/σ_0	σ_{xx}/σ_0	σ_{yy}/σ_0	σ_{xy}/σ_0
Boron/epoxy	-13.78	-5.97	-6.89	-10.19	-10.84	-8.45	-3.13	-22.61	-5.44
Boron/epoxy in hybrid laminate	-20.44	-8.92	-10.21	-15.25	-16.25	-12.65	-4.68	-34.10	-8.20
Glass/epoxy	-12.56	-8.01	-4.96	-9.96	-11.66	-6.41	-4.76	-19.60	-3.79
Glass/epoxy in hybrid laminate	-4.26	-2.66	-1.67	-3.16	-3.90	-2.09	-1.54	-6.75	-1.30

The distributions of lateral stresses at the critical section ($y/L = 0.1$) of the beam are shown in Fig. 4. Likewise the case of bending stresses, the glass/epoxy plies are found to experience greater effect of hybridization in terms of lateral stress than boron/epoxy plies; however, the effect associated with the lateral stress is found to decrease with the increase of ply angle from 30^o to 75^o (see Fig. 4(c) and (d)). As far as the shear stress component is concerned, the effect of hybridization is realized to be very similar to those of axial and lateral stress components. However, the hybridization effect is found to be most significant for both boron/epoxy and glass/epoxy plies with ply angle, $\theta = 45^o$. Observing the details of the stress fields it can be concluded that the stress level in an individual ply of a laminate can be well controlled by hybridizing the laminas of appropriate fiber stiffness and orientation. The critical values of stresses of individual plies of different laminates for three different fiber orientations ($\theta = 30^o$, 45^o and 75^o) are summarized in Table 3. For all the ply angles considered, laminate hybridization causes the increase in the magnitude of critical stresses for boron/epoxy ply, while an opposite characteristic is noticed for the glass/epoxy ply. Therefore, a careful analysis of ply stresses would be essential for reliable analysis of failure of hybrid laminated beams of the present type.

Finally, a 16-ply hybrid balanced laminate with a stacking sequence of $[\pm 75^B/\pm 30^G/\pm 75^G/\pm 45^B]_s$ is again considered for the beam under standard symmetric four-point bending for the comparison of present solutions with those of conventional computational approach. The laminated beam was modeled by 100×100 four-nodded, isoparametric layered shell finite elements. Fig. 5 illustrates the comparison of two solutions of stress distributions at the bottom supporting surface of the boron/epoxy ply with $\theta = 75^o$. The stresses are found to be in very good conformity with the corresponding FEM solutions with slight exceptions, particularly at the critical sections. In all cases, the present

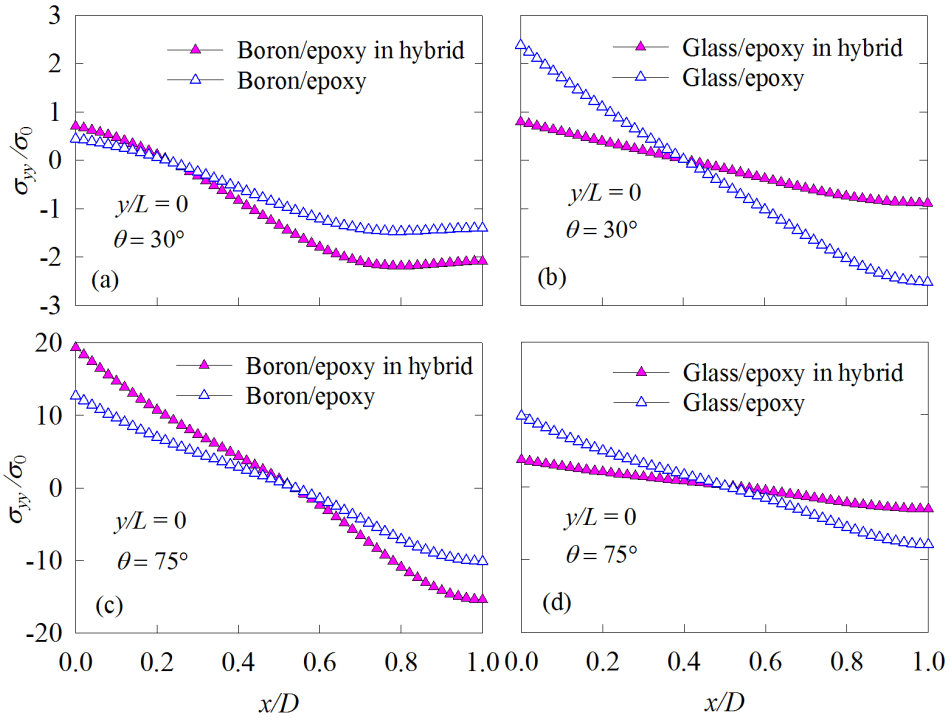

FIGURE 3. Distribution of bending stresses along the stiffened edges of identical plies of different laminates.

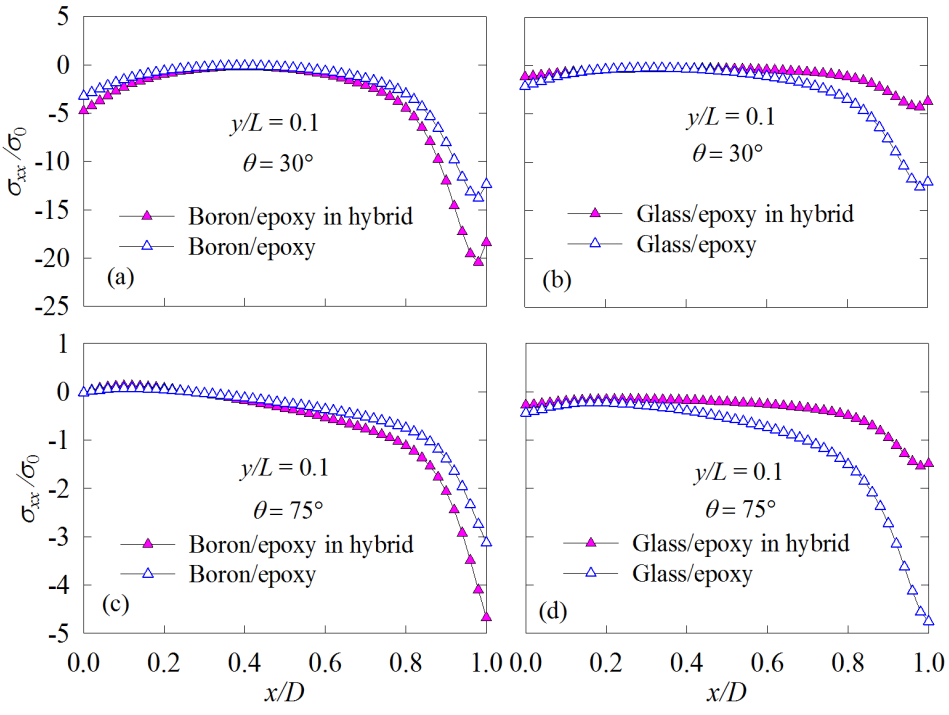

FIGURE 4. Distribution of lateral stresses at section, $y/L = 0.1$ of identical plies of different laminates.

solutions are however found to be conservative in terms of critical stresses, which, in turn, verifies the adequateness of the present computational approach in providing safe and economic design guides for thick hybrid beams.

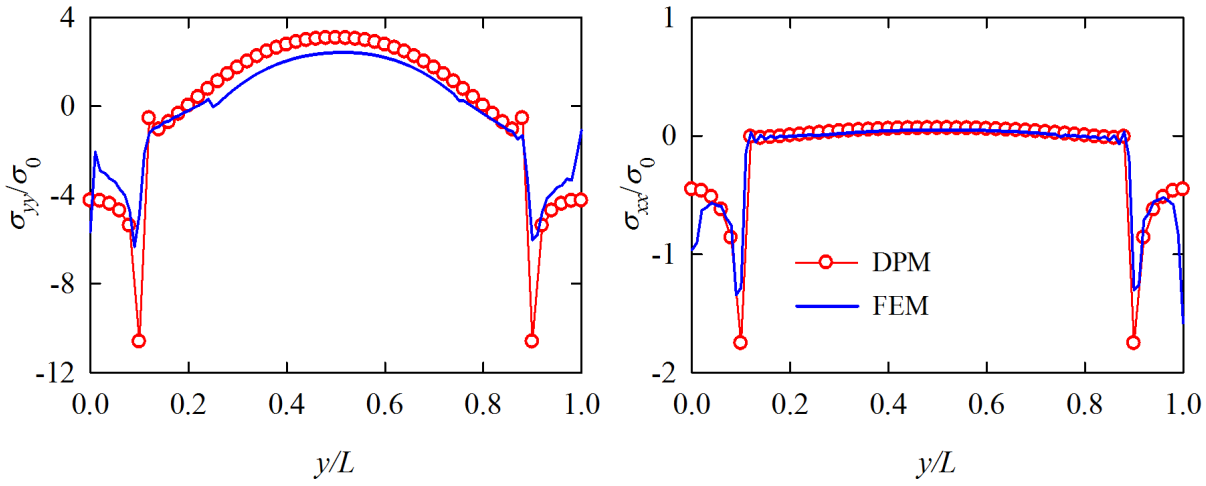

FIGURE 5. Comparison of stress distributions along the bottom surface of the boron/epoxy ply (75^o) of the hybrid beam under four-point bending.

CONCLUSIONS

The stress fields of the overall laminate as well as individual plies of a thick stiffened composite beam have been analyzed in the perspective of laminate hybridization. The effect of hybridization on the overall laminate stress is found to be nearly insignificant. However, the same is identified to be quite prominent in case of individual ply stresses, especially around the terminal points of the supporting region. Moreover, this effect of hybridization on ply stresses is further found to be influenced significantly by the orientation angles of fibers in individual plies of the laminate.

REFERENCES

[1] C. C. Chamis and R. F. Lark, "Hybrid composites state-of-the-art review: Analysis, design, application and fabrication," NASA Technical Memorandum TMX-73545 (NASA, 1979).
[2] T. W. Chou and A. Kelly, Annu. Rev. Mater. Sci. **10**, 229–59 (1980).
[3] S. Timoshenko and V. N. Goodier, *Theory of Elasticity*, 3rd ed. (McGraw-Hill, New York, 1979).
[4] T. W. Chou, "Mechanical behavior of hybrid composites, emerging technologies in aerospace structures, structural dynamics and materials," Tech. Rep. (American Society of Mechanical Engineers, New York, 1980).
[5] M. Koli and K. Chandrashekhara, Composite Science and Technology **44**, 354–361 (1996).
[6] U. K. Mallela and A. Upadhyay, Thin-walled structures **44**, 354–361 (2006).
[7] Y. X. Zhang and C. H. Yang, Composite Structures **88**, 147–157 (2009).
[8] A. Masud and M. Panchandeh, Journal of Engineering Mechanics **125**, 1115–1124 (1999).
[9] K. Biswal and A. Gosh, Journal of Engineering Mechanics **53**, 161–171 (1994).
[10] S. R. Ahmed and P. Modak, Applied Mathematics and Computation **258**, 465–482 (2015).
[11] P. Modak and S. R. Ahmed, Procedia Engineering **105**, 940–945 (2015).
[12] R. M. Jones, *Mechanics of Composite Materials* (McGraw-Hill, New York, 1975).
[13] A. A. M. S. R. Ahmed and P. Modak, International Journal of Mechanical Sciences **78**, 140–153 (2014).

ICME2015

International Conference on Mechanical Engineering 2015
(ICME 2015) 18 – 20 December, 2015, Dhaka, Bangladesh

Paper ID : 526

Solution Treatment Effect on Tensile and Fracture Behaviour of Al-12Si-1Mg Piston Alloy

M. S. Kaiser[a)]

Directorate of Advisory, Extension and Research Services, Bangladesh University of Engineering and Technology, Dhaka- 1000, Bangladesh

[a)]Corresponding author: mskaiser@iat.buet.ac.bd

Abstract. The effects of T6 solution treatment on tensile, fracture and impact properties of heat-treated Al–12%Si–1%Mg cast alloys were investigated. Alloy was prepared by controlled melting and casting. Cast alloy was given precipitation strengthen treatment having a sequence of homogenizing, solutionizing, quenching and aging. Both cast and solutionized samples are isochronally aged for 90 minutes at different temperatures up to 300°C. Tensile properties of the differently processed alloys have been carried out to understand the precipitation strengthening of the alloy. Fractograpy of the alloys were observed to understand the mode of fracture. It is observed that the improvement in tensile properties in the aged alloys through heat treatment mainly is attributed to the formation of the nonequilibrium Mg_2Si precipitates within the Al matrix. Solution treatment improves the tensile strength for the reason that during solution treatment some alloying elements are re-dissolved to produce a solute-rich solid solution. Impact energy decreases with ageing temperature due to formation of GP zones, $\beta^{/}$ and β precipitates. The fractography shows large and small dimple structure and broken or cracked primary Si, particles. Microstructure study of alloys revealed that the solution treatment improved distribution of silicon grains.

Keywords: Aluminium-silicon alloys, solutionizing, precipitation, fractography

INTRODUCTION

The use of Al-Si-Mg alloys in particular for automotive industry is attractive due to light weight and reasonable strength after ageing treatment [1]. The heat treatment of age hardenable aluminum alloys involves solutionizing the alloys, quenching, and then either aging at room temperature or at an elevated temperature [2-3]. The enhancement in mechanical properties after thermal treatment has largely been attributed to the formation of non-equilibrium precipitates within primary dendrites during aging and the changes occurring in Si particles characteristics from the solution treatment. The age hardening response depends on the fraction size, distribution and coherency of precipitates formed [4-6]. The influence of heat treatment on the mechanical properties including hardness and tensile strengths is also well studied, while the influence on plastic deformation behavior and elongation to fracture is less studied.

In the paper, is to present a study of the influence of solution treatment on the tensile, fracture and impact energy of the Al-12Si-1Mg piston alloy and to find out the area of their optimal values.

EXPERIMENTAL DETAILS

Melting was carried out in a resistance heating furnace under the suitable flux cover (degasser, borax etc.). In the process of preparation of the alloy the commercially used aluminium pistons were taken. The final temperature of the melt was always maintained at 750±15°C. Casting was done in cast iron metal moulds preheated to 200°C.

Mould sizes were 16 x 150 x 300 in millimeter. The alloy was analysed by wet chemical and spectrochemical methods simultaneously. The chemical composition of the alloy is given in Table 1. A portion of the cast alloy was homogenized in a Muffle furnace at 400°C for 18 hours and air cooled to relieve internal stresses. The homogenized samples was solutionized at 530°C for 2 hours followed by salt ice water quenching to get a super saturated single phase region. The cast and solutionized alloys were subjected to isochronal ageing for 90 minutes at different temperatures up to 300ºC. Tensile testing was carried out at room temperature in an Instron testing machine using cross head speed to maintain the strain rate of 10^{-3}/s. The samples used were according to ASTM specification. For impact test, standard sized of 10 x 10 x 55 mm have a V-shaped notch, 2 mm deep with 45° angle specimens were used. Testing was performed in accordance with ASTM E23. Tensile and Impact toughness were determined five test pieces at each test. Specimens of the cast and heat treated alloys were subjected to optical metallographic studies. The specimens were polished with alumina, etched with Keller's reagent and observed under a Versamet-II Microscope. Fractographic observations of the surfaces fractured by tensile testing were carried out by a Jeol Scanning Electron Microscope type of JSM-5200.

Table. 1: Chemical Composition of the Experimental Alloy (wt%)

Si	**Mg**	**Cu**	**Ni**	**Fe**	**Mn**	**Ti**	**Zr**	**Al**
12.280	0.919	1.120	1.306	0.521	0.038	0.061	0.001	Bal

Remarks: Alloy 1 (as cast) and Alloy 2 (solution treated)

RESULTS AND DISCUSSION

Tensile properties

The variation of ultimate tensile strength under various ageing conditions of the cast alloy 1 and solution treated alloy 2 are shown in Fig. 1. The test values obtained at a strain rate of testing 10^{-3} s^{-1} are used to plot the graphs. It can be found that the double aging peaks are present for both the alloys and attain the higher strength. In the ageing process of the alloys, GP zones and metastable phases can effectively strengthen the alloys and lead to the aging peak. In the early stage of aging, fine and profuse GP zones homogeneously distribute in the matrix and then their effects on strengthening are significant. On the other hand, metastable phases formed at the inter-mediate stage of aging and kept semi-coherence with the matrix are effectively resistant to the movement of dislocation, thus have certain strengthening effect. However, these GP zones remarkably dissolve before metastable phase formation in precipitation sequence of the alloy. It has been reported that the θ phase had been observed to have nucleated on dislocation [7]. Therefore these plate-like metastable phases nucleated and grown up on dislocation at the expense of fine and uniformly dispersed GP zones. In the stage of transition from GP zones to metastable phases, the number of GP zones decreases significantly for dissolution, while the metastable precipitates have not grown up and the size of them are too small to effectively resist the movement of dislocation. Therefore, the ageing effect of alloy must be low at this stage and it can be presumed that the stage of GP zones dissolution should be responsible for the aging value between two aging peaks of the alloys. At the final stage of ageing the strength decreases due to over ageing as well as precipitation coarsening.

Fig. 2 clearly delineates that improvement in yield strength of the alloys due to ageing is more than that for ultimate strength. Thus with the progress of ageing yield tensile ratio increases. Material toughness is related to this ratio. It is known that yield strength is a structure sensitive property of the material and hence formation of fine precipitates is more responsive to yield strength. Fig. 3 demonstrates the variation of elongation percent with ageing temperatures of alloys. The occurrence of ductility minima at the peak aged condition is easily understandable. This is reflected in the form of minimum percent elongation of the alloys aged whence the density of fine precipitates is maximum. However, the solution treated alloy shows higher strength. During solution treatment at 530°C for two hours, some alloying elements are re-dissolved to produce a solute-rich solid solution. It is to maximize the concentration of strengthening elements including copper, zinc, magnesium, silicon etc. in the solid solution. On the other hand the cast alloy is slowly cooled from an elevated temperature, alloying elements precipitate and diffuse from solid solution to concentrate at the grain boundaries, small voids, on undissolved particles, at dislocations, and other imperfections in the aluminum lattice [3].

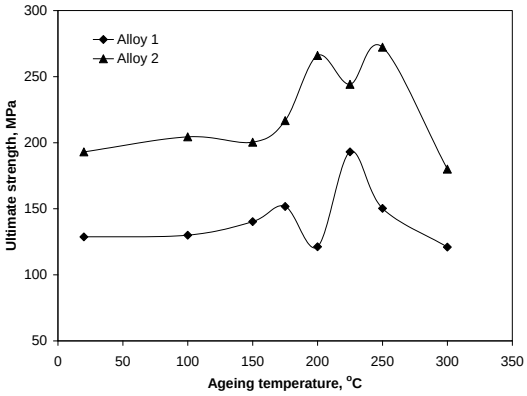

FIGURE 1. Variation of ultimate tensile strength with ageing temperature of cast and solution treated alloys isochronally aged for 90 minutes.

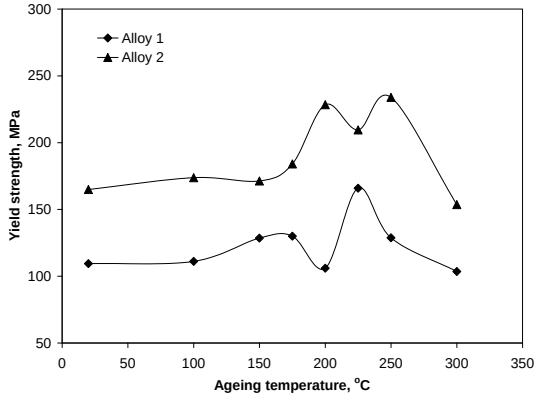

FIGURE 2. Variation of yield strength with ageing temperature of cast and solution treated alloys isochronally aged for 90 minutes.

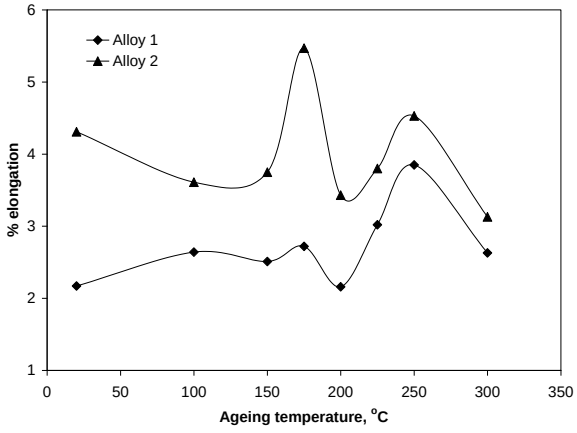

FIGURE 3. Variation of percent elongation with ageing temperature of cast and solution treated alloys isochronally aged for 90 minutes.

Impact properties

Figure 4 shows the impact toughness properties of the cast alloy 1 and solution treated alloy 2 at different ageing temperature. It is observed that the impact energy decreases with ageing temperature. This observation may be attributed to the precipitation of both Al_2Cu and/or Al_2CuMg and Mg_2Si phases, leading to a significant increase in the matrix strength at the expense of ductility. The absorbed energy decreased a maximum due to the precipitation of intermetallic phases at peakaged condition. The variation impact strength of alloy 1 is very small with increase in aging due to lower volume fraction of precipitates. The maximum decrease in absorbed energy for solutionized alloy 2 was observed in the aged condition because of higher volume fraction of precipitates. The impact energy increases significantly from peakaged to overaged due to microstructure softening at over ageing temperature [8]. But in case of cast alloy 1 is slowly cooled from an elevated temperature, alloying elements precipitate and diffuses from solid solution to concentrate at the grain boundaries, small voids, on undissolved particles, at dislocations and other imperfections in the aluminum lattice.

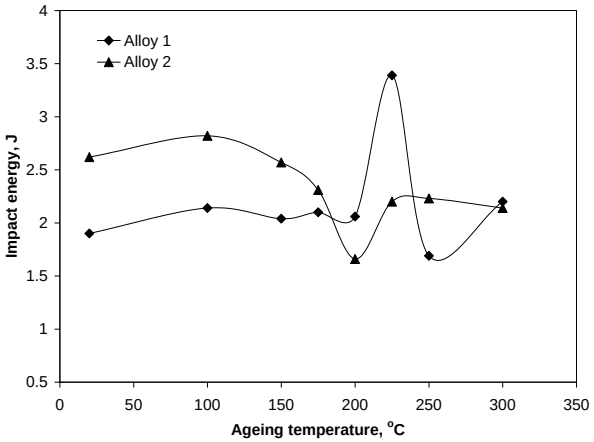

FIGURE 4. Variation of impact energy with ageing temperature of cast and solution treated alloys isochronally aged for 90 minutes.

Optical micrographs

The optical microstructure of cast alloy 1 and solution treated alloy 2 aged at 225°C for 90 minutes are shown in Fig. 5a and 5b respectively. The microstructure of this alloy includes alpha phase (aluminum), eutectic silicon and particles of the intermetallic compounds, which were reported to be Mg_2Si, Al_4CuNi, Al_9FeNi, Al_6Cu_3Ni and Al_3Ni etc. In the as-cast alloy, the eutectic silicon of thin plates and the large particles of the intermetallic compounds mainly exist between the aluminum grain boundaries or the dendrite arms. After T6 treatment, the silicon particles were rounded but agglomerated, and the sizes of the particles of the intermetallic compounds slightly decreased. However, they still existed at the grain boundaries. As observed in a previous work it contains uniformly distributed silicon particles in the Al matrix of fine equiaxed grains [9]. After artificial ageing treatment at 225°C for 90 minutes, precipitation occurred within the matrix but the precipitates cannot be revealed by optical microstructure.

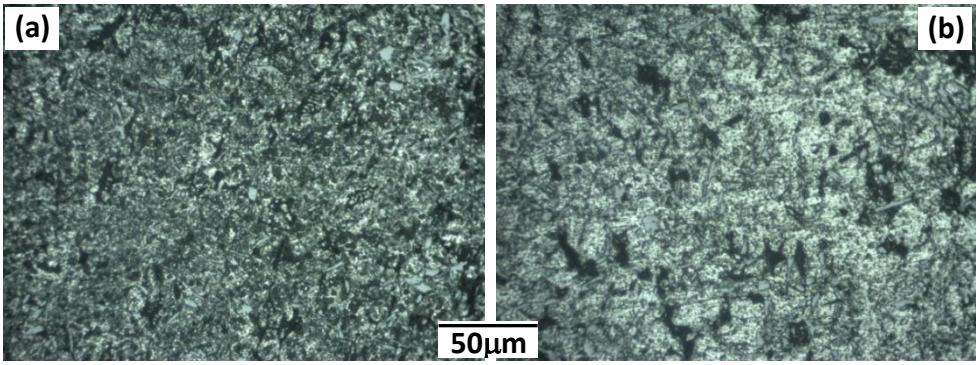

FIGURE 5. Microstructure of the alloys age at 225ºC for 90 minutes a) cast and b) solution treated

Scanning Electron Microscopy

Fig. 6 a) and b) show the fracture surface of the alloys aged at 225ºC for 90 minutes of as cast and at solution treated condition respectively. The fracture surfaces appear the mixed (ductile and brittle) fracture for the alloys at peak aged condition. This indicates that the fracture was ductile fracture in the Al matrix and brittle in the primary Si particles. The dimples are neither uniform nor circular in shape. The matrix-intermetallic particles decohesion is also observed for the alloys. The fracture mechanism is ductile, involving the nucleation, growth, and coalescence of voids in the matrix around the intermetallic particles. The voids grow under both the applied load and the influence of local plastic constrain until a coalescence mechanism is activated and this followed by the total failure of the alloys. The solution treated alloy 2 shows relatively small dimple structure and broken or cracked primary Si, particles. The morphology of the microstructure changed obviously after T6 heat treatment. The irregular eutectic phase was converted into fine spheroidized Si particles uniformly distributed in the Al matrix. Similar result was reported in literature of semi solid casting of A356 [10].

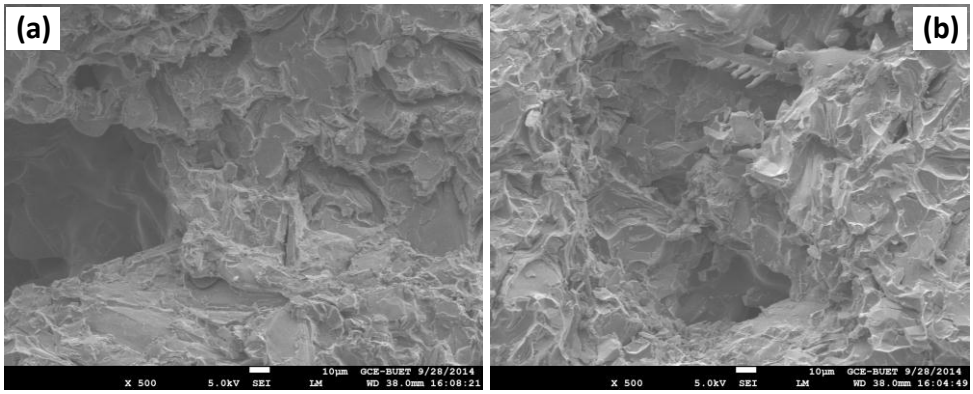

FIGURE 6. SEM fractograph of the alloys a) cast and b) solution treated, aged at 225ºC for 90 minutes and tensile tested at strain rate of $10^{-3}s^{-1}$

CONCLUSIONS

The double aging peaks are present for both the cast and solution treatment alloys. In the ageing process GP zones and metastable phases can effectively strengthen alloys and lead to the aging peak. Impact energy decreases with ageing temperature due to formation of GP zones, $\beta^{/}$ and β precipitate. Solution treatment improves the strength because during solution treatment some alloying elements are re-dissolved to produce a solute-rich solid solution.

The eutectic silicon was clearly fragmented and more spherical in solution treated alloy. The fractography shows large and small dimple structure and broken or cracked primary Si particles.

ACKNOWLEDGMENTS

This work is supported by CASR of Bangladesh University of Engineering and Technology and is part of project "Effect of trace zirconium on the chemical, electrical, mechanical and physical properties of cast and heat treated aluminium-silicon piston alloy". Thanks to Department of Glass and Ceramics Engineering for providing the laboratory facilities.

REFERENCES

1. S. Thompson, S.L. Cockcroft, and M.A. Wells, Materials Science and Technology, **20**, 194-200 (2004).
2. M. Abdulwahab, I.A. Madugu, F. Asuke, O.S.I. Fayom and F.A. Ayeni, J. Mater. Environ. Sci. 4, 87-92 (2013).
3. A.M. Samuel, P. Ouellet, F.H. Samuel and H.W. Doty, AFS Transactions, **105**, 951-962(1997).
4. S. Saxena, C.H. Tyagi and S. Kumar, International Journal of Mechanical Engineering and Robotics Research, **3**, 706-715 (2014).
5. H. Sablonniere and F.H. Samuel, International Journal of Cast Metals Research, **9**, 195-211 (1996).
6. E. Sjolander and S. Seifeddine, La Metallurgia Italiana **11-12**, 39-43 (2012).
7. R.X. Li, R.D. Li, Y.H. Zhao, L.Z. He, C.X. Li, H.R. Guan and Z.Q. Hu, Materials Letters **58**, 2096–2101 (2004).
8. A. Hossain and A. S. W. Kurny, International Journal of Technology Enhancements and Emerging Engineering Reserarch **1**, 5-8 (2013).
9. L. Fang, Y. Fuxiao, Z. Dazhi and Z. Liang, Light Metals, Edited by Carlos E. Suarez, (The Minerals, Metals & Materials Society 2012), 35-38
10. R. Akhter, L. Ivanchev and H.P. Burger, Mater. Sci. Eng. **447**, 192-196 (2007)

International Conference on Mechanical Engineering 2015
(ICME 2015) 18 – 20 December, 2015, Dhaka, Bangladesh

Paper ID : 555

Effects of Substrate Mechanical Behaviour on the Thermal Cycling Life of the Microprocessor Components

Ahmad Shahedi Shakil[1, a)], Toufiq Rahman[1], Shah Alam[1], Mohammad Motalab[1], Jeffrey C. Suhling[2]

[1]*Department of Mechanical Engineering, Bangladesh University of Engineering and Technology, Dhaka, Bangladesh*
[2]*Department of Mechanical Engineering, Auburn University, USA*

[a]Corresponding author: shakil6791@gmail.com

Abstract. The modern trend is to decrease the size of microprocessor components. At the same time, the number of I/O of the silicon chip microprocessors have been greatly increased over the last few years, which means high BUS speed, high amount of heat generation and much more elevated temperature operation. Plastic ball grid array (PBGA) is one of the most widely used microprocessor components in electronic packaging industries. Due to the complex nature of the geometric configuration of the package, thermal stresses are developed inside the package which is the result of package temperature fluctuation. Also thermal stresses may develop when exposed to harsh environments where fluctuation of temperature may occur e.g. spaceship, automobile etc. As a result, the solder balls of PGBA may fail resulting in disconnection of signal to the processor. In our study, the microscopic view of cross section of some PGBA packages were observed. It was found that the copper layer thicknesses of substrates vary from package to package which causes the variation in mechanical properties of the Bismaleimide-Triazine (BT) substrate material. Results show that the variation of mechanical properties of the substrate layer in the microprocessor package significantly affects the thermal cycling life of lead free solder joints which means the number of cycles before failure of the package.

INTRODUCTION

Modern microprocessors are often exposed to harsh environments where these are subjected to extreme change of temperatures. Finite element simulations of Accelerated Life Testing (ALT) for the PBGA assemblies are normally performed using thermal cycling, where the test assemblies are subjected to harsh changes in temperature over a much shorter period of time than the expected field exposure of the parts. This process also allows the determination of various characteristics of the packaging architecture during its life cycle, i.e. critical locations, failure modes, stress levels, etc. For the accurate prediction of the life of the PBGA packages, it is important to use the correct mechanical properties of the constituent materials. Furthermore, variation of the mechanical properties of a constituent material may also result in the variation of the life of the package. The orientation of different layers in a typical microprocessor is shown in Figure 1. The substrate material is placed just above the solder ball layer. These solder balls are also attached to the printed circuit board (PCB) at the bottom side (not shown in figure). During thermal cycling, the deformation and failure of the solder balls largely depends on the mechanical properties of the different materials of the package. From package to package, due to the variation in package architecture,

orientation of copper layers in the substrate are largely varied, which leads to the variation of the mechanical behaviour of the substrate material.

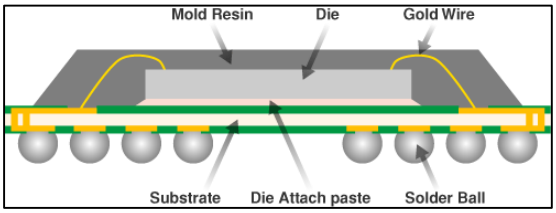

FIGURE 1. Schematic Diagram of PBGA Package.

Many researchers have investigated the stress, strain, and life to failure for a wide variety of microprocessors. Yanga, et al., [1] investigated the thermal stress and strain of Plastic Ball Grid Array (PBGA) for reliability evaluation and failure analysis. A one-eighth model is built to estimate the thermal stress and strain of PBGA under thermal cycling temperature (0°C–100°C). The results show that the maximum equivalent stress and equivalent plastic strain occur in the second outer solder joint and close to the position of chip. Yi, et al.,[2] on their paper provided a design and material selection guideline for a plastic ball grid array (PBGA) package in order to improve its reliability and manufacturing ability after post mold cure. Their study showed that the material properties such as modulus and CTE of molding compounds play an important role in warpages and reliability of PBGA packages. Lee, et al.,[3] presents a non-linear numerical study to investigate the effect of chip dimension and substrate thickness on the solder joint reliability of plastic ball grid array (PBGA) packages. Yuan, et al.,[4] showed that trace cracks in the substrate of a thin PBGA package were detected after temperature cycle testing during a product qualification. Numerical simulations with the finite element method were performed to investigate the impact of design parameters and material selection. Han,[5] investigated the thermo-mechanical behavior of a Flip Chip Plastic Ball Grid Array package assembly. The results reveal that the CTE of a substrate is one of the most critical design parameters to solder ball reliability. For the assembly with a relatively small chip analyzed in the study, a significant improvement of solder joint reliability is predicted by optimizing the CTE of the substrate.

This study has been performed to investigate how the predicted life of a PBGA microprocessor changes when there is variation in the mechanical properties of the BT-epoxy laminate (substrate) material. Also, an experimental procedure has been established to determine the actual mechanical properties of substrate materials by extracting tensile testing specimens from a real package. This gives the capability to check the vendor data for errors and to build a reliable model for the finite element analysis to accurately predict the life to failure due to accelerated life testing.

EXPERIMENTAL PROCEDURES

The PBGA components under current investigation became available from an anonymous motherboard. The intel® microprocessor on one of the PCBs is shown in Figure 2. Three test vehicles of the similar kind were selected for the experiments to measure the stress-strain data of the BT laminates of these packages. Initially the packages were separated from the motherboards using a precision cutting machine. After slitting the packages into two halves, one halves is allocated for microscopic analysis and another half is allocated for tensile testing. Figure 3 shows some of the processing stages of the PBGA components. The stress-strain properties of the BT substrate have been characterized using tensile specimens extracted from actual PBGA components. In this case, the PBGA components have been polished from the molding compound (top) side of the part until the die is exposed. The silicon was then removed using the etching process, and the remaining mold compound was polished away. This left only the BT laminate with attached solder balls. A second phase of polishing was then done to remove the solder balls and leave only the BT substrate, which could then be cut up into thin 31 mm × 3 mm × 0.6 mm tensile specimens.

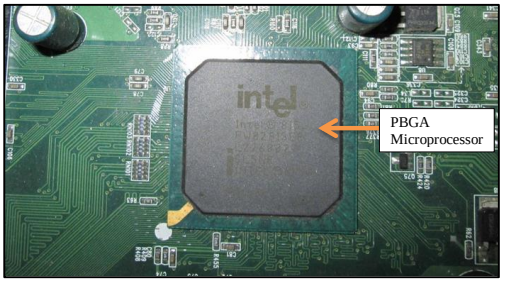

FIGURE 2. The test vehicle with the PBGA component.

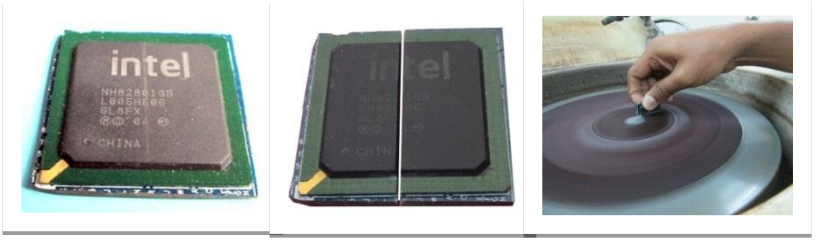

FIGURE 3. Processing of the PBGA component for the tensile testing of BT and for microscopic analysis.

Microscopic Analysis

Identification of different layers in the PBGA package and to determine their dimensions, microscopic analyses of the package cross section is performed. The results have been used in the finite element modeling of the package. Surface polishing is done for this purpose. Emery papers and velvet cloth rotator polishing machine were used for fine finishing of the cross section of the packages.After the polishing, the arrangements of different layers of the package are observed by an optical microscope. Figure 4 shows the cross section obtained from the microscope for package no. 1.

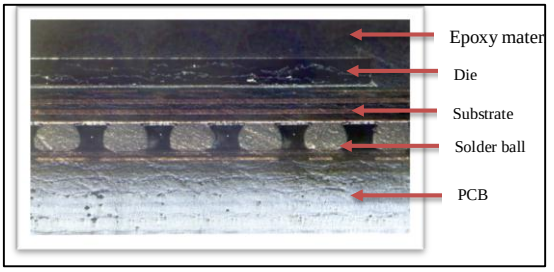

FIGURE 4. Cross Section of PBGA Microprocessor under the Optical Microscope.

Although the packages are identical in macroscopic observation but the substrates are different due to the differences in copper layer orientation. This leads to the variation of the mechanical properties of the substrate material from one package to other.

Tensile Test Results for Substrate Material

The stress-strain properties of the BT substrate have been characterized using tensile specimens extracted from actual PBGA components. Figure 5 shows the tensile test specimen. Tensile tests are done in Instron 2716-020 50KN testing machine. Stress-strain data were measured for each sample and modulus of elasticity was calculated from the curves.

The stress-strain curve for the substrate material extracted from different packages is shown in Figure 6. The elastic modulus, ultimate tensile strength, and the ultimate elongations are recorded from the test. The variation of the stress-strain curves in the substrate materials from three different packages can be visualized in Figure 6. As mentioned earlier, the differences are due to the variation in the orientation of copper layer in the substrate. The extracted values of the mechanical properties for all the specimens are listed in Table 1.

FIGURE 5. Tensile Test Specimen of the BT Substrate Material Extracted from PBGA Package.

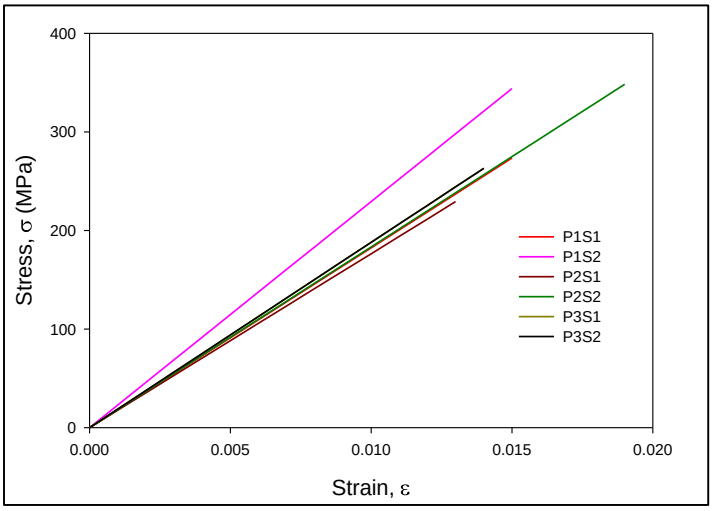

FIGURE 6. Stress-Strain Curves for the BT Substrate Materials from Different Packages.

Many manufacturers [6-9] are now producing the BT-epoxy substrate material for PBGA packages. As expected, wide variation of mechanical properties (i.e. elastic modulus, UTS, etc.) has been observed from the substrates made by different companies. The elastic modulus has been found as low as 13 MPa and as high as 28 MPa indicating large variations as shown in Figure 7.This range of elastic modulus has been used in the finite element simulations to investigate the effects of substrate elastic modulus on the microprocessor life. The CTE of the material was assumed as 0.3.

TABLE 1. Tensile Test Results of the BT Substrate Material

Package no	Sample no.	Load at max. load(kN)	Stress at max. load (MPa)	Modulus (Young) (MPa)	Strain at Max.Load (mm/mm)
1	1	.296939	164.966	18240	.014606
	2	.338005	187.781	22940	.014658615
2	1	.275922	153.290	17645	.013106
	2	.321650	178.695	18334	.0185
3	1	.325215	180.675	19776	0.015653846
	2	.287606	159.781	18800	.01387

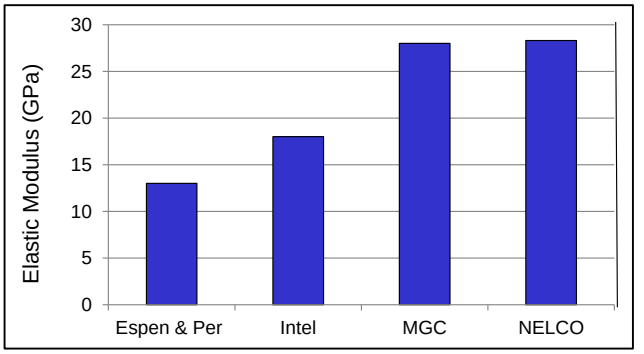

FIGURE 7. Variation of the Elastic Modulus of the BT Substrate Material Found in Literature [6-9].

Finite Element Modeling of PBGA Microprocessor

Three dimensional nonlinear finite element modeling of the anonymous microprocessor component has been used to calculate the accumulated strain energy dissipation per cycle in the solder joints as a result of thermal cycling between -40 to 125 ^{o}C. Figures 8(a) and 8(b) show the quarter symmetry model of the PBGA package that was developed and solved using ANSYS finite element software. The entire model utilized a structured finite element mesh with 650,450 elements and 703,110 nodes.

The quarter model has been appropriately constrained along the axes of symmetry, so that for a node in a symmetry plane, the displacement component perpendicular to the symmetry plane was required to be zer**o.** In addition, all three displacements were set to zero for the center node at the bottom surface of the PCB to prevent any rigid body motions. The entire assembly was subjected to a time dependent temperature distribution to reflect the -40 to +125 C thermal cycling performed in the life testing experiments. The ramp rate for this thermal cycling profile was 16.5 ^{o}C/min, and the high and low temperature dwell times were each 20 minutes. The stress-free temperature of the package has been assumed to be T = 220 ^{o}C, which is the solidification temperature of the lead free solder joints. The applied thermal loading including the cool down after solder joint reflow and the first several thermal cycles is shown in Figure 8(c).

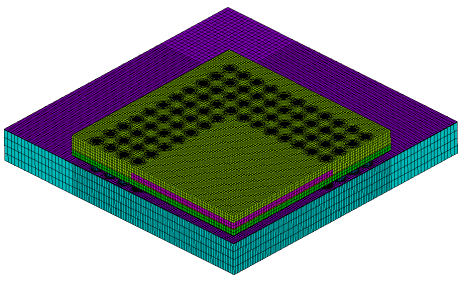

(a)

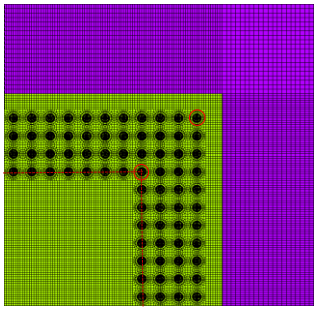

(b)

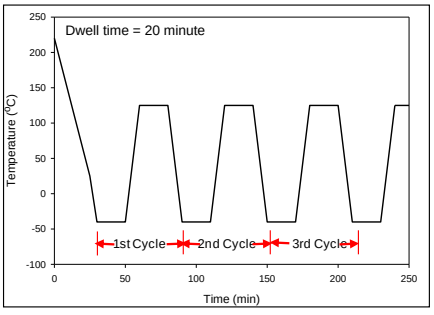

(c)

FIGURE 8. (a) Finite Element Mesh (Quarter Symmetry) (b) Top View Showing the Die Boundary and Probable Critical Solder Ball Locations (c) Applied Thermal Loading.

The solder balls were modeled in ANSYS with Solid185 structural elements with 8 nodes. This element is designed to solve both isochoric (volume preserving) rate-independent and rate-dependent large strain plasticity problems. For the other materials in the model, SOLID45 structural solid elements have been used, which are 8 node elements with plasticity, creep, large deflection and large strain capabilities. Iterative solution procedures have been used due to the nonlinear material and kinematic properties of the model. Typical solution run times were about 2 hours per thermal cycle using a workstation with quad core processor and 16 GB of memory. The solder balls have been modeled as viscoplastic material with the Anand model [10] .The properties of other materials have been used as listed in Table 2 [10].

TABLE 2. Room Temperature Material Properties used in the PBGA Model [10]

Material	Elastic Modulus (GPa)	Poisson's Ratio	CTE (ppm/C)
PCB	Ex = 16.90 Ey = 7.44 Ez = 16.90	PRxy = 0.39 PRyz = 0.39 PRxz = 0.11	CTEx = 14.5 CTEy = 67.2 CTEz = 14.5
Solder Mask	3.1	0.30	16.3
Copper Pad	128	0.34	17
Die Attachment Adhesive	1.5	0.35	65 ($T < T_g$) 200 ($T > T_g$) T_g = 60 °C
Die	169	0.28	2.54

FEA Simulation Results

For all analyses, the critical solder ball in this PBGA assembly was found to be the diagonal ball located near the corner of the package. The volume averaged inelastic energy dissipation ΔW = PLWK (plastic work) accumulated per cycle is often taken to be the metric for damage accumulation and failure of solder joints. Following Che, et al. [11], the outer ring of elements in the top two rows were used to calculate ΔW for the third thermal cycle. Figure 9 shows the mesh plot of the critical solder joint with the ring elements. It has been observed that the finite element analysis predicts the maximum plastic energy dissipation near the top right side of the critical solder joint. This is in agreement with the origination of crack in a similar package that is also shown in Figure 9 according to Lamaye, et al.[12], The effects of substrate elastic modulus on the calculated accumulated inelastic energy dissipation values are shown in Figure 10. It has been found that the inelastic energy dissipation increases by about 25% in the critical solder joint when the BT elastic modulus changes from 28 to 16 GPa.

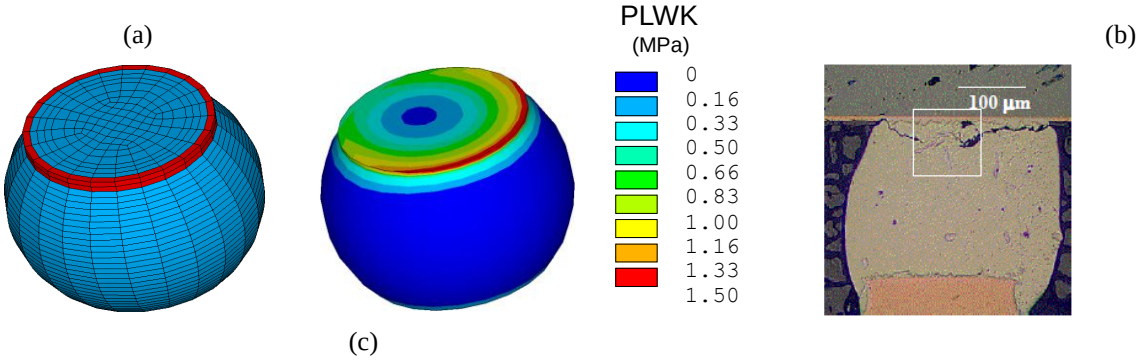

FIGURE 9. (a) Finite Element Mesh of a solder ball and the elements used for PLWK calculation (b) Contours of PLWK in the Critical Solder Joint (c) Crack Propagation in a PBGA Solder Ball [12].

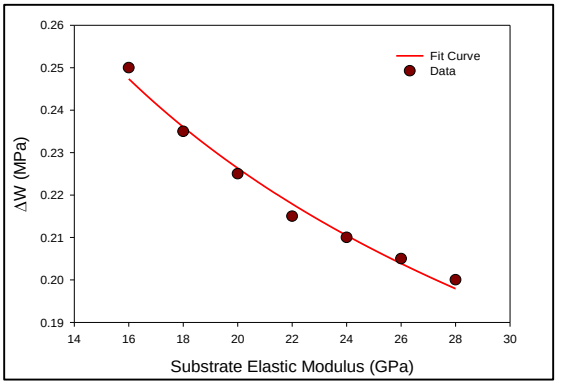

FIGURE 10. Variation of Plastic Energy Dissipation per Cycle with Substrate Elastic Modulus.

Darveaux [13] has presented energy dissipation based models for life prediction in solder joints subjected to cyclic loading.

$$N_i = K_1 (\Delta W)^{K_2} \tag{1}$$

$$\frac{da}{dN} = K_3 (\Delta W)^{K_4} \tag{2}$$

Where N_i is the number cycles to crack initiation, da/dN is the crack growth rate (assumed constant) occurring after crack initiation, ΔW is the energy dissipation per cycle in the solder sample (e.g. critical solder ball), and K_1, K_2, K_3, and K_4 are fitting constants that are used from Motalab, et al. [10] assuming non-aged configuration. Once the crack location and path are known in the solder joint, the number of cycles to failure can be estimated using:

$$N_f = N_i + \frac{a_c}{\left[\frac{da}{dN}\right]} \tag{3}$$

Where N_f is the number of cycles to failure, a_c is the length of the fully developed crack at failure/fracture, and N_i and da/dN are calculated from ΔW using eqs. (1-2).

The thermal cycling life of the PBGA assemblies can now be predicted for different values of substrate elastic modulus. Using the procedure described above, the thermal cycling life of the PBGA component has been calculated and the results are plotted in Figure 11. It has been found that the life of the solder joint decreases by about 60% when the BT elastic modulus changes from 28 to 16 GPa.

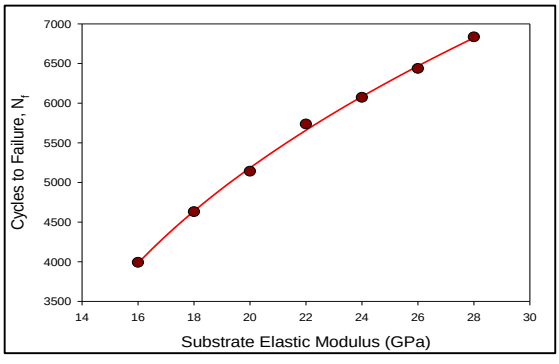

FIGURE 11. Variation of Cycles to Failure with Substrate Elastic modulus.

CONCLUSION

The effects of elastic modulus of the BT substrate material on the thermal cycling life (life of solder balls) of the PBGA (plastic ball grid array) microprocessor have been investigated in this research. For the accurate prediction of the life of the PBGA packages, it is important to use the correct mechanical properties of the constituent materials. The properties of the substrate material are very important in calculating solder life since the BT layer lies just above the solder balls. A wide variation of the elastic modulus (13~28 GPa) of substrate material for PBGA packages has been observed from the archival data. Also, a procedure has been established to extract the tensile test specimen of the substrate from the real processor assembly, which can help to check the vendor data for errors. Experimental results show that there is significant variation of the BT elastic modulus in the three identical PBGA packages mainly due to the differences in copper orientation in the substrate layers. Finite element simulation of the thermal cycling tests of the PBGA packages have been performed and the results show that the plastic energy dissipation (damage accumulation) in the critical solder ball increases by 25% if the elastic modulus of BT changes from 28 to 16 GPa. Also, the life of the critical solder ball decreases by 60% when the BT elastic modulus changes from 28 to 16 GPa, suggesting large degradation in solder life.

REFERENCES

1. Ping Yanga, JieGonga, HaiyingYangb&Xiushen Tang, Journal of Thermal Stresses **37(9),** 2014.
2. Sung Yi and Tatiana. M .Lam, Microelectronics International, Vol. 29 Issue: 3, pp.163 – 171, ISSN: 1356-5362.
3. S.W. Lee and J.H. Lau, *Circuit World* **23(1),** 16 – 19, (1997)
4. Yuan Yuan and Carpenter, B.J, "Trace Crack in Molded Thin Substrate Package, Root Causes and FEM Modeling", *Fifth International Conference on Electronic Packaging Technology Proceedings*, 2003. ICEPT 2003. Page(s): 449 – 454.
5. Bongtae Han, "Effect of Substrate CTE on Solder Ball Reliability of Flip Chip PBGA Package Assembly", *Surface Mount International 1996 Proceedings.*
6. EspenHaugan, Per Dalsjo, "Characterization of material properties of two FR4 printed circuit board laminates", *Norwegian Defence research establishment*, 2014.
7. http://www.mgc.co.jp/eng/products/lm/btprint/lineup/iccp.html
8. http://www.matweb.com/search/datasheet
9. http://www.intel.com/content/dam/www/public/us/en/documents/packaging-databooks/packaging-chapter-05-databook.pdf
10. Motalab, M., Basit, M., Suhling, J. C., Lall, P., "A Revised Anand Constitutive Model for Lead Free Solder That Includes Aging Effects." *Proceedings of InterPACK 2013*, pp. V001T05A009, San Francisco, 2013.
11. Che, F., X., Pang, J. H. L., Xiong, B. S., Xu, L., Low, T. H., "Lead Free Solder Joint Reliability Characterization for PBGA, PQPF and TSSOP Assemblies," *Proceedings of the 55th IEEE Electronic Components and Technology Conference*, pp. 916-921, 2005.
12. Limaye, P., B. Vandevelde, D.Vandepitte, and B. Verlinden, Circuits Assembly **17(2)**, 68-75 2006.
13. Darveaux, R., "Effect of Simulation Methodology on Solder Joint Crack Growth Correlation*", Proceedings of the 50th IEEE Electronic Components and Technology Conference*, pp. 1048-1058, 2000.

ICME2015

International Conference on Mechanical Engineering 2015
(ICME 2015) 18 – 20 December, 2015, Dhaka, Bangladesh

Paper ID : 563

Score-Stove™ Performance with Modified Resonating Tube Shape and Layouts

Md M Hossain[1, a)], M I Malek[1, b)], Md Ehsan[1, c)] and P H Riley[2]

[1]*Department of Mechanical Engineering, Bangladesh University of Engineering and Technology, Dhaka-1000, Bangladesh.*
[2]*Department of Electrical Engineering, University of Nottingham, Nottingham NG7 2RD, United Kingdom*

[a)]Corresponding author: mhossain.anik@gmail.com
[b)]mishrat150@gmail.com
[c)] ehsan@me.buet.ac.bd

Abstract. An electricity-generating stove using thermo-acoustic phenomena was introduced by SCORE team UK in 2007 and later a modified version of the stove was adopted by BUET SCORE team in 2013 which could use both pressurized kerosene burner and wood. The prototype was first tested in the laboratory and then demonstrated to potential end users in several rural communities. The feedback from the stakeholders showed great interest towards electricity generating stoves but identified – stove size, longer cooking time, cost of the stove and maintenance issues to be challenges needed to be addressed to make it truly feasible for use in Bangladesh. Further research is being carried out in these aspects to improve the acceptability of this new technology. This paper states the work carried out in order to reduce the overall dimensions of the stove in which orientation of the resonating tubes play a major part. The straight PVC pipes of original design were replaced by corrugated flexible PVC pipes in order to make the stove compact and space efficient. Corrugated flexible pipes give more flexibility in layout design with small change in resonance characteristics. After parametric study and successive test runs, suitable orientation layouts for corrugated flexible pipes were identified, without much compromising the stove performance. Use of the flexible piping and fixed angle PVC bends could successfully reduce the overall stove dimensions as well as improve compactness and aesthetics of the stove. Incorporating the present findings in Score-Stove design could improve its feasibility and acceptability to the end users

INTRODUCTION

Over one third of the total population of world use biomass like wood, animal wastes, agricultural residues for cooking, heating and lighting and about one sixth of the population are deprived from electricity grid [1]. In a developing country like Bangladesh the situation is even more serious. Only about 8% of total population of Bangladesh have access to the natural gas for cooking and remaining others depend on fuels like - kerosene, LPG and biomass. About 50% of the population still have no access to the electricity grid. ScoreStove™ which was built by a consortium of UK universities, offered a unique solution that the stove would be used for cooking and simultaneously be able to produce 5-20 Watt of electricity. Such small scale power generation could be useful for applications like mobile phone and LED light charging, typically in rural regions without grid electricity. Following that ScoreStove™version Demo-2.1 was successfully built by a team from Department of Mechanical Engineering, BUET. The original design was modified by the BUET team based on the popularity existing stoves and availability of fuels like wood and kerosene. Although ScoreStove™2.1 was designed to be used particularly within individual households,

it was found to be much more potential for small tea-stalls and restaurants in rural regions where stoves are kept burning continuously for a long period of time. Laboratory testing and subsequent field demonstrations were encouraging and created lot of enthusiasm among end-users, however they revealed a number of shortcomings of the current state of the stove design. These could be listed as follows:

Overall dimension: Current stove dimension was too large for most of the end users. The orientation and length of resonance tubes compromised the compactness of the design and movement flexibility during cooking.

Water condensation problem in the resonance air tube: It caused reduction in the linear alternator performance and required regular maintenance issues.

Sealing and higher pressurization of air: These factors are related to increasing the electric power generation but would require using more expensive materials, increasing the stove cost.

Longer cooking time: Flue gas passes through the thermo-acoustic engine convolute first and then flows to the cooking surface giving lower temperature and relatively longer cooking time. Reorientation of the design could induce less compromise on cooking time.

After conducting a number of test run and analyzing the performance with different layout on ScoreStove™ 2.1 the "CHA-WALA" version, this paper proposes ideas to overcome the first problem of the current model of ScoreStove™.

Nomenclature

AHX	Ambient Heat Exchanger	PVC	Poly Vinyl Chloride	TBT	Thermal Buffer Tube
HHX	Hot Heat Exchanger	TAE	Thermo-Acoustic Engine	WBT	Water Boiling Test

BACKGROUND AND WORKING PRINCIPLE

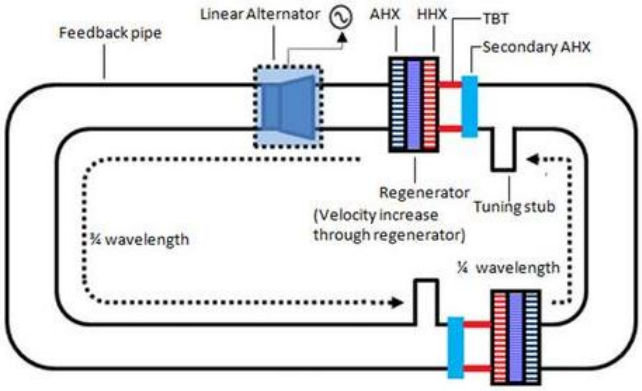

FIGURE 1(a). Functional diagram of ScoreStove

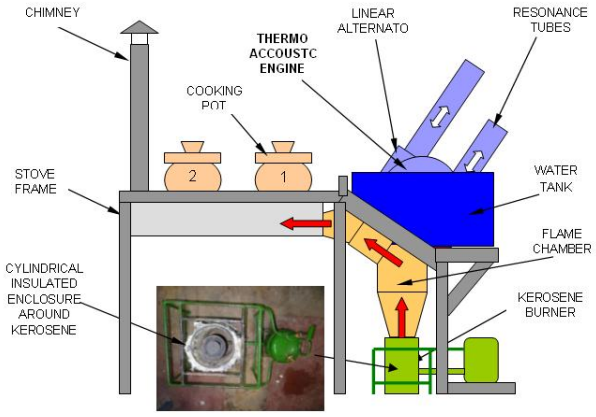

FIGURE 1(b). Schematic of "Cha-Wala" version of ScoreStove

Byron Higgins (1777) first documented the thermoacoustic phenomenon. A century later, Lord Rayleigh explained the phenomenon qualitatively [2] in 1878. The formal theoretical study of thermoacoustics started by Kramers in 1949 when he generalized the Kirchhoff theory of the attenuation of sound waves at constant temperature to the case of attenuation in the presence of a temperature gradient. From then until the 1990's others progressed understanding until progress became much more rapid through the theoretical work and the practical realisations lead by Swift at Los Alamos laboratories [3,4]. The thermo acoustic phenomena has been successfully applied into electricity generating stoves of various configurations [5,6,7,8] using waste heat of cooking.

Fig. 1(a) above shows the basic components of a dual full wavelength, looped tube traveling wave engine as used in the Score-Stove™.In a thermoacoustic engine, heat is supplied from a source to a gas (air in Score-Stove) via the

hot heat exchanger (HHX), heat is removed via the ambient heat exchanger (AHX) and the gas undergoes repetitive thermal expansion and rarefaction to produce acoustic energy (fig.1a). Between the HHX and AHX is a porous material called a regenerator, with a temperature gradient across it, to sustain a resonant acoustic wave and a linear alternator within the closed loop converts the acoustic wave into electricity. In the field trial Score-Stove design the linear alternator was implemented using a low-cost loudspeaker working in reverse. The SCORE team in Department of Mechanical Engineering, BUET successfully built, tested and demonstrated modified ScoreStove^{TM} versions with technical assistance from SCORE team of University of Nottingham in 2012-13. The basic stove design described in reference [6,7] was modified in two ways [8]. Firstly, the TAE working gas was pressurised and secondly, the waste heat from the TAE was used to pre-heat water for cooking called the "Cha-Wala" version (fig.1b). This paper describes follow up work regarding air resonance tube dimensions to reduce the special volume occupied.

METHODOLOGY OF MODIFYING SCORE-STOVE

The problem of larger space occupied by the Score-Stove was significantly contributed by the long length and orientation of the resonance tubes. To reduce the dimensions of the ScoreStove^{TM} two PVC pipes of the resonator were replaced by corrugated flexible PVC pipes. These pipes could be compressed to almost half of its initial length and expandable to 1.3 times of its initial length and could be bent in any direction with a wide range of radius of curvatures. A set of sensitivity tests were carried out in order to optimize the pipe length, with corrugated outer (1 cm per corrugation) and almost smooth inner surface and 8.5 cm inner diameter, as available in the market. The configuration was further reduced in space occupied by introducing bends with the corrugated PVC pipes. A set of sensitivity tests were carried out to optimize among – flexible pipe curvature, 90 degree and 120 degree PVC bends (fig.2). Finally, test runs with two different optimized layouts were conducted and results analysed to assess their space occupation requirement with cooking and power generation performance.

FIGURE 2. Replacing straight PVC tubes with corrugated ones and use of bends to reduce space occupied.

The length of the corrugated pipes was first calculated on the basis of same internal air volume with respect to the present configuration. First a set of tests were carried out to optimize the tube lengths of both the long and the shorter resonance studs for maximizing electric power generation. Second the effect of curving the optimized pipe lengths was studied. Curving the flexible pipes allowed reduction of volume occupied. It was observed that use of bends at the joints ahead of the corrugated pipes could change the flexibility of configuration significantly. Hence third, a set of tests were carried out to study the effect of the use of 90 degree and 120 degree PVC bends with flexible pipes, on stove performance. The findings of these three sets of tests resulted in optimized tube configuration layouts as shown in fig. 3(a), 3(b) and 3(c). These three layouts were finally tested and analyzed to evaluate the reconfigured ScoreStove performances.

(a)

(a)

(b)

(b)

(c)

(c)

FIGURE 3. Three different layouts with (a) PVC pipe (layout 1), (b) flexible pipe with 120O bends (layout 2) and (c) flexible pipe with 90O bends (layout 3)

RESULTS

Optimization of Resonance Stud lengths and Pipe Curvatures with Corrugated Pipes

Test run for one hour was performed and levels of electric power generated were recorded with variation of corrugated pipe (8.4 cm diameter) lengths for both the short-pipe and long-pipe studs. Results showed that the highest power level was achieved with 25cm of short-pipe and 58cm of long-pipe length as shown in fig. 4(a). The optimised corrugated tube lengths were 6 cm shorter for the short-pipe and 12 cm shorter for the long-pipe compared to present straight PVC pipes of 6.8 cm diameter.

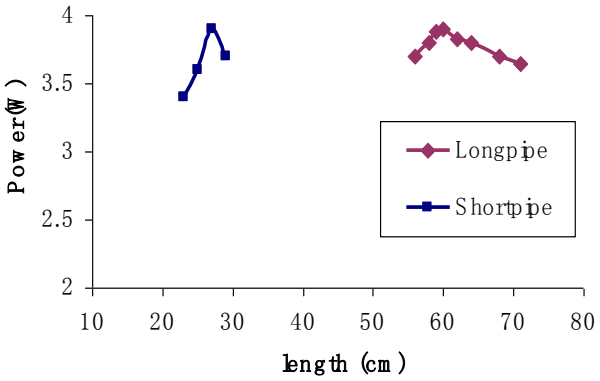

FIGURE 4(a). Optimization of corrugated stud lengths

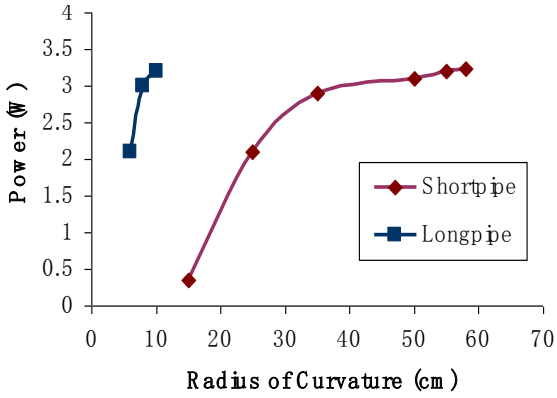

FIGURE 4(b). Optimization of corrugated pipe curvatures

One way of reducing the volume occupied by the studs could be achieved by curving them as far the corrugation allowed. However, this could affect the performance as the resonance condition for sound wave travel inside the tube would change, which was studied. As shown in fig.4(b) both tubes showed drop of performance as their radius of curvatures were reduced (sharper bends). The short-tube was very sensitive to change in curvature but the long-tube showed less variation of power generation with change of corrugated pipe curvatures up to a radius of 35 cm.

Optimization of pipe lengths with Bends

During the study an alternative way of reducing volume occupied by stud-pipe orientation was tried out. PVC bends available in the market with 90° and 120° angles could be used at the base of the stud-tubes. Using the bends allowed significant reduction in space occupation as the pipes could be redirected with much less need of curving their corrugations. The pipe lengths were optimized for maximum power generation for both tubes. The pipe lengths were optimized for maximum power generation for both tubes. The optimized values were not far different for 90° and 120° bends as shown in figure 5(a) and 5(b).

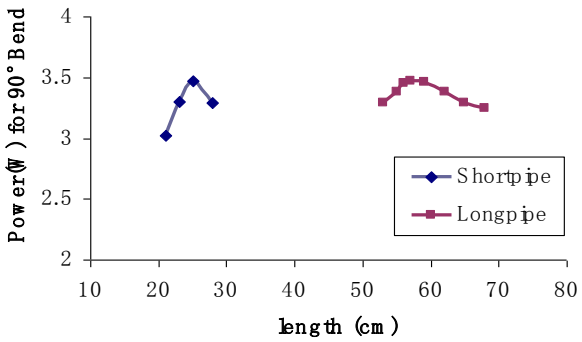

FIGURE 5(a). Optimization of corrugated stud lengths(90°)

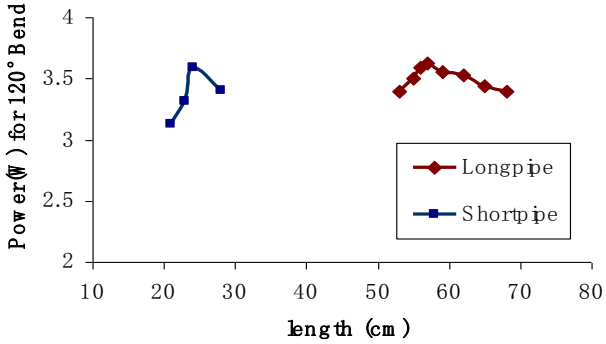

FIGURE 5(b). Optimization of corrugated stud lengths(120°)

Comparisons of power and peak pressure among three layouts

Based on the findings of the test runs for optimized pipe lengths, corrugation curvature radius and use of bends, three different configuration layouts were tested for score-stove performance for one hour runs. The thermal performance of the stove did not vary significantly with the change of optimized stud-pipe orientations (table-2). However, the electrical power generation and peak pressure attained were found to vary with the change of pipe orientations. The variations observed were checked against the error band of for measurement inaccuracy as shown in figure 6(a) and 6(b). Measurement error was estimated to be around ±3 % of the value for power measurement and around ±1% of the value for pressure measurement. For both reoriented layout-2 and layout-3 power and pressure were found to be decreased to some extent compared to the current layout-1. However, they offered significant saving in overall space occupied. The frequency of resonance was very similar (64Hz) for all three configurations.

Analysing the results revealed that layout-2 with optimized pipe lengths, curvatures a 120° bends showed about 5% reduction of electric power generation but saving 72% special volume occupancy compared to the current protruding studs. Layout-3 with optimized pipe lengths, curvatures a 90° bends showed saving of more than 78% special volume occupancy compared to the current layout but electric power generation was reduced by over 14%. Reducing special volume occupation of the tubes may increase the cooking convenience and improve the overall packing efficiency of the Score-Stove, with some compromise in electrical performance. However, availability of the three alternative layouts could allow more flexibility to the stove designers according to the customer requirement.

TABLE 1. Comparisons of reduction of power and occupied space

Configuration	Occupied Volume Over Cooking Area (m^3)	Steady State Power (W)	% Reduction In Volume	% Reduction In Power
Layout 1	0.572	4.1	-	-
Layout2	0.161	3.9	71.8%	4.9%
Layout3	0.124	3.5	78.2%	14.4%

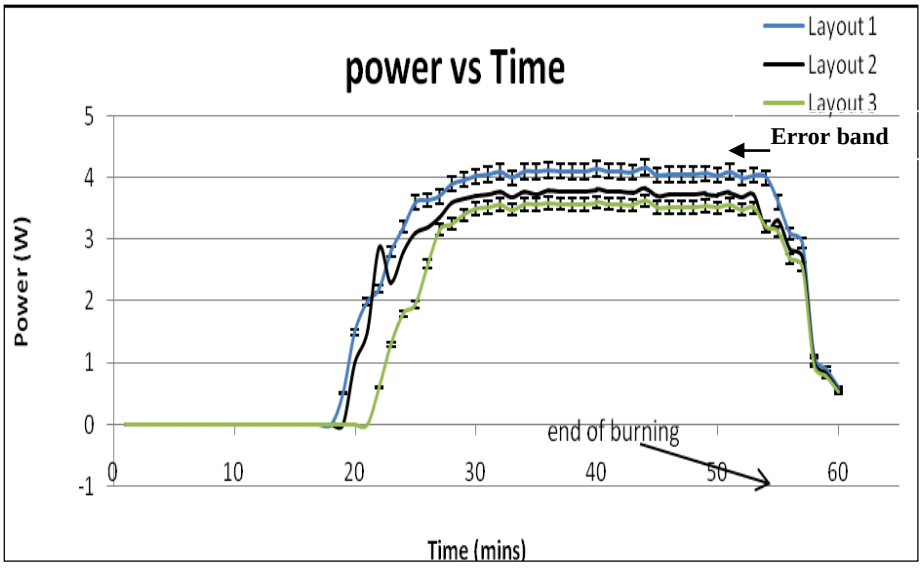

FIGURE6(a). Comparison of power generation with time among three layouts.

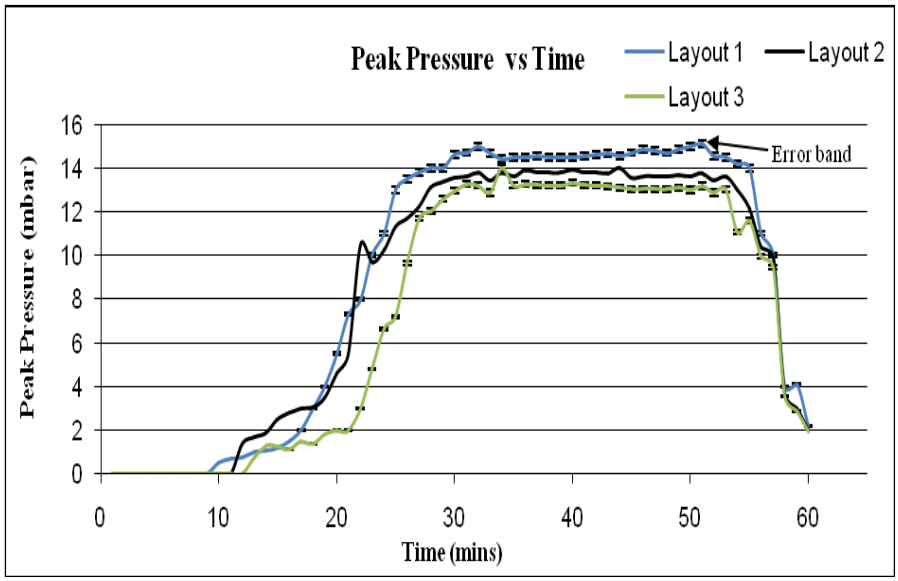

FIGURE6(b). Comparison of peak pressure during resonance with time among three layouts.

Energy Balance

Changes of resonance tube layouts were found not to affect the thermal performance of the stoves and the heat balance significantly. Some minor changes were observed in the heat flow which may be caused due to variations in kerosene burner flame shape and change of ambient condition. Water content of kerosene fuel is typically small and was neglected during the analysis. A typical distribution of energy during a water boiling test is given in table-2 below, about 11% of the energy spent was really used for boiling water and electric power generation is a very small part of the whole energy scenario. However, this could have significant implication in places where there is no electricity.

TABLE 2. Energy balance for test run of 54 minutes

INPUT ENERGY COMPONENT		**Component Share**
Burning of Fuel, 54 min, Room Tem 26°C	0.34 litres (0.272 kg)	
Burning efficiency Considered	95 %	
Input heating Rate	3372 W	
Input heat Energy during WBT test	10925 kJ	100 %
ENERGY CONSUMPTION COMPONENT (WBT 80°C, after 54 Min)		
Heat absorbed by Boiling Water(convection + evaporation in 2 pots)	1147.6KJ	10.58%
Heat absorbed by Cooling Water	1216 kJ	11.13%
Heat lost with Exhaust Gases	1112.9 kJ	10.18%
Heat loss from Cooking Pot	775 kJ	7.1%
Heat Loss From Water Tank	171 KJ	1.6%
Heat loss from Hot Stove surface	1805.76 KJ	16.5%
Heat loss from Chimney surface (open)	387 kJ	3.5%
Radiation heat loss from Exposed Flame	948KJ	8.68%
Heat absorbed by Metallic Mass (estimated, 90 kg)	810 kJ	16.1%
Energy as sound (Considering 5% alternator efficiency)	154.625 kJ	1.5%
Unaccounted Energy losses	1427 kJ	13 %

CONCLUSIONS

Score Stove^{TM} operation using re-oriented resonance tubes was possible using corrugated flexible PVC piping and bends. After parametric study of stove performance with - tube size, radius of curvature and bend angle two prospective configurations of tube layouts were identified. Both layouts showed significant reductions in special volume occupation, mostly affecting the overall vertical dimension. However, this was associated with small decrease of electric power generation compared to the current design. The thermal performance of the stove did not change significantly for any of the configurations. So resonance tube layouts could be optimized based on end user requirement, without compromising the stove performance significantly.

REFERENCES

1. www.worldenergy.org/work-programme/strategic-insight/global-energy-scenarios/ (2015).
2. J Lord Rayleigh, Nature, Lond. **18**, 319 (1878)
3. Swift, GW, J. Acoust. Soc. Am. 84: 1145–1180. doi:10.1121/1.396617 (1988).
4. Backhaus, S. & Swift, GW., Journal of the Acoustical Society of America **107**, 3148-3166 (2000).
5. Dennis, R. & Pullen, K. R. Development of a wood-fired cooking stove to incorporate a thermo-acoustic engine-generator unit. Proceedings of the Institution of Mechanical Engineers, Part A: Journal of Power and Energy, 227(7), pp. 740-751. (2013)
6. Riley, P.H, Journal of Applied Energy **132**, 308–316 (2014).
7. Riley, P.H., Saha, C., and Johnson, C.M., "Designing a Low-Cost, Electricity Generating Cooking Stove", Technology and Society Magazine IEEE, summer 2010. [Digital Object Identifier 10.1109/MTS.2010.937029, 1932-4529/10/ © IEEE 2010.
8. Ehsan Md., Sarker M., Mahmud R., Riley P. H., Journal of Power and Energy Engineering **3**, 458-466 (2015).

ICME2015

International Conference on Mechanical Engineering 2015
(ICME 2015) 18 – 20 December, 2015, Dhaka, Bangladesh

Paper ID : 565

Constitutive Modeling of the Human Anterior Cruciate Ligament (ACL) Under Uniaxial Loading Using Viscoelastic Prony Series and Hyperelastic Five Parameter Mooney-Rivlin Model

Souvik Chakraborty[a)],Debabrata Mondal[b)],Mohammad Motalab[c)]

Dept. of Mechanical Engineering, Bangladesh University of Engineering & Technology (BUET), Dhaka-1000, Bangladesh

[a)] Corresponding author: souvik919@gmail.com
[b)] debabrata.mondal5832@gmail.com
[c)]mtipuz@yahoo.com

Abstract. In this present study, the stress-strain behavior of the Human Anterior Cruciate Ligament (ACL) is studied under uniaxial loads applied with various strain rates. Tensile testing of the human ACL samples requires state of the art test facilities. Furthermore, difficulty in finding human ligament for testing purpose results in very limited archival data. Nominal Stress vs. deformation gradient plots for different strain rates, as found in literature, is used to model the material behavior either as a hyperelastic or as a viscoelastic material. The well-known five parameter Mooney-Rivlin constitutive model for hyperelastic material and the Prony Series model for viscoelastic material are used and the objective of the analyses comprises of determining the model constants and their variation-trend with strain rates for the Human Anterior Cruciate Ligament (ACL) material using the non-linear curve fitting tool. The relationship between the model constants and strain rate, using the Hyperelastic Mooney-Rivlin model, has been obtained. The variation of the values of each coefficient with strain rates, obtained using Hyperelastic Mooney-Rivlin model are then plotted and variation of the values with strain rates are obtained for all the model constants. These plots are again fitted using the software package MATLAB and a power law relationship between the model constants and strain rates is obtained for each constant. The obtained material model for Human Anterior Cruciate Ligament (ACL) material can be implemented in any commercial finite element software package for stress analysis.

INTRODUCTION

The knee ligaments, among other ligaments of the human body, are of greater interest because of their greater vulnerability. The Anterior Cruciate Ligament (ACL) will be the focus of our current study since it is more prone to injuries than any other knee-ligaments and recent studies show that almost 46% of the ligamentous injuries involve the ACL [1]. The ACL is crucial for stabilization of the knee as it connects the femur to the tibia and prevents any anterior motion of the tibia in relation to the femur. Certain movements put more strain on the ACL and when this strain becomes too large the ligament tears and such tearing of the ACL can require surgery depending upon the intensity of the injury and can also lead to more severe problems such as osteoarthritis as the patient gets aged [2].

It is very much complex to analyze the mechanical behavior of the ligament, by disintegrating the ligament into fibers, and analyzing the effects of load on each fiber, though each fiber particularly carries the load at different levels and there are variations in the number of completely straightened fibers with the increase of loading [4]. However, due to the complexities involved and lack of available literature and data, analyzing the mechanical behavior of the ACL disintegrating it into the comprising fibers is omitted in our present study. So, all through this study, the loading and mechanical behavior of the ligament is considered as a bulk. Figure 1 shows the picture of the major knee ligaments including the anterior cruciate ligament. It also demonstrates the wavy pattern of the collagen fibers while unloaded or mildly loaded, and subsequent straightening upon loading and finally tearing when the load exceeds the failure limit.

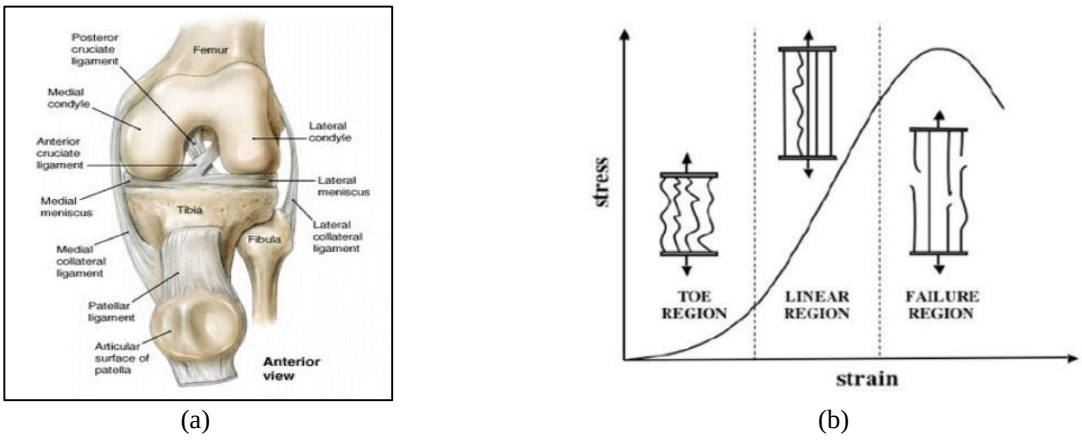

(a) (b)

FIGURE 1. (a) Knee Ligaments and the Anterior Cruciate Ligament (b) Typical ligament stress-strain relationship [3]

Under typical uniaxial loading the mechanical behavior of ligamentous tissue is nonlinear like other soft connective tissues. There are three distinct regions in the stress-strain curve: the "toe" region, the linear region, and the failure region, and they correlate the different structural changes occurring in the tissue during uniaxial loading [3, 5, 6, and 7]. Ligament stiffness and strength depend on collagen fibers. The tissue becomes less compliant as the load increases, and the collagen fibers straighten out and the curve of mechanical response tends to be linear. It is assumed that the collagen fibers start to break gradually until the ligament completely tears at the final stage. In our analysis the mechanical behavior of the Human Anterior Cruciate Ligament (ACL) is studied both from the viscoelastic and hyperelastic point of view.

The objective of this study is to analyze the mechanical behavior of the Human Anterior Cruciate Ligament from the data obtained from the literature, using the viscoelastic Prony Series model and also using the hyperelastic Mooney-Rivlin model which is a very popular model to analyze rubber like materials. The viscoelastic analysis is performed using the viscoelastic curve fitting tool of ANSYS, which is proved to be a reliable tool for analyzing viscoelastic behavior in many studies, using the Prony Series model. The Hyperelastic analysis is performed using the Hyperelastic Curve Fitting tool of ANSYS using the popular Mooney-Rivlin model. The ultimate goal of the study will be to analyze the curve fitting results, both from viscoelastic and hyperelastic analysis, and then to determine which behavior, either viscoelastic or hyperelastic, best describes the mechanical behavior of the ligaments. Both the Prony series model for viscoelastic analysis and the Mooney-Rivlin model of hyperelastic analysis involve determination of set of constants. The scope of this study also includes the determination of the trend of variation of the constants with strain rates for the most promising model (Prony Series or Mooney-Rivlin) and plotting them. These plots have also been used to propose a set of empirical equations for the model constants that can be used for any finite element simulation software like ANSYS that supports these constitutive models.

.

Stress-Strain Data for Human ACL

For our analysis we required reliable stress-strain data for Human Anterior Cruciate Ligament (ACL) since we need to provide instantaneous shear and bulk modulus (evaluated from strain rate) as an input for the viscoelastic analysis using the Prony series model in ANSYS. Also we need to provide the stress-strain data as input for the Hyperelastic analysis using the using the Mooney-Rivlin model for each individual strain rate. The effect of the strain rate on the stress-strain curves has been demonstrated with anterior cruciate ligament[8], tendon[9], the intrinsic and extrinsic wrist ligament [15], incisor periodontal ligament [16],and inferior glenohumeral ligament [10].

A study by D.P Pioletti et al. [11] attempted to develop a realistic three-dimensional viscoelastic constitutive law which takes into account the strain rate effect in soft tissue [11]. Results of tensile tests made on human anterior cruciate ligaments (ACL) were used for the identification of the constitutive law. The tests were performed under controlled temperature (37°C) and humidity (100%) at four different rates of elongation (0.3, 6, 9 and 12 mms^{-1}). The stress-strain data are shown in Fig.2. In this study, we have used these stress-strain curves and

extracted the data out of the curves using a software package. The rejuvenated data are used as input for the ANSYS curve fitting tools to extract the model constants for the constitutive models.

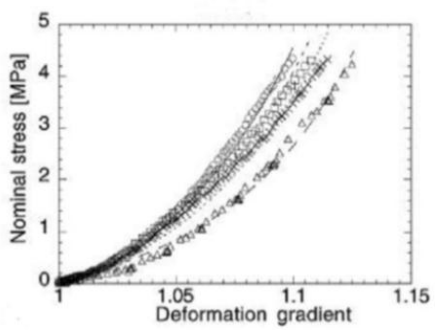

FIGURE 2. Experimental and theoretical stress-strain curves obtained at four different rates of elongation for one human ACL specimen. (¤) exp.(—) theory. 12 mms^{-1}; (□)exp. (---) theory.9 mms^{-1}; (×) exp.(- -)theory. 6 mms^{-1}; (Δ) exp. (-·-) theory.0.3 mms^{-1}[11].

VISCOELASTIC ANALYSIS WITH PRONY SERIES

The Generalized Maxwell Model (Prony Series) can be used in the modeling of more complicated viscoelastic materials. It consists of n Maxwell elements connected in parallel. An extra spring is added in parallel to represent the final (or equilibrium) modulus, E_∞ [12].

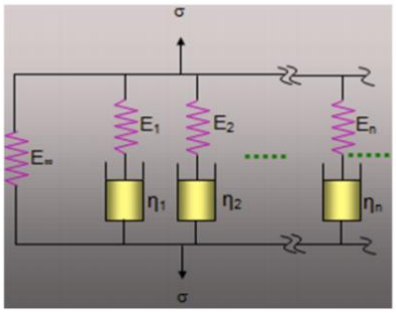

FIGURE 3. Schematic of Generalized Maxwell Model (Prony Series).

The three-dimensional constitutive equations for an isotropic linear viscoelastic material are-

$$\sigma_{ij} = \int_0^t 2G\,(t-\tau)\frac{de_{ij}}{d\tau}d\tau + \delta_{ij}\int_0^t K(t-\tau)\frac{d\Delta}{d\tau}d\tau \quad (1)$$

where σ_{ij} are the components of the Cauchy stress, e_{ij} are the deviatoric strain components, Δ is the volumetric part of the strain, G(t) and K(t) are the shear and bulk modulus functions, t and τ are current and past time, and δ_{ij} are the components of the unit tensor (Kronecker delta). The Prony series approach assumes:

$$G = G_\infty + \sum_{i=1}^{n_G} G_i \exp(-t/\tau_i^G) \quad (2)$$

$$K = K_\infty + \sum_{i=1}^{n_K} K_i \exp(-t/\tau_i^K) \quad (3)$$

G_∞, G_i = shear elastic moduli, K_∞, K_i= bulk elastic moduli, τ_i= relaxation time for each Prony component. Introducing the relative moduli:

$$\alpha_i^G = {}^{G_i}/_{G_0} \quad \text{and} \quad \alpha_i^K = {}^{K_i}/_{K_0}$$

and the instantaneous shear and bulk moduli: $G_0 = G_\infty + \sum_{i=1}^{n_G} G_i$ and $K_0 = K_\infty + \sum_{i=1}^{n_K} K_i$

The Prony series response functions can then be expressed by the following equations [12]

$$G = G_0\left[\alpha_\infty^G + \sum_{i=1}^{n_G} \alpha_i^G \exp(-t/\tau_i^G)\right] \quad (4)$$

$$K = K_0\left[\alpha_\infty^K + \sum_{i=1}^{n_K} \alpha_i^K \exp(-t/\tau_i^K)\right] \quad (5)$$

Shift Function

The William-Landel-Ferry (WLF) shift function which is used in this analysis specifies how the mechanical behavior of underfill changes with respect to temperature [12]. It is of the form-

$$log_{10}(A) = \frac{C_1(T-T_r)}{C_2+(T-T_r)} \quad (6)$$

Where C_1, C_2 = Material constants, T = Temperature at time t, T_r= Base temperature.

Prony Series Constants and Their Meanings

The curve fitting in ANSYS using Prony Series delivers the outputs by providing values of the Prony Series Constants after sufficient number of iterations. The constants along with their meanings are tabulated in Table 1.

TABLE 1. Prony Series Constants and their meanings [12]

Constants	Meaning
α	Relative Modulus
t	Relative Time
T_{ref}	Relative Temperature
C_1, C_2	WLF Constants

Viscoelastic Curve Fitting results using Prony Series Model in ANSYS

Viscoelastic curve fitting was done using the Prony Series model in ANSYS. For each set of stress-strain data, the time dependent shear modulus data and the time dependent bulk modulus data are listed and used for the ANSYS curve fitting tool. The sequential procedures for the Prony series viscoelastic curve fitting in ANSYS are described below:

The experimental data need to be given as a plain text file delimited by a space or a comma. The data can be read in the form of GUI or via batch commands, as a plain text file. The data includes Prony series expansion of shear and/or bulk moduli as well as shift function. The supported shift functions include WLF (Williams-Landel-Ferry) and TN (Tool-Narayanaswamy).

The Prony series viscoelastic curve fitting is a nonlinear least square regression analysis; the initial values of the model coefficients are selected in such a way to yield a good correlation between the fitted curve and the experimental data.

The curve-fitting results are written into the TB command format to the database for the finite element simulation using the viscoplastic constitutive law.

The curve fitting result for the data set of 12 mms^{-1} deformation rate is shown in Fig. next. Set of Prony Series Constants from the curve fitting results of 12 mms^{-1} deformation rate of Human ACL is tabulated in Table 2**.**

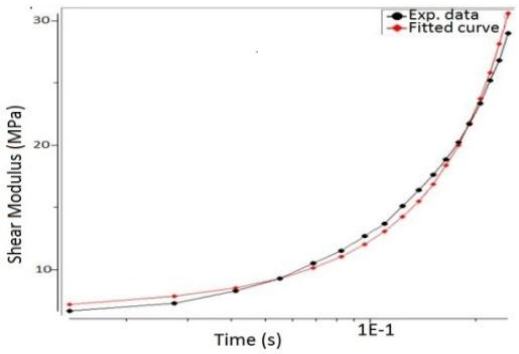

FIGURE 4. Viscoelastic Prony Series Curve Fitting results for Human ACL under deformation rate of 12mms^{-1}. The black line shows the experimental data and the red line shows the fitted curve.

TABLE 2. Prony Series Coefficients (model constants) under 12mms^{-1} deformation rate

Constant Index	Name of the co-efficient	Value of the co-efficient
1	A0 shear	0
2	A1 shear	2.5315
3	t1 shear	-0.1569
4	A0 bulk	-3.0884e-7
5	A1 bulk	6.5381
6	t1 bulk	-0.1569
7	A2 bulk	1.2575e-8
8	t2 bulk	-999.9976

The similar results are obtained for the other strain rates. The variations of the Prony series model constants with strain rates are also investigated. In order to implement the Prony series model including the strain rate effects, the relationship between the coefficients and the strain rates has be established. However, a trend could not be established for the variation of the model parameters with the strain rates that motivated the authors to reinvestigate the data using the hyperelastic Mooney-Rivlin model that is described in next section.

HYPERELASTIC ANALYSIS WITH FIVE PARAMETER MOONEY-RIVLIN MODEL

Mooney-Rivlin model is popular for modeling the large strain nonlinear behavior of incompressible materials. The expression for the Piola-Kirchhoff stress for the case of uniaxial deformation by the five parameter Mooney-Rivlin model is given by-

$$P_{1_{uniaxial}} = 2(1-\lambda^{-3})\left(\lambda C_{10} + 2C_{20}\lambda\left(I_{1_{uni}}-3\right) + C_{11}\lambda\left(I_{2_{uni}}-3\right) + C_{01} + 2C_{02}\left(I_{2_{uni}}-3\right) + C_{11}\left(I_{1_{uni}}-3\right)\right) \quad (7)$$

Here, C_{10}, C_{01}, C_{20}, C_{02}, and C_{11} are Mooney-Rivlin material parameters. They represent the material's distortion phenomena.

Hyperelastic curve fitting was done using the Five Parameter Mooney-Rivlin model in ANSYS. After providing the stress-strain data as input, the Mooney-Rivlin curve fitting tool fits the curve and generates values for these parameters after sufficient number of iteration for each strain rate. The stress-strain data for a particular strain rate are used to extract the model constants for that strain rate. Figure 5 shows the experimental stress-strain data of the human anterior cruciate ligament and their corresponding fit to the equation for the Mooney-Rivlin model given by equation (7). The fits are performed by the non-linear curve fitting tool in ANSYS and for the strain rates of 0.3mms^{-1}, 6mms^{-1}, 9mms^{-1}, and 12mms^{-1}.

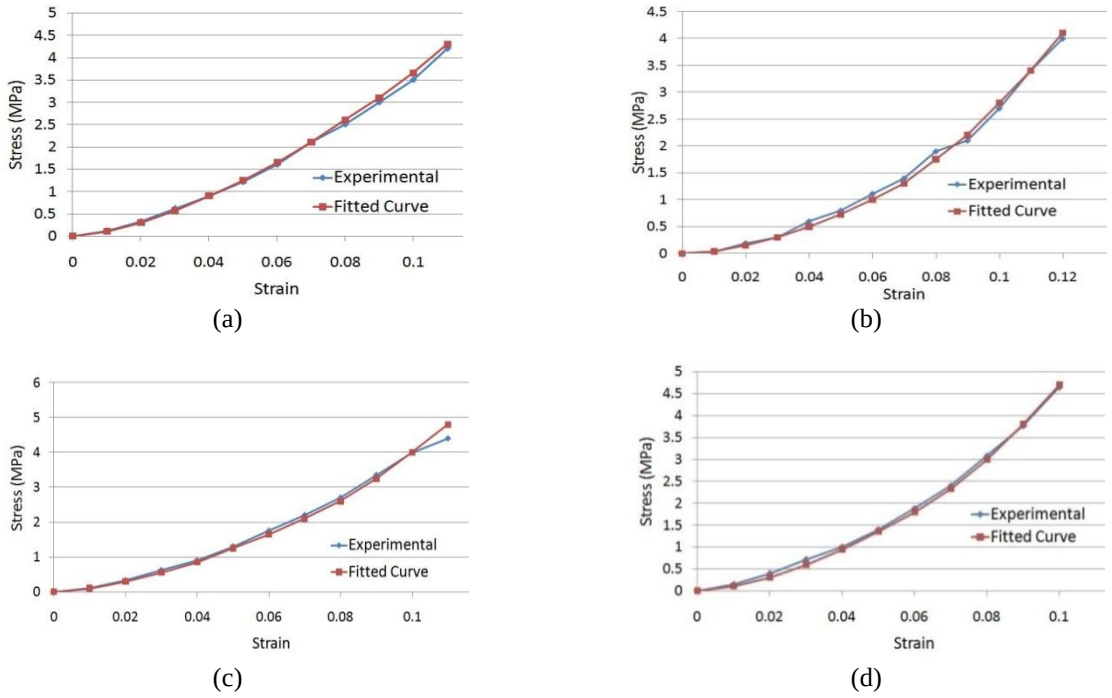

FIGURE 5. Hyperelastic Five Parameter Mooney-Rivlin Curve Fitting results for Human ACL under deformation rates of (a) 0.3mms^{-1} (b) 6mms^{-1} (c) 9mms^{-1}(d) 12mms^{-1}

For all the four strain rates, Fig. 5 shows very good correlation between the experimental data and the fitted curve. The extracted Mooney-Rivlin model parameters are C_{10}, C_{01}, C_{20}, C_{11}, and C_{02}. These parameters have been calculated for the four different strain rates and the results are given in Table 3.

TABLE 3. Variation of Mooney-Rivlin parameters with deformation rates.

Deformation Rate (mms^{-1})	Mooney-Rivlin Parameters				
	C_{10}	C_{01}	C_{20}	C_{11}	C_{02}
0.3	113.1961244	-113.49209	-8773.90940	20216.6831	-11710.52574
6	137.5552506	-136.69211	-18493.86825	41266.9744	-23146.82045
9	140.2683036	-139.41449	-32749.86026	71577.0164	-39247.71394
12	194.0035669	-192.99088	-56331.75471	123840.963	-68275.79384

The variation of each Mooney-Rivlin parameter is plotted and the curve fitting equation for the variation of each parameter with varying deformation rate is obtained using MATLAB. Figure 6 shows the variation of the model parameters with the deformation rates. The empirical equations with the coefficients for the dependence of the Mooney-Rivlin model parameters with the strain rates are given in Table 4.

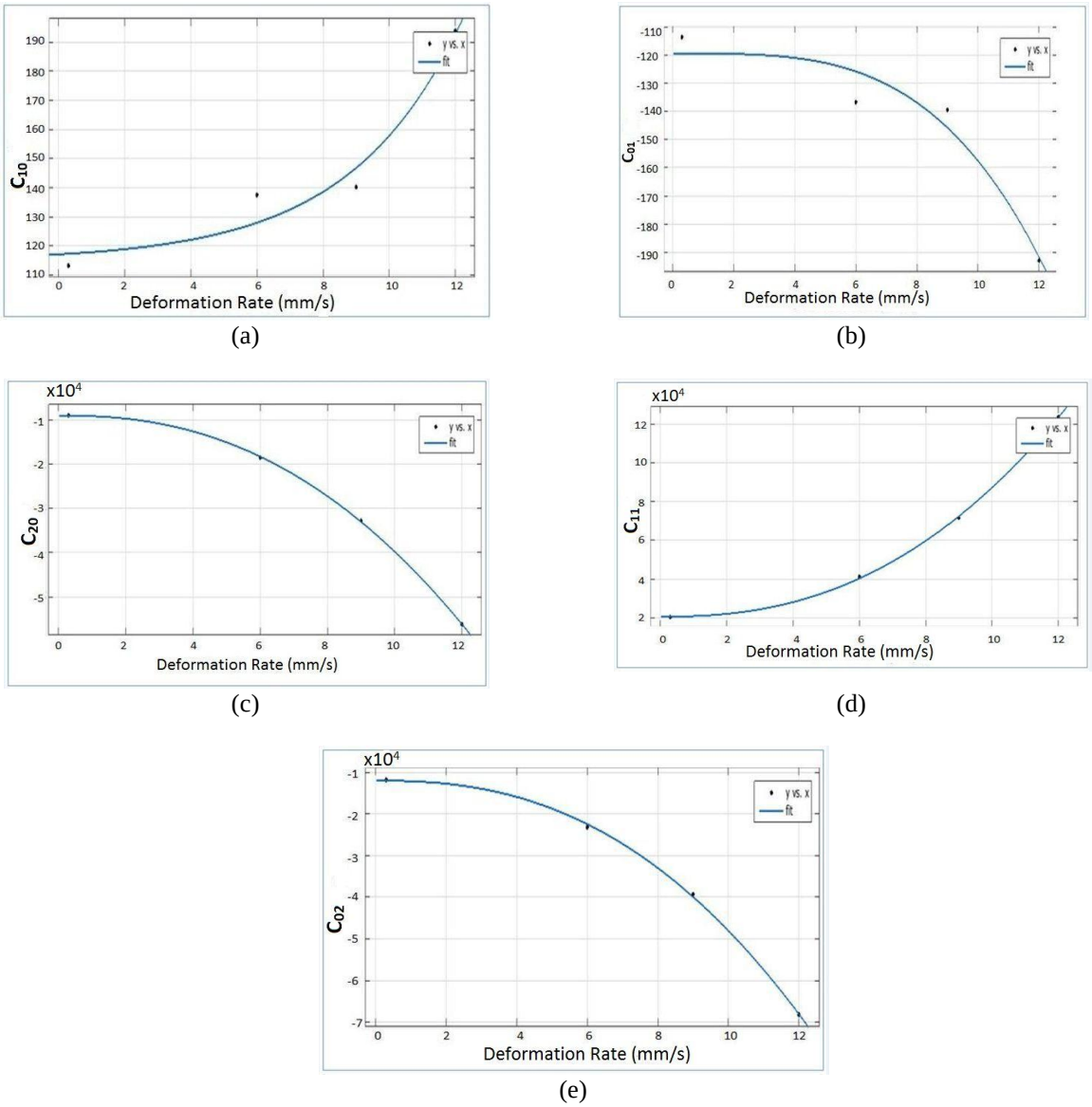

FIGURE 6. Variation of (a) C_{10}, (b) C_{01},(c) C_{20}, and (d) C_{11} (e) C_{02} with deformation rates.

TABLE 4. Curve fitting equation for Mooney-Rivlin parameters

Mooney-Rivlin Parameter for the human anterior cruciate ligament	**Equation for variation with strain rates (x = deformation rate)**
C_{10}	$C_{10} = 2.914e^{(0.2974x)} + 115$
C_{01}	$C_{01} = -0.01198x^{3.503} - 119.4$
C_{20}	$C_{20} = -140.4x^{2.343} - 8865$
C_{11}	$C_{11} = 276.5x^{2.383} + (2.054 \times 10^4)$
C_{02}	$C_{02} = -135.7x^{2.425} - (1.197 \times 10^4)$

The Five Parameter Mooney-Rivlin Model was largely used to analyze the mechanical behavior of rubber-like materials [13]. Also studies performed on hyperelastic analysis of ligaments [14] made us consider the Human ACL worth analyzing using the Hyperelastic Mooney-Rivlin model using five parameters. The curve fittings obtained using the Hyperelastic Five Parameter Mooney-Rivlin model in ANSYS appear to be highly conforming, since the

fitted curves closely follow the experimental curves for all deformation rates (Fig. 5) and the values obtained for the Mooney-Rivlin parameters display a smooth trend of variation with deformation rate- which implies that this constitutive model for the human anterior cruciate ligament is very promising for the finite element analysis.

CONCLUSION

There are enormous controversies about the mechanical behavior of the ligaments-whether they are viscoelastic or hyperelastic or a blend of both of these criteria. We analyzed the human Anterior Cruciate Ligament (ACL) from both viscoelastic and hyperelastic point of view. Many literatures defined ligaments as viscoelastic-which inspired us to perform the viscoelastic analysis using Prony Series. However, study revealed that the relationship between the Prony series coefficients and the strain rates for this constitutive model was very hard to establish. Rather, the hyperelastic analysis using the five parameter Mooney-Rivlin model provided good correlation between the experimental and predicted stress-strain curves. Furthermore, it was observed that the variation of the Mooney-Rivlin constants with strain rates was smooth and easier to establish the empirical equations that can be helpful in the finite element analysis of the human ACL using any commercial software (i.e. ANSYS) that supports the Mooney-Rivlin constitutive model. The derived expressions for the variation of the model constants with strain rates will be valid for a wide range of strain rates of $0 – 12$ mms^{-1}.

ACKNOWLEDGMENTS

We would like to thank Dr. Mohammad Abdul Motalab Tipu for his expert advice and encouragement throughout this difficult work. We are grateful to him for his patience in guiding us through all this way, helping us to overcome the difficulties we faced and for the inspiration he provided us relentlessly. We are beholden to him for his great patience in introducing us to ANSYS and other various necessary software packages, in which he holds a great expertise.We would also like to thank Dr.Nusrat J Chhanda, whose works and publications helped us to render a better projection on the various difficulties during this long process.

REFERENCES

1. S. Bollen,. British Journal of Sports Medicine **34(3),**227–228, 2000.
2. Tabatha Jordan Savage. Finite element analysis and modeling of the anterior cruciate ligament in the human knee. Thesis submitted to the faculty of the college of engineering and computer science, Florida Atlantic University Boca Raton, FL, December 2014.
3. Raffaella De Vita. Structural constitutive models for knee ligaments. School of Engineering. University of Pittsburgh, 2005.
4. Yang Liu, H.S Ramanath, Dong-A Wang., Trends In Biotechnology **26(4),** 201-209,(2008).
5. C. Hurschler, P. P. Provenzano, and R. Vanderby, Jr., Connective Tissue Research **44**,59–68(2003).
6. A. Viidik and R. Ekholm Z Anat Entwickl Gesch **127**,154–164(1968).
7. K. A. Hansen, J. A. Weiss, and J. K. Barton, Journal of Biomechanical Engineering, **124**,72–77(2002).
8. Kennedy, J.C., Hawkins, R.J., Willis, R.B., Danylchuk, K.D., Journal of Bone and Joint Surgery **58A**, 350-355 (1976)
9. Haut, R.C,. Journal of Biomechanical Engineering **105**,296-299(1983).
10. Ticker, J.B., Bigliani, L.U., Soslowsky, L.J., Pawluk, R.J., Flatow, E.L.,Mow, V.C., Journal Shoulder and Elbow Surgery **5**, 269-279(1996).
11. D.P. Pioletti, L.R. Rakotomanana, J.-F.Benvenuti, P.-F.Leyvraz. Journal of Biomechanics **31**,753-757(1998)
12. Nusrat J Chhanda.3D viscoelastic model for underfill material behavior. NSF Center for Advanced Vehicle and Extreme Environment Electronics. Auburn University.
13. Giovanni Berselli, Rocco Vertechy, Marcello Pellicciari and Gabriele Vassura (2011). Hyperelastic Modeling of Rubber-Like Photopolymers for Additive Manufacturing Processes, Rapid Prototyping Technology – Principles and Functional Requirements, Dr. M. Hoque (Ed.), ISBN: 978-953-307-970-7
14. E. Peña, B. Calvo, M.A. Martínez, M. Doblaré. International Journal of Solids and Structures **44(3-4)**,760-778(2007).
15. Nowalk, M.D., Logan, S.E.,. Journal of Biomechanical Engineering **113**, 85-93(1991).
16. Chiba, M., Komatsu, K.,. Journal of Biomechanics **26**,561-570(1993).

ICME2015

International Conference on Mechanical Engineering 2015
(ICME 2015) 18 – 20 December, 2015, Dhaka, Bangladesh

Paper ID :571

Antiloosening Ability of 5/8 Inch Stainless Steel BSW Threaded Fasteners

Bikash Panja[1,a)] and Santanu Das[2,b)]

[1]*Department of Mechanical Engineering, Narula Institute of Technology, Kolkata- 700109, West Bengal, India.*
[2]*Department of Mechanical Engineering, Kalyani Government Engineering College, Kalyani- 741235, West Bengal, India.*

[a)]b.panja_86@yahoo.co.in
[b)]Corresponding author: sdas.me@gmail.com

Abstract. Threaded fasteners are popular for temporary joining of different components due to the fact that they retain high clamping force and torque for long. However, they may loosen under vibrating conditions causing failure of the system. In this experimental work, antiloosening ability of various 5/8 inch BSW fastening elements, such as conventional nut and nylock nut with flat washer, spring washer, inside and outside serrated washers is tested with stainless steel (SS) bolts. A hybrid double nut using a simple nut and one nylock nut at the outside and a typical adhesive bonded nut with 5/8 inch BSW bolt are introduced to obtain resistance to loosening. Some hybrid double nut and adhesive bonded nut are recommended for stainless steel 5/8 inch BSW bolts under vibration.

INTRODUCTION

Threaded fasteners are used widely for temporary joining of various machine elements to facilitate servicing, repairing, replacement of damaged components, etc. These have operational simplicity and ability to provide high clamping torque and force. However, they show a tendency of loosening under vibration [1, 2]. Arresting loosening of threaded fasteners under vibration is a challenging task to engineers, and engineers all over world tried to develop different antiloosening fasteners.

Hongo [2] did experiments on variable axial loading of threaded fasteners way back in 1964 regarding their loosening tendency. He thought the cause of loosening to be the reduction in axial tensile force of bolt and plastic elongation of the bolt thread. Paland [3] tested various types of threaded fasteners in 1966 for axial loading, and introduced the rule of loosening. He measured tangential strain on the surface of the nut, and concluded that a loaded nut widens elastically in a radial direction at an area close to the bearing surfaces, and contracts in the upper part. Junker in 1969 described [4] the theory of self loosening of preloaded bolted joint subjected to vibratory condition, and built up a testing machine for evaluating locking tendency. Mechanism of self loosening of nut and bolt was found to be based on effect of friction between interacting solid bodies, and direction of external force.

A team of researchers lead by Fujii investigated [1, 5-7] in detail the performance of threaded fasteners under vibratory condition related to loosening tendency. One group lead by Fujii tested [6] the effectiveness of screw threads, spring washers, serrated washers, nylon inserted nuts, metal inserted nut, cover ring nut, double nuts and eccentric nuts to restrict loosening. Test results showed that popularly known anti-loosening fasteners mostly did not possess much resistance to loosening. Fujii and Sase [5] and Sase et al. [6] proposed a new shape of screw fasteners, named ‘Step-Lock Bolt’ (SLB), that had eight steps with zero lead angle at the circumference of the thread within a revolution. The effectiveness in preventing the initiation and progress of loosening was examined by applying a force cyclically at right angles to the centre line of a bolt. The SLB was found to have loosened the least among various combinations of conventional bolt and so-called anti loosening nuts available. They also found certain combinations of hardness of SLB and nut giving desirable performance of the SLB.

In another work, Pai and Hess [8] carried out experiments to observe the tendency of loosening of fasteners under dynamic shear loads and to propose few strategies to avoid loosening. Croccolo et al. [9] carried out experiments to validate finite element analysis (FEA) results relating the coefficient of friction in bolted joints to the preloading force and tightening torque requirement to avoid failure of aluminium components of a motor bike. Another group of researchers developed [10-12] a set up to test loosening of threaded fasteners. As loosening in screws occurs mainly when repetitive forces are applied at a right angle to the longitudinal axis of bolt, the set up was designed consideration this. Bhattacharya et al. [12] made detailed experimental investigation on the loosening tendency of different combinations of fastening elements (bolts, nuts and washers) with different clamping forces under repeated oscillatory motion. With this set up, series of experiments were carried out [11, 13-15] on anti-loosening characteristics of variety of threaded fasteners. Different groups across the world worked on loosening nature of threaded fasteners. Izumi et al. [16, 17], Sanclemente and Hess [18], Cheatham et al. [19], Eccles et al. [20], Dinger and Friedrich [21] did experimental and/or analytical studies on the loosening behaviour of different threaded objects. FEA of 3D was performed by Izumi et al. [16] to understand the effect of friction and loosening tendency between fastening elements. They also performed [17] similar analysis using double nut and spring washer, and validated the FEA results with that of the experimental observations. Sanclemente and Hess [18] did loosening tests of threaded fasteners under cyclic transverse loads, while Cheatham et al. [19] performed tests and finite element analysis of secondary locking features in threaded inserts, Eccles et al. [20] made a detailed overview and analysis of anti-loosening threaded fasteners, and prevailing torque nuts in particular, with respective to mechanisms of loosening and arresting it. Woo et al. [22] found out through FEA minimum number of bolts required related to the force applied to suppress its loosening. Dinger and Friedrich [21] in a more recent work, numerically assessed contact stresses, and tried to explore their effect on loosening of fasteners. Basava and Hess [23] experimented on the loss of clamping force in a bolted joint under axial vibration condition, and explored its reasons behind the same.

In this work, antiloosening ability of hybrid double nut and adhesive bonded nut with the 5/8 inch BSW stainless steel bolt is explored under a repetitive loading of 5 Hz frequency to compare with other standard threaded fasteners.

LOOSENING MECHANISM AND ITS PREVENTION

Two or more parts fastened using threaded fasteners are held together by the tensile force generated by the elongated bolt and by compression generated on to the objects being tightened. These forces (tensile on bolt and compression on object fastened) are called pretension force. Spontaneous decrease in pretension force indicates screw loosening, as reported by many [11-13]. Loosening mainly occurs in threaded fasteners either without relative rotation between bolt and nut or by relative rotation of the bolt and nut. These are described in detail by Hongo [2], Fujii and Sase [5] and Bhattacharya et al. [12]. Loosening can be reduced by change of thread design, or by the use of various locking nuts as stated below.

Loosening caused by relative rotation can be minimized by reducing lead angle and flank angle, and relative slip between the bearing surface of nut and fastened material by introducing a taper, etc. A variety of locking fasteners are employed nowadays by the major companies. Through the efforts of the American National Standards Subcommittee on locking fasteners, three basic categories of locking fasteners have been established. They are free spinning, friction locking and chemical locking. Nylock nuts are also used to increase friction between nut and bolt threads thereby reducing loosening tendency [5, 12]. Variations of the techniques discussed above have been proposed and are being used in different threaded joints.

DETAILS OF EXPERIMENTATION

An indigenously developed test set up (Fig. 1), as detailed in reference [10-13], is used for undertaking experiments to explore antiloosening ability of threaded fasteners. Compression type load cell and load indicator (Make– Sushma, Bengaluru, India, Model SLC-302) are employed to observe clamping force. A rocking plate strikes 300 times a minute on the clamped plate with an amplitude of 0.2 mm, and transmits vibration to a plate clamped to the fixed plate using nut and bolt assembly. Under this vibration, fasteners may loosen, decreasing the corresponding clamping force. Replications of tests are done twice. Details of nut and bolt assembly utilized for loosening tests are given in Table 1 and the clamping conditions and number of oscillations allowed for the repeated experiments are given in Table 2. Photographic view of a nylock nut and flat, spring, inside and outside serrated washers are shown in Fig. 2. In this work, epoxy based high strength ‘araldite’ (grade: Mechanik, make: Huntsman

Advanced Materials (India) Pvt. Ltd., India) adhesive (mixed in equal proportion) is used in one experiment set. Adhesive bonded nut fills up the gap between the male and female threads and bond them together. Thickness of adhesive is kept less than equal to 1mm, as the gap available between nut and bolt threads is less than 1 mm. The adhesive covered joint is kept for 24 hours for curing. While loosening the nut, application of somewhat high torque is found to be sufficient, and this does not damage the fastening element. Hybrid Double Nut is used in another set of experiments. It is a combination of one conventional nut and one nylock nut. In this case, first a conventional nut and then a nylock nut are used for clamping.

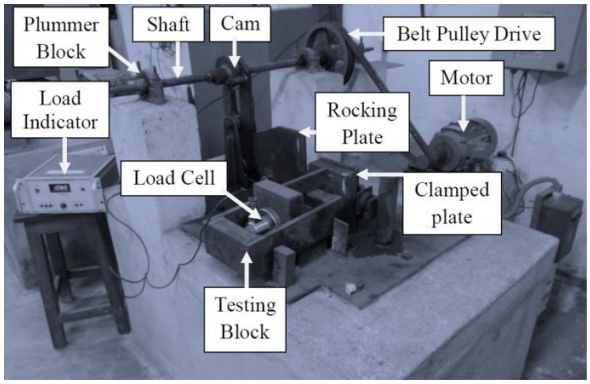

FIGURE 1. Pictorial view of the test rig

(a) (b) (c) (d) (e)

FIGURE 2. Photographic view of fastening elements used [a) nylock nut, b) flat washer, c) spring washer, d) inside serrated washer and e) outside serrated washer]

TABLE 1. Description of different fastening elements with Stainless Steel BSW 5/8 inch bolt other used in experiments

Pitch (TPI)	Bolt length (inch)	Nut used	Washer used	Comments
11	9	i) Conventional nut ii) Nylock nut iii) Adhesive bonded nut	i) Flat washer ii) Spring washer iii) Inside serrated washer iv) Outside serrated washer	These standard components are available in the market.

TABLE 2. Details of clamping conditions for testing with 6000 oscillations

Fastening Element Used	Initial Clamping Force (ton)		Final clamping force (ton)	
	Replication-1	Replication-2	Replication-1	Replication-2
Conventional Nut	1.271	1.273	1.216	1.218
Flat Washer	1.275	1.273	1.228	1.221
Spring Washer	1.273	1.272	1.238	1.234
Inside Serrated Washer	1.271	1.266	1.236	1.232
Outside Serrated Washer	1.269	1.274	1.237	1.239
Nylock Nut	1.275	1.277	1.247	1.252
Double Nut	1.275	1.270	1.261	1.252
Adhesive Bonded Nut	1.263	1.282	1.242	1.269

RESULTS AND DISCUSSIONS

From the experiment on 5/8 inch BSW SS bolt with conventional nut, results obtained from two replicated tests are shown in Fig. 3. The total loosening is about 55 kg for both experiments after 6000 oscillations of vibration.

Clamping force shows a decreasing trend even towards 6000 oscillations. Figure 4 shows the result using a flat washer. A reduction of 47 kg of clamping force for experiment 1 (1st replication) after final oscillations is seen. Experiment 2 (2nd replication), which is a repeat experiment 1, shows the loosening of only 52 kg. This loosening is lesser to some extent than that with conventional nuts. Loosening characteristics with using a spring washer are shown in Fig. 5. Total loosening found are 35 kg in experiment 1 and 38 kg in experiment 2. From these plots, it is observed that the use of spring washer prevents loosening more than the flat washer. Figure 6 shows the loosening characteristics for conventional 5/8 inch BSW SS bolt and nut with inside serrated washer under similar vibration. The average loosening is about 34.5 kg of both the two repeat experiments after end of final oscillations. Figure 7 shows the loosening characteristics when outside serrated washer was used. Here, 32 kg and 35 kg of clamping forces are lost in experiment 1 and experiment 2 respectively after 6000 oscillations. The plots (Fig. 6 and Fig. 7) show that the use of serrated washer (inside and outside) provides more resistance to loosening compared to flat and spring washer.

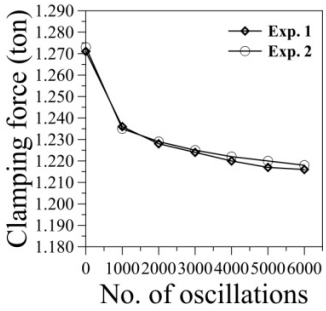

FIGURE 3. Testing results with conventional nut under vibration

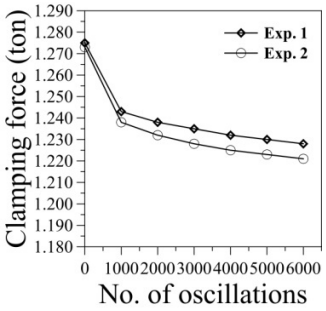

FIGURE 4. Testing results with flat washer under vibration

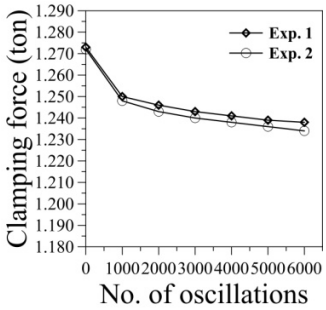

FIGURE 5. Testing results with spring washer under vibration

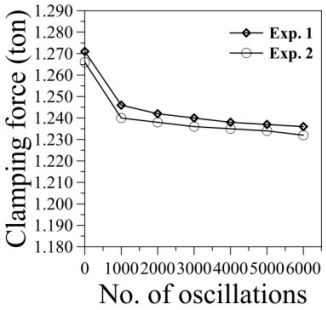

FIGURE 6. Testing results with inside serrated washer under vibration

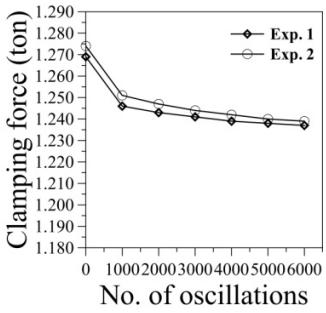

FIGURE 7. Testing results with outside serrated washer under vibration

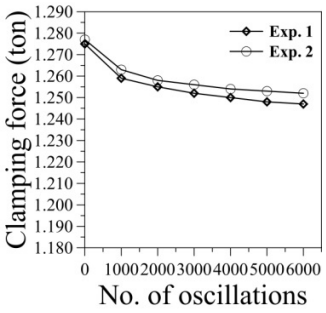

FIGURE 8. Testing results with nylock nut under vibration

From Fig. 8, it is observed that the total loosening for nylock nut is low, about 27 kg in average for both the two experiments. The curves become horizontal after some initial oscillations. So, it is clear that the nylock nut provides an extra friction grip due to presence of nylon insert inside the nut and for this, the bolt thread trends to resist loosening. Figure 9 shows the loosening characteristics for 5/8 inch BSW SS bolt with one conventional nut and one nylock nut, named a hybrid double nut subjected to vibration. Here, 14 kg and 18 kg of clamping forces are lost in

experiment 1 and experiment 2 respectively at the end of 6000 oscillations. From the figure, it is observed that the use of hybrid double nut in place of single nylock nut can prevent loosening quite effectively than a single nylock nut. Figure 10 shows the loosening characteristics for 5/8 inch BSW SS bolt with adhesive (Araldite) bonded conventional nut. Here, the total loosening are 21 kg in experiment 1 and 13 kg in experiment 2. From this figure, it is observed that the use of the adhesive bonded nut provides more resistance to loosening compared to nylock nut. This observation shows similar antiloosening nature with that using the hybrid double nut.

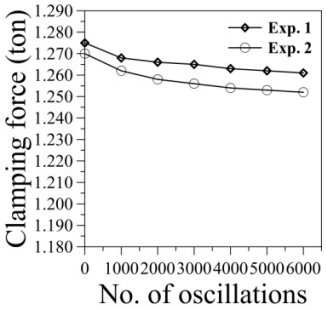

FIGURE 9. Testing results with hybrid double nut under vibration

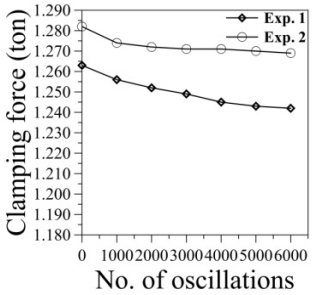

FIGURE 10. Testing results with adhesive bonded conventional nut under vibration

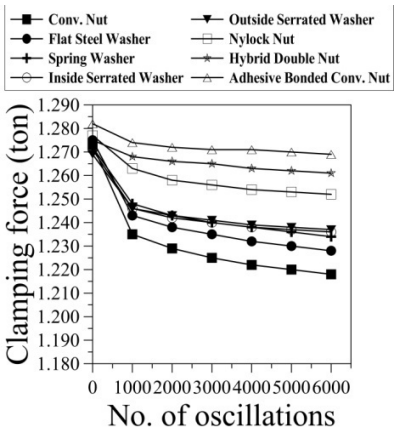

FIGURE 11. Comparison of loosening with different nuts and washers

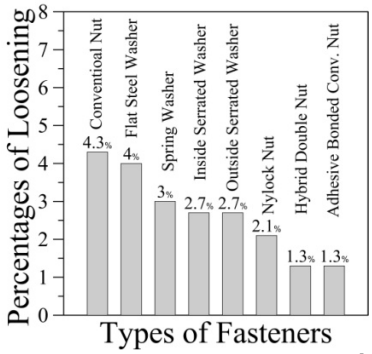

FIGURE 12. Loosening percentages with different nuts and washers

From the experiments of 5/8 inch BSW SS threaded bolt with different nuts and washers, results obtained are shown in Fig. 11 by averaging the data of two replications. It is observed that initially the rate of loosening is quite high in most of the tests. However, after certain number of oscillations, clamping force becomes almost constant showing little change in clamping force for most of the fasteners. The plots show that the use of spring washer can reduce the loss of clamping force to some extent, may be due to its ability to store some clamping force through its deformation. However, flat washer does not give any effect to arrest loosening under vibration, and shows similar loosening tendency as that of a conventional threaded fastener. Inside serrated washer and outside serrated washer can effectively reduce loosening. This may be due to arresting of free rotation of fastening elements due to small deformation of the serrations into contact regions. Hybrid double nut and adhesive bonded nut are found to be comparatively good antiloosening fasteners under vibration, followed by nylock nut. The nylon ring raises contact friction expectedly in nylock nut, and reduces loosening tendency. Adhesive bonded nut loosens less due to large friction obtained by providing adhesive in the nut-bolt interface region.

Loosening percentage for different combination of 5/8 inch BSW fasteners is presented in Fig.ure 12. It is seen that loosening of conventional and flat washer is around 4.3% and 4% respectively and loosening of spring washer is about 3%. From percentage analysis, spring washer is quite effective than conventional nut and flat washer. Another fastener is serrated washer (both inside and outside) which is more effective than spring washer because loosening of serrated washer is around 2.7%. Nylock nut gives loosening about 2.1%. However, hybrid double nut and adhesive bonded nut show the similar loosening effect which is about 1.3%. So, hybrid double nut and adhesive bonded nut are found to be comparatively good antiloosening fasteners under vibratory condition compared to the

said other combination of fasteners. Friction raising effect of nylon inserted nut and adhesive bonding may be the prime reason behind less loosening tendency of these fasteners.

CONCLUSIONS

Fastening elements such as nut and washer were found to play a key role behind antiloosening ability of fasteners. Initial tightening torque also plays a significant role. It is revealed that flat washer does not prevent loosening considerably. Even the use of spring washer, inside, or outside, serrated washer gives only marginal antiloosening characteristics for tested 5/8″ BSW stainless steel bolts. Nylock nut shows good antiloosening ability and less possibility to loosen in vibrating environment. The nylock nut provides an extra friction grip on the bolt thread to resist loosening. Hybrid double nut using one inside simple nut and one nylock nut on the outside is found to prevent loosening quite effectively compared to a single nylock nut. Use of the adhesive bonded nut also provides enough resistance to loosening in comparison with the nylock nut, and it shows similar locking characteristics as that of hybrid double nut for stainless steel bolts, and hence may be recommended.

ACKNOWLEDGMENTS

Authors acknowledge the All India Council for Technical Education, New Delhi, India for providing R&D grant (sanction letter Ref. 8018/RDII/BOR/R&D(244)/99-2000 dated March 24, 2000) with which the test rig was made.

REFERENCES

1. N. Sase, K. Nishioka, S. Koga and H. Fujii, J. Mat. Proc. Tech. **77**, 209 – 215 (1998).
2. K. Hongo, Trans. JSME. **30(215)**, 934 – 939 (1964) (In Japanese).
3. E. G. Paland, "Investigation of the locking features of dynamically loaded bolted connections," Dissertation submitted to Hannover University, Germany, 1966.
4. G. H. Junker, "New criteria for self-loosening of fasteners under vibration," (SAE International Automotive Engineering Congress, Paper No. 690055, 1969) pp. 934 – 939.
5. H. Fujii and N. Sase, "SLB concept for screw fastening and its anti loosening performance," Souvenir of the 18th AIMTDR Conference, (Kharagpur, India, 1998), pp. 25 – 34.
6. N. Sase, S. Koga, K. Nishioka and H. Fujii, J. Mat. Proc. Tech. **56**, 321 – 332 (1996).
7. N. Sase and H. Fujii, J. Mat. Proc. Tech. **119**, 174 – 179 (2001).
8. N. G. Pai and D. P. Hess, J. Sound and Vib. **253**, 585 – 602 (2002).
9. D. Croccolo, M. D. Agostinis and N. Vincenzi, J. Engg. Failure Analysis. **18(1)**, 364 – 373 (2011).
10. S. K. Saha, S. Srimani, S. Hajra, A. Bhattacharya and S. Das, "On the anti-loosening property of different fasteners," Proceedings of the 13th NaCoMM Conference, (Bengaluru, India, 2007), pp. 229 – 232.
11. K. N. Mahato and S. Das, "A study on antiloosening characteristics of different 3/8 BSW threaded fasteners," Proceedings of the 14th NaCoMM, (Durgapur, India, 2009), pp. 409 – 415.
12. A. Bhattacharya, A. Sen and S. Das, Mech. and Mach. Th. **45**, 1215 – 1225 (2010).
13. B. Panja and S. Das, "On the anti-loosening characteristics of M16 threaded fasteners under vibratory conditions," Proceedings of the 15th NaCoMM, (Chennai, India, 2011), pp. 273 – 282.
14. S. Samanta, S. Das, R. Roy, K. Bhukta, A. Pal and S. Das, Indian Sc. Cruiser. **26(6)**, 22 – 27 (2012).
15. S. Samanta, S. Das, R. Roy, K. Bhukta, A. Pal and S. Das, J. the Asso. of Engrs. India. **82(3&4)**, 34 – 43 (2012).
16. S. Izumi, T. Yokoyama, A. Iwasaki and S. Sakai, J. Engg. Failure Analysis. **12**, 604 – 615 (2005).
17. S. Izumi, T. Yokoyama, M. Kimura and S. Sakai, J. Engg. Failure Analysis. **16**, 1510 – 1519 (2005).
18. J. A. Sanclemente and D. P. Hess, J. Engg. Failure Analysis. **14**, 239 – 249 (2007).
19. C. A. Cheatham, C. F. Acosta and D. P. Hess, J. Engg. Failure Analysis. **16**, 39 – 57 (2009).
20. W. Eccles, I. Sherrington and R. D. Arnell, Towards an understanding of the loosening characteristics of prevailing torque nuts. Proceedings of the IMechE, Part C: J of Mech. Engg. Sc. **224**, 483 – 495 (2010).
21. G. Dinger and C. Friedrich, J. Engg. Failure Analysis. **18(8)**, 2188 – 2200 (2011).
22. T. K. Woo, B. C. Hwang, Y. J. Jang and C. Kim, Int. J. Prec. Engg. and Manuf. **10(1)**, 29 – 34 (2009).
23. S. Basava and D. P. Hess, J. Sound and Vib. **210(2)**, 255 – 265 (1988).

International Conference on Mechanical Engineering 2015
(ICME 2015) 18 – 20 December, 2015, Dhaka, Bangladesh

Paper ID : 576

Mechanical properties of a Polyethylene Glycol Diacrylate (PEGDA) scaffold

Morshed Khandaker[a)], Albert Orock, Stefano Tarantini, and Shahram Riahinezhad

University of Central Oklahama

[a)]Corresponding author:MKhandaker@uco.edu

Abstract. Nutrient conduit networks are introduced within the tissue construct to enable cells to survive in the matrix. But the effect of these networks on the mechanical integrity of the tissue scaffold is not known. The study aimed to explore the influence of the network architecture on the maximum tensile stress of Polyethylene glycol diacrylate (PEGDA) gels. Particularly, the effects of photo initiator concentration, gel temperature and incubation time on the maximum tensile stress of the networked PEGDA samples were investigated. Flat dumbbell shaped PEGDA tension test samples with and without nutrient conduit networks at the gauge section were designed and fabricated by UV-photo polymerization process. PEGDA solution was added to different concentrations of photo initiator (0.2% and 0.6%) solution to make the specimen. Tension test were conducted on those samples at different temperatures (23°C and 37°C) and incubation time (0 and 7 days) after the fabrication of the specimen. Our study found statistically significant effect of network architecture, photo initiator concentration, temperature and wait time on the failure stress of PEGDA samples (P value<0.05).

INTRODUCTION

Tissue engineering is a new field that allows the combination of engineering, biology and material methods for developing new techniques with potential to create tissues and organs [1]. The ability of networked three dimensional structure to elicit altered cell behaviors, including cell adhesion, has raised heightened interest in the scaffold materials for various biomedical applications, including orthopedic repair, and regeneration [2]. Cells in-vitro usually do not reproduce in a three dimensional fashion unless allowed to grow on scaffolding. The scaffolds should have appropriate characteristics such as pore size, shape and mechanical properties to enable cells to grow in every dimension. The cells have to be able to attach, migrate, proliferate and differentiate into various organs in the scaffold. Several engineered tissue grafts have been developed for the reconstruction of the injured hard and soft tissues [3]. Yasar *et al*. [4] used Lindenmayer systems, system, an elegant fractal-based language algorithm framework, in designing vasculature networks that could potentially be incorporated in hydrogel scaffolds like PEGDA. The reason of using PEGDA over other materials is that PEGDA is 3D networked structures can be manufactured easily to allow for the cell growth at higher depth using photolithograph process. Photolithography is a process which is commonly used in micro-fabrication to produce the desired scaffolds with a high level of detail and precision. It has been found to be a valid method to manufacture multiple-layer scaffolds for allowing the constructions of channels within the scaffold to better distribute nutrients to the cells. This system is comprised of three major parts: 1) a UV light source, 2) mold and 3) a polymer solution. The role of the mold is to allow the PEGDA to polymerize in the desired shape. Tissue scaffolds, with nutrient conduit networks, need to be designed with intricate architecture, porosity, pore size and shape, and interconnectivity in order to provide the required

structural strength, transport nutrients and the micro-environment for cell and tissue in-growth. By selecting the appropriate unit cell interior structures, structural properties such as the tensile strength, diffusion and permeability characteristics of PEGDA structure can be controlled. The relationship between the interior nutrient conduit network structure and structural property of PEGDA is not understood yet. Knowledge of the structural properties of the networked PEGDA constructs with respect to the photo initiator concentration, temperature, and time is also necessary to adequate design and effective use of PEGDA for tissue engineering constructs.

To understand the effect of nutrient conduit networks on the PEGDA structural properties, this study compared the failure stress of PEGDA flat dumbbell shaped mold with and without nutrient conduit networks from the displacement controlled tension tests. Similar failure assessments of the PEGDA molds were also conducted in this study as a function of the photo initiator concentration, temperature, and time.

MATERIALS AND METHODS

Mold Preparation

A silicon (Casting Craft Easymold Silicone Rubber, Environmental Technology Inc. Fields Landing, CA) mold was fabricated to make ASTM E855-90 standard [5] flat dumbbell-shaped without network PEGDA tension test samples. Two additional ABS plastic pieces, fabricated using Dimension Elite 3D Printer (Stratasys, Inc.), were assembled with the silicon mold to fabricate networked PEGDA specimen. Each plastic piece has an array of holes (diameter: ~2mm and spacing: ~1 mm) .The bottom piece has 7x2 holes, whereas the side piece has 7x3 holes. A total amount of 35 pins were inserted through these holes in the gauge section of the hydrogel specimen.

Specimen preparation

Two solution, PEGDA (M_n =700; Sigma-Aldrich) with the Phosphate Buffer Solution (PBS) solvents, and the photo initiator, Alpha-alpha-dimethoxy-alpha-phenylacetophenone (M_w =256.35 g/mol; Sigma-Aldrich) with the 1-vinyl-2-pyrrolidone (M_w =111.14 g/mol; Fluka) solvents, were used to fabricate the gel solutions. The 20 wt% PEGDA solution was produced by mixing 2ml of PEGDA with 8 ml of PBS. The PI solution was produced by mixing 0.3 g of PI with 1 ml of solvent in dark room to prevent premature crosslinking. The 0.2 wt% and 0.6 wt% PI gel solution was produced by mixing 4µl and 12µl of PI with 2 ml of PEGDA solution, respectively. The solution was poured in the custom made mold to cure the mixture in a flat dumbbell shape gel. The solution was exposed to 365nm long wave UV (B-100SP Ultraviolet Lamp, UVP, LLC) light for 3 min. The silicon mold was disassembled by careful removal of pins. The mold was bended to extract the PEGDA specimen. The specimen was stored in PBS solution before the mechanical tests. Eight groups of specimen were prepared

Tensile tests

A custom made tension test setup was designed and fabricated for determining the tensile failure stresses of the specimens at room (laboratory) and physiological (NuAire NU-4750 incubator) temperatures. The complete test setup is shown in **Error! Reference source not found.**. An electric connection was developed using the utility side access port of the incubator to the test specimens inside incubator. The specimens were placed in the holders in an unstressed state. Cover plates as shown in **FIGURE 1(**g), same sizes as the holders, were placed above the specimen to restrict upward movement of the specimen. A precision actuator (Newport™ LTA-HL®) was used in the setup to extend the specimens at a rate of 0.01 mm/sec until failure of specimen. Force was measured using 1lb load cell (Futek™ LRM200) consistently throughout extension. Load cell was calibrated before testing. The force and displacement data were recorded simultaneously by a user written labview program 10.0 (National Instruments) from the load cell and actuator, respectively. The stress-strain curves were developed for each of the samples. Stress was calculated by the magnitude of the force divided by the cross-sectional area (~5.5 mm x ~7.5 mm) at the center of the gage length. Gage length (~15.7 mm) for the specimen was determined as the distance between the holders at the initiation of positive load to the specimen. Stress was calculated by the magnitude of the displacement after the initiation of load force divided by the gage length. Statistical analyses were performed using Student's t-test for the

different groups of specimen using Microsoft Excel 2000 statistical analysis toolkit. Data sets with a *p*-value of lower than 0.05 was considered significantly different.

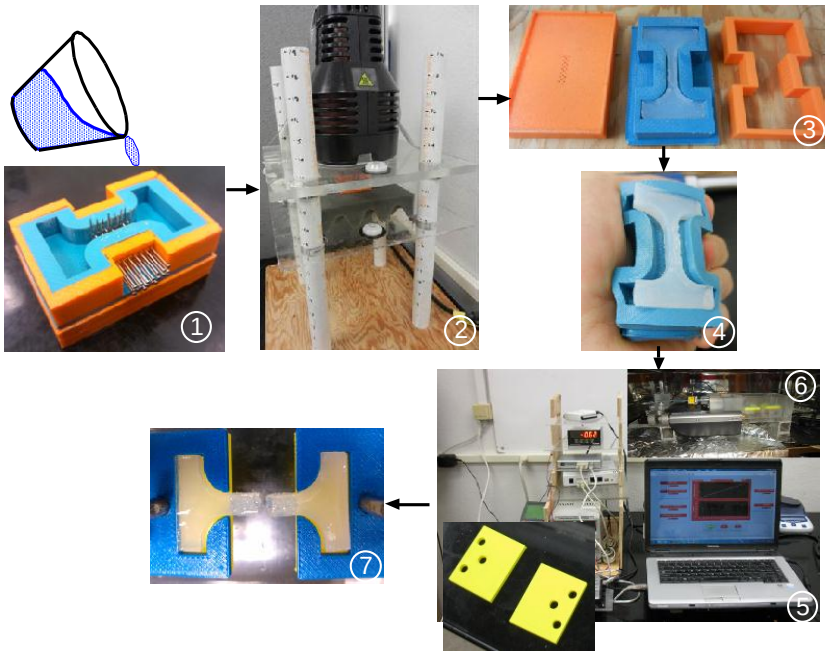

FIGURE 1. Steps that are performed for the finding the failure stress of a networked PEGDA. Step 1: 20% PEGDA in PBS mixture was added to the desired concentration of photoinitiator mixture and poured in the custom made mold to cure the mixture in flat dumbbell shape. Step 2: The solution was exposed to UV light for 3 min. Step 3: The mold was disassembled by the careful removal of pins. Step 4 The silicon mold was flexed to easily extract the specimen without damaging the PEGDA specimen. Step 5: Tension test on PEGDA samples at room and incubator (body) conditions. Step 6: Analysis of load and displacement data for the calculation of the failure stress of the specimen.

RESULTS AND DISCUSSION

Using the manufacturing techniques mentioned above a significant amount of specimens were produced to find the effects the effect of photo initiator concentration, temperature, and time on the failure stress of the specimen. The highest stress values were recorded from the stress versus strain plot (**FIGURE 2**) and this data was used to characterize PEGDA hydrogel in respect to temperature, time, photo initiator concentration and strain rate. The **TABLE 1** summarizes the experiments conducted for channeled PEGDA hydrogel specimen. The photo initiator concentrations were chosen to be the least harmful to cell proliferation. The temperatures used were room temperature and physiological temperature of the human body. The time selected were 0 days and 7 days to evaluate how biodegradation of the hydrogel affects the ultimate strength of the hydrogel. Lastly the strain rate was varied to establish an ideal strain rate to use for the mechanical characterization.

TABLE 1. Statistical parameters determined from the tensile tests of different kinds of PEGDA samples with nutrient conduit networks. PEGDA samples with nutrient conduit networks are represented by letters A to H, where samples A have photo initiator concentration = 0.2%, test temperature = 23°C and test wait time = 0 day, samples B have photo initiator concentration = 0.2%, test temperature = 37°C and test wait time = 0 day, samples C have photo initiator concentration = 0.2%, test temperature = 23°C and test wait time = 7 days, samples D have photo initiator concentration = 0.2%, test temperature = 37°C and test wait time = 7 days, samples E have photo initiator concentration = 0.6%, test temperature = 23°C and test wait time = 0 day, samples F have photo initiator concentration = 0.6%, test temperature = 37°C and test wait time = 0 day, samples G have photo initiator concentration = 0.6%, test temperature = 23°C and test wait time = 7 days, and samples H have photo initiator concentration = 0.6%, test temperature = 37°C and test wait time = 7 days. P-values from the *t*-tests of failure stresses of two groups of specimen are represented by ( ).

Test conditions	A	B	C	D	E	F	G	H
Failure stress								
No of samples	4	6	3	6	6	3	6	4
Average	49.30	36.17	40.45	29.68	62.95	47.64	50.35	39.12
St. Dev.	4.24	2.40	2.30	3.37	5.63	3.03	3.90	1.75
P values								
Temperature effect		0.007 (AB)		0.004 (CD)		0.003 (EF)		0.001 (GH)
Wait time effect	0.031 (AC)		0.007 (BD)		0.003 (EG)		0.039 (FH)	
Photo initiator concentration effect					0.005 (AE)	0.017 (BF)	0.006 (CG)	0.001 (DH)

The results of this study showed a clear difference of maximum tensile stress between the various PEGDA samples fabricated in this study without and with networked conduit channels (**FIGURE 3**). The average maximum tensile stress (ultimate strength) of PEGDA samples without networked conduit channels was 535.92 ± 54.72 kPa (n = 3), which was 8.5 times equal or higher than any of the other PEGDA samples without networked conduit channels as reported in **TABLE 1**. This result clearly shows the nutrient conduit networked significantly decreased the mechanical integrality of the PEGDA gel. The failure stress of the nutrient conduit networked PEGDA samples are significantly lower than the liver's reported failure stress of 232 kPa [6] and breaking stress 451 kPa [7].

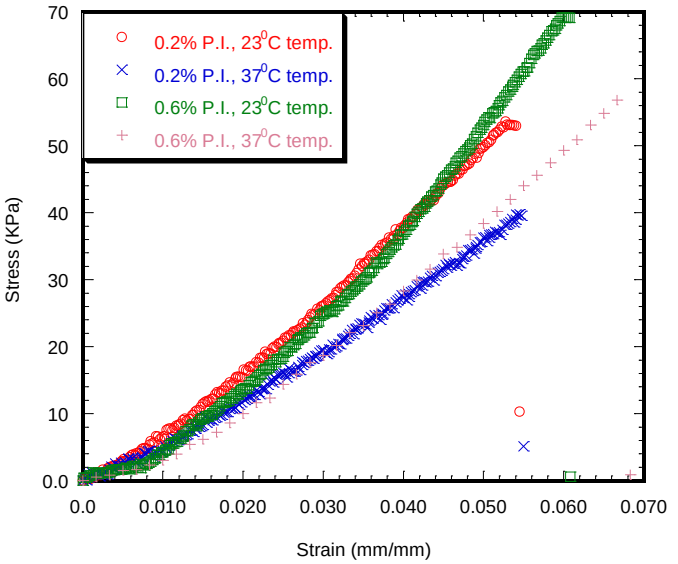

FIGURE 2 Typical stress versus strain diagram derived from the tension test on the flat dumbbell-shaped PEGDA sample having variable PI concentrations (0.2% and 0.6%) and test temperatures (23°C and 37°C). The tension tests were performed on these samples immediately after the preparation of the specimen at 0.01 mm/sec. strain rate.

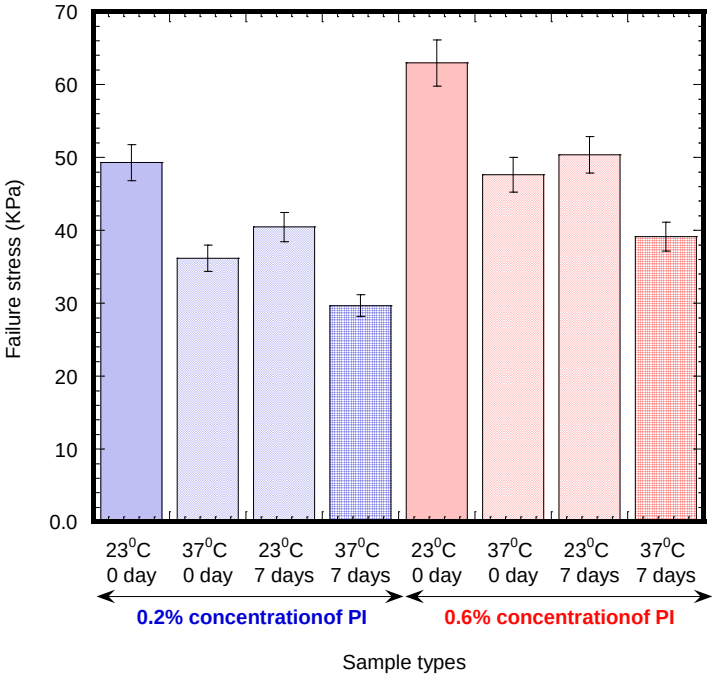

FIGURE 3. Tension test results of different PEGDA specimens showing the variation of the failure stress of the specimen due to photo initiator (PI) concentration, test time, test temperature and strain rate applied to the specimen during testing.

CONCLUSION

In this work the photolithography system has been successfully developed to fabricate the PEGDA networked structures. This study will focus on the manufacturing a stage apparatus to construct scaffolds and testing mechanical properties of various scaffold constructs The results showed that PEGDA tissue constructs had the strongest tensile strength when they are at room temperature compared to body temperature. Also PEGDA hydrogel was found to lose ultimate strength when tested a week after production. This result was expected since PEGDA is a biodegradable material. Higher concentration of photo initiator contributes to toughen the hydrogels, increasing their ultimate strength, however 0.6% photo initiator concentration was found to be detrimental to the health of the cells. The effect of strain rate on the PEGDA hydrogel constructs was not conclusive. This is because no particular pattern could be observed from the gathered data.

ACKNOWLEDGEMENTS

This publication was made possible by Grant Number P2PRR016478 from the National Center for Research Resources (NCRR), a component of the National Institutes of Health (NIH) and CURE-STEM faculty scholar award support from University of Central Oklahoma (UCO). Its contents are solely the responsibility of the authors and do not necessarily represent the official views of NCRR or NIH or UCO.

REFERENCES

[1] D. W. Hutmacher, "Scaffolds in tissue engineering bone and cartilage," *Biomaterials*, vol. 21, pp. 2529-2543, 2000.

[2] K. Y. Lee and D. J. Mooney, "Hydrogels for tissue engineering," *Chemical Reviews*, vol. 101, pp. 1869-1879, 2001.

[3] W. Sun, A. Darling, B. Starly, and J. Nam, "Computer-aided tissue engineering: Overview, scope and challenges," *Biotechnology and Applied Biochemistry*, vol. 39, pp. 29-47, 2004.

[4] O. Yasar, B. Starly, and S.-F. Lan, "A Lindenmayer systems based approach for the design of nutrient delivery networks in tissue constructs," *Journal of Biofabrication*, vol. 1, 2009.
[5] ASTM, "Annual book of ASTM standards: section 3 - Metals test methods and analytical procedures " vol. 03.01, 1994.
[6] J. W. Melvin, R. L. Stalnaker, and V. L. Roberts, " Impact injury mechanisms in abdominal organs," *SAE Transactions*, vol. 730968, pp. 115-126, 1973.
[7] S. Seki and H. Iwamoto, "Disruptive forces for swine heart, liver, and spleen: their breaking stresses," *Journal of Trauma*, vol. 45, pp. 1079-1083, 1998.

ICME2015

International Conference on Mechanical Engineering 2015
(ICME 2015) 18 – 20 December, 2015, Dhaka, Bangladesh

Paper ID : 581

Analysis of an off Road 4WD Vehicle's Suspension System Modification – Case Study of Aftermarket Suspension Lift and Modification of Wheel Track Size

J. Ross[1], M. A. Hazrat[1, a)] and M. G. Rasul[1]

[1]*School of Engineering and Technology, Central Queensland University, Queensland 4702, Australia*

[a)]Corresponding author: h.ali@cqu.edu.au

Abstract. In this research, a four wheel drive (4WD) suspension of a vehicle has been modified by increasing the ride height to investigate stability and cornering potential of the vehicle through load transfer and variation of roll angle. Further investigation has been conducted to observe the characteristics which are deemed desirable for off road application but detrimental to the on road application. The Constant Radius Cornering Test (CRCT) was chosen as a base method for experimental investigation to observe the effect of the suspension modifications. The test was carried out by undertaking a known radius and cambered corner at a constant speed. For this test, the acceleration and gyroscopic data were measured to check and compare the accuracy of the analysis performed by OptimumDynamics model. The tests were conducted by means of negotiating the curve at the speed of 80 km/h and it was gradually achieved to allow a good consensus of the amount of body roll the vehicle experienced. Using a surveyor's wheel, the radius of the corner was estimated as 160 m and using the gyroscopic sensor, the corner camber was measured at 4 degrees. While comparing the experimental results with the simulation results, the experimental constraints led to higher values than those of the analytical results. The total load transfer reduced by 2.9% with the increased track size. It has been observed that the dynamic load transfer component is lesser than the standard suspension with the aftermarket suspension lift and the upgraded anti-roll bar (ARB). With the simulation of the fitment of the other modifications aimed to improve the characteristics of the raised vehicle, the vehicle showed a reduced tendency towards roll angle due to the stiffened anti-roll bar and the maximum increased wheel track demonstrated reduced lateral load transfer and body roll. Even with these modifications however, the decrease in load transfer is minimal in comparison to what was expected.

INTRODUCTION

Standard passenger vehicles generally perform poorly under Australian off road conditions due to insufficient underbody clearance, suspension travel and articulation, and fitting of open differentials.Towing a heavy load, such as a large caravan or boat on factory suspension can cause the suspension to sag, reducing the ride quality, safety and travel of the suspension. Even the top of the line four wheel driver touring vehicles from popular manufacturers such as Toyota, Nissan, or Land Rover which have a reputation for being the toughest on the market will suffer under these conditions, where it is often seen that the suspension at the rear end is nearly bottomed out. This may not be too much of an issue when driving on a good quality road, but this can cause major issues when trying to get to your desired location if it involves any off road travel or the driver were to hit an imperfection in the road surface at high speed such as a pothole. For those who wish to travel around Australia, the dreaded corrugations convince most to upgrade their suspension systems, and for those who do not will generally suffer a terribly uncomfortable ride, and risk potentially damaging their vehicle.

The passive suspension systems installed in the majority of today's vehicles are unfortunately often a compromise with driving conditions[1]. This compromise is almost always governed by the major contributor to all vehicle components quality and performance, cost. A suspension system from the factory also needs to be designed to perform acceptably under the likely driving conditions for that vehicle type; this means that it won't always be ideal for an individual's driving conditions. One of the most prominent examples of this would be for four wheel

drive (4WD) vehicles. Due to the majority of these vehicles being bought primarily for use in urban conditions with the occasional off road or towing encounter, they aren't designed exactly up to the standard some would hope for. Those who choose to upgrade their vehicle to be capable in off road terrain, will almost always choose to upgrade to a suspension kit with longer springs and shock absorbers in order to gain greater ground clearance, further suspension travel and install larger tyres, which will give extra ground clearance under the differential, axles and also further clearance for the under body. The majority of 4WD owners who decide to upgrade their suspension system generally install a system that will give more under body clearance and more suspension travel; however it is not unknown for 4WD vehicles to be upgraded in the opposite direction if it is known the vehicle will only be used for on road use. As the vehicle is designed from the factory to be able to perform acceptably in the most likely conditions, swapping out the suspension system for a system suited to your needs will almost always give a very noticeable improvement. Suspension modification is required either for towing a heavy caravan around the country or off road adventures.

There is strong prejudice towards suspension modifications of four wheel drive vehicles, with a common view that any deviation from the original setup dramatically hinders the handling capability of a vehicle. Crash statistics research conducted by Keall& Newstead[2] found that sports cars, which have superior braking and handling systems in comparison to 4WD vehicles show a considerably higher risk of crash involvement. Many suspension manufacturers have come up with different methods to provide some level of diversity, however these advanced systems are generally only available on higher end vehicles. The most common solution being employed currently is adjustable damping, which allows damping to be controlled electronically, providing some level of improvement between surface conditions. This solution is limited however, as it can only affect the damping properties of the suspension system whereas a suspension system is made up primarily of two components, a spring and a damper. A mechanical spring cannot be varied between surface conditions so the current adjustable suspension systems are once again, a compromise.

In this article, both the experimental and simulation analyses are presented by modifying a 4WD vehicle. The objective was to improve the vehicle's suspension performance in off-road conditions. Due to the nature of the modification being an increase in ride height, the main investigation is to observe the effects on the stability and cornering potential of the vehicle due to this modification by means of the load transfer and roll angle of the vehicle. The investigation aims to observe how the characteristics which are deemed desirable for off road handling will be detrimental to the on road handling and the methods that could be employed to counteract these effects.

CONSIDERATIONS ON MODIFICATION OF 4WD VEHICLE

Few of the considerations undertaken for this experiment are presented as in the following subsection.

Lift Modification

There are various types of lift modifications that are aimed to increase the off road capability of a vehicle. All these methods have their own benefits and drawbacks. The most common types of four wheel drive vehicle modification that are aimed to increase vehicle clearance have been simplified to three types for this experiment. This includes the fitment of oversized tyre, suspension lifts and body lifts. Suspension lift could be achieved either by fitting a longer spring and shock absorber or by the fitment of spacer kits between the suspension and chassis mount and an extended shackle for a leaf spring suspension system. When a suspension kit is installed it causes the vehicle to sit higher, the height gained in static ride will be lost in the available down travel of the suspension. Besides, the centre of gravity of the vehicle is affected due to lift modification. In this research, the vehicle was fitted with an Independent Front Suspension (IFS) setup using the double wishbone configuration.

Body lift is one of the least common types of lift modifications carried out on a 4WD vehicle, albeit arguably one of the safest for on road conditions if installed correctly. A body lift is achieved by placing spacer blocks between the mounts of the body of the vehicle (i.e. the cab) and the chassis. The advantage of a body lift over other types of lift modifications is that the body of the vehicle is almost a negligible amount of mass in comparison to the remainder of the vehicle, hence producing a minimal effect on the vehicles centre of gravity. Fitment of oversized tyres[3] (large diameter tyre combined with aggressive tread pattern) is deemed beneficial for off-road vehicles but detrimental to on road application. Oversized tyre could be effective when installed with other two types of modifications. This type of lift raises the vehicle centre of gravity equal to the increased tyre diameter as both the sprung and unsprung masses of the vehicle are raised. The most common drawbacks are change of gearing and requirement of higher ratio differentials, which are to be improved to maintain secured drivability of the vehicle.

Handling Characteristics

Good handling characteristics for an on road vehicle is defined as high cornering potential with minimal body movement while good off road handling characteristics are defined as good vehicle articulation and stability throughout the full range of suspension travel. The largest contributor of the modifications for off road capability is the centre of gravity of the vehicle. When the centre of gravity is raised, the static and transient lateral acceleration potential of the vehicle is altered. The camber angle is effective for on road application, but insignificant for off road uses. Increasing the track width of the wheels on a vehicle is the simplest way to counteract the stability issues caused due to a raised centre of gravity however it also has negative consequences. The Static Stability Factor (SSF) is a static determination of a vehicle's resistance to rollover using the most influential geometric characteristics of the vehicle[4, 5]. It is defined as the track width of the vehicle divided by twice the height of the centre of gravity of the vehicle. It is important to note that the SSF is only derived from the geometric relationships of the vehicle characteristics and the effects of the suspension are not taken into account. It is a simple way of determining the intensity of vehicle instability due to lift modifications. As the load is transferred to the outer wheel, the available traction for this tyre increases, however the traction available to the inner wheel is reduced then. Under extreme circumstances, when the load transfer is equal to over half of the vehicles total weight, it would start to roll over.

Australian Codes and Regulations

In order to be confident that the vehicle is still legal to be driven on Queensland public roads without the requirement of a certificate of compliance to be issued to the vehicle which would require third party testing and inspection, scrutiny of these codes and regulations have been undertaken prior to any modification being undertaken. The modifications were performed as minor category modifications according to both the Queensland Code of Practice (QCOP) and the National Code of Practice (NCOP)[6, 7].

METHODOLOGY

The first and most important specification to be determined for the vehicle is the mass distribution of the vehicle. Through the use of load cells provided by Dobinsons Suspension[8], the mass distribution was determined by measurement of the mass at each wheel as seen in Fig. 1. Then, with the known spring rate from aftermarket suspension kit manufacturer, the unsprung mass was determined. The Hooke's law was applied to experimentally determine the sprung mass. The anti-roll bar used in this experiment was of similar material as the original anti-roll bar, so the calculation was performed with Puhn's formula[9] as in Fig. 2.

FIGURE 1. Determination of mass distribution of the sample vehicle (Mitsubishi Triton)

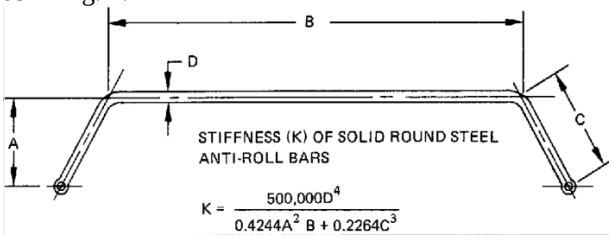

FIGURE 2. Sway Bar Stiffness Estimation by Puhn's formula[9]

To conduct the Constant Radius Cornering Test (CRCT), some adjustments were performed to suit with the experimental objectives. The acceleration and gyroscopic data was measured as a means to test and compare the accuracy of the OptimumDynamics model. The test place was a national highway including a turn-off to another road (Tee-junction), where maximum speed limit was 100 km/h. The other test speeds were of 60 km/h, 70 km/h and 80 km/h. By using a surveyor's wheel, the radius of the corner was estimated as 160 m and using the gyroscopic sensor, the corner camber was measured at 4 degrees. The centre of gravity of the vehicle could be determined by the following formula (1)[10]:

$$CG_h = \frac{W_b \times (m_2 - m_1)}{m_T \times tan\,\theta} \quad (1)$$

Here, the parameters, CG_h= height of the centre of gravity (m), W_b=wheelbase length (m), m_1=front vehicle mass at ground level (kg), m_2= front vehicle mass at raised condition (kg), m_T= total vehicle mass (kg), $\theta=\sin^{-1}$(total raise-wheelbase length).

Using the characteristics of the vehicle found, the simulation model using OptimumDynamics could be created to illustrate the behaviour of the vehicle under various simulations. When the measured data of accelerometer was exported the OptimumDynamics model for simulation, noise recorded by the sensors were filtered bypassing the data through the Butterworth[11] filter in Matlab.During simulation, the rear suspension was made as the rear suspension was modelled with coil springs when in reality the vehicle uses a leaf sprung suspension system. The springs were defined with the correct characteristics however, so the only variation in the model is visual.

RESULTS AND DISCUSSION

Both the experimental investigation and computational analysis are discussed as follows:

Experimental Determination

The vehicle was weighed without occupants in the vehicle, which when taken into account would cause the symmetry to shift, dependent on the mass and layout of occupants. According to the experiment, the total corner mass (kg), sprung mass (kg) and unsprung mass (kg) respectively of the driver side (front) were 527, 472.52, 54.48; passenger side (front) 562, 507.20, 54.80; driver side (rear) 453, 353, 100; and passenger side (rear) 450, 350, 100. The front of the vehicle was only separated by 35kg which can be attributed to be factors such as the offset of the engine and the transfer case mass being influenced towards the driver side to allow the prop-shaft to navigate to the front differential, which is also offset towards the driver's side of the vehicle. In order to establish the unsprung mass of the vehicle, the mass distribution was used in conjunction with the displacement of the coil spring. The front spring preload was determined by using the Hooke's law (F=kx; where, F is load in kg-wt, k is stiffness const. and x is the displacement of the sprint at the defined load condition), which is 219.385 kg (with aftermarket assembly). As the measured corner mass at the front driver side corner was 527 kg, it is known that of the sprung segment of this measured mass will first need to exceed this spring preload of 219 kg prior to any further displacement of the spring occurs. The sprung mass on this side was calculated with the total displacement of spring for preloaded mass, which was 28 mm. Then the constant of Table 1 was used to determine the desired sprung mass from the Hooke's law. The unsprung mass corner mass was determined as the difference between total corner mass and sprung corner mass.

When measured from the ground plane with standard tyres fitted, the centre of gravity height was found as 716.8 mm (with standard suspension) and 757.9 mm (aftermarket suspension). As only the sprung mass is being raised with the suspension lift, the increase in height of the centre of gravity is not equal to the suspension lift. It can be seen here that the aftermarket suspension fitment relates to an increase in centre of gravity height of 41.1 mm compared to the 50 mm lifted. The stiffness constants were found as follows in Table 1. The aftermarket front spring is considerably stiffer as a medium duty spring was chosen to allow the future addition of accessories such as a bull bar without causing suspension sag. The rear spring chosen was a 'comfort' spring as the vehicle does not haul large loads, and as such, the high stiffness rating of the original springs was not required. It is expected that the softer rear spring will allow the suspension to more effectively absorb road imperfections, and an expected side effect is that the oversteer characteristics of the vehicle to be slightly reduced as the vehicle is able to more efficiently transfer load to the rear of the vehicle.

TABLE 1. Stiffness constants of various springs of suspension system

Description of constants	With original springs (N/mm)	With aftermarket springs (N/mm)
Front Spring Constant	71.31	165.495
Rear Spring Constant	104.045	40.74
Tyre Vertical Stiffness	296.262	296.262
Anti-Roll Bar Stiffness	21.89	52.45

From the measured spring and wheel travel, the motion ratio (ratio between wheel travel and spring travel) for the front and rear suspension setups were found as 2.08 and 1.5 for front and rear suspensions respectively.Using the

CAD tool, the roll centres for both the standard and aftermarket suspension setups were found. The difference in height between the roll centre height and the centre of gravity height is known as the roll moment, which is the primary contributing factor to how much chassis roll the vehicle will experience. Standard suspension front roll centre height was -21.35 mm, and that of aftermarket suspension was -41.29 mm.

Simulation Results

In order to test the model under various scenarios, experimental data was gathered from the vehicle. In case of input data collection from experiment, this experimental data was limited to what was able to be gathered legally on public roads due to project constraints. The lateral acceleration and body roll were measured. Lateral acceleration is useful to contribute towards load transfer over the suspensions and it's a key handling characteristic of the vehicle. The measured body roll was used to validate the simulation result, i.e. comparing simulation result of body roll with experimental result instead of using as input. Various other characteristics, e.g. suspension geometry, centre of gravity height and roll centre height, etc. can be explained with the validation of body roll. Fig. 3(left side) is the filtered accelerometer data that was used for the simulation testing at 80 km/h. It is important to note that this is simply set up as a magnitude, not taking into account direction.

Validation of Simulated Results with Experimental Determinations

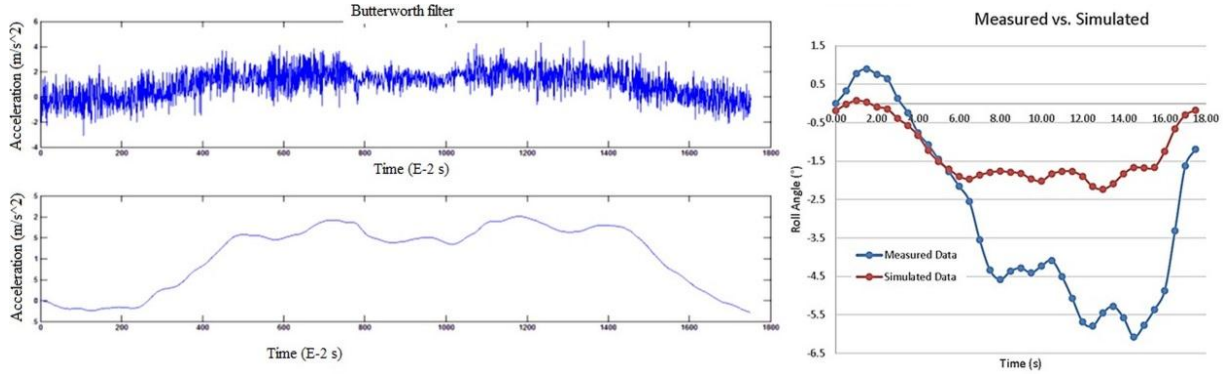

FIGURE 3. Filtration of acceleration data (left), and comparison between measured and simulated roll angle (right)

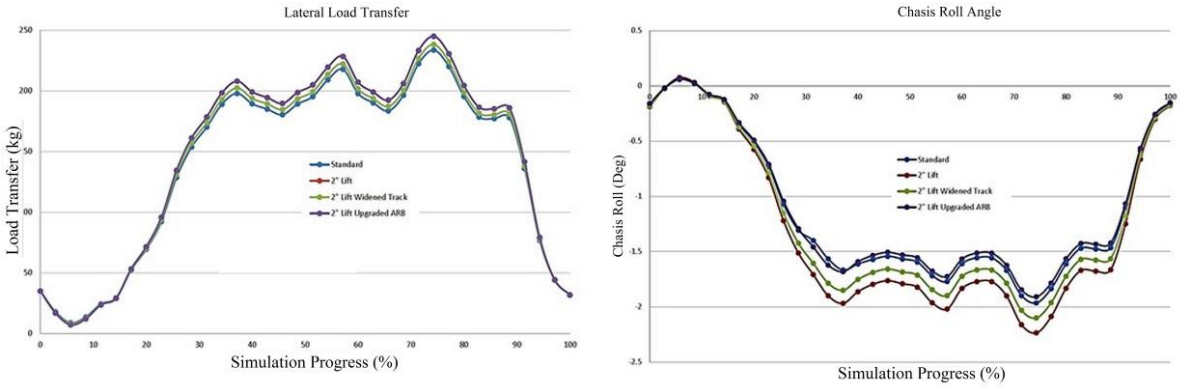

FIGURE 4. Lateral load transfer (left) and chassis roll angle (right) variation for experimental and simulated investigations

Figure3 shows the comparison of the simulated and measured data of the constant radius corner negotiated at a constant 80 km/h. It is observed in this figure that the degree of roll angle achieved by the actual vehicle is significantly higher than that was shown by the simulation software. The simulation peaks the body roll at 2.24 degrees in comparison to the measured 6.08 degrees, a variation of 271 percent. As discussed, the cause of this variation is likely due to the experimental nature used to evaluate the specifications of the vehicle. Another factor to be taken into consideration is that the software uses a steady state simulation method, indicating that the dampening

characteristics of the shock absorbers are not taken into account. This could have a considerable effect on the accuracy of the results.

Moreover, Fig. 4 shows the results of experimental and simulated investigation for total load transfer with and without modification. It shows that the total load transfer is reduced from 244.95 kg to 238.18 kg (i.e. ~2.9% reduction) with the track increase from the simulated results. As the lateral load transfer component is only dependent on the centre of gravity height, wheel track width and the lateral acceleration experienced, the upgraded anti-roll bar will not have any effect on this major contributor towards the total load transfer. The upgraded anti-roll bar acted to stiffen up the vehicle, reducing the body roll experienced, i.e. effect on the dynamic load transfer caused by the motion of the centre of gravity of the sprung mass. Unfortunately, at this small displacement of chassis roll, the dynamic load transfer is so small that the effect of the upgraded anti-roll bar is negligible and cannot be seen in the reduction of the total load transfer. When observing the chassis roll angle in Fig. 4 (right side), it can be seen that when the upgraded anti-roll bar is fitted, the roll angle achieved by the vehicle is actually reduced to a level below that of when the standard suspension is fitted. It could be observed from this figure that the dynamic load transfer component is actually lesser than the standard suspension with the aftermarket suspension lift and the upgraded anti-roll bar. It has been observed here how the stiffer sway bar could be more effective at higher lateral accelerations as the potential dynamic load transfer components increased from the higher potential roll angles achieved by the vehicle.The comparative analysis of load distribution on track and anti-roll bar showed that the load was transferring from front to rear, which was also the similar case with standard suspension. Besides, the widened wheel track and upgraded anti-roll bar have no effect on the load transfer towards the rear of the vehicle.

CONCLUSION

The vehicle model which was considered in this experiment was Mitsubishi Triton 4WD. The effect of modifying the vehicle by fitments of suspension lift, widened wheel track and upgraded front anti-roll bar were analysed both experimentally and computationally with some limitations in each sections. Without taking into consideration the effects of the damping effects of the standard and aftermarket shock absorbers, the simulation results showed the predicted results of enhanced tendency towards roll angle due to the increase in roll moment with just the fitment of the suspension lift. The softer rear springs also demonstrated a slightly improved ability for the load to transfer towards the rear of the vehicle, illustrating a slightly reduced tendency to demonstrate oversteering characteristics. With the simulation of the fitment of the other modifications aimed to improve the characteristics of the raised vehicle, the vehicle showed a reduced tendency towards roll angle due to the stiffened anti-roll bar and the maximum increased wheel track demonstrated reduced lateral load transfer and body roll. Even with these modifications however, the decrease in load transfer is minimal in comparison to what was expected. The aftermarket suspension actually showed less roll angle than that was found in the simulated results due to no damping effect consideration in the software. As a result, the simulated displayed higher roll moment and greater centre of gravity height. From this it can be assumed that the standard damping used in the vehicle is considerably ‘softer’, designed for comfort, whereas the aftermarket is ‘harder’, designed to reduce the dynamic load transfer component and other handling effects of excessive body roll such as undesirable camber gains. To observe real effect the modifications, the damping effect of the suspensions, which was not considered as the aftermarket suspension dampers should be considered. A better and expensive computational tool like MSC Adams could be more effective in providing details analysis. Moreover, the facility of more sophisticated but safe experimental investigation and data management could be beneficial to provide industry scale results of modifying the 4WD vehicles for off-road conditions.

ACKNOWLEDGEMENTS

The authors would like to acknowledge the significant contribution by Central Queensland University.

REFERENCES

1. 4wdonline, in *4WD Suspension* (http://www.4wdonline.com/A.hints/Suspension.html, 2013).
2. M. Keall and S. Newstead, Report No. 262, 2007.
3. AAMVA, in *Study Findings* (American Association of Motor Vehicle Administrators, 2003).
4. R. Elvik, A. Hoye, T. Vaa and M. Sorensen, *The Handbook of Road Safety Measures*, 2nd ed. (Emerald Group Publishing Limited, UK, 2009).

5. E. A. Harwin and H. K. Brewer, Journal of Traffic Medicine, Vol. 18, No. 3, 1990, p. 109-122 (1990).
6. TMR, in *Vehicle Modifications* (The State of Queensland (Department of Transport and Main Roads), Australia, 2015).
7. NCOP, in *Section LS Tyres, Rims, Suspension and Steering (Version 2)* (Australian Government-Department of Infrastructure and Transport in Canberra, Australia, 2011).
8. Dobinsons, (Dobinsons Spring & Suspension™), Vol. 2015.
9. F. Puhn, *How to Make Your Car Handle*. (H. P. Books, 1976).
10. Longacre, in *http://www.longacreracing.com/technical-articles.aspx?item=42586* (Longacre Racing Products, 2002), Vol. 2015.
11. Butter, in *MATLAB butter* (MathWorks, 2015).

ICME2015

International Conference on Mechanical Engineering 2015
(ICME 2015) 18 – 20 December, 2015, Dhaka, Bangladesh

Paper ID : 605

Effect of Variable Physical Properties on the Thermal Behavior of Thin Metallic Wires under a DC Field

Avishek Kumar Dey[1,a)], Abhishek Kumar Ghosh[1,b)] and S. Reaz Ahmed[1,c)]

[1]*Department of Mechanical Engineering, Bangladesh University of Engineering and Technology, Dhaka-1000, Bangladesh*

[a)]Corresponding author: avishek.protik@gmail.com
[b)]abhishek.ghosh053@gmail.com
[c)]srahmed@me.buet.ac.bd

Abstract. The effect of variable physical properties on the electro-thermal response of a thin metallic wire is investigated under a uniform direct current field. A general governing differential equation is derived for steady-state heat conduction in conductive wires with surface convection and Joule heating, in which the associated material as well as physical properties of the thermal and electrical problems are modeled as a function of temperature. The resulting nonlinear boundary-value problem is then solved by converting into an equivalent initial-value problem through a trial-and-error based numerical scheme. The electro-thermal characteristics of the wire are realized to be affected significantly when the physical properties are expressed as appropriate functions of temperature.

INTRODUCTION

Day by day, the electronic devices are getting smaller and smaller. As a result, the accuracy of the corresponding analyses of electro-thermal behavior of current carrying devices is becoming more and more important. The flow of current through conductors induces Joule heating, which, in turn, causes the raise in temperature of the conductor. This increase in temperature is realized to be one of the most influential factors for the failure of modern electronics devices. The resulting state of temperature of the conductor eventually affects various physical properties associated with the conducting material. However, for simplicity, the variations of properties of the conducting material are neglected for most of the electro-thermal analyses, which makes the analysis limited to practical applications, especially when the rise in temperature is relatively high.

The problem of heat conduction in a conducting material under direct current flow has been explained theoretically by Carslaw and Jaeger [1]. Greenwood and Williamson [2] treated the case of a conductor subjected to a direct current flow, in which temperature dependent material properties were considered. The method was further extended by Jang et al. [3] to give a general solution to the coupled nonlinear problem of steady-state electrical and thermal conduction across an interface between two dissimilar half spaces. Heat conduction in a symmetric body subjected to a current of symmetric input and output was analyzed by Saka et al. [4] by introducing a new electro-thermal parameter, Joule heating residue vector. Recently, the temperature field of a 2D electro-thermal problem near the corner composed of two dissimilar materials in an angled metal line has been analyzed under a direct current flow by Saka and Zhao [5]. On the other hand, the use of temperature dependent thermal properties is emphasized by several researchers in designing thermal fins [6, 7].

A nonlinear analysis of electro-thermal response of a conducting wire of dissimilar materials has been reported by Rahman et al. [8], in which variable thermal conductivity was assumed. Ghosh et al. [9] predicted the elector-thermal response of FGM lines subjected to a DC field. A new analysis of heat conduction-convection problem of a thin metallic wire coupled with an electrical problem is reported in the present paper. Here, all the physical properties involved in the analysis, namely, thermal conductivity, electrical resistivity and convection coefficient are assumed to be functions of temperature. The resulting nonlinear boundary-value problem is then numerically solved by converting into an equivalent initial-value problem through a trial-and-error based numerical scheme. Finally, the effects of vari-

able physical properties are realized by comparing the present results with those obtained considering the properties independent of temperature.

MATHEMATICAL FORMULATION

Electrical Problem

Ohm's law for the distribution of electrical potential, φ in a conductive material (resistivity, ρ),

$$\frac{d\varphi}{dx} = -\rho(x)J(x) \tag{1}$$

The differential equation which governs the distribution of electric potential within the material body can be obtained by applying divergence operator on equation (1), which eventually takes a form like,

$$\frac{d^2\varphi}{dx^2} = -\left(J(x)\frac{d\rho(x)}{dx} + \rho\frac{dJ(x)}{dx}\right) \tag{2}$$

For uniform cross sectional area, A current density J will be constant. Hence, the equation (2) becomes

$$\frac{d^2\varphi}{dx^2} = -J(x)\frac{d\rho(x)}{dx} \tag{3}$$

For the solution of electrical problem, end conditions of the metal line are simulated by following relation,

$$\frac{d\varphi}{dx} = \pm\rho J \tag{4}$$

Negetive sign of equation (4) is applicable to the end where the current is being injected and positive sign corresponds to the current outlet port.

Thermal Problem

The general governing equation for heat transfer in a metallic wire (perimeter, p), under steady state condition, the surface of which losses heat by convection to the surrounding atmosphere (T_∞) is,

$$\frac{1}{A}\frac{d}{dx}\left[Ak\frac{dT}{dx}\right] - \frac{Hp}{A}\left[T - T_\infty\right] + g = 0 \tag{5}$$

Due to the application of direct current field, joule heating, g is induced in the wire. By incorporating the effect of joule heating and geometrical uniformity of wire equation (5) becomes

$$\frac{d}{dx}\left[k\frac{dT}{dx}\right] - \frac{Hp}{A}\left[T - T_\infty\right] + \frac{1}{A_m}\rho J^2 = 0 \tag{6}$$

Here, A_m is mechanical equivalent of heat. Thermal conductivity, k of metallic materials is a function of temperature and, in general, it decreases with temperature. Amongst the common metals, silver shows the highest thermal conductivity whereas bismuth shows the lowest. From the available experimental data [10] thermal conductivity of copper can be well approximated as a quadratic function of temperature for the range shown below, as follows.

$$k\,(T) = a + bT + cT^2 \qquad [\ 200 \le T \le 800\ K\ ] \tag{7}$$

Where, the constants, $a = 433.4$, $b = -0.1179$ and $c = 4.297\times10^{-5}$. On the other hand, resistivity of a metal generally increases with temperature and is represented by the following equation

$$\rho\,(T) = \rho_0\left[1 + \alpha\,(T - T_0)\right] \tag{8}$$

Here, α is temperature coefficient of resistivity (for copper, $\alpha_{Cu} = 0.00386\ K^{-1}$) and ρ_0 is the resistivity at T_0 ($273K$). Convection heat transfer coefficient, H depends on several factors like, fluid properties, type of convection

heat transfer (natural/forced), surface temperature, as well as geometry of the solid surface. Considering transfer of heat from metallic wire to the surrounding air through natural convection, the variation of convective heat transfer coefficient can be determined as a function of surface temperature from the following relation:

$$H(T) = \frac{Nu(T)\,k_f(T)}{d} \tag{9}$$

Considering the metallic wire as a horizontal cylinder, the average Nusselt number, Nu for natural convection can be expressed as a function of Rayleigh (Ra) and Prandtl (Pr) numbers through the following empirical correlation [11]

$$Nu = \left[0.6 + \frac{0.387Ra^{\frac{1}{6}}}{\left[1 + \left(\frac{0.0559}{Pr}\right)^{\frac{9}{16}}\right]^{\frac{8}{27}}}\right]^2 \tag{10}$$

The Rayleigh number is again a function of various parameters, like, Prandtl number, kinematic viscosity and surface temperature. Therefore, from equation (9) and (10) it can be said that convection coefficient is a function of thermal conductivity (k_f), kinematic viscosity and Prandtl number of the surrounding fluid. These properties associated with the surrounding air generally vary with temperature, which are generally evaluated at film temperature, an average of surface and ambient temperatures. Since the surface temperature varies along the axis of the wire, the fluid properties must be evaluated at each film temperature. Empirical relations of various air properties with temperature has been developed using available experimental data [12] by regression models which are shown in Table 1. Expressing thermal conductivity, electrical resistivity and convective coefficient as a function of temperature, Eq. (6) can be rewritten in a more general form as follows:

TABLE 1. Empirical relations of required air properties with temperature

Properties	**Empirical relations with temperature** ($^\circ C$)	**Range of temperature**
Thermal conductivity of air, k_a	$k_a = 2.36 \times 10^{-2} + 7.427 \times 10^{-5}T - 1.956 \times 10^{-8}T^2$	
Kinematic viscosity of air, ν	$\nu = 1.314 \times 10^{-5} + 9.570 \times 10^{-8}T + 6.588 \times 10^{-11}T^2$	$[\,-30 \le T \le 700\,^\circ C\,]$
Prandtl number of air, Pr	$Pr = 0.6297 + 0.1061 \times \mathrm{e}^{-3.983\times10^{-3}T} + 1.064 \times 10^{-4}T$	

$$\left(a + bT + cT^2\right)\frac{d^2T}{dx^2} + [b + 2Tc]\left(\frac{dT}{dx}\right)^2 - \frac{H(T)p}{A}[T - T_\infty] + \frac{1}{A_m}\rho_0\,[1 + \alpha\,(T - T_0)]\,J^2 = 0 \tag{11}$$

For the present thermal problem, the temperatures at the two ends of the wire are assumed to be known. It is mentioned that all possible physical conditions at the ends can readily be accommodated.

Electro-thermal heat flux

Electro-thermal heat flux of a conductive wire is realized as summation of thermal heat flux and heat flux representing the effect of electrical heating in the wire. The overall heat flux vector (P) related to the coupled electro-thermal problem, which is known as the joule heating residue vector [4], is defined by the following equation.

$$P = -k(T)\;grad[T + \frac{A_m}{2k(T)\rho(T)}\varphi^2] \tag{12}$$

METHOD OF SOLUTION

Analytical solution to the present problem would be extremely difficult because of the nonlinear characteristic of the governing differential equation. Therefore, attempt is made to solve the present steady-state heat conduction-convection nonlinear boundary value problem using the classical 4^{th}-order R-K method. The problem is first converted into an equivalent initial-value problem by using shooting technique. For this purpose, the governing equation (11) of the thermal problem has been converted into a set of 1st order equations as follows:

$$\frac{dT}{dx} = z \tag{13}$$

$$\frac{dz}{dx} = \frac{\left[-(b+2Tc)z^2 + \frac{H(T)p}{A}[T(x)-T_\infty] - \frac{1}{A_m}\rho_0[1+\alpha(T-T_0)]J^2\right]}{(a+bT+cT^2)} \tag{14}$$

The above set of equations is solved assuming a suitable initial value of z. Then a trial and error based iterative method has been used to find more precise value of z, which eventually converges the solution to satisfy the given boundary condition at $x = L$. In a similar fashion, the governing equation for electrical problem equation (3) is also converted into a set of first-order equation as follows.

$$\frac{d\varphi}{dx} = w \tag{15}$$

$$\frac{dw}{dx} = -J\rho_0\alpha z \tag{16}$$

The resulting set of equations are then solved to find the potential distribution along the wire, for which the nodal temperature and temperature gradient are used from the solution of previously solved thermal problem coupled with electrical problem. At last electro-thermal heat flux distribution of the wire is evaluated by nodal temperature gradient, nodal potential, nodal thermal conductivity and electrical resistivity of the wire using equation (12).

STATEMENT OF ELECTRO-THERMAL PROBLEM

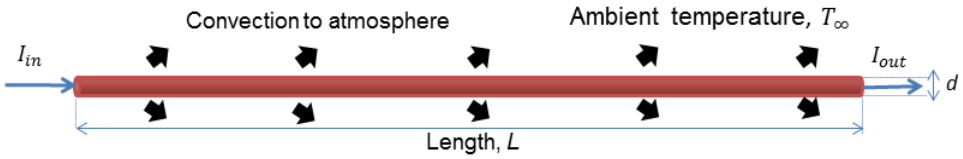

FIGURE 1. Model of a uniform metallic wire under a DC field

The physical model of a uniform metallic wire under current flow is delineated in Fig. 1. For the present analysis material of the wire is considered as copper. The overall length, L and diameter, d of the wire is considered as 50 cm and 1 mm, respectively. For the thermal problem, fixed temperature end conditions are used and the end temperatures are assumed to be equal to the ambient temperature ($300K$). The surface of the wire is assumed to transfer heat by natural convection to the surrounding fluid (air). The wire is considered be subjected to a 5 Amp direct current flow and thermal conductivity, electrical resistivity, and convection coefficient are considered to vary with surface temperature of the wire.

ANALYSIS OF ELECTRO-THERMAL BEHAVIOR

Electro-thermal behavior of a copper wire is analyzed under different considerations of property variation along with change in temperature and compared. Fig. 2(a) compares the temperature distribution along the axis of the wire for three different condition of property variation, namely, all the properties (k, ρ, H) independent of temperature, all the properties dependent on temperature, k and ρ depend on temperature but H is independent of temperature. The figure depicts a significant effect of three different considerations on the temperature distribution of the metal wire. It is seen that maximum temperature along the wire is highest for the case when k and ρ were assumed dependent on temperature, but H is constant. This is because of the fact that thermal conductivity decreases and resistivity increases with temperature, both of which eventually affect the increase of maximum wire temperature. Maximum wire temperature is found to be the lowest when all the physical properties are assumed to be dependent on temperature. Thus, it can be concluded that temperature distribution is highly dependent on convection heat transfer coefficient which is a function of Nusselt number and it increases with temperature. This increase in Nusselt number also increases the convection coefficient, which, in turn, causes more heat to transfer through convection from the surface, thereby decreasing the surface temperature. Fig. 2(b) shows the temperature dependent effect of property on the distribution of electrical potential over the wire. The figure shows no substantial effect of temperature dependency of the properties, as both the curves almost coincide with each other. Fig. 2(c) shows the distribution of electro-thermal heat flux along the wire

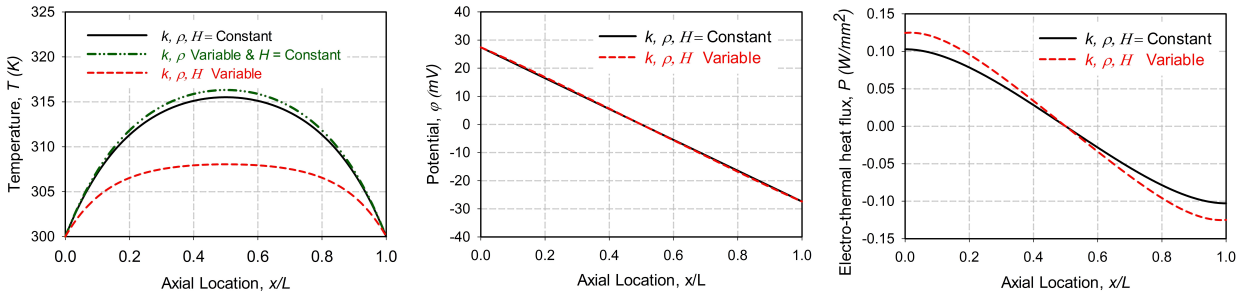

(a) Temperature distribution (b) Potential distribution (c) Electro-thermal heat flux

FIGURE 2. Comparison of (a) Temperature distribution and (b) Potential distribution and (c) Electro-thermal heat flux distribution of pure copper wire considering all the physical properties as constant and varying with temperature for constant temperature boundary condition.

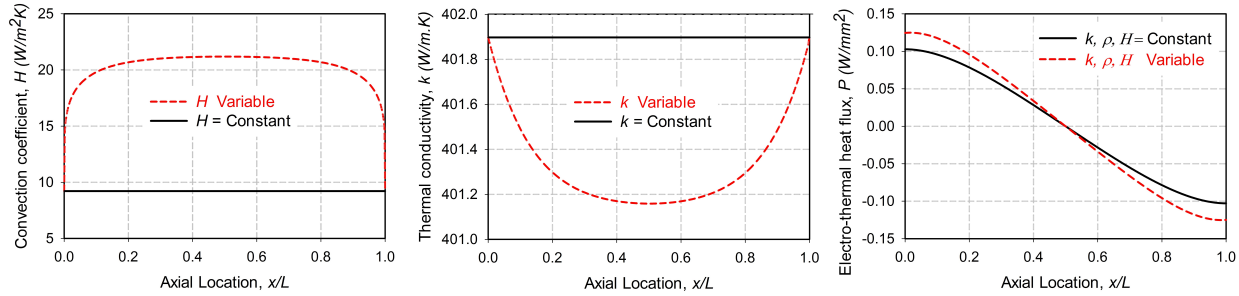

(a) Convection coefficient (b) Thermal conductivity (c) Electrical resistivity

FIGURE 3. Variation of (a) Convection coefficient, (b) Thermal conductivity (c) Electrical resistivity with temperature along the axial direction of the wire.

length for two different states of property variation, namely, variable and constant physical properties. In this case, the distribution assumes a higher magnitude of heat flux for the case of temperature dependent property variation. However, the nature of variation is found to be almost similar in both the cases.

Figure 3 depicts the effect of temperature variation on the various material properties of interest. The resulting variations of convective heat transfer coefficient, thermal conductivity and the electrical resistivity along the length of the copper wire are shown in Figs. 3(a), (b) and (c), respectively. When these properties are assumed to be independent of temperature, they will naturally remain constant throughout the length of the wire. However, if the analysis is carried out considering them to be the functions of temperature, they are identified to be the functions of spatial coordinate of the wire, as the current flow causes the temperature to vary along the wire length. Moreover, the variations of the properties show significant change in magnitude when they are considered to be dependent on temperature. Finally, the maximum change in the magnitude of properties due to temperature dependency is observed at the mid-length position of the wire, as this is the location where maximum rise in temperature is observed.

CONCLUSION

A new investigation of thermal response of a metallic wire has been conducted under the influence of a direct current field, in which all the physical properties associated with the electro-thermal problem are assumed to be functionally related to the primary dependent variable, i.e, temperature. The solution of the resulting nonlinear boundary-value problem shows that thermal behavior is affected significantly by the temperature-dependent properties, whereas that of electrical potential is less affected by the properties. The present investigation also suggests that appropriate temperature-dependent functional relationships of the physical properties would be of utmost importance for accurate and reliable prediction the maximum current carrying capacity or the electrical failure of the conducting wires [13], especially with solder joints.

REFERENCES

[1] Carslaw, Horatio Scott, and John Conrad Jaeger. "Conduction of heat in solids." Oxford: Clarendon Press, 1959, 2nd ed. 1 (1959).

[2] Greenwood, J. A., and J. B. P. Williamson. "Electrical conduction in solids. II. Theory of temperature-dependent conductors." Proceedings of the Royal Society of London A: Mathematical, Physical and Engineering Sciences. Vol. 246. No. 1244. The Royal Society, 1958.

[3] Jang, Yong Hoon. "Electrothermal crack analysis in a finite conductive layer with temperature-dependent material properties." Journal of Physics D: Applied Physics 38.14 (2005): 2468.

[4] Saka, M., Y. X. Sun, and S. Reaz Ahmed. "Heat conduction in a symmetric body subjected to a current flow of symmetric input and output." International Journal of Thermal Sciences 48.1 (2009): 114-121.

[5] Saka, M. and Zhao, X., 2012. Analysis of the temperature field near a corner composed of dissimilar metals subjected to a current flow, International Journal of Heat and Mass Transfer, 55, p. 6090-6096.

[6] Laor, K., and H. Kalman. "Performance and optimum dimensions of different cooling fins with a temperature-dependent heat transfer coefficient." International Journal of Heat and Mass Transfer 39.9 (1996): 1993-2003.

[7] Razelos, P., and K. Imre. "The optimum dimensions of circular fins with variable thermal parameters." Journal of Heat Transfer 102.3 (1980): 420-425.

[8] Rahman, SM Mahbobur, Anik Adhikary, and S. Reaz Ahmed. "Nonlinear analysis of electro-thermal response of a conducting wire of dissimilar materials with variable thermal conductivity." Proc. of the ICME, Dhaka. 2011. 1-6.

[9] Ghosh, A. K., Anik Adhikary, and S. Reaz Ahmed. "Prediction of electro-thermal responses of non-uniform functionally graded metal lines under a direct current field." Procedia Engineering 56 (2013): 807-813.

[10] "Thermal Conductivity: Copper." efunda. eFunda, Inc. Sunnyvale, CA 94088, 17 Feb. 2013. Web. 03 Aug. 2015.

[11] Churchill, Stuart W., and Humbert HS Chu. "Correlating equations for laminar and turbulent free convection from a horizontal cylinder." International Journal of Heat and Mass Transfer 18.9 (1975): 1049-1053.

[12] Cengel, Y. A. "Heat and mass transfer: A practical approach." (2007). Appendix 1, Table A-15.

[13] Syed, Ahmer. "Factors affecting electromigration and current carrying capacity of FC and 3D IC interconnects." Electronics Packaging Technology Conference (EPTC), 2010 12th. IEEE, 2010.